JUSTUS-LIEBIG-
UNIVERSITÄT
GIESSEN

Institut für theoretische Physik

Dissertation

Dynamic Critical Phenomena in the Classical Approximation on a Lattice

Author
Dominik Schweitzer

Supervisor
Prof. Dr. Lorenz von Smekal

12. Mai 2021

Abstract

The critical behaviour of a relativistic scalar field theory with Z_2 symmetry is investigated near a second-order phase transition. Two sets of dynamic equations are employed, allowing to control conservation laws of both order parameter and energy density. We calculate spectral functions of the order parameter as well as unequal-time correlation functions of the energy momentum tensor at zero and non-vanishing spatial momenta from first-principles classical-statistical lattice simulations in real-time. For both, we investigate general properties and relevant degrees of freedom in distinct regions of the phase diagram. Close to the critical point, we find signatures of dynamic scaling behaviour and calculate the dynamic critical exponent z controlling the divergence of the critical time scale. For both the order parameter spectral function as well as the energy density autocorrelation, we extract universal dynamic scaling functions.

Modifying the simulation framework to include dynamically changing temperature and external field allows us to study non-equilibrium phenomena. For the special case of instant quenches to the critical point, we identify universal scaling behaviour controlled by the initial magnetization, and calculate the related additional dynamic critical exponent. We extract the universal non-equilibrium scaling functions for the evolution of both the order parameter as well as the correlation length.

Zusammenfassung

In dieser Arbeit wird das kritische Verhalten einer relativistischen skalaren Feldtheorie mit Z_2-Symmetrie in der Nähe eines Phasenübergangs zweiter Ordnung untersucht. Zwei fundamental unterschiedliche Bewegungsgleichungen werden verwendet, die es erlauben, sowohl Energieerhaltung als auch Erhaltung des Ordnungsparameters zu kontrollieren. Wir berechnen sowohl Spektralfunktionen des Ordnungsparameters als auch nichtgleichzeitige Korrelationsfunktionen des Energie-Impuls-Tensors mithilfe klassisch-statistischer Realzeit-Gittersimulationen. Für beide werden generelle Eigenschaften und relevante Freiheitsgrade in unterschiedlichen Regionen des Phasendiagrams untersucht. Nahe des kritischen Punktes finden wir Hinweise auf dynamisches Skalierungsverhalten und berechnen den dynamisch-kritischen Exponenten z, der die Divergenz der charakteristischen Zeitskala kontrolliert. Für sowohl die Spektralfunktionen des Ordnungsparameters als auch Korrelationsfunktionen des Energie-Impuls-Tensors extrahieren wir universale dynamische Skalenfunktionen.

Die Modifikation des Simulationsapparats hin zu dynamisch veränderlicher Temperatur und externem Feld erlaubt uns das Studium von Nichtgleichgewichtsphänomenen. Im hier betrachteten Spezialfall eines instantanen Quenchs auf den kritischen Punkt identifizieren wir Skalierungsverhalten mit der initialen Magnetisierung und berechnen den entsprechenden zusätzlichen dynamisch-kritischen Exponenten θ. Wir extrahieren universelle Nichtgleichgewichts-Skalenfunktionen für die Zeitentwicklung sowohl des Ordnungsparameters als auch der Korrelationslänge.

For my dear Elka,
whose snoring accompanied
writing this thesis.

Contents

1 Introduction **5**

2 Real-time field theory **9**
2.1 From the Keldysh contour to classical fields 9
2.2 Dynamical Models 19
2.3 Spectral function 27

3 Technical realization **29**

4 Order parameter dynamics in equilibrium **34**
4.1 Static universality and scale setting 34
4.2 Spectral functions of the order parameter 41
4.3 Critical dynamics and scaling functions 53
4.4 Conclusions 78

5 Energy-momentum tensor on the lattice **80**
5.1 Definition 81
5.2 Transport coefficients 88
5.3 Equilibrium dynamics of the energy density 96

6 Non-equilibrium phenomena **106**
6.1 Setup and Theory 107
6.2 Non-equilibrium scaling 110
6.3 Conclusions 116

7 Summary & Outlook **117**

Appendices **129**

A Vertex structure **130**

B Hydrodynamic Green's functions **132**

C Breit-Wigner function **134**

D Structure of the spectral function at low temperatures **137**

1 | Introduction

The theory of quantum chromodynamics (QCD) may well be one of the greatest achievements of theoretical physics in the last century. Describing the strong interaction between quarks and gluons, it provides a description of physical processes determining the structure and properties of hadronic matter and the early universe. In the last decades, we have uncovered significant parts of the phase diagram of QCD. Due to its strong coupling, its relevant low-energy degrees of freedom are given by hadronic bound states. At high temperatures or densities, these bound states dissolve, and one finds that its fundamental building blocks appear asymptotically free in a quark-gluon plasma (QGP) phase.

From lattice simulations, it is known that the transition from hadronic matter to QGP is a smooth cross-over for very low or vanishing net baryon density [1, 2, 3]. On the other hand, considerations of effective theories and models provide ample evidence that in addition to the well-known liquid-gas transition, there is at least one more first-order phase transition on the zero-temperature axis [4, 5]. At higher baryon chemical potential, chiral symmetry is no longer spontaneously broken. Several model calculations suggest that the approximate chiral symmetry restoration happens via a first-order transition [6, 7]. By those observations one is lead to suspect the existence of a second-order phase transition at finite temperature and baryon density, at the critical endpoint (CEP) of a first-order transition line separating phases of spontaneously broken and nearly-restored chiral symmetry.

The search for the QCD critical endpoint has gained a substantial amount of attention in the span of the past decade, from the theoretical as well as the experimental side alike [8, 9]. Dedicated heavy-ion collision experiments currently set up at RHIC as well as the future FAIR and NICA facilities are equipped to probe the QCD phase diagram at large baryon densities, the region where the CEP supposedly is located. This leaves theorists with the challenge of developing methods for extracting its precise location from the obtained data. Unfortunately, the go-to workhorse for first-principle calculations, namely lattice QCD, currently cannot address this region of the phase diagram due to the sign problem [10]. One therefore has to fall back to employing effective theories, making the most of prior knowledge about the critical behavior [11].

When a thermodynamic system comes close to a critical point, competing processes maximizing entropy and minimizing free energy cause strong fluctuations on all length scales. These in turn lead to scale-invariant physics and thus universal behavior, meaning microscopically different systems are governed by quantitatively identical universal scaling functions only differing by overall amplitudes. This allows extremely efficient effective descriptions of critical phenomena via simple models with matching universality classes. Considering the nature of the QCD critical point as endpoint of the first-order chiral transition, one finds that it belongs to the same

static universality class as the three-dimensional Ising model [12].

However, the collision experiments used to probe the QCD phase diagram are dynamic processes, and it is therefore imperative to develop an understanding for signatures of the CEP in dynamic observables, such as multi-time correlation functions and relaxation rates. To fully characterize the dynamics of critical phenomena, one must additionally take into account the equations of motion of the system. Incorporating conservation laws and dynamic mode couplings, Halperin and Hohenberg [13] devised a scheme of dynamic universality classes called "Models." In some of these, the dynamic critical exponent z, which controls the divergence of time scales relative to that of the length scales, follows from static exponents via hyperscaling relations. Generally however, the precise determination of z presents a significant numerical challenge, even in deceptively simple cases like Model A, corresponding e.g. to the Ising model coupled to a heat bath [14].

In this study we investigate a relativistic scalar theory in the static Z_2 Ising universality class of the QCD CEP. Employing different equations of motion, we examine four different dynamic universality classes, namely Models A, B, and their counterparts with energy conservation. While the dynamic universality class at the QCD CEP is believed to be that of Model H [15], we focus on these simpler Models not requiring the explicit treatment of an additional conserved transverse vector field. We reason that this course of action provides important steps toward characterizing critical real-time dynamics in a systematic fashion, and pave the way to treat more complicated systems such as Model H in the future, which will then be of direct relevance to QCD.

An important mainstay for our analysis of dynamic critical phenomena is based on real-time correlation functions. Specifically, we thoroughly investigate spectral functions of the order parameter. Spectral functions are of great interest in many areas of condensed matter, nuclear and particle physics due to the abundance of information they contain. In strong-interaction matter, they are essential for our understanding of the physics ranging from the Early Universe to heavy-ion collisions and neutron stars. Containing the spectrum of all possible excitations of the system in the given channel, they can be used to identify the relevant degrees of freedom for effective descriptions. Furthermore, one typically can also obtain transport coefficients from particular low-energy limits of spectral functions [16].

Emergent dynamic critical phenomena close to a second-order phase transition strongly effect spectral functions. The characteristic time scale of the system diverges, and thus slow modes dominate the dynamics, leading to the formation of infrared-divergent power laws. The spectral indices of those power laws are controlled by both the dynamic critical exponent z as well as static critical exponents of the system. Additionally, one can show that scale invariance with respect to both time and space implies that, similar to static quantities, the low-energy behavior of spectral functions is fully described by universal scaling functions.

In order to capture these highly non-trivial infrared phenomena, the spectral functions must necessarily be calculated non-perturbatively. This is generally very challenging for the otherwise highly successful equilibrium field theory methods in Euclidean spacetime, as for example first-principles lattice QCD simulations. Additionally, it is necessary to analytically continue correlators in Euclidean time to the real-time domain. Analytic continuation based on a finite amount of points is however a numerically ill-posed inverse problem. While different reconstruction

schemes exist, ranging from Maximum Entropy methods [17, 18, 19], the Backus-Gilbert method [20], Tikhonov regularization [21] or the Schlessinger-Point (or Resonances-via-Padé) method [22, 23] to Machine Learning [24], all of these come with limited ranges of applicability (see, e.g. Ref. [25] for a recent comparison). A powerful alternative to reconstructing spectral functions from Euclidean data is in principle provided by non-perturbative functional methods, e.g. based on 2-PI [26, 27], Dyson-Schwinger [28, 29, 30] or Functional Renormalization Group (FRG) equations [31, 32, 33, 34, 35, 36, 37, 38], as the functional equations can be analytically continued or even formulated directly on the closed-time path in order to actually calculate spectral functions from real-time correlation functions. However, in one way or another, all these functional methods require prescriptions to obtain a closed set of equations from an originally infinite hierarchy. Controlling truncation errors then becomes important for the systematics, and any prior knowledge of the structure of correlations in the theory is obviously beneficial as additional input or benchmark.

The classical-statistical framework lends itself here several reasons. Unlike Euclidean formulations, which are by construction limited to Hamiltonian-like, non-dissipative dynamics, the classical-statistical approach can be applied to any dynamical model. Furthermore, this approach is especially useful for studying critical phenomena, which are dominated by slow long-range modes. Since the classical theory at finite temperature becomes exact in the infrared, the universal part of the dynamics is captured exactly.

In this work, we calculate spectral functions of a single-component scalar field theory employing classical-statistical lattice simulations in real-time [39, 40, 41]. We use the fluctuation-dissipation relation or Kubo-Martin-Schwinger (KMS, [42, 43, 44]) condition to obtain the spectral function from the statistical function, which in the classical limit can be calculated from an elementary unequal-time correlation function of classical fields. Using different equations of motion, we study Models encompassing conservation laws of order parameter and energy density. We quantify the divergence of the characteristic time scale ξ_t in the vicinity of the critical point and extract the respective dynamic critical exponents for the different dynamic universality classes. Analyzing modes of the spectral function at finite spatial momenta, we extract new universal scaling functions governing the infrared limit of the dynamics close to the critical point.

Moreover, in an effort to bridge the gap to an effective classical model mapping the dynamics of Model H, we study the energy-momentum tensor of the lattice models. After some general considerations about its definition and effects of the reduced spatial translation symmetry, we focus on dynamic properties of the energy density. Applying the same methodology as for the order parameter, we calculate spectral functions of the energy density and investigate their general features. We show that one can observe similar scaling behavior in spectral functions respectively auto-correlation functions of components of the energy-momentum tensor, and extract the underlying universal scaling functions.

We do however not limit ourselves to equilibrium dynamics, since the machinery can trivially be extended to study non-equilibrium processes as well. First estimates have shown that in collision experiments closing in on the QCD CEP, the factor restricting the magnitude of critical effects is most likely finite time rather than finite system size [5, 45]. It is therefore vital to develop a precise understanding of non-equilibrium critical phenomena, and to find observables which retain enough

information to reconstruct the location of the critical point from final-state data [46, 47, 48].

By investigating the dynamics of Model A after a quench to the critical point, we determine the so-called initial-slip exponent θ' in addition to the dynamic critical exponent z. It turns out that the most reliable methods to this end make use of non-equilibrium phenomena, observing the process of thermalization at the critical point [49, 50, 51, 52, 53, 54, 55]. Using results for both exponents, we confirm that the evolution of both order parameter and correlation length in this scenario is governed by universal non-equilibrium scaling functions. Knowing these universal functions allows to make strong predictions about thermalization processes at the critical point with different initial conditions.

This thesis is organized as follows: The next chapter introduces the Keldysh formalism for describing real-time dynamics of quantum field theories, and how from there the classical-statistical limit naturally emerges, before introducing the specific models employed by us. It is followed by some remarks concerning the technical realization and implementation of numerics, to ease reproducibility and continuation of the project. The fourth chapter contains the results obtained for order-parameter dynamics in thermal equilibrium, starting with the static critical behavior, before presenting spectral functions of the order parameter and their universal dynamic critical behavior. Subsequently, we provide in the fifth chapter the definition of the energy-momentum tensor on the lattice. We provide some critical remarks on recent efforts to extract transport coefficients via Kubo relations, before presenting our results on the dynamic behavior of the energy density. The sixth chapter is then concerned with non-equilibrium processes and universal behavior after a quench to the critical point. Finally, we provide conclusions as well as an outlook on possible future projects in the last chapter. Several appendices contain some mathematical intricacies concerning the definition of diffusive dynamics, properties of the Breit-Wigner function and details on the order-parameter spectral functions at low temperature.

Parts of this thesis concerning the order-parameter dynamics in equilibrium of Models A and C have already been published in [56]. Publications on Models B and D as well as non-equilibrium phenomena are currently in preparation.

2 | Real-time field theory

2.1 From the Keldysh contour to classical fields

The quantum field theory (QFT) framework developed over the past century is a flexible and powerful language, and has been used to describe an immense range of physical problems. Its most popular manifestation as finite-temperature equilibrium QFT employs the imaginary-time Matsubara formalism [57]. We introduce here the much more powerful non-equilibrium QFT developed by Schwinger [58] and Keldysh [59], which for reasons probably related to its higher complexity has not yet made its way into standard undergraduate curricula. This framework allows us to ask questions about real-time quantities without undergoing the often cumbersome analytical continuation procedure from imaginary to real time. It also provides a natural connection to the classical-statistical systems used in this project.

Some details and tedious algebra will be skipped in favor of readability; for those, the reader is referred to a relevant textbook such as the one by Kamenev [60], chapters one through five.

2.1.1 Closed time path

Assume a general quantum many-body system, the state of which is at some time $t \to -\infty$ deep in the past known to be described by the many-body density matrix $\hat{\rho}(-\infty)$, and whose dynamics are governed by some (possibly time-dependent) Hamiltonian $\hat{H}(t)$. Critically, we assume that at $t = -\infty$ there are *no interactions* in the system, although they may adiabatically emerge at some finite time prior to any observation. The Hamiltonian $\hat{H}(t)$ may however contain truly time-dependent perturbations at finite times, driving the system away from thermal equilibrium. Generally, the time evolution of such a system is then given by the von Neumann equation for the density matrix,

$$\partial_t \hat{\rho}(t) = -\mathrm{i}\left[\hat{H}(t),\, \hat{\rho}(t)\right], \tag{2.1}$$

which is formally solved by the unitary evolution operator

$$\hat{U}_{t,t'} = \mathbb{T}\exp\left(-\mathrm{i}\int_{t'}^{t} \hat{H}(t)\mathrm{d}t\right), \tag{2.2}$$

$$\hat{\rho}(t) = \hat{U}_{t,-\infty}\hat{\rho}(-\infty)\hat{U}_{-\infty,t}, \tag{2.3}$$

where $\mathbb{T}$ symbolizes the time-ordering operator. The expectation value of a general observable $\hat{O}$ is given by its trace with the density matrix,

$$\langle \hat{O}(t)\rangle \equiv \frac{\mathrm{Tr}\left\{\hat{O}\hat{\rho}(t)\right\}}{\mathrm{Tr}\left\{\hat{\rho}(t)\right\}} = \frac{1}{\mathrm{Tr}\left\{\hat{\rho}(t)\right\}}\,\mathrm{Tr}\left\{\hat{U}_{-\infty,t}\hat{O}\hat{U}_{t,-\infty}\hat{\rho}(-\infty)\right\}, \tag{2.4}$$

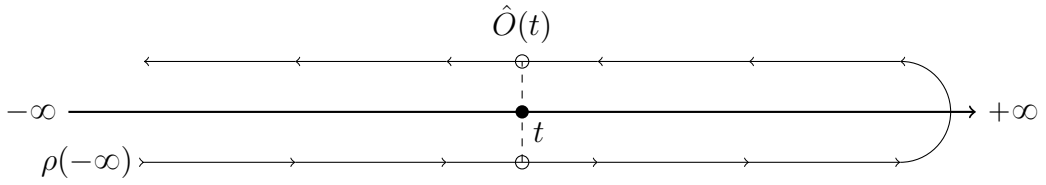

Figure 2.1: Closed time contour $\mathcal{C}$, visualizing the evolution under the operator $\hat{U}_{\mathcal{C}}$. It turns out to be irrelevant whether the observable is inserted on either the forward or backward path, making the half-sum of both a practical choice (see Eq. (2.7)).

where the trace is taken over the associated many-body Hilbert space. The trace allows the already performed cyclic permutation of operators, alluding to the alternative interpretation of evolving the observable operator rather than the density matrix, in spirit of the Heisenberg picture. One notes that the expression contains *both forward and backward evolution* in time. It will be convenient to extend the evolution in time to $t = +\infty$ by inserting a factor of unity as $\hat{1} = \hat{U}_{t,+\infty}\hat{U}_{+\infty,t}$, such that

$$\langle \hat{O}(t) \rangle = \frac{1}{\mathrm{Tr}\left\{\hat{\rho}(-\infty)\right\}} \mathrm{Tr}\left\{\hat{U}_{-\infty,\infty}\hat{U}_{\infty,t}\hat{O}\hat{U}_{t,-\infty}\hat{\rho}(-\infty)\right\}, \tag{2.5}$$

where we also changed the normalization factor, since under von Neumann evolution the trace of $\hat{\rho}(t)$ does not change over time. We establish the *generating function* of the above expectation value as

$$Z[V] \equiv \frac{\mathrm{Tr}\left\{\hat{U}_{\mathcal{C}}[V]\hat{\rho}(-\infty)\right\}}{\mathrm{Tr}\left\{\hat{\rho}(-\infty)\right\}}, \tag{2.6}$$

where the Hamiltonian governing the evolution was modified to now read $\hat{H}_V^{\pm}(t) \equiv \hat{H}(t) \pm \hat{O}V(t)$, where the sign indicates the scope of the Hamiltonian as either the forward or backward part of the evolution. One now obtains the expression (2.5) from Eq. (2.6) by differentiating with respect to the auxiliary field term,

$$\langle \hat{O} \rangle = \frac{\mathrm{i}}{2} \left.\frac{\delta Z[V]}{\delta V}\right|_{V=0}. \tag{2.7}$$

In Eq. (2.6), we have introduced the evolution operator on the closed time path $\hat{U}_{\mathcal{C}}$ describing evolution along the contour depicted in Fig. 2.1. In the following, we develop a functional integral representation for the generating function $Z[V]$ in Eqs. (2.6) and (2.7), allowing e.g. the application of well-known methods from equilibrium and zero-temperature perturbation theory.

2.1.2 Bosonic coherent states

We begin by considering bosonic particles occupying a single energy level. Working in the basis of pure number states, a many-body state with n bosons is denoted by $|n\rangle$, and these states form a complete orthonormal basis. We denote by $\hat{b}, \hat{b}^\dagger$ bosonic ladder operators acting on states in the many-body Hilbert space as $\hat{b}\,|n\rangle = \sqrt{n}\,|n-1\rangle$, $\hat{b}^\dagger\,|n\rangle = \sqrt{n+1}\,|n+1\rangle$. Based on those, we define *coherent* states as right eigenstates of the annihilation operator $\hat{b}$ with (complex) eigenvalue φ as

$$\hat{b}\,|\varphi\rangle = \varphi\,|\varphi\rangle, \quad |\varphi\rangle = \sum_{n=0}^{\infty} \frac{\varphi^n}{\sqrt{n!}}\,|n\rangle = \sum_{n=0}^{\infty} \frac{\varphi^n}{n!}\left(\hat{b}^\dagger\right)^n |0\rangle, \tag{2.8}$$

where $|0\rangle$ denotes the vacuum state, i.e. $\hat{b}\,|0\rangle = 0$. In this basis, the matrix elements of any normally ordered operator $\hat{O}(\hat{b}^\dagger, \hat{b})$ are given by

$$\langle\varphi|\,\hat{O}(\hat{b}^\dagger, \hat{b})\,|\varphi'\rangle = O(\bar{\varphi}, \varphi'). \tag{2.9}$$

One finds that the overlap of two coherent states is given by $\langle\varphi\,|\,\varphi'\rangle = e^{\bar{\varphi}\varphi'}$, where $\bar{\varphi}$ denotes the complex conjugate of φ. Coherent states form an over-complete basis of the many-body Hilbert space. As can easily be shown, we can thus express unity in the coherent-state basis as

$$\hat{1} = \int \mathrm{d}\,[\bar{\varphi}, \varphi]\, e^{-|\varphi|^2}\,|\varphi\rangle\langle\varphi|\,, \tag{2.10}$$

where the integration $\mathrm{d}\,[\bar{\varphi}, \varphi] \equiv \mathrm{d}\Re(\varphi)\,\mathrm{d}\Im(\varphi)/\pi$ independently runs over both real and imaginary part. The trace of some operator $\hat{O}$ in the coherent-state basis becomes

$$\mathrm{Tr}\{\hat{O}\} \equiv \int \mathrm{d}\,[\bar{\varphi}, \varphi]\, e^{-|\varphi|^2}\,\langle\varphi|\hat{O}|\varphi\rangle\,. \tag{2.11}$$

2.1.3 Partition function

We now turn to developing the real-time formalism for the simplest possible many-body quantum system, namely a set of bosons occupying a single state. The simplicity of this example eases notational effort, and it turns out that only minor changes are needed for the generalization to a theory of interacting fields. Consider therefore the Hamiltonian

$$\hat{H} = \omega_0 \hat{b}^\dagger \hat{b}, \tag{2.12}$$

and define the partition function

$$Z = \mathrm{Tr}\left\{\hat{U}_\mathcal{C}\hat{\rho}\right\} / \mathrm{Tr}\left\{\hat{\rho}\right\}. \tag{2.13}$$

While the initial density matrix is in general some function of the Hamiltonian, we simplify the following derivations by assuming thermal equilibrium at some time early in the past, namely $\hat{\rho}_0 \equiv \exp\left[-\beta(\hat{H} - \mu\hat{N})\right]$, such that we have for the trace

$$\mathrm{Tr}\left\{\hat{\rho}_0\right\} = \sum_{n=0}^{\infty} e^{-\beta(\omega_0-\mu)n} = \left[1 - \rho(\omega_0)\right]^{-1}, \tag{2.14}$$

where $\rho(\omega_0) = \exp(-\beta(\omega_0 - \mu))$. Since the density matrix evolution is governed by the von Neumann equation, this trace is constant in time, and may therefore be omitted from here on.

In order to evaluate the contour evolution operator $\hat{U}_\mathcal{C}$ for this system, one applies a Suzuki-Trotter decomposition, discretizing the contour into $(2N-2)$ intervals δ_t with boundary conditions $t_1 = t_{2N} = t_0$, $t_N = t_{N+1} = \infty$. Between the individual evolution operators, one inserts unity in the coherent-state basis (2.10) to obtain

$$\begin{aligned}\mathrm{Tr}\left\{\hat{U}_\mathcal{C}\hat{\rho}(t_0)\right\} = \int \prod_{j=1}^{2N} \mathrm{d}[\bar{\varphi}_j, \varphi_j]\, &\langle\varphi_{2N}|\hat{U}_{-\delta_t}|\varphi_{2N-1}\rangle \ldots \langle\varphi_{N+2}|\hat{U}_{-\delta_t}|\varphi_{N+1}\rangle\langle\varphi_{N+1}|\hat{1}|\varphi_N\rangle \\ &\cdot\langle\varphi_N|\hat{U}_{+\delta_t}|\varphi_{N-1}\rangle \ldots \langle\varphi_2|\hat{U}_{+\delta_t}|\varphi_1\rangle\langle\varphi_1|\hat{\rho}(t_0)|\varphi_{2N}\rangle\,,\end{aligned} \tag{2.15}$$

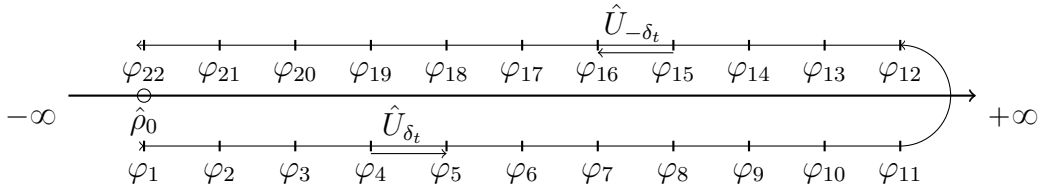

Figure 2.2: Closed time contour $\mathcal{C}$, decomposed into $N = 11$ discrete evolution steps per direction. At early times, the state of the system is given by the density matrix $\hat{\rho}_0$.

where the infinitesimal evolution operator $\hat{U}_{\pm\delta_t}$ is introduced. Its matrix elements are given by

$$\begin{aligned}\langle\varphi_j|\hat{U}_{\pm\delta_t}|\varphi_{j-1}\rangle &\equiv \langle\varphi_j|e^{\mp\mathrm{i}\hat{H}(b^\dagger,b)\delta_t}|\varphi_{j-1}\rangle \approx \langle\varphi_j|1\mp\mathrm{i}\hat{H}(b^\dagger,b)\delta_t|\varphi_{j-1}\rangle \\ &= \langle\varphi_j|\varphi_{j-1}\rangle\left(1\mp\mathrm{i}H(\bar{\varphi}_j,\varphi_{j-1})\right)\delta_t \approx e^{\bar{\varphi}_j\varphi_{j-1}}e^{\mp\mathrm{i}H(\bar{\varphi}_j,\varphi_{j-1})\delta_t},\end{aligned} \tag{2.16}$$

up to linear order in δ_t, using that $\langle\varphi|\rho^{\hat{b}^\dagger\hat{b}}|\varphi'\rangle = e^{\bar{\varphi}\varphi'\rho}$. Note that this holds for general *normally-ordered* Hamiltonians. Applying the assumption of an initial state in thermal equilibrium, one substitutes $\langle\varphi_1|\exp\left(-\beta(\omega_0)-\mu\right)b^\dagger b|\varphi_{2N}\rangle = \exp\left[\varphi_1\varphi_{2N}\rho(\omega_0)\right]$ to obtain for the partition function the Gaussian integral expression

$$Z = \frac{1}{\mathrm{Tr}\left\{\hat{\rho}(t_0)\right\}}\int\prod_{j=1}^{2N}\mathrm{d}\left[\bar{\varphi}_j,\varphi_j\right]\exp\left(\mathrm{i}\sum_{j,j'=1}^{2N}\bar{\varphi}_j G^{-1}_{jj'}\varphi_{j'}\right), \tag{2.17}$$

with the variance matrix

$$\mathrm{i}G^{-1}_{jj'} \equiv \left[\begin{array}{ccc|ccc} -1 & & & & & \rho(\omega_0) \\ h_- & -1 & & & & \\ & h_- & -1 & & & \\ \hline & & 1 & -1 & & \\ & & & h_+ & -1 & \\ & & & & h_+ & -1 \end{array}\right], \quad \text{where } h_\pm \equiv 1 \pm \mathrm{i}\omega_0\delta_t. \tag{2.18}$$

The elements on the main diagonal originate from the expression for unity (2.10), the lower sub-diagonal follows from the matrix elements (2.16), and the upper right elements in the off-diagonal blocks are crucial for normalization.

The presence of the non-zero off-diagonal blocks means that we have to exercise some care when using continuum notation. We formally assume sufficiently fine discretization and large N when we write

$$Z = \int\mathbf{D}\left[\bar{\varphi},\varphi\right]e^{\mathrm{i}S[\bar{\varphi},\varphi]}, \tag{2.19}$$

$$\mathbf{D}\left[\bar{\varphi},\varphi\right] \equiv \left(\mathrm{Tr}\{\hat{\rho}_0\}\right)^{-1}\prod_{j=1}^{2N}\mathrm{d}\left[\bar{\varphi}_j,\varphi_j\right], \tag{2.20}$$

$$S\left[\bar{\varphi},\varphi\right] \equiv \sum_{j=2}^{2N}\delta t_j\left[\mathrm{i}\bar{\varphi}_j\frac{\varphi_j-\varphi_{j-1}}{\delta t_j}-\omega_0\bar{\varphi}_j\varphi_{j-1}\right]+\mathrm{i}\bar{\varphi}_1\left[\varphi_1-\mathrm{i}\rho(\omega_0)\varphi_{2N}\right] \tag{2.21}$$

$$\to S\left[\bar{\varphi},\varphi\right] = \int_{\mathcal{C}}\bar{\varphi}(t)\hat{G}^{-1}\varphi(t)\mathrm{d}t, \quad \hat{G}^{-1} = \mathrm{i}\partial_t-\omega_0. \tag{2.22}$$

Some remarks are in order: First, note that δt_j changes sign depending on whether $j \leqslant N$ or not, i.e. if it is defined on the forward or backward branch of the contour. Second, it appears as if the upper right element of (2.18) is seemingly absent in the continuum notation of (2.22). However, note that due to the presence of the zero mode $\exp(-\mathrm{i}\omega_0 t)$, the expression $\mathrm{i}\partial_t - \omega_0$ is not uniquely invertible, making it therefore necessary to include the boundary term for a unique definition of $\hat{G}^{-1}$.

For reasons of convenience, one rewrites the integration over the time contour and instead splits the integrand into parts defined on either the forward (φ^+) or the backward (φ^-) part of the contour. The rewritten action then reads

$$S\left[\bar{\varphi},\varphi\right] = \int_{\mathcal{C}} \mathrm{d}t \left[\bar{\varphi}^+(t)(\mathrm{i}\partial_t - \omega_0)\varphi^+(t) - \bar{\varphi}^-(t)(\mathrm{i}\partial_t - \omega_0)\varphi^-(t)\right], \tag{2.23}$$

still keeping in mind the implicit boundary terms. While from Eq. (2.23) one might get the impression that φ^+ and φ^- are unrelated, they are actually connected due to the boundary term. We will in the following exploit this interdependence to derive a continuum representation that incorporates all correlations without carrying implicit terms. For the moment, we revert to the discrete notation, to observe that Gaussian integration yields for correlation functions of fields

$$\left\langle \varphi_j \bar{\varphi}_{j'} \right\rangle \equiv \int \mathbf{D}\left[\bar{\varphi},\varphi\right] \varphi_j \bar{\varphi}_{j'} \exp\left(\mathrm{i} \sum_{k,k'=1}^{2N} \bar{\varphi}_k G^{-1}_{kk'} \varphi_{k'} \right) = \mathrm{i} G_{jj'}, \tag{2.24}$$

the matrix elements of the inverse of (2.18). Splitting the time contour, we identify four block matrices in $\hat{G}$,

$$\left\langle \varphi^+_j \bar{\varphi}^-_{j'} \right\rangle \equiv \mathrm{i} G^<_{jj'} = \frac{\rho h_+^{j'-1} h_-^{j-1}}{\det\left[-\mathrm{i}\hat{G}^{-1}\right]}, \tag{2.25}$$

$$\left\langle \varphi^-_j \bar{\varphi}^+_{j'} \right\rangle \equiv \mathrm{i} G^>_{jj'} = \frac{h_+^{N-j} h_-^{N-j'}}{\det\left[-\mathrm{i}\hat{G}^{-1}\right]}, \tag{2.26}$$

$$\left\langle \varphi^+_j \bar{\varphi}^+_{j'} \right\rangle \equiv \mathrm{i} G^{\mathbb{T}}_{jj'} = \frac{h_-^{j-j'}}{\det[-\mathrm{i}\hat{G}^{-1}]} \times \begin{cases} 1, & j \geqslant j' \\ \rho(h_+ h_-)^{N-1}, & j < j' \end{cases}, \tag{2.27}$$

$$\left\langle \varphi^-_j \bar{\varphi}^-_{j'} \right\rangle \equiv \mathrm{i} G^{\tilde{\mathbb{T}}}_{jj'} = -[\hat{G}^{\mathbb{T}}]^\dagger, \tag{2.28}$$

where the relation between the last two stem from the fact that $h_+^* = h_-$. The symbols $\mathbb{T}$ and $\tilde{\mathbb{T}}$ stand for time ordering respectively anti-time ordering, while $<$ ($>$) conveniently indicates that the first argument is taken before (after) the second one. In order to return to continuum notation, we take the limit $N \to \infty$ while keeping the product $N\delta_t$ constant. Evaluating the determinants, we thus have

$$\left\langle \varphi^+(t)\bar{\varphi}^-(t') \right\rangle = \mathrm{i} G^<(t,t') = n_B e^{-\mathrm{i}\omega_0(t-t')}, \tag{2.29}$$

$$\left\langle \varphi^-(t)\bar{\varphi}^+(t') \right\rangle = \mathrm{i} G^>(t,t') = (n_B+1) e^{-\mathrm{i}\omega_0(t-t')}, \tag{2.30}$$

$$\left\langle \varphi^+(t)\bar{\varphi}^+(t') \right\rangle = \mathrm{i} G^{\mathbb{T}}(t,t') = \theta(t-t')\mathrm{i}G^>(t,t') + (1-\theta(t-t'))\mathrm{i}G^<(t,t'), \tag{2.31}$$

$$\left\langle \varphi^-(t)\bar{\varphi}^-(t') \right\rangle = \mathrm{i} G^{\tilde{\mathbb{T}}}(t,t') = \theta(t'-t)\mathrm{i}G^>(t,t') + (1-\theta(t'-t))\mathrm{i}G^<(t,t'), \tag{2.32}$$

where we introduced the step-function $\theta(t)$ with $\theta(0) = 1$, as well as the bosonic occupation number

$$n_B(\omega_0) = \frac{\rho(\omega_0)}{1 - \rho(\omega_0)}. \tag{2.33}$$

Immediately, one observes that these correlation functions are not linearly independent, but for $t \neq t'$ obey the relation[1]

$$G^{\mathbb{T}}(t,t') + G^{\tilde{\mathbb{T}}}(t,t') - G^{>}(t,t') - G^{<}(t,t') = 0. \tag{2.34}$$

This linear dependence implies that a linear change of coordinates may significantly simplify the correlator matrix by eliminating a dependent component. One performs the *Keldysh rotation* by changing the variables as

$$\varphi^{\mathrm{cl}}(t) = \frac{1}{\sqrt{2}}\left(\varphi^{+}(t) + \varphi^{-}(t)\right), \quad \varphi^{\mathrm{q}}(t) = \frac{1}{\sqrt{2}}\left(\varphi^{+}(t) - \varphi^{-}(t)\right) \tag{2.35}$$

where if the indices $\alpha, \beta \in \{\mathrm{cl}, \mathrm{q}\}$ label the new components, the new block matrix of Green functions becomes

$$\left\langle \varphi^{\alpha}(t)\bar{\varphi}^{\beta}(t')\right\rangle \equiv \mathrm{i}G^{\alpha\beta}(t,t') = \mathrm{i}\begin{pmatrix} G^{K}(t,t') & G^{R}(t,t') \\ G^{A}(t,t') & 0 \end{pmatrix}. \tag{2.36}$$

The retarded (R), advanced (A) and Keldysh (K) propagator for *different* times $t \neq t'$ become[2]

$$G^{R}(t,t') = G^{\mathrm{cl,q}}(t,t') = \theta(t-t')\left(G^{>} - G^{<}\right), \tag{2.37}$$

$$G^{A}(t,t') = G^{\mathrm{q,cl}}(t,t') = \theta(t'-t)\left(G^{<} - G^{>}\right), \tag{2.38}$$

$$G^{K}(t,t') = G^{\mathrm{cl,cl}}(t,t') = G^{<} + G^{>}. \tag{2.39}$$

Employing the representation of the un-rotated Green functions in the time domain in Eqs. (2.29) to (2.32), one finds for the Keldysh-rotated propagators in both time and frequency (ω) domain

$$G^{R} = -\mathrm{i}\theta(t-t')e^{-\mathrm{i}\omega_0(t-t')} \qquad \to (\omega - \omega_0 + \mathrm{i}\varepsilon)^{-1} \tag{2.40}$$

$$G^{A} = \quad \mathrm{i}\theta(t'-t)e^{-\mathrm{i}\omega_0(t-t')} \qquad \to (\omega - \omega_0 - \mathrm{i}\varepsilon)^{-1} \tag{2.41}$$

$$G^{K} = -\mathrm{i}(1 + 2n_B(\omega_0))e^{-\mathrm{i}\omega_0(t-t')} \qquad \to -2\pi\mathrm{i}(1 + 2n_B(\omega_0))\delta(\omega - \omega_0) \tag{2.42}$$

with some infinitesimal $\varepsilon > 0$ to shift the poles off the real axis, realizing the Heaviside function $\theta(t)$. In thermal equilibrium, i.e. if $\rho = \exp\left(-\beta(\omega_0 - \mu)\right)$, the Green functions are related via a *fluctuation-dissipation relation*

$$G^{K}(\omega) = \coth\frac{\omega - \mu}{2T}\left(G^{R}(\omega) - G^{A}(\omega)\right). \tag{2.43}$$

Generating function for the Keldysh correlators is the closed-time-path partition function

$$\left\langle \varphi^{\alpha}(t)\bar{\varphi}^{\beta}(t')\right\rangle \equiv \mathrm{i}G^{\alpha\beta}(t,t') = \int \mathbf{D}\left[\varphi^{\mathrm{cl}}, \varphi^{\mathrm{q}}\right]\varphi^{\alpha}(t)\bar{\varphi}^{\beta}(t')e^{\mathrm{i}S[\varphi^{\mathrm{cl}},\varphi^{\mathrm{q}}]} \tag{2.44}$$

[1] For $t = t'$, the right-hand side of Eq. (2.34) becomes one, as a consequence of the regularization of $\theta(0) = 1$.

[2] On the diagonal, one generally has $G^{R}(t,t) + G^{A}(t,t) = 0$ and $G^{R}(t,t) - G^{A}(t,t) = -\mathrm{i}$. For all practical purposes, one can however extend Eqs. (2.37) and (2.38) to the diagonal by interpreting $\theta(0) = 0$, as usually only the sum contributes.

with the Keldysh action

$$S[\varphi^{\mathrm{cl}},\varphi^{\mathrm{q}}]=\int\!\!\int_{-\infty}^{\infty}\mathrm{d}t\mathrm{d}t'(\bar{\varphi}^{\mathrm{cl}},\,\bar{\varphi}^{\mathrm{q}})\begin{pmatrix}0 & [G^{-1}]^{A}\\ [G^{-1}]^{R} & [G^{-1}]^{K}\end{pmatrix}_{t,t'}\begin{pmatrix}\varphi^{\mathrm{cl}}\\ \varphi^{\mathrm{q}}\end{pmatrix}. \tag{2.45}$$

The retarded/advanced components of the inverse propagator are obtained by the condition $[G^{-1}]^{R(A)}\circ G^{R(A)}=\delta(t-t')$, i.e.

$$\left[G^{-1}\right]^{R(A)}=\omega-\omega_0\pm\mathrm{i}\varepsilon\;\rightarrow\;\delta\left(t-t'\right)\left(\mathrm{i}\delta_{t'}-\omega_0\pm i\varepsilon\right), \tag{2.46}$$

where again the infinitesimal offset acts as a reminder that these are not truly diagonal, but lower(upper) triangular. The Keldysh component of the inverse propagator is obtained by the relation

$$\left[G^{-1}\right]^{K}=-\left[G^{R}\right]^{-1}\circ G^{K}\circ\left[G^{A}\right]^{-1}. \tag{2.47}$$

2.1.4 Thermal systems

Up to this point, we treated an isolated system of bosons. In the following, we prepare the formalism for more realistic systems by introducing interactions with infinitely many harmonic oscillators, arriving at the real-time version of the Caldeira-Leggett model of a quantum particle in a heat-bath. To this end, we start by parametrising complex boson field $\varphi(t)$ by real fields $\pi(t),\phi(t)$ as

$$\varphi(t)=\frac{1}{\sqrt{2\omega_0}}\left(\pi(t)+\mathrm{i}\omega_0\phi(t)\right),\;\bar{\varphi}(t)=\frac{1}{\sqrt{2\omega_0}}\left(\pi(t)-\mathrm{i}\omega_0\phi(t)\right). \tag{2.48}$$

Inserting these into Eq. (2.23), we find then for the contour action

$$S\left[\phi,\pi\right]=\int_{\mathcal{C}}\mathrm{d}t\left[\pi\dot{\phi}-\frac{1}{2}\pi^2-\frac{\omega_0^2}{2}\phi^2\right]=\int_{\mathcal{C}}\mathrm{d}t\left[\frac{1}{2}\dot{\phi}^2-\frac{\omega_0^2}{2}\phi^2\right], \tag{2.49}$$

where we performed the Gaussian integral over π. Boundary terms implicit in the continuum notation were omitted. Equation (2.49) is recognized as the Feynman action of the harmonic oscillator. Although the inclusion of interactions requires a bit more care, it is convenient to work with some arbitrary ϕ-dependent potential term $V(\phi)$ to absorb additional complications.

Splitting the integration contour in forward/backward parts and performing a Keldysh rotation of $\phi(t)$ yields

$$S[\phi]=\int_{\mathcal{C}}\mathrm{d}t\left[\frac{1}{2}\dot{\phi}^2-V(\phi)\right],\quad\phi(t)\rightarrow\phi^{\mathrm{cl/q}}\equiv\frac{1}{2}\left(\phi^{+}(t)\pm\phi^{-}(t)\right) \tag{2.50}$$

$$\Rightarrow\quad S[\phi^{\mathrm{cl}},\phi^{\mathrm{q}}]=\int_{-\infty}^{+\infty}\mathrm{d}t\left[-2\phi^{\mathrm{q}}\ddot{\phi^{\mathrm{cl}}}-V(\phi^{\mathrm{cl}}+\phi^{\mathrm{q}})+V(\phi^{\mathrm{cl}}-\phi^{\mathrm{q}})\right]. \tag{2.51}$$

From this form of the action it becomes clear how the quantum and classical components ϕ^{q}, ϕ^{cl} get their names: If the quantum component $\phi^{\mathrm{q}}\propto(\varphi^{+}-\varphi^{-})$ is small, one can linearize the action and perform the integral over ϕ^{q}, such that

$$\int\mathcal{D}[\phi^{\mathrm{q}}]e^{\mathrm{i}\int_{\mathcal{C}}\mathrm{d}t\phi^{\mathrm{q}}\left[\ddot{\phi^{\mathrm{cl}}}+V'(\phi^{\mathrm{cl}})\right]}=\delta\left(\ddot{\phi^{\mathrm{cl}}}+V'(\phi^{\mathrm{cl}})\right). \tag{2.52}$$

One is then left with a delta functional forcing the classical component $\phi^{\mathrm{cl}} \sim \varphi^+\varphi^-$ along trajectories where $\ddot{\phi}^{\mathrm{cl}} = -V'(\phi^{\mathrm{cl}})$, i.e. those fulfilling the *Newtonian equations of motion*.

Going back to the harmonic oscillator action with $V(\phi) = \omega_0^2\phi^2/2$, we can write the action as a quadratic form

$$S[\phi] = \frac{1}{2}\int \mathrm{d}t\, \overrightarrow{\phi}^T \hat{D}^{-1} \overrightarrow{\phi}, \tag{2.53}$$

with the Green functions in equilibrium[3]

$$\hat{D}^{\alpha\beta}(t,t') = \begin{pmatrix} D^K(t-t') & D^R(t-t') \\ D^A(t-t') & 0 \end{pmatrix}, \tag{2.54}$$

$$D^{R(A)}(\omega) = \frac{1}{2}\left((\omega \pm \mathrm{i}\varepsilon)^2 - \omega_0^2\right)^{-1}, \tag{2.55}$$

$$D^K(\omega) = \coth\left(\omega/2T\right)\left(D^R(\omega) - D^A(\omega)\right). \tag{2.56}$$

We will employ this representation of harmonic oscillators in the following to model a heat bath. Consider therefore some particle in contact with an environment of harmonic oscillators, such that its Keldysh action is written in three terms as

$$S[\phi,\varphi] = S_p[\phi] + S_b[\varphi] + S_{\mathrm{int}}[\phi,\varphi], \tag{2.57}$$

$$S_p[\phi] = \int \mathrm{d}t \left[-2\phi^{\mathrm{q}}\ddot{\phi}^{\mathrm{cl}} - V(\phi^{\mathrm{cl}} + \phi^{\mathrm{q}}) + V(\phi^{\mathrm{cl}} - \phi^{\mathrm{q}})\right], \tag{2.58}$$

$$S_{\mathrm{bath}}[\varphi] = \sum_s \frac{1}{2}\int \mathrm{d}t\, \overrightarrow{\varphi}_s^T \hat{D}_s^{-1} \overrightarrow{\varphi}_s, \tag{2.59}$$

$$S_{\mathrm{int}}[\varphi] = \sum_s g_s \frac{1}{2}\int \mathrm{d}t\, \overrightarrow{\phi}^T \hat{\sigma}_1 \overrightarrow{\varphi}, \tag{2.60}$$

where $\hat{\sigma}_1$ is the first Pauli matrix, leading to interactions of the form $g_s\left(\phi^+\varphi_s^+ - \phi^-\varphi_s^-\right)$, and integrals over the time coordinate are understood to run from $t = -\infty$ to $+\infty$. By completing the square one can integrate out the heat-bath degrees of freedom φ_s of $S_{\mathrm{bath}}, S_{\mathrm{int}}$, to arrive at the dissipative part of the action

$$S_{\mathrm{diss}} = \frac{1}{2}\int\int \mathrm{d}t\mathrm{d}t' \overrightarrow{\phi}^T(t) \mathfrak{D}^{-1}(t-t') \overrightarrow{\phi}(t'), \tag{2.61}$$

$$\mathfrak{D}^{-1}(t-t') \equiv -\hat{\sigma}_1 \left(\sum_s g_s \hat{D}_s(t-t')\right) \hat{\sigma}_1. \tag{2.62}$$

The propagators of the oscillators $\hat{D}_s$ are given by Eq. (2.54). Sending the number of heat-bath oscillators to infinity, one may make the spectral density $J(\omega') = \pi\sum_s (g_s^2/\omega_s)\delta(\omega' - \omega_s)$ continuous in ω'. Choosing the couplings such that $J(\omega') = 4\gamma\omega'$, one arrives at the *Ohmic* bath, where the retarded (advanced) propagator becomes

$$\left[\mathfrak{D}^{-1}\right]^{R(A)}(\omega) = 4\gamma \int \frac{\mathrm{d}\omega'}{2\pi} \frac{\omega'^2}{\omega'^2 - (\omega \pm \mathrm{i}\varepsilon)^2} = \mathrm{const} \pm 2\mathrm{i}\gamma\omega. \tag{2.63}$$

[3] In order to perform the Gaussian integral, the matrix $\hat{D}^{-1}$ has to be symmetric, corresponding to $D^K(\omega)$ being an even function. Thus, the chemical potential of a real field must vanish.

The constant contribution is the same for both components and can be absorbed in the definition of the quadratic part of the potential $V(\phi)$. In equilibrium, one obtains the Keldysh component of the correlator from the fluctuation-dissipation theorem as

$$\left[\mathfrak{D}^{-1}\right]^K = 4\mathrm{i}\gamma\omega \coth\frac{\omega}{2T}, \tag{2.64}$$

which becomes non-local in the time domain. The full action $S = S_p + S_{\mathrm{diss}}$ then reads

$$\begin{aligned} S[\phi] = \int_{-\infty}^{+\infty} \mathrm{d}t \Bigg[&- 2\phi^{\mathrm{q}}\left(\partial_t^2 + \gamma\partial_t\right)\phi^{\mathrm{cl}} - V(\phi^{\mathrm{cl}} + \phi^{\mathrm{q}}) + V(\phi^{\mathrm{cl}} - \phi^{\mathrm{q}}) \\ &+ 2\mathrm{i}\gamma\left(2T(\phi^{\mathrm{q}})^2 + \frac{\pi T^2}{2}\int_{-\infty}^{+\infty}\mathrm{d}t' \frac{(\phi^{\mathrm{q}}(t) - \phi^{\mathrm{q}}(t'))^2}{\sinh^2\left(\pi T(t-t')\right)}\right)\Bigg]. \end{aligned} \tag{2.65}$$

2.1.5 Classical approximation

Earlier, we saw that by linearizing the action around small values of the quantum component $\phi^{\mathrm{q}} \to 0$, the bosonic system reduced to classical equations of motion for ϕ^{cl}. However, since we introduced the heat bath, we have to be somewhat more careful with regards to units. The safe course of action is to take the limit $\hbar \to 0$ of the Keldysh action (2.65) of the Caldeira-Leggett model. To this end, we first must reintroduce $\hbar$ at the appropriate locations, namely in the form of $\hbar^{-1}$ as overall factor to make the action itself dimensionless, then re-scale $\phi^{\mathrm{q}} \to \hbar\phi^{\mathrm{q}}$, and finally take care of the unit of temperature by replacing $T \to T/\hbar$. The dissipative Keldysh action and its limit then read

$$\begin{aligned} \frac{1}{\hbar}S\left[\phi\right] =& \frac{1}{\hbar}\int_{-\infty}^{\infty}\mathrm{d}t\left[-2\hbar\phi^{\mathrm{q}}\left(\ddot{\phi}^{\mathrm{cl}} + \gamma\dot{\phi}^{\mathrm{cl}}\right) - V\left(\phi^{\mathrm{cl}} + \hbar\phi^{\mathrm{q}}\right) - V\left(\phi^{\mathrm{cl}} - \hbar\phi^{\mathrm{q}}\right)\right] \\ &+ \frac{2\mathrm{i}\gamma}{\hbar}\int_{-\infty}^{\infty}\mathrm{d}t\left[\frac{2T}{\hbar}\left(\hbar\phi^{\mathrm{q}}\right)^2 + \frac{\pi T^2}{2\hbar^2}\int_{-\infty}^{\infty}\mathrm{d}t' \frac{\hbar^2\left(\phi^{\mathrm{q}}(t) - \phi^{\mathrm{q}}(t')\right)^2}{\sinh^2\left[\pi T(t-t')/\hbar\right]}\right], \end{aligned} \tag{2.66}$$

$$\lim_{\hbar\to 0}\frac{1}{\hbar}S[\phi] = \int_{-\infty}^{\infty}\mathrm{d}t\left(-2\phi^{\mathrm{q}}\left[\ddot{\phi}^{\mathrm{cl}} + \gamma\dot{\phi}^{\mathrm{cl}} + V'\left(\phi^{\mathrm{cl}}\right)\right] + 4\mathrm{i}\gamma T\left(\phi^{\mathrm{q}}\right)^2\right). \tag{2.67}$$

The non-local term becomes local and drops out completely, while the term quadratic in ϕ^{q} survives. The limits $\gamma \to 0$, $\hbar \to 0$ commute, see Eq. (2.51).

If it were not for the last term of Eq. (2.67), one could simply perform the integral over ϕ^{q} and be left with a delta function forcing ϕ^{cl} along classical Newtonian trajectories, however with an additional viscous friction force. To get rid of $(\phi^{\mathrm{q}})^2$, one employs a Hubbard-Stratonovich transformation, introducing an auxiliary field ξ as

$$\exp\left[-4\gamma T\int\mathrm{d}t(\phi^{\mathrm{q}}(t))^2\right] = \int\mathbf{D}[\xi(t)]\exp\left[-\int\mathrm{d}t\frac{1}{4\gamma T}\xi^2(t) - 2\mathrm{i}\xi(t)\phi^{\mathrm{q}}(t)\right], \tag{2.68}$$

where the integration measure is normalized to yield $\int\mathbf{D}[\xi(t)]e^{-\int\mathrm{d}t\frac{1}{4\gamma T}\xi^2(t)} = 1$. The remaining terms are now at most linear in ϕ^{q}, allowing to perform the integral. For

the expectation value of some observable $\hat{O}$, one thus has

$$\langle \hat{O}[\phi^{\mathrm{cl}}] \rangle = \int \mathbf{D}[\phi^{\mathrm{cl}}, \phi^{\mathrm{q}}] \hat{O}(\phi^{\mathrm{cl}}) e^{\mathrm{i}S[\phi^{\mathrm{cl}}, \phi^{\mathrm{q}}]} \tag{2.69}$$

$$= \int \mathbf{D}[\xi] e^{-\frac{1}{4\gamma T}\int \mathrm{d}t \xi^2(t)} \int \mathbf{D}[\phi^{\mathrm{cl}}, \phi^{\mathrm{q}}] \hat{O}(\phi^{\mathrm{cl}}) e^{-2\mathrm{i}\int \mathrm{d}\phi^{\mathrm{q}} \left(\ddot{\phi^{\mathrm{cl}}} + \gamma \dot{\phi^{\mathrm{cl}}} + V'(\phi^{\mathrm{cl}}) - \xi \right)} \tag{2.70}$$

$$= \int \mathbf{D}[\xi] e^{-\frac{1}{4\gamma T}\int \mathrm{d}t \xi^2(t)} \int \mathbf{D}[\phi^{\mathrm{cl}}] \hat{O}(\phi^{\mathrm{cl}}) \delta \left(\ddot{\phi^{\mathrm{cl}}} + \gamma \dot{\phi^{\mathrm{cl}}} + V'(\phi^{\mathrm{cl}}) - \xi \right), \tag{2.71}$$

with the δ-functional only contributing for $\phi^{\mathrm{cl}}(t), \xi(t)$ such that its argument vanishes, therefore enforcing a *Langevin*-type equation of motion on the classical field

$$\ddot{\phi^{\mathrm{cl}}} = -\gamma \phi^{\mathrm{cl}} - V'(\phi^{\mathrm{cl}}) + \xi, \tag{2.72}$$

with some stochastic driving force ξ. We now have in principle a prescription for the numerical computation of $\langle \hat{O}[\phi^{\mathrm{cl}}] \rangle$:

1. Choose some arbitrary force history $\xi(t)$,
2. solve Eq. (2.72) numerically,
3. calculate $\hat{O}[\phi^{\mathrm{cl}}]$ over the solution and
4. average over sufficiently many different $\xi(t)$ and weigh with the Gaussian weight $\exp\left[-\int \mathrm{d}t \xi(t)/4\gamma T\right]$.

An efficient way to realize this lies in a kind of importance-sampling method: By drawing $\xi(t)$ from a Gaussian random distribution such that

$$\langle \xi(t) \rangle = 0, \ \langle \xi(t') \xi(t) \rangle = 2\gamma T \delta(t - t') \tag{2.73}$$

ensures that the resulting force histories are distributed with the correct weight, and one can simply average over solutions of Eq. (2.72) with this specific Gaussian noise.

2.1.6 Field theory

Generalizing the formalism outline above to $d+1$-dimensional fields turns out to be as trivial as replacing

$$\hat{H} = \omega_0 \hat{b}^\dagger \hat{b} \to \hat{H} = \sum_k \omega_k \hat{b}^\dagger \hat{b}, \quad \omega_k = \frac{|\mathbf{k}|^2}{2m}, \tag{2.74}$$

$$\varphi(t), \ \bar{\varphi}(t') \to \varphi(\mathbf{k}, t), \ \bar{\varphi}(\mathbf{k}', t), \tag{2.75}$$

and extending the integration measure as well as the action to take into account all spatial momentum vectors $\mathbf{k}$

$$\mathbf{D}[\varphi^{\mathrm{cl}}, \varphi^{\mathrm{q}}] = \frac{1}{Tr\left\{\rho_0\right\}} \prod_{\mathbf{k}} \prod_{j=1}^{N} \frac{\mathrm{d}\Re\varphi_j^{\mathrm{cl}}(\mathbf{k}) \mathrm{d}\Im\varphi_j^{\mathrm{cl}}(\mathbf{k})}{\pi} \frac{\mathrm{d}\Re\varphi_j^{\mathrm{q}}(\mathbf{k}) \mathrm{d}\Im\varphi_j^{\mathrm{q}}(\mathbf{k})}{\pi}, \tag{2.76}$$

thus arriving at the Keldysh action for non-interacting bosonic fields

$$S_0[\varphi^{\mathrm{cl}}, \varphi^{\mathrm{q}}] = \sum_{\mathbf{k}} \int_{-\infty}^{+\infty} \mathrm{d}t \left(\bar{\varphi}^{\mathrm{cl}}, \bar{\varphi}^{\mathrm{q}} \right) \begin{pmatrix} 0 & \mathrm{i}\partial_t - \omega_{\mathbf{k}} - \mathrm{i}\varepsilon \\ \mathrm{i}\partial_t - \omega_{\mathbf{k}} + \mathrm{i}\varepsilon & 2\mathrm{i}\varepsilon F(\omega_{\mathbf{k}}) \end{pmatrix} \begin{pmatrix} \varphi^{\mathrm{cl}} \\ \varphi^{\mathrm{q}} \end{pmatrix}. \tag{2.77}$$

Comparing to Eq. (2.45), one finds that we effectively only replaced $\omega_0 \to \omega_{\mathbf{k}}$. The q–q-component in the free theory again acts solely as a regulator, with $F(\omega) = \coth\left((\omega-\mu)/2T\right)$ for the system in thermal equilibrium. Since $\omega_{\mathbf{k}} \equiv \mathbf{k}^2/2m$, one finds for the retarded (advanced) propagator in coordinate representation

$$[G^{-1}]^{R(A)} = \mathrm{i}\partial_t + \nabla^2/2m \pm \mathrm{i}\varepsilon. \tag{2.78}$$

Before we introduce a local interaction, we remark that one crucial step of the formalism relied on the element $\langle\varphi_1|\hat{\rho}_0|\varphi_{2N}\rangle$ in Eqs. (2.17) and (2.18) being quadratic in the fields, leading to the outlined form of $\hat{G}^{-1}$. If one therefore assumes thermal equilibrium, the interactions must be turned on over time adiabatically, i.e. infinitely slowly, such that the energy levels of the system are shifted, but no transitions may occur.

We introduce a local interaction potential $V(\phi(x))$, which contributes the interaction part of the Keldysh action

$$S_{\mathrm{int}} = -\int \mathrm{d}^d x \int_{\mathcal{C}} \mathrm{d}t V(\phi(x)) = \int \mathrm{d}^d x \int_{-\infty}^{+\infty} \mathrm{d}t V(\phi^{\mathrm{cl}}(x)+\phi^{\mathrm{q}}(x)) - V(\phi^{\mathrm{cl}}(x)-\phi^{\mathrm{q}}(x)). \tag{2.79}$$

A natural choice is $V(\phi) = \frac{\lambda}{4!}\phi^4$, for which the interaction part of the Keldysh action becomes

$$S_{\mathrm{int}} = -\int \mathrm{d}^d x \int_{-\infty}^{+\infty} \mathrm{d}t \frac{\lambda}{3}\left(\phi^{\mathrm{q}}(x)(\phi^{\mathrm{cl}}(x))^3 + (\phi^{\mathrm{q}}(x))^3\phi^{\mathrm{cl}}(x)\right). \tag{2.80}$$

The Keldysh rotation generates two vertices, one with three classical fields and one quantum component, and another one with three quantum fields and only one classical component. Of these, obviously only the "classical" vertex linear in the quantum component ϕ^{q} survives the classical limit $\hbar \to 0$, while the "quantum" vertex vanishes. This is the first manifestation of a feature that is visibly absent in the classical approximation. One can use this to benchmark functional approaches: By eliminating all diagrams containing a quantum vertex, the classical limit should be recovered, and truncation errors can be estimated by comparing to classical-statistical first-principle simulations.

2.2 Dynamical Models

We consider the scalar Landau-Ginzburg-Wilson model in $d = 2, 3$ spatial dimensions. The equilibrium distribution of the order-parameter field $\phi(x) \equiv \phi(\boldsymbol{x}, t)$ is given by

$$\mathcal{P}[\phi] \propto \exp\left(-\beta\mathfrak{H}[\phi]\right), \tag{2.81}$$

$$\mathfrak{H}[\phi] = \int \mathrm{d}^d x \left\{\frac{1}{2}\phi(x)\left(-\nabla^2 + m^2\right)\phi(x) + \frac{\lambda}{4!}\phi^4(x) - J\phi(x)\right\}, \tag{2.82}$$

where $\beta = 1/T$ refers to the inverse temperature. In case of vanishing explicit symmetry breaking ($J = 0$), this model is invariant under Z_2 transformations of the order parameter field $\phi(x) \to -\phi(x)$. If one chooses a negative square-mass $m^2 < 0$, the symmetry is spontaneously broken for temperatures $0 \leqslant T < T_c$ below some non-zero critical temperature, but restored above T_c after undergoing a second-order

phase transition in the Z_2 (Ising) universality class. We study the dynamic critical behavior of this model in both 2+1 and 3+1 dimensions. If not stated otherwise, the model parameters are set to $m^2 = -1$, $\lambda = 1$, as well as $J = 0$.

For the dissipative dynamics of Model A [13] we use as the stochastic evolution equation of the order parameter field ϕ an equation of motion with uncorrelated white noise of the same form as in [56],

$$\ddot{\phi}(\boldsymbol{x},t) = -\frac{\delta\mathfrak{H}[\phi]}{\delta\phi(\boldsymbol{x},t)} - \gamma\dot{\phi}(\boldsymbol{x},t) + \sqrt{2\gamma T}\,\eta(\boldsymbol{x},t), \tag{2.83}$$

$$\langle\eta(\boldsymbol{x},t)\rangle = 0,\ \langle\eta(\boldsymbol{x}',t')\eta(\boldsymbol{x},t)\rangle = \delta(\boldsymbol{x}'-\boldsymbol{x})\delta(t'-t), \tag{2.84}$$

where, in slight abuse of notation, the functional derivative is defined as a d-dimensional one at a fixed time t. The real parameter γ represents the Langevin coupling to a heat bath via the Gaussian random noise $\eta(\boldsymbol{x},t)$. Dots are used for partial time derivatives of the fields, in particular, defining $\pi(\boldsymbol{x},t) \equiv \dot{\phi}(\boldsymbol{x},t)$ to be used below.

In the case of the diffusive dynamics of Model B, when the order parameter $Q = \int \mathrm{d}^d x\,\phi(\boldsymbol{x},t)$ is conserved, i.e. $\dot{Q} = 0$, we consider equations of motion of the form

$$\ddot{\phi}(\boldsymbol{x},t) = \mu\nabla^2\frac{\delta\mathfrak{H}[\phi]}{\delta\phi(\boldsymbol{x},t)} - \gamma\dot{\phi}(\boldsymbol{x},t) + \sqrt{2\gamma T}\,\eta(\boldsymbol{x},t), \tag{2.85}$$

$$\langle\eta(\boldsymbol{x},t)\rangle = 0,\ \langle\eta(\boldsymbol{x}',t')\eta(\boldsymbol{x},t)\rangle = -\mu\nabla^2\delta(\boldsymbol{x}'-\boldsymbol{x})\delta(t'-t), \tag{2.86}$$

where μ is the mobility coefficient. In our numerical simulations, we set $\mu = 1$ in lattice units (see below), however we keep the symbol in our notation where it is necessary to avoid confusion of units.

If one decouples the systems from the heat bath by setting the Langevin coupling $\gamma = 0$, there is another conserved scalar quantity in the system, which can be identified with the total energy.

It may not be immediately obvious that both sets of dynamic equations reproduce the same stationary order-parameter distribution (2.81). We therefore go on to explicitly show that Eq. (2.81) solves the Fokker-Planck equation

$$\begin{aligned}\frac{\mathrm{d}\mathcal{P}}{\mathrm{d}t} =& \frac{\partial\mathcal{P}}{\partial t} + \int \mathrm{d}^d x \left\{ \frac{\delta}{\delta\phi_{\boldsymbol{x}}}\left(\dot{\phi}_{\boldsymbol{x}}\mathcal{P}[\phi,\pi]\right) + \frac{\delta}{\delta\pi_{\boldsymbol{x}}}\left(\dot{\pi}_{\boldsymbol{x}}\mathcal{P}[\phi,\pi]\right)\right\} \\ &- \gamma T\int \mathrm{d}^d x\mathrm{d}^d y\,\langle\eta_{\boldsymbol{x}}\eta_{\boldsymbol{y}}\rangle\,\frac{\delta^2}{\delta\pi_{\boldsymbol{x}}\partial\pi_{\boldsymbol{y}}}\mathcal{P}[\phi,\pi] \stackrel{!}{=} 0\end{aligned} \tag{2.87}$$

for both processes, where the implicit time dependence is given by the equal-time Poisson brackets as usual, with subscripts $\boldsymbol{x}$ as shorthand notations for the spatial functional derivatives w.r.t. the fields at fixed times. Generally, we can separate so-called *drift* and *collision* (or sometimes *diffusion*) terms, the latter one originating from interactions with the heat bath and therefore proportional to the Langevin coupling γ. We argue that the equilibrium distribution must not depend on the value of the coupling γ, and thus require both sets of terms to vanish independently.

As a brief recap, the equilibrium distribution of the order-parameter field for the standard Langevin evolution in Eq. (2.83) of course corresponds to the Boltzmann distribution,

$$\mathcal{P}_{\mathrm{A}}[\phi,\pi] = Z^{-1}\exp\left\{-\beta\mathfrak{H}[\phi] - \beta\int \mathrm{d}^d x\,\frac{\pi^2(x)}{2}\right\}. \tag{2.88}$$

It is the stationary solution to the Fokker-Planck equation for the Itô-Langevin process described by Eqs. (2.83) and (2.84) with Model-A dynamics, whose drift term vanishes and hence

$$\frac{\mathrm{d}\mathcal{P}_{\mathrm{A}}}{\mathrm{d}t} \;=\; \frac{\partial\mathcal{P}_{\mathrm{A}}}{\partial t} - \int \mathrm{d}^d x \left(\frac{\delta\mathfrak{H}[\phi]}{\delta\phi_{\boldsymbol{x}}} \frac{\delta}{\delta\pi_{\boldsymbol{x}}} - \pi_{\boldsymbol{x}} \frac{\delta}{\delta\phi_{\boldsymbol{x}}} \right) \mathcal{P}_{\mathrm{A}}[\phi,\pi] \;=\; 0\,. \tag{2.89}$$

In general, the right hand side of the Fokker-Planck equation is given by the collision term. For our Model-A dynamics it reads

$$\frac{\mathrm{d}\mathcal{P}_{\mathrm{A}}}{\mathrm{d}t} \;=\; \gamma \int \mathrm{d}^d x\; C_{\mathrm{A}}(\boldsymbol{x},\boldsymbol{x},t)\,, \quad \text{with} \;\; C_{\mathrm{A}}(\boldsymbol{x},\boldsymbol{y},t) \;=\; \frac{\delta}{\delta\pi_{\boldsymbol{x}}} \left[\pi_{\boldsymbol{y}}\mathcal{P}_{\mathrm{A}} + T\frac{\delta}{\delta\pi_{\boldsymbol{y}}}\mathcal{P}_{\mathrm{A}} \right], \tag{2.90}$$

and separately also vanishes in equilibrium, simply because $T\delta\mathcal{P}_{\mathrm{A}}/\delta\pi_{\boldsymbol{x}} = -\pi_{\boldsymbol{x}}\,\mathcal{P}_{\mathrm{A}}$.

By the same line of arguments, the equilibrium distribution for our diffusive Model-B dynamics is in turn given by

$$\mathcal{P}_{\mathrm{B}}\,[\phi,\pi] = Z^{-1} \exp\left\{ -\beta\mathfrak{H}[\phi] + \beta \int \mathrm{d}^d x\, \frac{1}{2\mu}\, \pi(x)\nabla^{-2}\pi(x) \right\}. \tag{2.91}$$

This is the stationary solution to

$$\frac{\mathrm{d}\mathcal{P}_{\mathrm{B}}}{\mathrm{d}t} \;=\; \frac{\partial\mathcal{P}_{\mathrm{B}}}{\partial t} + \int \mathrm{d}^d x \left(\left(\mu\nabla^2 \frac{\delta\mathfrak{H}[\phi]}{\delta\phi_{\boldsymbol{x}}} \right) \frac{\delta}{\delta\pi_{\boldsymbol{x}}} + \pi_{\boldsymbol{x}} \frac{\delta}{\delta\phi_{\boldsymbol{x}}} \right) \mathcal{P}_{\mathrm{B}}[\phi,\pi] \;=\; 0\,, \tag{2.92}$$

and it also nullifies the collision integral, where the kernel now gets modified according to

$$C_{\mathrm{B}}(\boldsymbol{x},\boldsymbol{y},t) \;=\; \frac{\delta}{\delta\pi_{\boldsymbol{x}}} \left[\pi_{\boldsymbol{y}}\mathcal{P}_{\mathrm{B}} - T\mu\nabla^2 \frac{\delta}{\delta\pi_{\boldsymbol{y}}}\mathcal{P}_{\mathrm{B}} \right]. \tag{2.93}$$

And finally, for completeness, away from equilibrium the full Fokker-Planck equation for our Model-B process reads as follows:

$$\frac{\partial\mathcal{P}_{\mathrm{B}}}{\partial t} \;=\; -\int \mathrm{d}^d x \left[\left(\left(\mu\nabla^2 \frac{\delta\mathfrak{H}[\phi]}{\delta\phi_{\boldsymbol{x}}} \right) \frac{\delta}{\delta\pi_{\boldsymbol{x}}} + \pi_{\boldsymbol{x}} \frac{\delta}{\delta\phi_{\boldsymbol{x}}} \right) \mathcal{P}_{\mathrm{B}}[\phi,\pi] - \gamma\, C_{\mathrm{B}}(\boldsymbol{x},\boldsymbol{x},t) \right]. \tag{2.94}$$

Note that the Model-A version of the equilibrium distribution in (2.88) is given by the usual exponentiated Hamiltonian of the corresponding scalar field theory with a single real field variable $\phi(x)$ and its conjugate momentum field $\pi(x) \equiv \dot{\phi}(x)$. It is therefore tempting to also identify the equilibrium distribution in Eq. (2.91) with the Boltzmann distribution $\mathcal{P}_{\mathrm{B}} \propto \exp\left(-\beta H_{\mathrm{B}}\right)$ of an effective total energy H_{B}, i.e.,

$$H_{\mathrm{B}} = \int \mathrm{d}^d x \left\{ -\frac{1}{2\mu}\,\pi(x)\nabla^{-2}\pi(x) + \frac{1}{2}\phi(x)\left(-\nabla^2 + m^2\right)\phi(x) + \frac{\lambda}{4!}\phi^4(x) - J\phi(x) \right\}. \tag{2.95}$$

However, the time derivative $\pi(x) = \dot{\phi}(x)$ is then no longer the conjugate momentum variable of the field $\phi(x)$. On the other hand, by introducing a canonical momentum field $K(x)$ as the solution to $\pi(x) = -\mu\nabla^2 K(x)$ as the scalar field conjugate to $\phi(x)$, it is straightforward to show that the Hamiltonian

$$H_{\mathrm{B}}\,[\phi,K] = -\int \mathrm{d}^d x\, \frac{\mu}{2}\, K(x)\nabla^2 K(x) + \mathfrak{H}[\phi] = \int \mathrm{d}^d x\, \frac{\mu}{2}\left(\nabla K(x)\right)^2 + \mathfrak{H}[\phi] \tag{2.96}$$

generates the conservative part of the equation of motion (2.85) with $\dot{\phi}(\mathbf{x},t) = -\mu\nabla^2 K(\mathbf{x},t)$.

An intuitive interpretation of $K(\mathbf{x},t)$ is obtained from recalling that the diffusive dynamics of Model B result from the conservation of the total magnetization Q, i.e. the order parameter field obeys a continuity equation

$$\dot{\phi}(\mathbf{x},t) + \nabla\cdot\mathbf{J}(\mathbf{x},t) = 0, \tag{2.97}$$

where the magnetization current $\mathbf{J}(\mathbf{x},t) = \mu\nabla K(\mathbf{x},t)$ is proportional to the gradient of the conjugate momentum field $K(x)$, related by the mobility coefficient. The coupling of the magnetization current to the heat bath must then be consistent with Eq. (2.85), such that we have for its evolution

$$\dot{\mathbf{J}}(\mathbf{x},t) = \mu\nabla\dot{K}(\mathbf{x},t) - \gamma\mathbf{J}(\mathbf{x},t) - \sqrt{2\gamma\mu T}\,\boldsymbol{\zeta}(\mathbf{x},t) \tag{2.98}$$

$$= -\mu\nabla\frac{\delta H_{\mathrm{B}}}{\delta\phi(\boldsymbol{x},t)} - \gamma\mathbf{J}(\mathbf{x},t) - \sqrt{2\gamma\mu T}\,\boldsymbol{\zeta}(\mathbf{x},t), \tag{2.99}$$

with a d-component vectorial noise $\boldsymbol{\zeta}(\mathbf{x},t)$, related to the noise in Eq. (2.86) by $\sqrt{\mu}\,\nabla\cdot\boldsymbol{\zeta} = \eta$, and hence with zero mean and covariance $\langle\zeta_i(\mathbf{x}',t')\zeta_j(\mathbf{x},t)\rangle = \delta_{ij}\delta(\mathbf{x}'-\mathbf{x})\delta(t'-t)$.

In particular, this confirms that $\dot{K}_{\boldsymbol{x}} = -\dfrac{\delta}{\delta\phi_{\boldsymbol{x}}}H_{\mathrm{B}}[\phi,K]$.

Note, however, that there is yet another possible Hamiltonian H'_{B} which results in the same equations of motion. Its form for $\lambda = 0$ is that of a free massive longitudinal vector field $\nabla\phi$, i.e.

$$H'_{\mathrm{B}} = \int \mathrm{d}^d x \left[\frac{1}{2}\,\pi^2 + \frac{\mu}{2}\left((\nabla^2\phi)^2 + m^2(\nabla\phi)^2\right)\right]. \tag{2.100}$$

In addition to the Z_2 symmetry of the effective Hamiltonian H_{B}, this expression is invariant under constant displacements of the field $\phi'(x) \to \phi(x)+c$, implying that the spatial integral over the rate of change of the order parameter field (i.e. $\dot{\phi}(\boldsymbol{p}=0)$) is also a conserved quantity. Setting $\dot{\phi}(\boldsymbol{p}=0,t=0)=0$ then results in the conservation of the order parameter $\phi(\boldsymbol{p}=0,t)$ itself. Unfortunately, the interaction part of the Hamiltonian is then no longer local. It has however a compact representation in Fourier space, which is given in Appendix A, Eq. (A.14).

2.2.1 Covariant formulation

Both dynamic models can be written in a Lorentz-covariant manner. The model without conserved order parameter is described by the usual Lagrangian density of a self-interacting relativistic scalar field,

$$\mathcal{L}_{\mathrm{A}} = \dot{\phi}\,\frac{\delta H_{\mathrm{A}}}{\delta\pi} - \frac{1}{2}\pi^2 - \frac{1}{2}(\nabla\phi)^2 - V(\phi) = \frac{1}{2}(\partial_\mu\phi)\partial^\mu\phi - V(\phi)\,, \tag{2.101}$$

with

$$V(\phi) = \frac{m^2}{2}\phi^2 + \frac{\lambda}{4!}\phi^4\,,$$

and West-coast metric with signature $(+,-,-,-)$. The Euler-Lagrange equation yields the equation of motion $\partial_\mu\partial^\mu\phi + V'(\phi) = 0$ for the non-dissipative system

($\gamma = 0$) with Model-C dynamics. Adding the coupling to the heat bath, we have to specify its local rest frame. Denoting the four-velocity of the bath by u^μ, with $u_\mu u^\mu = 1$, we can then write,

$$0 \;=\; \partial_\mu \partial^\mu \phi + V'(\phi) + \gamma\, u_\mu \partial^\mu \phi - \sqrt{2\gamma T}\,\eta \tag{2.102}$$

as the covariant version of the equation of motion for our realization of Model-A dynamics, where Eq. (2.83) is recovered with $u^\mu = (1,0,0,0)$ as the rest frame of the heat bath.

In order to translate the Hamiltonian (2.96) and the equation of motion Eq. (2.85) with Model-B dynamics to covariant form, we introduce some notation from relativistic hydrodynamics: Along with the local rest-frame velocity u_μ, we denote the corresponding timelike derivative in the local rest frame by $D_\tau \equiv u_\mu \partial^\mu$. For the spacelike gradient one first introduces the four-dimensionally transverse projector, $\Delta^{\mu\nu} \equiv g^{\mu\nu} - u^\mu u^\nu$ and with this, $\nabla^\mu \equiv \Delta^{\mu\nu}\partial_\nu$, so that $\partial^\mu = u^\mu D_\tau + \nabla^\mu$. The corresponding spatial Laplacian is analogously written as $\Delta = -\nabla_\mu \Delta^{\mu\nu}\nabla_\nu = -\nabla_\mu \nabla^\mu$. Moreover, we introduce the spacelike four-vector

$$\nu^\mu \equiv \Delta^{\mu\nu} J_\nu = -\mu \nabla^\mu K\,, \;\; \text{such that} \;\; u_\mu \nu^\mu = 0\,. \tag{2.103}$$

We can then write our Model-B equation of motion in the form of Eq. (2.98) as

$$D_\tau \nu^\mu \;=\; -\mu D_\tau(\nabla^\mu K) - \gamma \nu^\mu - \sqrt{2\gamma\mu T}\,\zeta_\perp^\mu\,, \tag{2.104}$$

where the spacelike noise vectors, with $u_\mu \zeta_\perp^\mu = 0$, now obey

$$\langle \zeta_\perp^\mu(x)\zeta_\perp^\nu(x')\rangle = \Delta^{\mu\nu}\delta(x-x')\,, \tag{2.105}$$

with $d{+}1$ dimensional δ-function. They are related to the scalar noise η by $\sqrt{\mu}\,\nabla_\mu \zeta_\perp^\mu = \eta$, whose variance is now given by the covariant form of the spatial Laplacian $\Delta = -\nabla_\mu \nabla^\mu$,

$$\langle \eta(x)\eta(x')\rangle = -\mu\Delta\,\delta(x-x')\,. \tag{2.106}$$

In the spacelike projection of Eq. (2.104) we can now use $\Delta^{\mu\nu} D_\tau \nabla_\nu = \nabla^\mu D_\tau$ to commute timelike and spacelike derivatives of the momentum field K on the right hand side. For the timelike derivative of K we furthermore use

$$D_\tau K = \Delta\phi - V'(\phi)\,, \tag{2.107}$$

where we now have $\phi \equiv u_\mu J^\mu$, and Eq. (2.104) thus now becomes

$$\Delta^{\mu\nu} D_\tau \nu_\nu \;=\; -\gamma\Big(\nu^\mu - \frac{\mu}{\gamma}\,\nabla^\mu\big(V'(\phi) - \Delta\phi\big)\Big) - \sqrt{2\gamma\mu T}\,\zeta_\perp^\mu\,. \tag{2.108}$$

In this hydrodynamic form, the conserved current J^μ in the continuity equation (2.97), $\partial_\mu J^\mu = 0$, is thus decomposed as $J^\mu = \phi u^\mu + \nu^\mu$, and Eq. (2.108) assumes the role of an Israel-Stewart relaxation equation [61, 62] with relaxation time $1/\gamma$ and vector force $I^\mu = \nabla^\mu\big(V'(\phi) - \Delta\phi\big)$. In the non-interacting scalar field theory, for example, the corresponding diffusion rate is thus given by $D_{\rm diff}(\boldsymbol{k}) = (\mu/\gamma)\,(m^2 + \boldsymbol{k}^2) = (\mu/\gamma)\,\chi^{-1}(\boldsymbol{k})$, i.e. inversely proportional to the respective static susceptibility $\chi(\boldsymbol{k})$ as expected.

By taking the limit of vanishing Langevin coupling $\gamma \to 0$, the dynamics then conserve the total energy, and one arrives at the relativistic version of Model-D dynamics. We show in Appendix B that in this limit, the structure of the low-energy spectrum of the theory changes significantly.

The analogous procedure as used for our Model A or C (without dissipation, i.e. $\gamma = 0$) Lagrangian $\mathcal{L}_{\rm A}$ in Eq. (2.101) above, now first leads to a Lagrangian for the non-dissipative ($\gamma = 0$) part of our theory with conserved order parameter, which is of the form

$$\begin{aligned} \mathcal{L}_{\rm B} &= -\frac{1}{2\mu}\,\dot{\phi}\nabla^{-2}\dot{\phi} - \frac{1}{2}(\nabla\phi)^2 - V(\phi) \\ &= \frac{\mu}{2}\,K\nabla^2 K + K\dot{\phi} - \frac{1}{2}(\nabla\phi)^2 - V(\phi)\,, \end{aligned} \tag{2.109}$$

where we have reintroduced K as a Gaussian auxiliary field, whose equation of motion implements the constraint

$$\frac{\partial\mathcal{L}_{\rm B}}{\partial K} = \dot{\phi} + \mu\nabla^2 K = 0\,. \tag{2.110}$$

Together with the equation of motion for the ϕ field,

$$\frac{\partial\mathcal{L}_{\rm B}}{\partial\phi} = \nabla^2\phi - V'(\phi) = \dot{K}\,, \tag{2.111}$$

we thus recover the non-dissipative part of Eq. (2.85),

$$\ddot{\phi} = -\mu\partial_t\nabla^2 K = -\mu\nabla^2\big(\nabla^2\phi - V'(\phi)\big)\,. \tag{2.112}$$

Note, however, in order to get there we had to commute the time derivative with the spatial Laplacian, which becomes a bit subtle in the covariant formulation when the local rest-frame velocity is spacetime dependent, for the same reason that we needed the transverse projection in the Israel-Stewart equation (2.108) in order to be able to commute the timelike and spacelike derivatives on K. In the covariant version of the equation of motion for the scalar field ϕ, the necessary commutator is readily worked out to be

$$D_\tau\Delta = \Delta D_\tau + \mu(\partial_\mu u^\mu)a^\nu\nabla_\nu\,, \tag{2.113}$$

where the spacelike vector $a^\mu = D_\tau u^\mu$ describes the acceleration of the local fluid element, and $\partial_\mu u^\mu$ its expansion. Hence, the spatial Laplacian $\Delta = -\nabla_\mu\nabla^\mu$ commutes with the timelike derivative $D_\tau = u^\mu\partial_\mu$ for incompressible fluids with $\partial_\mu u^\mu = 0$. We observe that the non-dissipative part of Eq. (2.85) describes noisy Israel-Stewart hydrodynamics in the limit of infinite relaxation time, which we denote by Model D.

Moreover, using the decomposition of the four-vector $J^\mu = \phi u^\mu + \nu^\mu$, which is inverted by $\phi = u_\mu J^\mu$ and $\nu^\mu = -\mu\nabla^\mu K$, see Eq. (2.103) above, one readily verifies that the current conservation law in covariant form reads,

$$\begin{aligned} \partial_\mu J^\mu &= D_\tau\phi + (\partial_\mu u^\mu)\phi + \partial_\mu\nu^\mu \\ &= D_\tau\phi - \mu\,\partial_\mu\nabla^\mu K\,, \end{aligned} \tag{2.114}$$

where we have again assumed incompressibility ($\partial_\mu u^\mu = 0$) in the second line. We thus need the covariant equation of motion of the K field to yield Eq. (2.114).

This is achieved by the following covariant version of the Lagrangian for relativistic Model-D dynamics,

$$\mathcal{L}_{\mathrm{B}} = \frac{\mu}{2}(\nabla_\mu K)\nabla^\mu K + K D_\tau \phi + \frac{1}{2}(\nabla_\mu \phi)\nabla^\mu \phi - V(\phi)\,, \tag{2.115}$$

where the corresponding conservative equations of motion in covariant form are obtained from

$$D_\tau \frac{\partial \mathcal{L}_{\mathrm{B}}}{\partial (D_\tau \phi)} - \frac{\partial \mathcal{L}_{\mathrm{B}}}{\partial \phi} = D_\tau K + \partial_\mu \nabla^\mu \phi + V'(\phi) = 0\,, \tag{2.116}$$

$$\frac{\partial \mathcal{L}_{\mathrm{B}}}{\partial K} = D_\tau \phi - \mu\, \partial_\mu \nabla^\mu K = 0\,. \tag{2.117}$$

Finally, note that in general, $\partial_\mu \nabla^\mu \neq \nabla^\mu \partial_\mu$ and neither of the two is equal to $\nabla_\mu \nabla^\mu = -\Delta$, but one has

$$\partial_\mu \nabla^\mu = \nabla_\mu \nabla^\mu - a^\mu \partial_\mu\,, \tag{2.118}$$

$$\nabla^\mu \partial_\mu = \nabla_\mu \nabla^\mu + (\partial_\mu u^\mu) D_\tau\,. \tag{2.119}$$

For an incompressible fluid without acceleration $a^\mu = D_\tau u^\mu$ these distinctions are luckily unnecessary.

2.2.2 Lattice Regularization

We employ a lattice regularization to supply an ultraviolet cutoff to possible spatial variations in the order parameter field $\phi(x)$. The entropy functional then becomes a sum over the field at discrete lattice sites

$$\mathfrak{H}[\phi_x] = \sum_x a^d \left\{ -\frac{1}{2a^2} \sum_{y\sim x} \phi_x \phi_y + \left(\frac{m^2}{2} + \frac{d}{a^2}\right)\phi_x^2 + \frac{\lambda}{4!}\phi_x^4 + J\phi_x \right\}, \tag{2.120}$$

where the sum $\sum_{y\sim x}$ runs over all lattice sites y adjacent to the site x, and $\sum_x$ denotes the sum over the lattice volume. We approximate the Laplacian $\nabla^2 \phi_x \equiv \nabla_b \nabla_f \phi_x = a^{-2}\left(\sum_{y\sim x}\phi_y - 2d\phi_x\right)$ by applying a forward after a backward derivative. To simplify the notation, we from here on let the lattice spacing $a = 1$ be unity. For Model C, the discretization of the Hamiltonian is trivial, and we obtain for the lattice Hamiltonian and the equations of motion

$$H_A = \sum_x \frac{\pi_x^2}{2} - \frac{1}{2}\sum_{y\sim x}\phi_x\phi_y + \left(\frac{m^2}{2} + d\right)\phi_x^2 + \frac{\lambda}{4!}\phi_x^4 + J\phi_x, \tag{2.121}$$

$$\dot{\phi}_x = \frac{\partial H_A}{\partial \pi_x} = \pi_x, \tag{2.122}$$

$$\dot{\pi}_x = -\frac{\partial H_A}{\partial \phi_x} - \gamma\pi_x + \sqrt{2\gamma T}\eta_x(t) \tag{2.123}$$

$$\frac{\partial H_A}{\partial \phi_x} = -\sum_{x\sim y}(\phi_y - \phi_x) + \left(m^2 + \frac{\lambda}{6}\phi_x^2\right)\phi_x + J, \tag{2.124}$$

where $\eta_x(t)$ is a zero-mean Gaussian white noise at every lattice site with $\langle \eta'_x(t')\eta_x(t)\rangle = \delta_{x,x'}\delta(t'-t)$.

For Models B and D, we begin the discretization by considering again the pair of conjugate variables $\{\phi(x), K(x)\} \to \{\phi_x, K_x\}$, which are defined on the sites of the lattice. One obtains the magnetization current $\mathbf{J}(x) = \nabla K(x)$ by an external derivative, which is ambiguous on the lattice. We choose to define the components of the discretized magnetization current $J^i(x) \to J^i_x$ on the links connecting the sites $(x + \hat{i}, x)$, therefore interpreting the derivative in

$$\mathbf{J}_x = \mu \nabla_f K_x \tag{2.125}$$

as the *forward* derivative. In order to relate the current $\mathbf{J}_x$ to the time derivative π_x on the sites, we interpret the derivative in the discretized version of the continuity equation (2.97) as the *backward* derivative

$$\pi_x + \nabla_b \cdot \mathbf{J}_x = 0, , \tag{2.126}$$

which leads to the equations of motion for the discretized current and time derivative

$$\dot{\mathbf{J}}_x = \mu \nabla_f \left(\partial_t K_x\right) - \gamma \mathbf{J}_x + \sqrt{2\mu\gamma T}\zeta_x(t) = -\nabla_f \frac{\partial H_2}{\partial \phi_x} - \gamma \mathbf{J}_x + \sqrt{2\mu\gamma T}\zeta_x(t), \tag{2.127}$$

$$\begin{aligned} \dot{\pi}_x &= -\nabla_b \dot{\mathbf{J}}_x = \mu \nabla_b \nabla_f \frac{\partial H}{\partial \phi_x} + \gamma \nabla_b \mathbf{J}_x - \sqrt{2\mu\gamma T}\nabla_b \zeta_x(t) \\ &= \mu \nabla^2 \frac{\partial H}{\partial \phi_x} - \gamma \pi_x - \sqrt{2\mu\gamma T}\nabla_b \zeta_x(t). \end{aligned} \tag{2.128}$$

We thus have for the equations of motion and the lattice Hamiltonian for Model D

$$H_B = \sum_x \left\{ -\frac{\mu}{2} K_x \sum_{y\sim x} (K_y - K_x) - \frac{1}{2}\sum_{y\sim x} \phi_x \phi_y + \left(\frac{m^2}{2} + d\right)\phi_x^2 + \frac{\lambda}{4!}\phi_x^4 + J\phi_x \right\}, \tag{2.129}$$

$$\dot{\phi}_x = \frac{\partial H_B}{\partial K_x} = -\mu \sum_{y\sim x} (K_y - K_x) = -\mu \nabla^2 K_x \equiv \pi_x, \tag{2.130}$$

$$\dot{\pi}_x = \mu \sum_{y\sim x} \left(\frac{\partial H_B}{\partial \phi_y} - \frac{\partial H_B}{\partial \phi_x} \right) - \gamma \pi_x + \sqrt{2\mu\gamma T}\nabla_b \zeta_x(t), \tag{2.131}$$

where $\partial H_B/\partial\phi_x = \partial H_A/\partial\phi_x$ is given in Eq. (2.124). For practical reasons, in both cases we work with ϕ_x and its time derivative π_x.

Concerning the noise term in Eq. (2.128) we remark that by the affine transformation of a d-component vector of Gaussian random numbers with unit covariance, we generate random variables with a distribution approaching the correct continuum limit in Eq. (2.86)

$$\eta_x(t) = \nabla_b \cdot \zeta_x(t), \ \left\langle \zeta^i_x(t)\zeta^j_y(t')\right\rangle = \delta_{i,j}\delta_{x,y}\delta(t-t'), \tag{2.132}$$

$$\begin{aligned} \left\langle \eta_x(t)\eta_y(t')\right\rangle &= \left\langle \left(\nabla_b \cdot \zeta_x(t)\right)\left(\nabla_b \cdot \zeta_y(t')\right)\right\rangle = (\overbrace{\nabla_b^T}^{=-\nabla_f}\nabla_b)\delta_{xy}\delta(t-t') \\ &= -\nabla^2\delta_{xy}\delta(t-t'). \end{aligned} \tag{2.133}$$

In order to generate an initial thermal distribution of the time derivative field π_x matching the stationary solutions, the lattice variables are drawn from a Gaussian

multivariate distribution with the covariance given by T for Models A and C respectively $-T\nabla^2$ for Models B and D. The latter is realized by taking the backward derivative of a vector noise with the Boltzmann distribution,

$$\left\langle \zeta_x^i \right\rangle = 0, \ \left\langle \zeta_x^i \zeta_y^j \right\rangle = T\delta_{x,y}\delta^{i,j}, \tag{2.134}$$

$$\pi_x(t_i) = \nabla_b \cdot \zeta_x = \sum_i^d \left(\zeta_x^i - \zeta_{x-\mathbf{e}_i}^i\right), \tag{2.135}$$

$$\Rightarrow \ \langle \pi_x(t_i)\pi_y(t_i)\rangle = -T\nabla^2\delta_{x,y}, \tag{2.136}$$

where $\mathbf{e}_i$ is a unit vector in the direction i.

2.3 Spectral function

Spectral functions of bosonic operators $\hat{O}(t, \mathbf{x})$ in a quantum field theory are defined by a decomposition of the two-point function (with translational invariance in space and time),

$$\begin{aligned} G_O(t-t', \mathbf{x}-\mathbf{x}') &= \left\langle \mathbb{T}\hat{O}(t,\mathbf{x})\hat{O}^\dagger(t',\mathbf{x}') \right\rangle \\ &= F(t-t', \mathbf{x}-\mathbf{x}') - \frac{\mathrm{i}}{2}\rho(t-t', \mathbf{x}-\mathbf{x}')\,\mathrm{sgn}\,(t-t'), \end{aligned} \tag{2.137}$$

where $\mathbb{T}$ denotes the time-ordering operator, and we have introduced the spectral (ρ) and statistical (F) correlation functions

$$\rho\,(t-t', \mathbf{x}-\mathbf{x}') = \mathrm{i}\left\langle \left[\hat{O}(t,\mathbf{x}), \hat{O}^\dagger(t',\mathbf{x}')\right] \right\rangle, \tag{2.138}$$

$$F\,(t-t', \mathbf{x}-\mathbf{x}') = \frac{1}{2}\left\langle \left[\hat{O}(t,\mathbf{x}), \hat{O}^\dagger(t',\mathbf{x}')\right]_+ \right\rangle - \langle \hat{O}(t,\mathbf{x})\rangle\langle \hat{O}^\dagger(t',\mathbf{x}')\rangle, \tag{2.139}$$

with $[\,,\,]_+$ representing the anti-commutator. While the spectral function ρ is relevant to describe the (linear) response of the system to an external perturbation, and thus provides the spectrum of possible excitations, the statistical correlation function F in general describes the quantum and thermal statistical fluctuations present in the system.

Based on the Kubo-Martin-Schwinger (KMS) [42, 43, 44] condition in thermal equilibrium, F and ρ are related via the fluctuation-dissipation relation

$$F(\omega, \mathbf{p}, T) = \left(n_T(\omega) + \frac{1}{2}\right)\rho(\omega, \mathbf{p}, T). \tag{2.140}$$

Note that, for practical reasons, we defined the Fourier transformations of F and ρ as

$$F(\omega, \mathbf{p}, T) = \int \mathrm{d}t\mathrm{d}^d x\, e^{\mathrm{i}(\omega t - \mathbf{px})} F(t, \mathbf{x}, T), \tag{2.141}$$

$$\rho(\omega, \mathbf{p}, T) = -\mathrm{i}\int \mathrm{d}t\mathrm{d}^d x\, e^{i(\omega t - \mathbf{px})} \rho(t, \mathbf{x}, T), \tag{2.142}$$

where the additional factor of $-i$ in (2.142) ensures that the spectral function $\rho(t)$, which is an odd function under space-time reflections $\rho(-t, -x) = -\rho(t, x)$, is real in

both the time ($\rho(t)$) and frequency domain ($\rho(\omega)$). In the classical limit, the thermal distribution becomes

$$n_T(\omega) + 1/2 = \frac{1}{e^{\beta\omega} + 1} + \frac{1}{2} \approx T/\omega, \tag{2.143}$$

and the spectral can be computed directly as

$$\rho(t, \mathbf{p}, T) = -\frac{1}{T}\partial_t F(t, \mathbf{p}, T). \tag{2.144}$$

Close to the critical point, the dynamics of the system are dominated by its slow infrared modes with frequencies $\omega \ll T$ very small compared to the temperature scale where quantum effects are relevant. Therefore, the classical description suffices to fully capture the dynamic critical behavior of the model.

We are interested in the spectral function of the order parameter field ϕ, which in the classical-statistical field theory is formally defined via the Poisson bracket of the fields as

$$\rho(t - t_0, \mathbf{x} - \mathbf{x}_0) = -\left\langle \{\phi(t, \mathbf{x}), \phi(t_0, \mathbf{x}_0)\} \right\rangle_{\mathrm{cl}}. \tag{2.145}$$

While it is in principle possible to evaluate the Poisson brackets directly (see e.g. [63, 64]), we follow previous works and instead exploit the classical KMS condition to calculate the spectral function in thermal equilibrium [39, 40, 41]. By virtue of Eq. (2.144), we can compute this spectral function $\rho(t, \mathbf{x}, T)$ via the statistical two-point function $F(t, \mathbf{x}, T)$ directly from the classical lattice fields,

$$\rho(t, \mathbf{x}, T) = -\frac{1}{2T}\left\langle \pi(t, \mathbf{x})\phi(0, \mathbf{0}) - \phi(t, \mathbf{x})\pi(0, \mathbf{0}) \right\rangle. \tag{2.146}$$

3 | Technical realization

The aim of this chapter is to enable the reader to fully reproduce any numerical results given in the subsequent chapters, by giving all necessary details concerning the technical realization of the field theory apparatus. We provide the code as a public repository under `https://gitlab.com/nierenstein23/phi4lattice`.

The main simulation is implemented in C++ [65] and CUDA [66], and built using both CUDA's `nvcc` compiler as well as the C++-compiler of the GNU Compiler Collection [67] `g++`, where the build process is automated using `cmake` [68]. Almost all features[1] are implemented both as pure CPU code, parallelized using OpenMP [69], as well as GPU-accelerated CUDA code. The user can either select the desired architecture at runtime, or de-select the parts containing CUDA code at compile time, e.g. if CUDA is not available in a certain environment.

Data used for the study at hand was generated mainly on the local heterogeneous Cluster of the group of Prof. Lorenz von Smekal in Gießen, consisting of both mixed GPU hardware as well as eight Intel Xeon Phi 7250 nodes. Some additional computation time was granted on the GPU Cluster of Bielefeld University [70] as well as on the facilities of Cori at NERSC [71].

Evaluation of data was done using a mixture of Python 3/NumPy [72, 73], `awk` [74] and GNU Bash [75] scripts. Gnuplot [76] was used for extraction of some fit parameters and general visualization of processed data.

3.0.1 Lattice representation

The lattice fields are implemented as linear arrays, with an indexing function taking care of dimensionality $d \in \{2, 3\}$ and periodic boundary conditions. Hamiltonian dynamics are supported for fields with $N_c < 16$ components[2]; diffusion dynamics are as now limited to single-component fields; the generalization would however require minimal effort.

Most operations on the fields are of low algorithmic intensity and therefore memory-bound. To optimize memory access, the fields are stored in memory with indices in ascending order are c, x, y, z.

Since the fields are evolved using a leapfrog scheme, it is useful to simultaneously hold the fields ϕ_x, π_x as separate arrays in memory at all times.

[1] As of May 12, 2021, some functionality regarding the energy-momentum tensor is only available for single-component fields on the GPU architecture.

[2] The upper limit on N_c is a compile-time constant.

3.0.2 Integrator scheme

We integrate Eqs. (2.123) and (2.131) using a velocity Verlet method, also known as "leapfrog" integration, where the equations of motion are evaluated and updated at interleaved time points.

To evolve the system from times t to $t + \Delta t$ in N_t time steps, one starts with a half-step in the fields ϕ_x, followed by alternating full steps in π_x, ϕ_x, and finishes with an appropriate half-step to bring both variables to the same time coordinate,

$$\begin{aligned}
\phi_x\left(t + \frac{\delta_t}{2}\right) &= \phi_x(t) + \frac{\delta_t}{2}\pi_x \\
&\dots \\
\pi_x\left(t + i\,\delta_t\right) &= \pi_x\left(t + (i-1)\,\delta_t\right) + \delta_t\, F\left[\phi_x\left(t + (i-1/2)\,\delta_t\right), \pi_x\left(t + (i-1)\,\delta_t\right)\right] \\
\phi_x\left(t + (i+1/2)\,\delta_t\right) &= \phi_x\left(t + (i-1/2)\right) + \delta_t\,\pi_x \\
&\dots \\
\pi_x\left(t + \Delta t\right) &= \pi_x(t + (N_t-1)\delta_t) + \delta_t\, F\left[\phi_x\left(t + (N_t-1/2)\,\delta_t\right), \pi_x(t + (N_t-1)\delta_t)\right] \\
\phi_x\left(t + \Delta t\right) &= \phi_x\left(t + (N_t-1/2)\,\delta_t\right) + \frac{\delta_t}{2}\pi_x,
\end{aligned}$$

where we defined $\delta_t \equiv \Delta t/N_t$, and the counter variable i runs from 1 to $N_t - 1$. We abbreviate the left-hand side of the equation of motion by $\dot{\pi}_x = \ddot{\phi}_x = F[\phi_x, \pi_x]$. The error of this scheme is in $O(\delta_t^2)$. For real-time simulations, we typically use $\Delta t = 1$ and $N_t = 160$, where we tested that there are no remaining step-size effects on the final results.

3.0.3 Random number generator

If there is a finite heat-bath coupling $\gamma > 0$, the equations of motion involve Gaussian noise terms. Gaussian random numbers x, y with unit variance are obtained from two uniform random numbers $u, v \in (0, 1]$ via the Box-Muller method [77]

$$x = \sqrt{-2\ln(u)}\sin(2\pi v), \quad y = \sqrt{-2\ln(u)}\cos(2\pi v). \tag{3.1}$$

In order to generate large amounts of uniform pseudo-random numbers with a very long cycle in parallel, a linear feedback shift register (Tausworthe) random number generator (RNG) is employed [78, 79]. We define an array of RNG states with one state per lattice site. This array is initialized using `lrand48()`, seeded with a large number typically between 10^9 and $10^{10} - 1$, which allows exact reproduction of any simulation run independent of hardware.[3] If no seed is specified, we take the time from the UNIX epoch in seconds as default seed.

3.0.4 Hybrid Monte-Carlo

In order to obtain the equilibrium results of the classical theory shown in Section 4.1, one has to compute observables of the form

$$\langle O(\phi_x)\rangle = \int \mathcal{D}\left[\phi_x\right] O(\phi_x) P(\phi_x) \tag{3.2}$$

[3] While the sequence of pseudo-random numbers is defined by the seed, differences in the implementation related to optimizations lead to minimal changes in observables, especially those concerning sums over large arrays.

with the equilibrium distribution of the order parameter field given by Eq. (2.81). While one could in theory solve the above integral by generating random configurations of ϕ_x and computing the corresponding weight factors, this turns out to be computationally very inefficient: Almost all configurations have minuscule weights, and very few configurations with relatively high weight dominate the result. One goes around this problem by generating configurations of ϕ_x with abundancies reflecting their weight factor $P(\phi_x)$ using a Metropolis-Hastings algorithm.

The algorithm generates a sequence of configurations ϕ_x using a Markov process, asymptotically converging on a stationary distribution $P(\phi_x)$. A sufficient condition for the existence of a stationary distribution $P(\phi_x)$ is *detailed balance*, i.e.

$$P(\phi'_x|\phi_x)P(\phi_x) = P(\phi_x|\phi'_x)P(\phi'_x), \tag{3.3}$$

where $P(\phi'_x|\phi_x)$ denotes the transition probability from the configuration ϕ_x to ϕ'_x. One now separates the transition into a *proposal* and *acceptance/rejection*. The proposal distribution is denoted as $p(\phi'_x|\phi_x)$ and the acceptance/rejection as $a(\phi'_x|\phi_x)$, giving the conditional probabilities of proposing/accepting the new configuration ϕ'_x after ϕ_x. The total transition probability is then the product $P(\phi'_x|\phi_x) = p(\phi'_x|\phi_x)a(\phi'_x|\phi_x)$. Inserting into Eq. (3.3) and ordering the terms yields

$$\frac{a(\phi'_x|\phi_x)}{a(\phi_x|\phi'_x)} = \frac{P(\phi'_x)p(\phi_x|\phi'_x)}{P(\phi_x)p(\phi'_x|\phi_x)}\,. \tag{3.4}$$

Letting

$$a(\phi'_x|\phi_x) = \min\left(1, \frac{P(\phi'_x)p(\phi_x|\phi'_x)}{P(\phi_x)p(\phi'_x|\phi_x)}\right) \tag{3.5}$$

fulfills the detailed-balance condition for any proposal function.

Therein now lies the strength of the hybrid Monte-Carlo (or Hamiltonian Monte-Carlo) method. (For a detailed review, see [80].) Here, one generates ϕ'_x by evolving ϕ_x using the Hamiltonian equations of motion (2.122) and (2.123). One initializes ϕ_x randomly and draws the conjugate momentum π_x from a Gaussian distribution with variance T. After evolving for some time Δt using the leapfrog integrator described above, one arrives at the proposal $\phi'_x = \phi_x(t+\Delta t)$, $\pi'_x = \pi_x(t+\Delta t)$. Since Hamiltonian dynamics are exactly reversible and the leapfrog integrator is exactly symmetric in time, one has $p(\phi'_x, \pi'_x|\pi_x, \phi_x) = p(\phi_x, \pi_x|\phi'_x, \pi'_x)$. At finite step size however, the Hamiltonian H may not be exactly conserved, i.e. $\Delta H = H(\phi'_x, \pi'_x) - H(\phi_x, \pi_x) \neq 0$. One therefore has for the acceptance/rejection probability

$$a(\phi'_x|\phi_x) = \min\left(1, \frac{e^{-\beta H(\phi'_x,\pi'_x)}p(\phi_x, \pi_x|\phi'_x, \pi'_x)}{e^{-\beta H(\phi_x,\pi_x)}p(\phi'_x, \pi'_x|\phi_x, \pi_x)}\right) = \min\left(1, e^{-\beta\Delta H}\right), \tag{3.6}$$

with the inverse temperature $\beta \equiv 1/T$. The resulting stationary distribution of the Markov process is given by

$$P(\phi_x, \pi_x) = Z^{-1}e^{-\beta(\mathfrak{H}(\phi_x)+\pi_x^2/2)} = P(\phi_x)P(\pi_x), \tag{3.7}$$

which, as suggested by the notation, factorizes such that the configurations ϕ_x follow the desired distribution $P(\phi_x) = e^{-\beta\mathfrak{H}(\phi_x)}$. One may confirm that the stationary solution is also unique by checking the ergodicity of the process.

The recipe for the HMC method now reads as follows:

1. Choose some random initial conditions for ϕ_x.
2. Draw π_x from a Gaussian distribution with variance T.
3. Evolve the system under the equations of motion (2.122) and (2.123) for some time $\overline{\Delta t} = \bar{N}_t\, \bar{\delta}_t$.
4. Draw a random number α from a uniform distribution in $[0, 1]$. If $\alpha \leqslant e^{-\beta \Delta H}$, accept the new configuration ϕ'_x, π'_x. If not, reject the new configuration and count the old one twice.
5. Start over at step 2 until enough configurations $\{\phi_x\}$ were generated.

To compute the expectation value of some observable $O(\phi)$, one averages the function $O(\phi_x)$

$$\langle O(\phi) \rangle = \int \mathcal{D}\phi_x O(\phi_x) P(\phi_x) = \sum_{\phi_x \in \{\phi_x\}} O(\phi_x) \tag{3.8}$$

over every configuration of ϕ_x generated by the HMC. One however has to beware some caveat: Concerning the random initial condition on ϕ_x, also called a "hot start", one notices that depending e.g. on the temperature T the first few states are far from the equilibrium distribution, especially for low temperatures, and therefore have very low weight, such that they are overrepresented at the beginning of the run. One way to mitigate this is by ignoring all configurations at the start, monitoring for large changes in observables, and only begin measuring as soon as the system has thermalized.

One also must carefully consider the choice of parameters $\bar{N}_t$, $\bar{\delta}_t$. The acceptance rate typically depends only on the integrator step-size $\bar{\delta}_t$. If the acceptance rate is very low, the autocorrelation between configurations grows large. If on the other hand the acceptance rate is very high, one wastes precious resources on unnecessarily fine integration. We therefore typically aim for an acceptance rate between 0.5 and 0.6. The parameter $\bar{N}_t$ is then tuned such that the total trajectory length induces sufficient change in the system, i.e. the autocorrelation dies down fast enough. Here, we generally aim for decorrelation after ~ 10 HMC steps.

3.0.5 Correlation functions

When studying equilibrium dynamics, we are mostly interested in unequal-time correlation functions, e.g. the order-parameter spectral function in Eq. (2.146). During the simulation, discrete time histories of observables like ϕ, π, $T^{\mu\nu}$ and finite-momentum modes thereof are recorded. In the evaluation stage, they are correlated and averaged longitudinally employing time-translation symmetry. For the spectral function of the order parameter specifically, we get

$$\rho(t_i, \mathbf{p}) = \frac{-1}{2T} \sum_{t_j=0}^{\mathcal{N}_t - t_i} \frac{\bar{\pi}^*(t_j + t_i, \mathbf{p}) \bar{\phi}(t_j, \mathbf{p}) - \bar{\pi}(t_j, \mathbf{p}) \bar{\phi}(t_j + t_i, \mathbf{p})}{\mathcal{N}_t - t_i}, \tag{3.9}$$

where $\mathcal{N}_t$ denotes the total number of measurement time points in the given history, and we used that $\phi(-\mathbf{p}) = \phi^*(\mathbf{p})$ for fields that are real in coordinate space. Possible disconnected parts are dealt with by transforming $\bar{\phi}(t_i, \mathbf{p}) \equiv \phi(t_i, \mathbf{p}) - \langle \phi(\mathbf{p}) \rangle$ and

similarly for the time derivative $\bar{\pi}(t_i, \mathbf{p})$. The result is extended to negative t_i by setting $\rho(-t_i, \mathbf{p}) \equiv \rho(t_i, \mathbf{p})$, before applying a discrete Fourier transform (DFT) in the time direction to obtain $\rho(\omega_i, \mathbf{p})$. Both for the correlation and the DFT we employ a fast implementation from the NumPy library [73].

4 Order parameter dynamics in equilibrium

In this chapter, we analyze the equilibrium dynamics of the models defined in Section 2.2. Before we address the real-time dynamics of the systems, we briefly investigate the static critical behaviour of our models in 2 and 3 spatial dimensions. Measuring the non-universal amplitudes of the critical power laws will allow us to express our later results in terms of dimensionless quantities, enabling a more direct comparison to results obtained from microscopically different models of the same universality class. Additionally, this study serves as a plausibility check for our numerics setup.

We continue by investigating spectral functions of the order parameter, starting with determining the spectral functions in mean-field approximation. Subsequently we present numerical results for the spectral functions at different regions in the phase diagram, and compare our findings to the mean-field results. Having identified the dominant degrees of freedom, we analyze their dispersion relations and temperature dependence.

The outcome suggests singular behaviour close to the critical temperature, motivating a closer analysis of critical spectral functions and signatures of universal behaviour. We quantify the divergence of the characteristic time scale, and extract both the dynamic critical exponent z as well as the universal scaling functions of the spectral functions at either vanishing reduced temperature or spatial momentum.

4.1 Static universality and scale setting

For the full quantum theory, computing thermal expectation values amounts to solving expressions of the form

$$\langle \hat{O} \rangle = \frac{\mathrm{Tr}\left[\exp\left(-\beta \hat{H}\right) \hat{O}\right]}{\mathrm{Tr}\left[\exp\left(-\beta \hat{H}\right)\right]} \,. \tag{4.1}$$

A popular ansatz is to interpret $e^{-\beta \hat{H}}$ as the evolution operator along some imaginary time axis $\tau = -it$ from $\tau = 0$ up to β. After application of a Suzuki-Trotter decomposition on the evolution operator, one finds the Euclidean path integral

Table 4.1: Critical exponents of the ferromagnetic transition in the Ising model. In 2D, they are analytically known from Onsager's solution [82]. The high-precision calculations for the 3D Ising exponents were obtained from the conformal bootstrap approach [83, 84].

	2D	3D
β	0.125	0.326419
γ	1.75	1.237075
δ	15.0	4.78984
ν	1.0	0.629971
η	0.25	0.036298
ω	2.0	0.82966

representation of the partition function

$$Z(\beta) = \mathrm{Tr}\left[e^{-\beta\hat{H}}\right] = \int \mathcal{D}\left[\phi(\tau)\right] e^{-S_E(\beta)}, \tag{4.2}$$

$$S_E = \int_0^\beta \mathrm{d}\tau \int \mathrm{d}^d x \left(\frac{1}{2}\dot{\phi}^2(\tau) + V(\phi(\tau))\right), \tag{4.3}$$

where the Euclidean action S_E is given by the integral over the Wick-rotated Lagrangian with periodic boundary conditions in the τ-direction. The latter property can be used to turn the integral over imaginary time into a discrete sum over the Matsubara frequencies; for deeper insights on thermal field theory, see e.g. [81]. In the classical theory, we neglect quantum fluctuations altogether, meaning the fields do not change along the imaginary-time direction. This is equivalent to only taking into account the zeroth Matsubara mode, and just evaluating

$$Z_{\mathrm{cl}}(\beta) = \int \mathcal{D}[\phi] e^{-\beta V(\phi)}. \tag{4.4}$$

In case of the Landau-Ginzburg-Wilson model, $V(\phi) = \mathfrak{H}(\phi)$ as defined in Eq. (2.82) in continuum respectively Eq. (2.120) on the lattice. Computing expectation values of observables then amounts to calculating the integral

$$\langle O(\phi)\rangle = \int \mathcal{D}[\phi] O(\phi) e^{-\beta\mathfrak{H}(\phi)}. \tag{4.5}$$

We solve these expressions by employing a hybrid Monte-Carlo method outlined in Chapter 3, Section 3.0.4. In most cases we record 10^4 trajectories after the system has thermalized. The raw data is then further subjected to jackknife resampling, in order to obtain sensible error estimates despite remaining autocorrelation.

The basic observables we want to look at are the order parameter in form of the magnetization M and the corresponding susceptibility χ, which are defined as

$$M = \frac{1}{V}\sum_x \phi_x, \tag{4.6}$$

$$\chi = \frac{\partial\langle M\rangle}{\partial J} = \frac{V}{T}\left(\left\langle M^2\right\rangle - \langle M\rangle^2\right). \tag{4.7}$$

Since in the absence of explicit symmetry breaking ($J = 0$) the magnetization defined in Eq. (4.6) vanishes identically $\langle M\rangle = 0$ in any finite volume, we instead consider

$$M(J=0) = \frac{1}{V}\left|\sum_x \phi_x\right| \tag{4.8}$$

in that case.

When extracting the spatial correlation length ξ, we compute the plane-correlation function $\bar{G}(n)$ between the field-average $S(n)$ over lines for $d = 2$ (respectively planes for $d = 3$):

$$S(n) \equiv L^{1-d} \sum_{j(,k)}^{N} \phi_{n\mathbf{e}_x + j\mathbf{e}_y (+k\mathbf{e}_z)}, \tag{4.9}$$

$$\bar{G}(n) = L^{d-1} \left(\langle S(n) S(0) \rangle - M^2 \right), \tag{4.10}$$

which for sufficiently large separations n is expected to follow an exponential behavior of the form [85]

$$\bar{G}(n) = A \left(\exp(-n/\xi) + \exp\left((n - L)/\xi\right) \right). \tag{4.11}$$

Based on this behavior, we deduce an effective correlation length $\xi_{\text{eff.}}(n)$ from the data by considering the logarithmic derivative

$$\xi_{\text{eff.}}(n) = \frac{-1}{\ln\left(\bar{G}(n+1)/\bar{G}(n)\right)}. \tag{4.12}$$

and subsequently look for a plateau in a range of separations n, which is then used to determine the spatial correlation length ξ.

We provide a compact summary of our static results in Figs. 4.1 to 4.3, where we show the behavior of the order parameter M and susceptibility χ (Fig. 4.1), visualize the extraction of the spatial correlation length (Fig. 4.2), and illustrate the behavior of the correlation length ξ as a function of temperature T and external field J (Fig. 4.3). We follow common procedure and express the temperature dependence of our results in terms of the reduced temperature τ

$$\tau = \frac{T - T_c}{T_c}, \tag{4.13}$$

where T_c is the critical temperature given in Table 4.2. For all of the aforementioned observables, we approach the thermodynamic limit: By comparing data points of at least two different lattice volumes for any given point in the phase diagram, we can select a range of data where finite volume effects are negligible.

Based on our results in Figs. 4.1 and 4.3, we extract the non-universal amplitudes of the critical power laws either as functions of τ at vanishing external field, $J = 0$, or as functions of a dimensionless variable $\bar{J} \equiv J/J_0 \geqslant 0$ at $\tau = 0$. We follow the notation of [86] and distinguish the various non-universal amplitudes by superscripts, marking the region of the phase diagram that they describe. Specifically, the superscript of $X^{\pm}$ indicates the sign of τ and marks the amplitude on the $J = 0$ axis, whereas X^c denotes the corresponding amplitude on the $\tau = 0$ axis. Motivated by [86] and [87], we extract the critical temperature and non-universal amplitudes, including the leading scaling corrections, by fitting the following ansätze to correspondingly

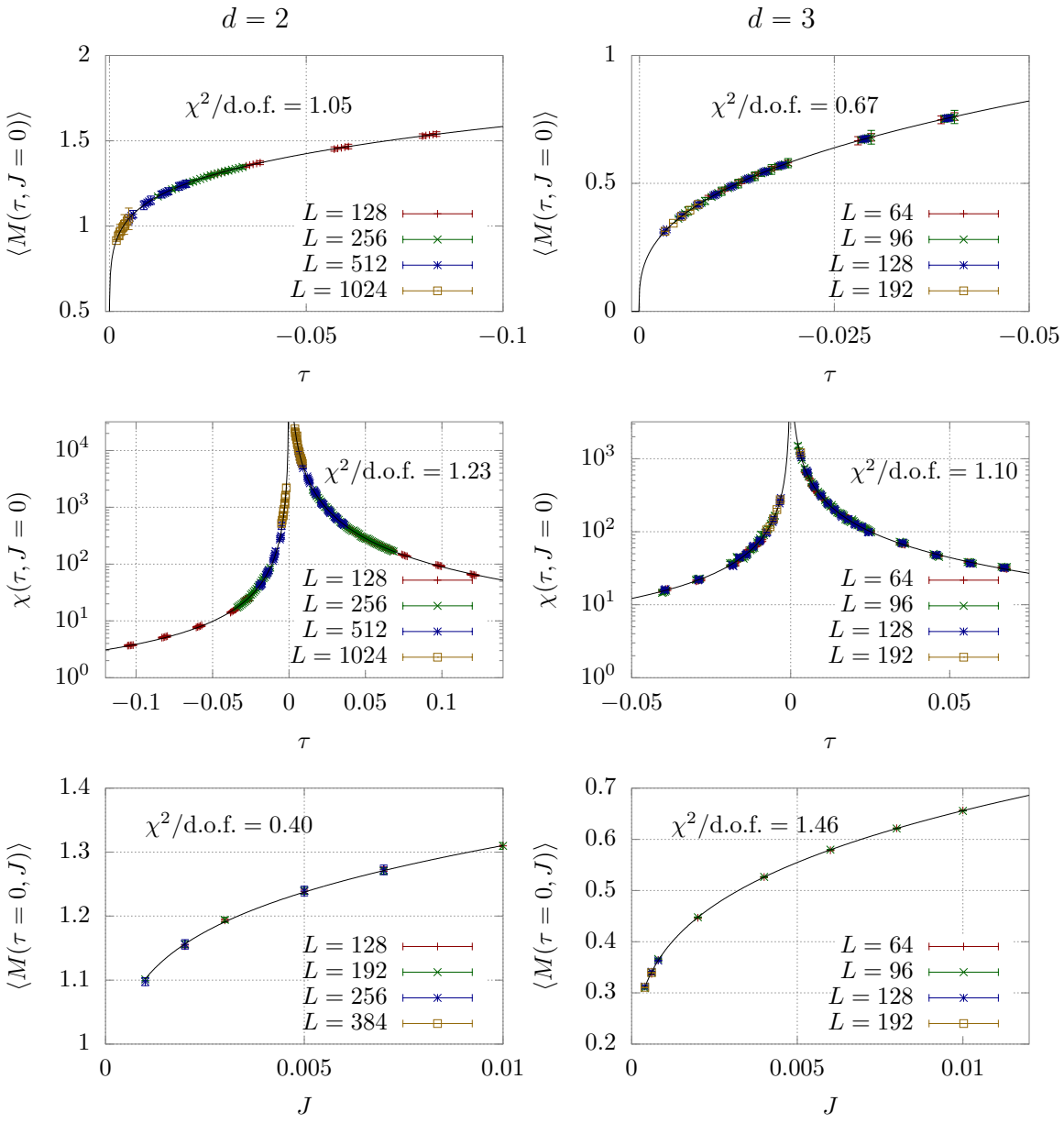

Figure 4.1: Near-critical behavior of the order parameter M and susceptibilities χ in $d = 2$ (left panels) and $d = 3$ (right panels) spatial dimensions. Solid lines show fits to Eq. (4.14) ff., with the corresponding χ^2-values given in each figure. By taking into account the first two sub-leading corrections to scaling, we obtain excellent agreement between data and fits.

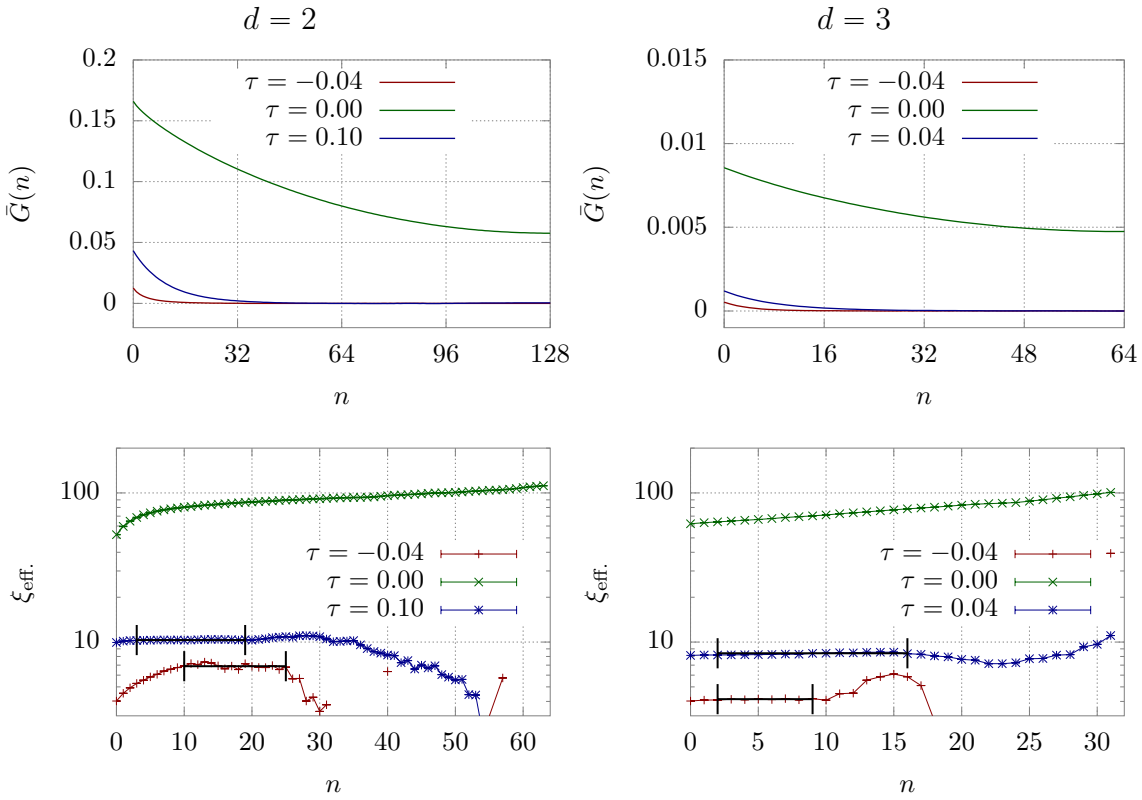

Figure 4.2: Extraction of the correlation length $\xi(\tau, J)$ from the two-point function $\bar{G}(n)$. Upper panels show exemplary data for the slice correlator $\bar{G}(n)$ at different temperatures τ; lower panels show the effective correlation length $\xi_{\text{eff.}}(x)$ defined by Eq. (4.12). We extract the correlation length $\xi(\tau, J)$ by looking for a plateau in $\xi_{\text{eff.}}(x)$ and fitting a constant if possible. Black lines with vertical marks in the lower plots indicate both range and result of the fit.

Table 4.2: Asymptotic amplitudes and corrections to scaling, as obtained from fits to Eq. (4.14) ff. The given uncertainties only include statistical errors. If a correction amplitude does not improve the χ^2/d.o.f. of a fit, it is set to zero and denoted by a dash.

	2D	3D
T_c	4.4629(10)	9.37074(28)
B	2.0203(16)	1.937(17)
C^+	1.4059(63)	0.830(42)
f^+	0.9176(76)	0.918(27)
B^c	1.7425(13)	1.5291(22)
C^c	0.1222(16)	0.3173(97)
f^c	0.3489(95)	0.537(16)

	2D	3D
B_1	-1.1(2)	0.9(1)
B_2	0.56(3)	-1.0(3)
B_1^c	-	0.83(1)
B_2^c	20.4(8)	-
C_1^+	-	2.8(8)
C_2^+	1.33(8)	-5.2(1.9)
C_1^-	-	2.6(2)
C_2^-	-9.7(3)	-
C_1^c	302(48)	2.2(4)
f_1^+	11.6(1.9)	0.4(2)
f_1^-	-	0.5(3)
f_1^c	-	1.5(6)

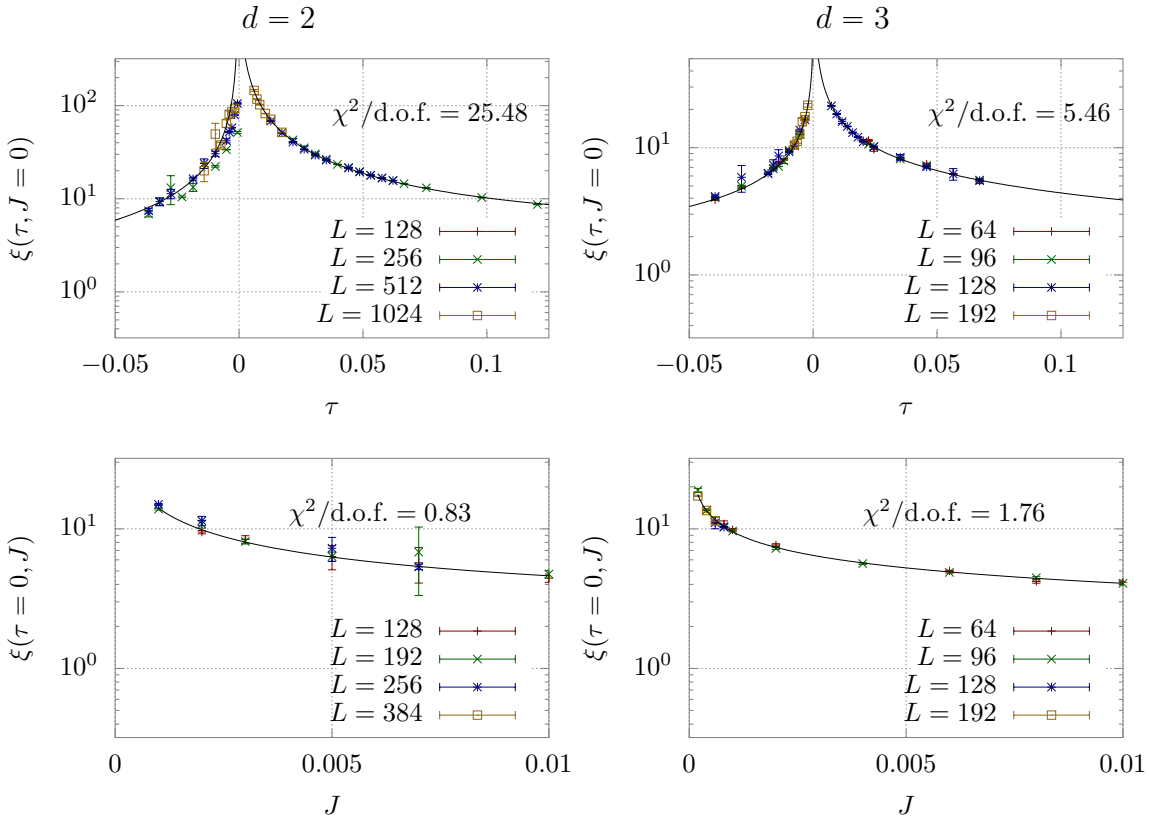

Figure 4.3: Near-critical behavior of the spatial correlation length $\xi(\tau, J)$ as function of the reduced temperature τ at vanishing symmetry breaking $J = 0$ (top panels), respectively as function of J at the critical temperature $\tau = 0$ (lower panels). Solid lines show fits to Eq. (4.18) with the corresponding χ^2-values indicated in each figure.

selected points,

$$\langle M(\tau)\rangle = B(-\tau)^{\beta}\left(1 + B_1(-\tau)^{\omega\nu} - B_2\tau\right), \quad \tau < 0\,, \tag{4.14}$$

$$\left\langle M(\bar{J})\right\rangle = B^c J_0^{1/\delta}\,\bar{J}^{1/\delta}\left(1 + B_1^c\bar{J}^{\omega\nu_c} + B_2^c\bar{J}\right), \tag{4.15}$$

$$\chi(\tau) = C^{\pm}|\tau|^{-\gamma}\left(1 + C_1^{\pm}|\tau|^{\omega\nu} + C_2^{\pm}|\tau|\right), \tag{4.16}$$

$$\chi(\bar{J}) = C^c J_0^{-\gamma_c}\,\bar{J}^{-\gamma_c}\left(1 + C_1^c\bar{J}^{\omega\nu_c}\right), \tag{4.17}$$

$$\xi(\tau) = f^{\pm}|\tau|^{-\nu}\left(1 + f_1^{\pm}|\tau|^{\omega\nu}\right), \tag{4.18}$$

$$\xi(\bar{J}) = f^c J_0^{-\nu_c}\,\bar{J}^{-\nu_c}\left(1 + f_1^c\bar{J}^{\omega\nu_c}\right), \tag{4.19}$$

where $\gamma_c \equiv \gamma/\beta\delta = 1 - 1/\delta$ and $\nu_c \equiv \nu/\beta\delta = (1+1/\delta)/d$ from scaling and hyperscaling relations. We note that J_0 is chosen such that $B^c J_0^{1/\delta} = B$, and $C^c J_0^{-\gamma_c} = B/(\delta J_0)$ (as well as $J_0^{-\nu_c} = (B^c/B)^{\nu/\beta}$); and in the absence of scaling corrections, the magnetic equation of state can be written in the Widom-Griffiths form, $y = f(x)$, with dimensionless magnetization $\overline{M} = M/B$,

$$y = \bar{J}/\overline{M}^{\delta}, \quad x = \tau/\overline{M}^{1/\beta} \tag{4.20}$$

and normalization $f(0 = 1)$, $f(-1) = 0$.

By virtue of the Z_2 symmetry of our model, we know that its critical behavior is described within the Ising universality class. Our model and method are not optimized for computing static critical exponents; we therefore reduce the degrees of

freedom in our calculations by taking the critical exponents from the literature. In $d = 2$ spatial dimensions, the critical exponents are exactly known from the analytic solution by Onsager [82]. For the numeric values of the exponents in $d = 3$ spatial dimensions, we take those obtained by the conformal bootstrapping method [83, 84], which are listed in Table 4.1 alongside their counterparts in $d = 2$.

The asymptotic scaling amplitudes along with the coefficients of the scaling corrections extracted from the fits to the data are listed in Table 4.2. The comparison between ansatz and data is shown in Figs. 4.1 and 4.3. For most quantities, we obtain a χ^2/d.o.f. close to unity, indicating sufficient agreement between fit and data. For $d = 2$, our procedure for the correlation length at $J = 0$ does not work too well, especially for $\tau < 0$, leading to a relatively large resulting value of χ^2. This is primarily due to heavily fluctuating data in the low-temperature phase, as well as probably an underestimation of the error of the correlation length ξ in our extraction.

It is a useful cross-check to validate the measured amplitudes by comparing the known universal amplitude ratios. We use a subset that relates all of the amplitudes we measure:

$$U_2 = C^+/C^-, \tag{4.21}$$
$$U_\xi = f^+/f^-, \tag{4.22}$$
$$R_\chi = C^+ B^{\delta-1}/\left(B^c\right)^\delta, \tag{4.23}$$
$$Q_2 = \left(f^c/f^+\right)^{2-\eta} C^+/C^-, \tag{4.24}$$
$$\delta = B^c/C^c. \tag{4.25}$$

The ratios we measured are shown alongside their literature values in Table 4.3. For most of the ratios, we find results in the right ballpark, with exception of U_ξ and Q_2 in $d = 2$ dimensions: Those ratios are the ones including amplitudes of ξ.

Different definitions of ξ lead to slightly different U_ξ, see e.g. the difference between second-moment correlation length and inverse mass gap in [86]. Since our definition again differs from the aforementioned ones, we are bound to get (slightly) different amplitudes. Nevertheless, it is strongly related to the definition by the inverse mass gap, so we would expect $U_\xi \approx 2$. Since we do not rely on exact estimates of the correlation length for the purpose of this study, we accept these residual ambiguities for now.

When studying dynamic critical behavior, we will normalize our results using the non-universal amplitudes. In this process, we will also obtain a timescale by fitting the amplitude f_t^+ of the correlation time ξ_t, which will be determined in a later section (see Eq. (4.92) in Sec. 4.3.3). If not stated otherwise, we give all results in terms of dimensionless scaling variables, which are indicated by a bar and constructed as follows:

$$\bar{J} = J/J_0 = J(B^c/B)^\delta, \tag{4.26}$$
$$\bar{p} = pf^+, \tag{4.27}$$
$$\bar{t} = t/f_t^+, \tag{4.28}$$
$$\bar{\omega} = \omega f_t^+. \tag{4.29}$$

Table 4.3: Universal amplitude ratios. The given uncertainties only include statistical errors. The ratios are shown alongside their literature values, which were taken from [86].

	2D		3D	
	meas.	lit.	meas.	lit.
U_2	40.05(35)	37.69	4.29(24)	4.76(2)
U_ξ	3.14(38)	2	1.939(90)	1.896(10)
R_χ	6.40(10)	6.778	1.331(80)	1.660(4)
Q_2	2.12(11)	2.836	0.913(93)	1.195(10)
δ	14.26(19)	15	4.82(15)	4.78984(1)

4.2 Spectral functions of the order parameter

Based on our analysis of static critical phenomena, we will now investigate the behavior of the spectral function at different points in the phase diagram. We proceed as outlined in the beginning of this chapter and calculate the classical-statistical spectral function of the order parameter field first in mean-field approximation and then non-perturbatively from lattice simulations using Eq. (2.144) resp. Eq. (2.146). We prepare ~ 30 independent thermal configurations as initial conditions, which we then evolve for $\sim 10^4 - 10^5 a$, using and Euler-Maruyama scheme. Notably, we find that in the vicinity of the critical point, the time step Δt in the integrator has to be chosen sufficiently small to avoid discretization errors. If not stated otherwise, we employ $\Delta t = .00625\, a$, and we have checked that discretization errors are negligible for the results presented here.

By recording the evolution of the Fourier modes of the order parameter field, we subsequently compute the spectral function $\rho(t, p)$ from Eqs. (2.144) and (2.146). Statistical errors are estimates from point-wise averages of $\rho(t, p)$ and respectively $\rho(\omega, p)$ over different configurations. If not stated otherwise, the spectral functions shown in this section are obtained for vanishing external field $J = 0$ on lattice volumes of 256^2 respectively 256^3, where we have the smallest remaining finite volume effects.

4.2.1 Mean-field spectral functions

To build the correct expectations, it is instructive to consider the system in mean-field approximation, which coincides with the limit of low temperatures $T \to 0$ of the classical system. For negative square mass $m^2 < 0$, one has non-trivial minima of the Hamiltonians $H_{A/B}$ where $\phi^2 = -6m^2/\lambda \equiv \bar{\phi}^2$. Expanding H around $\phi = \bar{\phi}$ yields a mean-field effective squared mass of $\bar{m}^2 = -2m^2$.

To evaluate the spectral function in the mean-field approach, we consider the equations of motion (2.83) and (2.85) in Fourier space, upon which we get

$$(\mathrm{i}\omega)^2\phi(\omega, \mathbf{p}) = -\left[(\mu p^2)^\alpha(\bar{m}^2 + p^2) + \gamma(\mathrm{i}\omega)\right]\phi(\omega, \mathbf{p}) + (\mu p^2)^\alpha J(-\omega, -\mathbf{p}) \tag{4.30}$$

$$\Leftrightarrow \quad \left[-\omega^2 + \mathrm{i}\omega\gamma + (\mu p^2)^\alpha(\bar{m}^2 + p^2)\right]\phi(\omega, \mathbf{p}) = (\mu p^2)^\alpha J(-\omega, -\mathbf{p}), \tag{4.31}$$

where we abbreviate $p = |\mathbf{p}|$, and the variable α differentiates between dissipative Model-A ($\alpha = 0$) and diffusive Model-B ($\alpha = 1$) dynamics. One obtains the statistical

two-point function by taking the derivative w.r.t. the external source term J

$$\langle\phi\phi'\rangle = \frac{\partial}{\partial J'}\langle\phi\rangle = \frac{(\mu p^2)^\alpha}{(\mu p^2)^\alpha\left(p^2+\bar{m}^2\right)-\omega^2+\mathrm{i}\gamma\omega}\delta\left(\omega+\omega'\right)\delta\left(\mathbf{p}+\mathbf{p}'\right). \tag{4.32}$$

From there one can calculate the spectral function by taking the imaginary part of the correlator (4.32). This yields for dissipative Model-A dynamics induced by the equation of motion (2.83)

$$\rho_A(\omega,\mathbf{p}) = \frac{\gamma\omega}{\left(\omega^2-\left(p^2+\bar{m}^2\right)\right)^2+\gamma^2\omega^2}, \tag{4.33}$$

and for diffusive Model-B dynamics under the equation of motion (2.85)

$$\rho_B(\omega,\mathbf{p}) = \frac{\mu p^2\gamma\omega}{\left(\omega^2-\mu p^2\left(p^2+\bar{m}^2\right)\right)^2+\gamma^2\omega^2}. \tag{4.34}$$

We thus expect the spectral function at least at low temperatures to be described by a Breit-Wigner shape with dispersion $\omega_p^2 = (\bar{m}^2+p^2)$ for Model A and $\omega_p^2 = \mu p^2(\bar{m}^2+p^2)$ for Model B. One obtains of course the same result taking the spectral function directly from the Israel-Stewart two-point function given in Appendix B after inserting the correct model parameters.

It will be useful to be aware of the extremal behavior of the mean-field spectral function. We list the relevant limits for a single extremal parameter below, making again use of the parameter $\alpha \in \{0,1\}$ distinguishing the dynamical models.

$$\lim_{\omega\to 0}\rho(\omega,\mathbf{p}) = \frac{(\mu p^2)^\alpha\gamma\omega}{\omega_p^4} \qquad +O\left(\omega^3\right) \tag{4.35}$$

$$\lim_{\omega\to\infty}\rho(\omega,\mathbf{p}) = \frac{(\mu p^2)^\alpha\gamma}{\omega^3} \qquad +O\left(\omega^{-5}\right) \tag{4.36}$$

$$\lim_{p\to 0}\rho(\omega,\mathbf{p}) = \frac{(\mu p^2)^\alpha\gamma\omega}{\left(\omega^2-(1-\alpha)\,m^2\right)^2+\gamma^2\omega^2} \qquad +O\left(p^{2+\alpha}\right) \tag{4.37}$$

$$\lim_{p\to\infty}\rho(\omega,\mathbf{p}) = \frac{\gamma\omega}{(\mu p^2)^\alpha p^4} \qquad +O\left(p^{-6-\alpha}\right) \tag{4.38}$$

$$\lim_{\gamma\to 0}\rho(\omega,\mathbf{p}) = \frac{(\mu p^2)^\alpha\gamma\omega}{\left(\omega^2-(\mu p^2)^\alpha\left(p^2+m^2\right)\right)^2} \qquad +O\left(\gamma^3\right) \tag{4.39}$$

$$\lim_{\gamma\to\infty}\rho(\omega,\mathbf{p}) = \frac{(\mu p^2)^\alpha}{\gamma\omega} \qquad +O\left(\gamma^{-3}\right) \tag{4.40}$$

4.2.2 Overview

In Figs. 4.4 and 4.5, we give an overview over the behavior of spectral functions for dissipative (Model A/C) dynamics at different temperatures. At high temperatures ($T \gg T_c$), the spectral function is well approximated by a relativistic Breit-Wigner peak shape, with the peak position shifting with spatial momentum p according to the relativistic dispersion relation $\omega^2 - p^2 = m^2(T)$. This is compatible with earlier studies: In [39], the zero-momentum ($p = 0$) mode of the spectral function was investigated in a scalar theory without phase transition. The study was done at high temperatures, so that $T \gg \omega$ in the region of interest and the classical-statistical

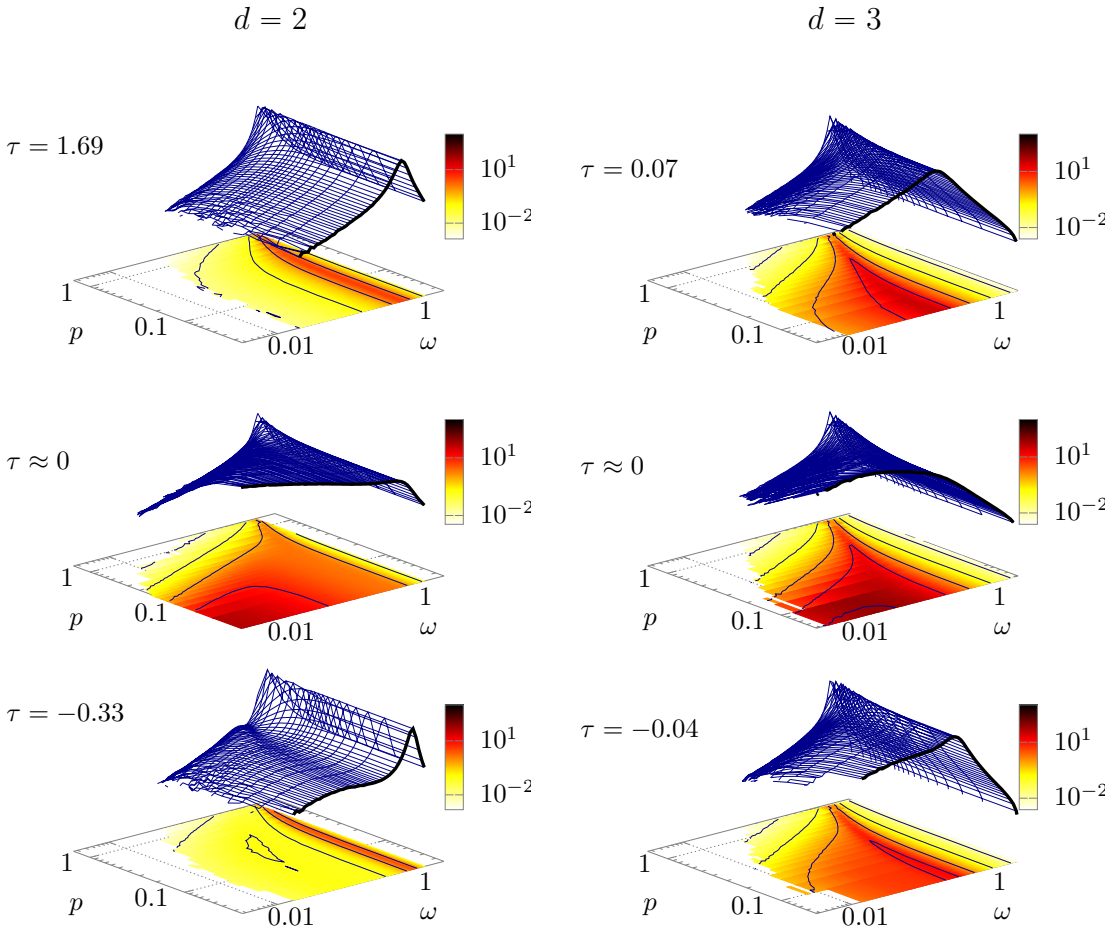

Figure 4.4: Overview of the behavior of the spectral function $\rho(\omega, p)$ for dissipative dynamics (Model A, $\gamma = 0.1$) at different points in the phase diagram, above T_c (top panels), near T_c (central panels), and below T_c (bottom panels) in 2+1 (left panels) and 3+1 (right panels) dimensions. Heat maps at the bottom of each panel visualize support and spectral strength in the (p, ω) plane. The axes are scaled logarithmically, and the smallest non-zero momentum modes are highlighted by a black solid line on the 3D surface. Spectral functions away from the critical temperature are dominated by a Breit-Wigner structure with dispersion relation $\omega_c^2 = (m^2 + p^2)$ and close to constant decay width. Close to the critical point, the dispersion relation changes, and a very broad structure emerges in the infrared.

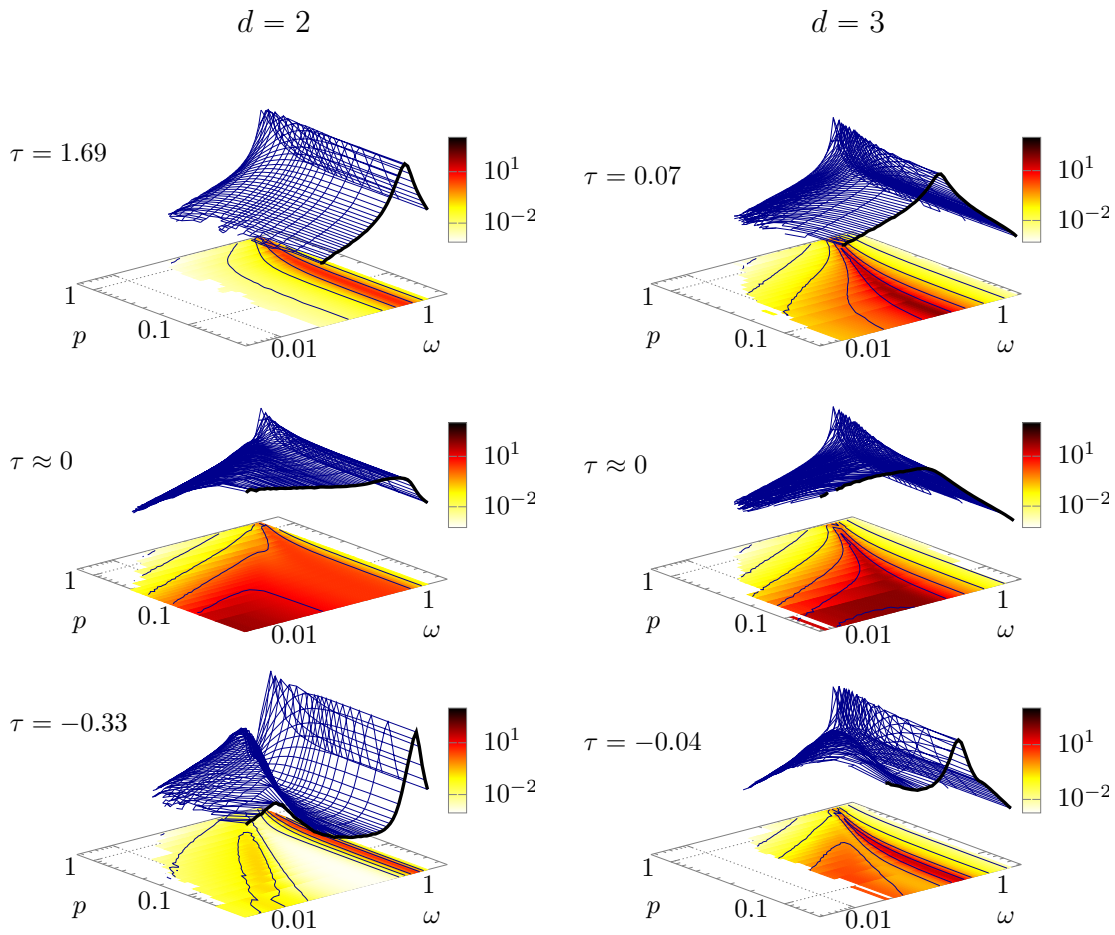

Figure 4.5: Overview of the behavior of the spectral function $\rho(\omega, p)$ for Hamiltonian dynamics (Model C, $\gamma = 0$) at different points in the phase diagram, illustrated analogously to Fig. 4.4. While the general spectral shapes stay the same as in Fig. 4.4 at $\gamma = 0.1$, the structures overall become narrower. At low temperatures, a pronounced low-frequency mode with a different dispersion relation indicative of a soft collective excitation emerges. From this presentation, one can already guess that this soft mode turns into the dominant infrared divergence at the critical temperature.

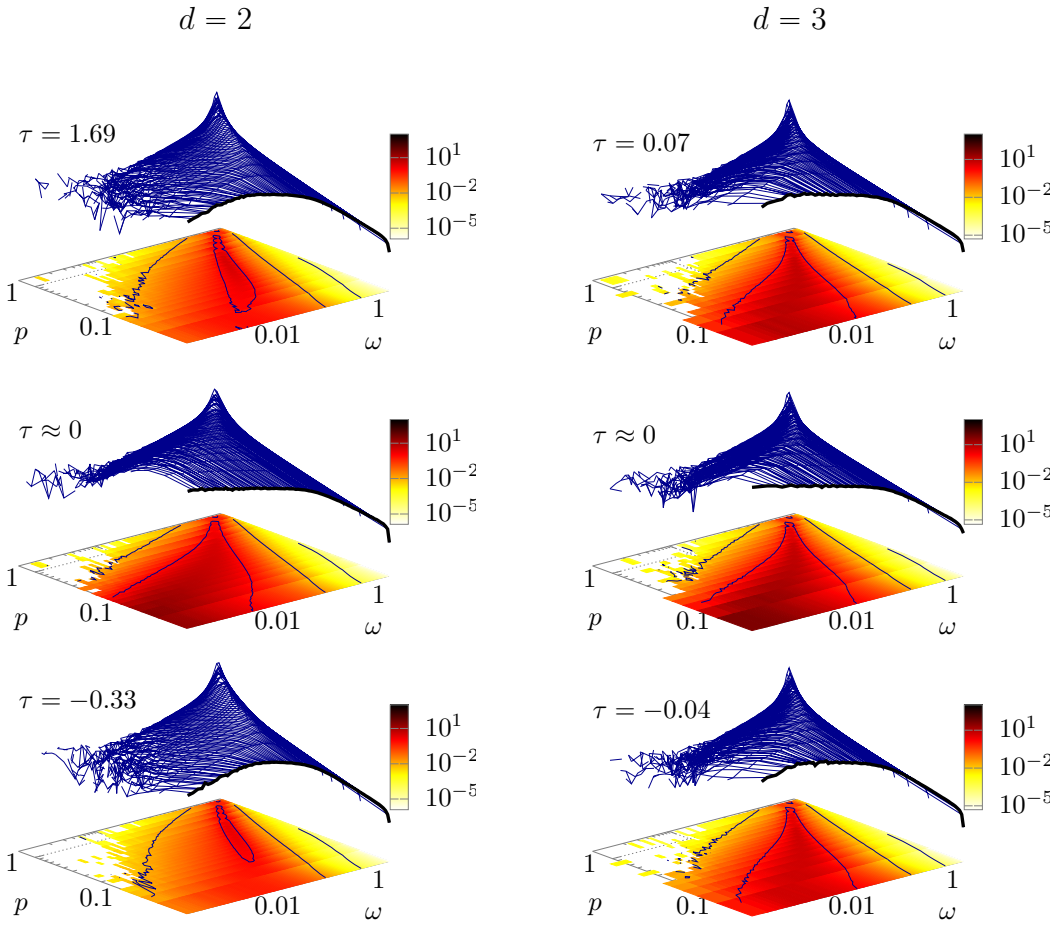

Figure 4.6: Overview of the behavior of the spectral function $\rho(\omega, p)$ for diffusive dynamics (Model B, $\gamma = 0.1$) at different points in the phase diagram, illustrated analogously to Fig. 4.4. Spectral functions away from the critical temperature are dominated by a Breit-Wigner structure with dispersion relation $\omega_c^2 = \mu p^2(m^2 + p^2)$. Decay widths are bounded from below by the Langevin damping parameter γ, and otherwise increase with some power of the spatial momentum p. Since the central frequencies do not have a lower bound (as opposed to the case with dissipative dynamics), the structures become relatively broad in the infrared. Close to the critical point, the dispersion relation changes, and central frequencies at low spatial momentum shift even further into the infrared, leading to a dominating broad structure at low frequencies.

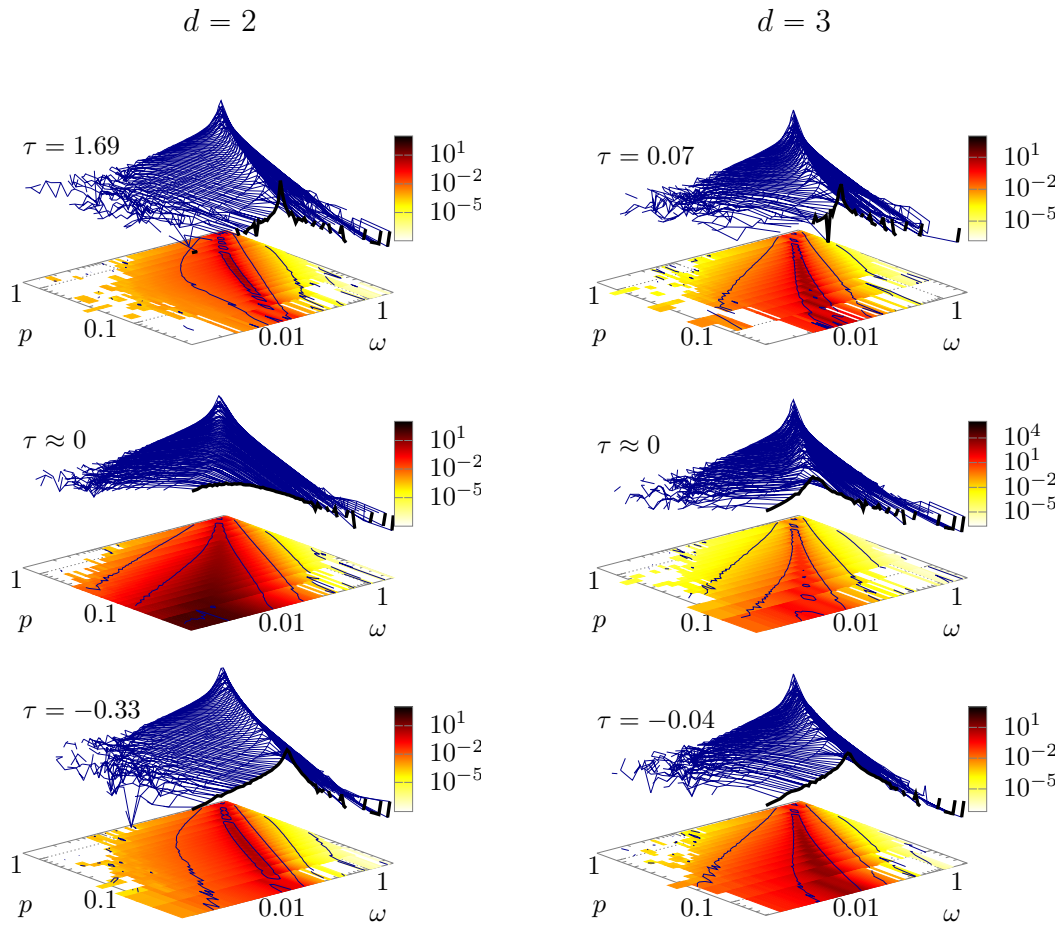

Figure 4.7: Overview of the behavior of the spectral function $\rho(\omega, p)$ for diffusive dynamics (Model D, $\gamma = 0$) at different points in the phase diagram, illustrated analogously to Fig. 4.4. Spectral functions away from the critical temperature are still dominated by a Breit-Wigner structure with dispersion relation $\omega_c^2 = \mu p^2(m^2 + p^2)$, but much narrower than at finite heat-bath coupling in Fig. 4.6. Decay widths follow some power of the spatial momentum p unbounded from below, leading to very narrow peaks at the lower end of the momentum range. Close to the critical point, the effective thermal mass vanishes and both central frequencies and widths presumably become regular in momentum p. While the shift of central frequencies towards the infrared still yields relatively broad structures at low spatial momentum, they are much more distinct compared the case of $\gamma = 0.1$ in Fig. 4.6. In 3+1D, even the modes with lowest spatial momentum retain a rather narrow peak structure at the critical point.

approach was justifiable. It was found that both masses and widths of the measured spectral function agree well with the analytical predictions from resummed two-loop perturbation theory. We find here a very similar Breit-Wigner shape, and since we also calculate the spectral function at finite spatial momenta, we can check for the correct dispersion relation of the quasi-particle mass.

When the system approaches criticality from above, the effective mass $m^2(T)$ decreases, and the quasi-particle peak becomes less and less pronounced. Close to the critical point, an infrared power law behavior builds up at low frequencies and momenta which, as we will discuss shortly in Section 4.3, encodes the dynamic critical behavior of the spectral function. The slope of this power law is related to the dynamic critical exponent z, which is the main subject of the next section. With increasing spatial momentum p, the cut-off imposed by p suppresses the critical contribution. Specifically, at high momenta the spectral function retains its Breit-Wigner shape even in this near-critical regime, however with significantly smaller quasi-particle mass. Comparing the different columns of Fig. 4.5 one further notices that the window of reduced temperatures τ, where a critical enhancement of the spectral function can be observed, is much smaller in 3+1 than in 2+1 dimensions, as can be expected from the larger influence of infrared fluctuations in lower dimensions.

Below the critical temperature, in the ordered phase, the effective quasi-particle mass $m^2(T)$ increases again, and gradually approaches its mean-field value of $\sqrt{-2m^2} = \sqrt{2}$ in the limit $T \to 0$, where all thermal fluctuations are suppressed. However, in addition to the quasi-particle peak, a second low-frequency excitation arises for finite spatial momenta, with a different spectral shape and a dispersion relation indicative of soft collective excitations such as thermally driven capillary waves, see Appendix D. While in 3+1 dimensions the contributions from this soft mode only carry a small fraction of the spectral weight, it is more pronounced in 2+1 dimensions, where by looking at the lower left panel of Fig. 4.5, one can easily discern the valley in the spectral function that separates it from the quasi-particle peak.

By comparing the spectral functions in the symmetry-broken phase at $\tau < 0$ and the vicinity of the critical point $\tau \approx 0$ in Fig. 4.5, one is led to speculate that it is this second excitation at $\tau < 0$ that might turn into the critical IR divergence close to the critical point. Indeed, by tracing the maxima of both excitations, one observes an avoided-crossing behavior near T_c, before the low-frequency mode eventually disappears at $\tau > 0$. A similar avoided crossing was already observed in the classical-statistical lattice simulations of O(4)-model spectral functions in 3+1 dimensions in [41]. Although this study was restricted to vanishing spatial momenta where, in agreement with the results presented here, there is no comparable soft mode in the longitudinal σ-spectral function of the order parameter fluctuations, an avoided crossing does nevertheless show up at zero momentum in the transverse π-spectral function of the O(4)-model.

Figures 4.6 and 4.7 show the spectral functions of the systems with order-parameter–conserving dynamics (Model B/D) at different points in the phase diagram for 2+1 and 3+1 dimensions. We find that the spectral functions are well described by a single Breit-Wigner structure over a wide range of parameters. At vanishing Langevin-coupling $\gamma = 0$, the peaks in the spectral functions are generally very narrow, only becoming relatively wide at the critical temperature in 2+1D. If the heat-bath coupling is set to a finite value of $\gamma = 0.1$, this changes dramatically, and in

all cases the spectral functions at low spatial momentum become much more broad, while high-momentum modes stay narrow. Clearly, the dispersion relation is not that of a quasi-particle, as the central frequencies do not approach a fixed value at low spatial momentum. There is however a visible kink in the momentum-dependence of the central frequencies for temperatures away from the critical point.

Close to the critical point, the central frequencies at low spatial momentum visibly shift into the infrared, indicating a change in the dispersion relation akin to a drop in the effective mass. For finite heat-bath coupling $\gamma = 0.1$, the absolute decay widths stay mostly the same. However, since the central frequencies decrease, the low-frequency part of the spectral functions is then dominated by structures with large relative widths, which closely fit the limit of diverging $\Gamma \to \infty$ of the mean-field spectral function in Eq. (4.40).

4.2.3 Dispersion relations of Breit-Wigner structures

Based on the results in Figs. 4.4 to 4.7 we will now quantitatively investigate some properties of the spectral functions extracted from lattice data.

First, we focus on dissipative dynamics (Model A/C). We start by confirming the relativistic dispersion relation of the quasi-particle peak, before going on to study the temperature dependence of the peak parameters and analyze the effect of the Langevin damping γ on the spectral function. In order to compute the dispersion relation, we fit the peaks in the spectral function with a relativistic Breit-Wigner ansatz

$$\rho_{\mathrm{BW}}(\omega, p) = \frac{\Gamma(p)\omega}{(\omega^2 - \omega_c^2(p))^2 + \omega^2\Gamma^2(p)}, \tag{4.41}$$

where the central frequency of the effective mass resonance is expected to follow the relativistic energy-momentum relation

$$\omega_c^2(p) = m_{\mathrm{eff}}^2 + p^2. \tag{4.42}$$

Visualizations of the fits to the spectral function are given in the left panels of Fig. 4.8, where the top left panel shows the symmetric phase $\tau > 0$ and the bottom left panel the ordered phase ($\tau < 0$), while Fig. 4.9 shows the extracted values of the peak-frequency ω_p and damping rates $\Gamma(p)$. Clearly, the fit to the Breit-Wigner function describes the spectral function very well at high temperatures, where the quasi-particle excitation is the only discernible structure. While in the low temperature phase, shown in the bottom left panel of Fig. 4.8, the Breit-Wigner fit still accurately describes the dominant quasi-particle peak, one also clearly observes the additional low-energy excitation for finite spatial momenta ($p > 0$) additional to a subdominant peak on the high-frequency shoulder of the quasi-particle excitation.

So far we have focused on the general behavior of the spectral function for Hamiltonian dynamics (Model C), which we will now compare to the spectral functions for Langevin dynamics (Model A). Since the key difference between Hamiltonian and Langevin dynamics lies in the introduction of an additional frequency-independent damping and noise coupling to the heat bath, one naturally expects the additional damping to contribute to the resonance decay width $\Gamma(p)$ of the (non-critical) spectral functions. Explicit comparisons of the results for Hamiltonian ($\gamma = 0$) and Langevin ($\gamma = 0.1$) dynamics, shown in Fig. 4.9, confirm this expectation, indicating further that differences in the numerically extracted damping rates $\Gamma_{\gamma=0.1}(p) - \Gamma_{\gamma=0}(p) \simeq \gamma$

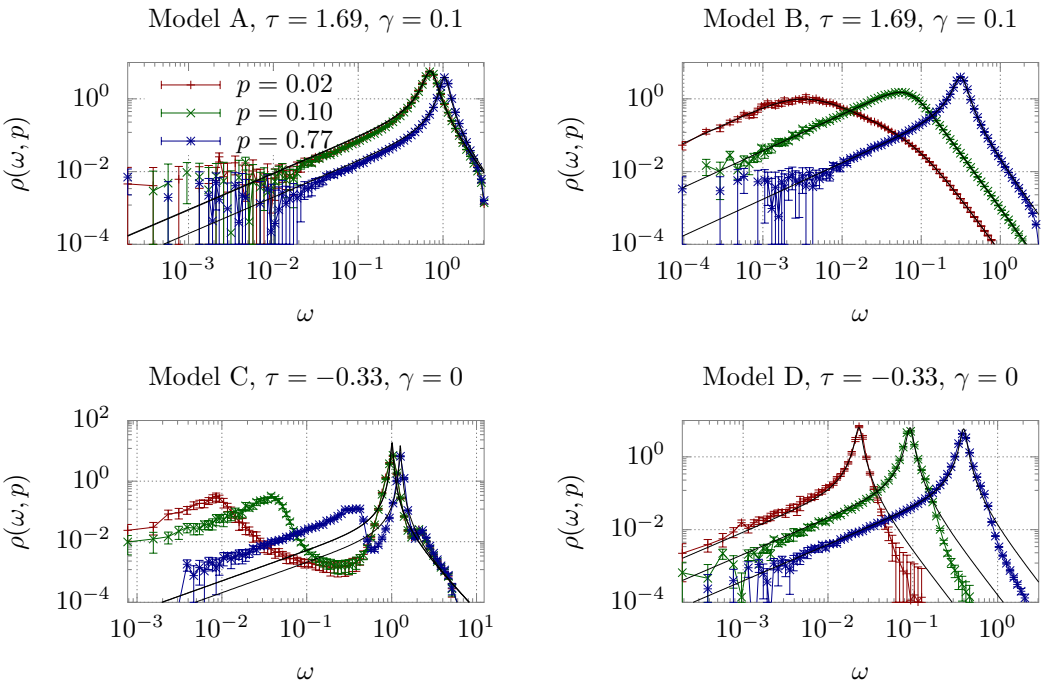

Figure 4.8: Cuts of the spectral function at different spatial momenta p along the frequency axis, in the symmetric (top panels) as well as the ordered phase (bottom panels), for both dissipative (left panels) and diffusive dynamics (right panels). While for the upper panels there is a finite heat-bath coupling $\gamma = 0.1$, we set $\gamma = 0$ in the lower panels to enhance the visibility of the soft mode in the ordered phase. Black lines represent a fit to the Breit-Wigner ansatz (4.41), where the γ- and momentum-dependence of the parameters is given by Eq. (4.42) resp. Eqs. (4.43) to (4.45), leaving only two free parameters per panel, namely the thermal mass $m(T)$ and the amplitude of the decay widths $\bar{\Gamma}(T)$.

are in fact close to the value of the Langevin coupling. While far away from criticality, especially at high temperatures, the qualitative and quantitative features of the spectral functions are very similar between conservative and weakly dissipative systems, the change in conservation laws does subtly affect the dynamic critical behavior, as we will discuss in more detail in Section 4.3.

We continue our analysis by considering the systems with order-parameter-conserving diffusive dynamics (Models B and D). In contrast to the systems with non-conserved order parameter, there are no additional excitations visible in either 2+1D or 3+1D anywhere in the phase diagram (compare Figs. 4.6 and 4.7). Thus, we fit the full spectral functions with the ansatz Eq. (4.41), with the central frequency ω_p and the decay width Γ as free parameters. The results for ω_p^2, Γ are shown in Fig. 4.10. Our findings for the central frequencies ω_p^2 nearly perfectly satisfy the mean-field–like dispersion

$$\omega_p^2 = \mu p^2 (m^2(T) + p^2) \tag{4.43}$$

far from the critical point, with no measurable dependence on the Langevin coupling. For the width of the spectral function we find that the Langevin coupling γ appears as an additional momentum-independent shift

$$\Gamma(p, \gamma) = \Gamma(p, \gamma = 0) + \gamma, \tag{4.44}$$

and we obtain for the momentum dependence of the decay width without the heat

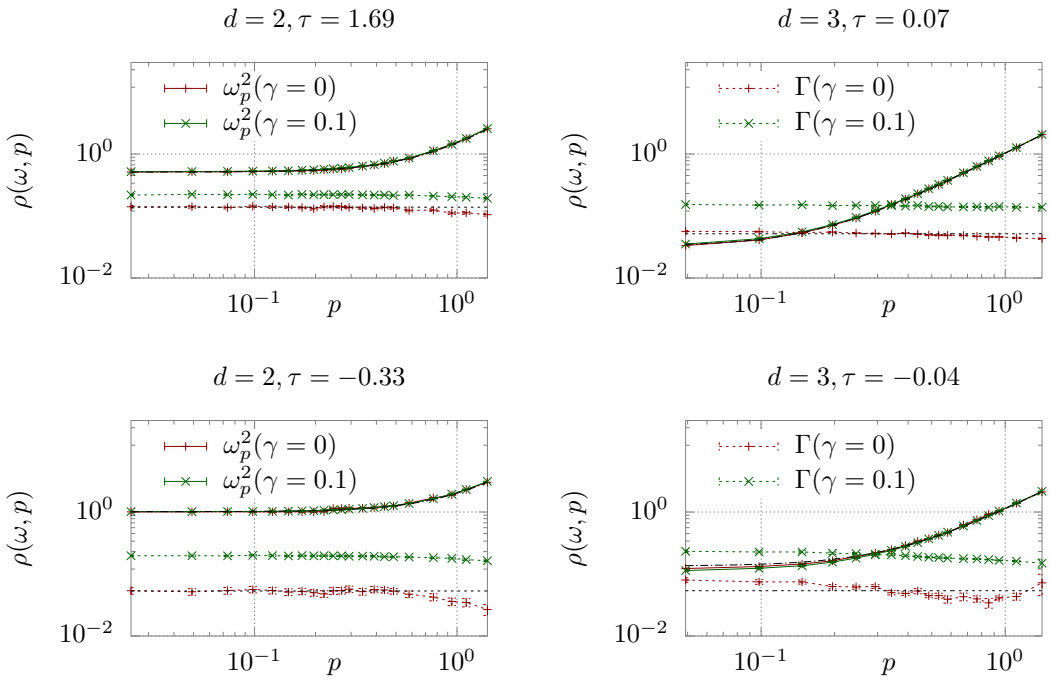

Figure 4.9: Resulting parameters of Breit-Wigner fits in Model A/C given in lattice units. Red data corresponds to a Langevin coupling parameter of $\gamma = 0$, green data to $\gamma = 0.1$. Fits to an ansatz for the momentum dependencies are shown as dotted lines for Γ and dash-dotted lines for ω_p^2. Top panels depict results in the symmetric phase at high temperatures, bottom panels show results from the ordered phase corresponding to low temperatures. Central frequencies ω_p^2 are fitted with a function of the form $\omega_p^2 = m^2 + p^2$. In all cases, the decay widths $\Gamma(p)$ appear close to constant in spatial momentum.

bath

$$\Gamma(p, \gamma = 0) = \bar{\Gamma}(T) \cdot \begin{cases} p, & T \ll T_c, \\ p^2, & T \gg T_c. \end{cases} \tag{4.45}$$

In fact, Eqs. (4.43) to (4.45) capture the momentum dependence of the spectral function so well, that one can satisfyingly describe the spectral functions at different temperatures and γ by just two parameters, namely the effective mass $m(T)$ and the amplitude of the decay power law $\bar{\Gamma}(T)$. This is demonstrated in the right panels of Fig. 4.8, where we show comparisons between fixed-momentum cuts of the spectral function and the parametrizations given by Eqs. (4.41) to (4.45), both deep in the ordered and the symmetric phase. Even though there are only two free parameters per panel, the fit describes the data nearly perfectly, with some minor deviations at low temperatures and $\gamma = 0$ in the ultraviolet.

We conclude our discussion of the non-critical spectral functions by investigating the temperature dependence of the central frequencies and decay widths of the Breit-Wigner structures for both dissipative and diffusive dynamics, which are summarized in Fig. 4.11. By defining $m_{\text{eff}} = \sqrt{(\mu p^2)^{-\alpha} \omega_c^2(p) - p^2}$, curves for different momenta p should coincide whenever the quasi-particle peaks satisfy the dispersion relation in Eq. (4.42) for dissipative ($\alpha = 0$) dynamics, or Eq. (4.43) in case of diffusive ($\alpha = 1$) dynamics. Starting from the low temperature phase, the resonances turn into sharp δ-peaks in the limit $T \to 0$, where $m_{\text{eff}}(T = 0) = \sqrt{-2m^2}$ assumes its mean-field value and the decay width $\Gamma(T = 0) = 0$ vanishes.

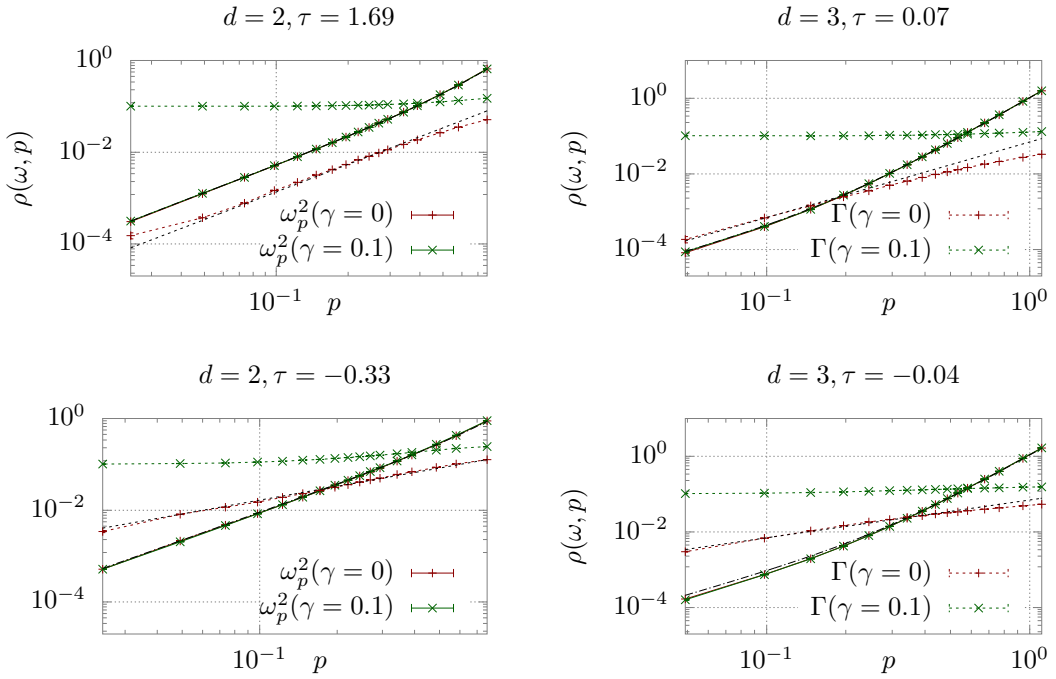

Figure 4.10: Resulting parameters of Breit-Wigner fits in Model B/D given in lattice units. Red data corresponds to a Langevin coupling parameter of $\gamma = 0$, green data to $\gamma = 0.1$. Fits to an ansatz for the momentum dependencies are shown as dotted lines for Γ and dash-dotted lines for ω_p^2. Central frequencies ω_p^2 are fitted with a function of the form $\omega_p^2 = \mu p^2(m^2 + p^2)$. In the disordered phase at high temperatures (top panels), we find a momentum dependence of widths suggestive of $\Gamma(p) \propto p^2$. Bottom panels depict results in the ordered phase corresponding to low temperatures. In this regime, the momentum dependence of the widths fits $\Gamma(p) \propto p$.

Even at the lowest temperatures shown, the effective masses are still rather large, but then decrease as the system approaches the critical temperature, while the decay width $\Gamma(T)$ increases simultaneously. For diffusive dynamics, the dispersion relation (4.43) is no longer fulfilled as precisely as for the even lower temperature shown in Fig. 4.8. Near the critical temperature, the behavior of the spectral function for dissipative dynamics at low momentum can no longer be described by a simple quasi-particle structure, as already seen in Fig. 4.5. However, when increasing the temperature above the critical point, the quasi particle structure at low momentum is restored, with the mass increasing monotonously as a function of temperature for $T > T_c$. Conversely, for the modes with large spatial momenta, this process is continuous. While the effective mass reaches a finite minimum at $\tau = 0$, the spectral function retains its Breit-Wigner form across the transition. For diffusive dynamics, the spectral shape stays similar to the Breit-Wigner form even near to the critical point, with some deviations close to the peak at low momentum. The dispersion relation however changes to an algebraic one, as we show in the next section. At high temperatures, the effective masses converge again and the mean-field dispersion relation (4.43) is restored. Effective masses then increase monotonously as a function of temperature for $T > T_c$, where again this process is completely continuous for high-momentum modes. Decay widths exhibit a non-trivial momentum dependence that changes its analytical form as the system crosses the critical point, however all

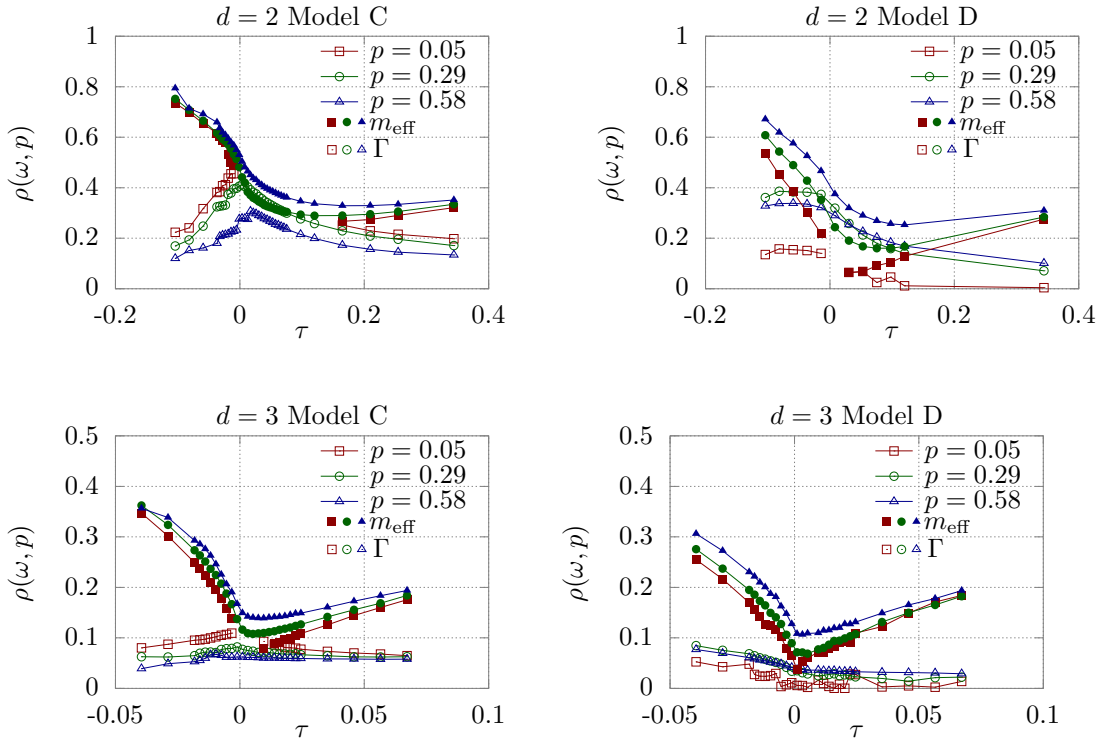

Figure 4.11: Temperature dependence of the effective mass parameter $m_{\text{eff}} \equiv ((\mu p^2)^{-\alpha}\omega_p^2 - p^2)^{1/2}$ and damping rates $\Gamma(p)$ as a function of reduced temperature. Left panels show dissipative dynamics ($\alpha = 0$), right panels show diffusive dynamics ($\alpha = 1$), both in 2+1D (top panels) and 3+1D (bottom panels). Results shown are obtained at vanishing Langevin coupling $\gamma = 0$, which affects only the damping rates. Immediately, one notices that the effective masses have about the same magnitude in both dissipative and diffusive dynamics. Near the critical point ($\tau \approx 0$) the effective mass drops and the damping rate generally increases. While at low momentum p the spectral function is no longer exactly described by a Breit-Wigner structure, the behavior of high-momentum modes is remarkably smooth across the phase transition.

with an absolute maximum close to the critical temperature.

In summary we find that, in the non-critical regime, the measured spectral functions behave mostly as expected. The mean-field dispersion relation is fulfilled by the dominant excitations, and we find the expected temperature dependence on both sides of the phase transition.

In Models A and C, it is interesting to see how, for low spatial momenta $p \ll 1$, the spectral shape and dispersion relation changes at different temperatures and shows critical scaling, while at larger spatial momenta $p > 1$, the spectral function retains its Breit-Wigner shape and moves across the transition in a completely continuous fashion. In the non-critical regime, introducing a finite Langevin damping γ leads to broadening of resonances, as one expects from the structure of the equations of motion. Close to the critical point, we see the same effect of the Langevin damping γ on the remaining quasi-particle contribution to the spectral function, whereas the infrared-divergent critical part appears qualitatively unchanged. However, as we will show in detail in Section 4.3, the slope of the infrared divergent power law is modified slightly.

For diffusive systems (Models B and D), the spectral shape changes hardly at all, with only minimal deviations from the Breit-Wigner shape even at criticality. The introduction of a finite Langevin damping γ leads to an additive broadening of the Breit-Wigner resonance in all cases. Close to the critical point, the dispersion relation changes as the effective mass vanishes, and the momentum dependence of the decay widths transforms as well. Similar to the case of Models A and C, these processes appear continuous at higher spatial momenta. In the next section, we will find that the changes in the infrared dispersion are compatible with critical scaling laws.

4.3 Critical dynamics and scaling functions

In the following section we investigate the critical behavior of spectral functions. We focus on the determination of a universal scaling function for the spectral function, as well as the extraction of the dynamic critical exponent z.

Dynamic critical phenomena have been studied since the late 60s, with the first numerical results for Ising models in the 90s [88, 89, 49, 50, 52, 14, 90, 91]. These studies were mostly concerned with finding the dynamic critical exponent z of the Ising model with Glauber dynamics (2D Model A), where a multitude of results ranging from $z = 1.7$ to $z = 2.7$ have been published, however slowly converging towards $z \approx 2.2$. Nightingale and Blöte [14] were the first to calculate z in 2D Model A in an Ising model with high precision using a variance-reducing Monte Carlo algorithm, albeit on rather small lattices up to 15×15. They found $z = 2.1665(12)$, quoting a two-sigma error, in accordance with the former trend.

In 2004, Dunlavy and Venus measured critical slowing down in ferromagnetic ultra-thin films [92], governed by 2D Model A dynamics as well. The resulting critical exponent of 2.09(6), giving the 95% confidence interval, is close to the Monte Carlo result, but the difference of nearly 2.5σ is somewhat large.

The most recent result by Zhong et al. [93] for a two-dimensional scalar ϕ^4 model with local Metropolis updates seems to confirm the results for 2D Model A by Nightingale and Blöte from [14], as they find $z_A = 2.17(3)$ and $z_A = 2.19(3)$ for two different values of the coupling constant. Additionally, they demonstrated that quantities derived from the two-point function follow a scaling behavior.

In 2010, a precursor study [40] of the present one first tried to confirm the dynamic critical exponent in 2D Model C, $z = 2 + \alpha/\nu = 2$ for an Ising-like scalar field theory with conservative dynamics, and found $z = 2.0(1)$.

Naturally, numerical simulations in $d = 3$ are more expensive than in $d = 2$, and thus there are fewer and less precise results for the dynamic critical exponents. Studies from the nineties for 3D Model A yield values of e.g. $z = 2.05(5)$ [49], or a compatible 2.09(4) [50]. A very recent and precise result from Monte-Carlo simulations of an improved Blume-Capel model by Hasenbusch [94] shows $z = 2.0245(15)$ for 3D Model A, taking into account corrections to the leading scaling behavior. In Ref. [94] the reader can also find a thorough historical overview of previous results both from field theory methods and Monte-Carlo simulations. Although experimental evidence on the dynamic critical exponent is sparse, a recent study on critical slowing down near the multiferroic phase transition in $MnWO_4$ by Niermann et al. [95] found $\nu z \approx 1.3$, which implies $z \approx 2.06$, compatible with the result by Hasenbusch within the assumed uncertainty of the measurement. We are not aware of any previous

Monte-Carlo studies on the dynamic critical exponent of Model C in $d = 3$; however, based on the classification scheme by Halperin and Hohenberg the dynamic critical exponent is known there by virtue of the same scaling relation ($z = 2 + \frac{\alpha}{\nu}$) as in $d = 2$, which amounts to $z \approx 2.17$ for a model in the 3D Ising universality class.

Changing the dynamic equations such that now the order parameter is constant over time, i.e. diffusive dynamics, the classification scheme by Hohenberg and Halperin [13] suggests that we are dealing with the dynamics of Model B in case of the theory coupled to the heat bath ($\gamma > 0$). A dynamic renormalization group analysis shows that, due to the order parameter being conserved, there are no ε-dependent contributions to the response propagator, therefore conventional theory holds [96, 13, 97]. One thus has for the dynamic critical exponent of the order parameter $z_B = 4 - \eta$.

If the heat-bath coupling is turned off ($\gamma = 0$), there is an additional conserved quantity in the system, namely the energy density. For the first-order non-relativistic version of Model D (as defined e.g. in [96, 97]), one can show that the additional conserved density compared to Model B does not affect the dynamic critical exponent, but the secondary density itself is governed by a different exponent $z_C = 2 + \alpha/\nu$, the same as for the order parameter in Model C. We will see that this is not the case in our relativistic version of Model D, since the way we achieve energy conservation by setting $\gamma = 0$ fundamentally alters the low-energy spectrum of the theory and we obtain for the order parameter (and later also the energy density) a dynamic critical exponent close to that of Model C.

An early numerical study by Yalabik and Gunton [98] applied the Monte-Carlo renormalization group approach on a 2D Ising model with Kawasaki dynamics, finding $z = 3.80$ in very good agreement with $4 - \eta = 3.75$. In 2001, Zheng [55] found in a study on the critical dynamics of the two-dimensional Ising model with Kawasaki dynamics, i.e. nearest-neighbor spin flips, found that short-time correlations exhibit scaling behavior with a dynamic critical exponent $z = 3.95(10)$, slightly larger than expected. When changing to a different scheme where spin exchanges happen over larger distances, such that the spin is no longer locally, but still globally conserved, they found a different exponent $z = 2.325(10)$. Such a drastic change of z upon seemingly slight changes of the dynamics is not unheard of in systems with conserved order parameter: A study on a quasi-2D lipid bi-layer in water [99] (Models B/H/HC) found that the exponent of the time scale of time-dependent correlation functions changed from $z_{\text{eff}} \sim 2$ to $z_{\text{eff}} \sim 3$, depending on the ratio of the correlation length of the fluctuations to a hydrodynamic length scale set by transport coefficients.

4.3.1 Overview

We start with some remarks on the shape of the critical spectral functions. Exemplary data of fixed-momentum cuts is shown in Fig. 4.12. For dissipative dynamics without order-parameter conservation (Models A/C), one observes a dominating structure emerging at low spatial momenta in the infrared, which is clearly distinct from the quasi-particle peak. On the other hand, for diffusive dynamics (Models B/D), fixed-momentum cuts of spectral functions are still well described by a single Breit-Wigner shape even at the critical temperature. Only at low to intermediate momenta and finite heat-bath coupling, the spectral functions differ from the Breit-Wigner shape around the peak. We will see that in all cases, the infrared structure of the spectral

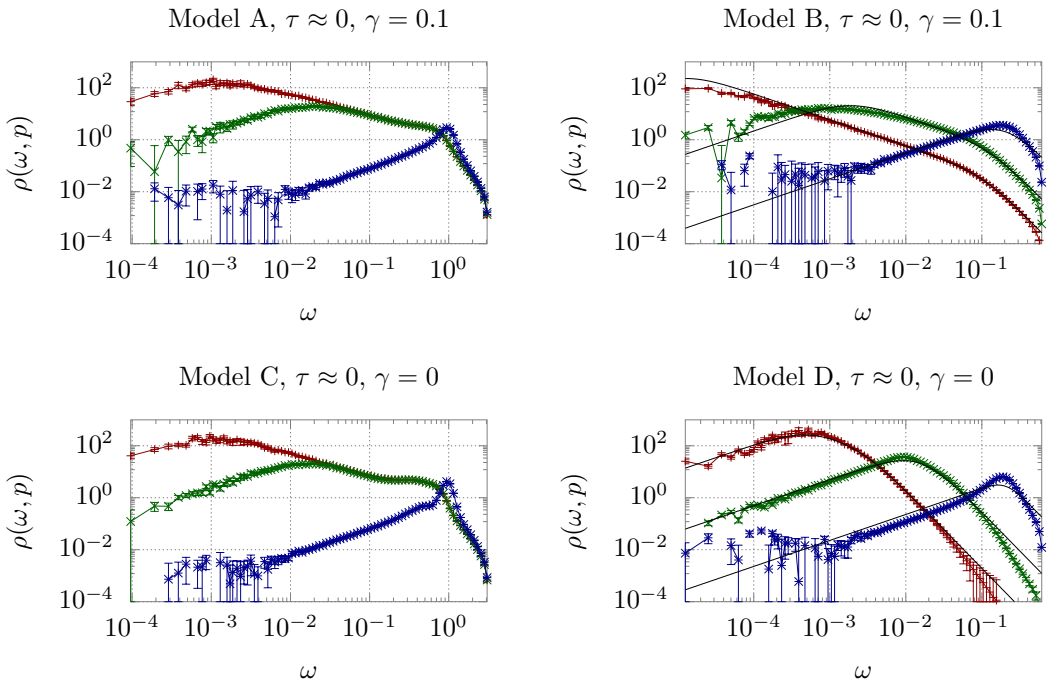

Figure 4.12: Spectral functions of the order parameter in 2+1D at the critical temperature, at spatial momentum $p = .025$ (red), $p = .098$ (green), $p = .390$ (blue). Left panels show results for dissipative dynamics, Model A in the top and Model C in the bottom panel, right panels the diffusive Models B (upper) and D (lower). Since the results for Models B and D very much retain the Breit-Wigner shape, we include in the right panels black lines representing the mean-field form Eq. (4.41) with algebraic dispersion $\omega_p^2 \sim p^{4-\eta}$, $\Gamma \sim p^{z_\Gamma}$. Extracted fit parameters are illustrated in Fig. 4.13. Results for 3+1D qualitatively agree and are thus omitted.

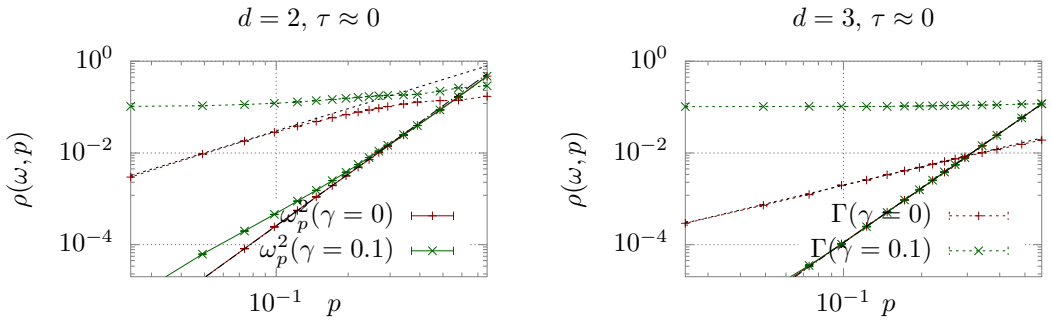

Figure 4.13: Extracted parameters from fits of critical spectral functions obtained with diffusive dynamics (Models B and D) to the Breit-Wigner shape (4.41). Numerical values are given in lattice units. Close to criticality at $T \approx T_C$, central frequencies show algebraic behavior, $\omega_p^2 \sim p^{z_B}$ with the dynamic critical exponent of Model B $z_B = 4 - \eta$. Decay widths at vanishing heat-bath coupling $\gamma = 0$ seem to follow a power law $\Gamma(p) - \gamma \sim p^{z_\Gamma}$ as well, with a much smaller exponent.

function is controlled by an underlying universal scaling function.

Encouraged by the qualitative assessment, we proceed by fitting the critical spectral functions obtained with diffusive dynamics (Models B and D) to the Breit-Wigner ansatz (4.41). Results for central frequencies ω_p^2 and decay widths Γ are shown in Fig. 4.13. Both the central frequencies and decay width at vanishing Langevin coupling $\gamma = 0$ evidently follow some power law, suggestive of dynamic scaling. The exponent of the power law controlling the central frequencies matches $\omega_p^2 \sim p^{4-\eta} = p^{z_B}$ the dynamic critical exponent of Model B, independently of the heat-bath coupling. For the decay widths Γ, we find that at vanishing heat-bath coupling it follows a power-law shape $\Gamma(\gamma = 0) \sim p^{z_\Gamma}$ with some exponent $z_\Gamma \approx 2$. The additive relation $\Gamma(\gamma) = \Gamma(\gamma = 0) + \gamma$ still holds.

For dissipative dynamics (Models A/C), the infrared part of the critical spectral functions does not fit a Breit-Wigner structure. One finds however that the Langevin-coupling γ hardly has any effect on the qualitative features of the infrared structure, while smearing out the remnant of the quasi-particle excitation at larger momenta.

4.3.2 Dynamic scaling functions

Since the spectral function is derived directly from the two-point correlation function, one expects the critical behavior to be governed by the following scaling form [40]

$$\rho\left(\omega, p, \tau\right) = s^{2-\eta} \rho\left(s^z \omega, sp, s^{\frac{1}{\nu}} \tau\right), \tag{4.46}$$

in the limit of small ω, p, and $\tau \to 0$, where we omit any residual dependencies on the finite volume. If not stated otherwise, we will restrict ourselves to positive frequencies ($\omega > 0$) to compactify notation, noting that the behavior for negative frequencies ($\omega < 0$) is trivially obtained from the symmetry of the spectral function $\rho(-\omega, p, \tau) = -\rho(\omega, p, \tau)$.

We give our results for the universal scaling functions in terms of dimensionless scaling variables normalized by the related critical amplitudes, namely

$$\bar{p} = p f^+, \tag{4.47}$$
$$\bar{\omega} = \omega f_t^+, \tag{4.48}$$
$$\bar{t} = t / f_t^+, \tag{4.49}$$

where f_t^+ denotes the amplitude of the correlation time with temperature in the limit of small but nonzero spatial momentum, i.e.

$$\lim_{p \to 0} \xi_t(p, \tau > 0) = f^+ |\tau|^{-\nu z}. \tag{4.50}$$

If the order parameter is not conserved, the limit is continuous and we measure $\xi_t(p = 0, \tau > 0)$ in Section 4.3.3.

In Models B and D however, this amplitude is not directly accessible, since it involves taking the limit of vanishing spatial momentum; compare Section 4.3.3. If one assumes that the correlation time is related to the correlation length via a temperature-independent amplitude as $\xi_t \sim a \xi^z$, one can obtain it by using the universal ratio

$$\frac{f_t |p|^{-z}}{|p|^{-z}} = \frac{\xi_t}{\xi^z} = \frac{f_t^+ |\tau|^{-\nu z}}{(f^+ |\tau|^{-\nu})^z} = \text{const.} \tag{4.51}$$
$$\Rightarrow \quad f_t (f^+)^z = f_t^+. \tag{4.52}$$

The scaling law in Eq. (4.46) allows us to define three alternative scaling functions f_ω, f_p and $f_\tau^\pm$ according to

$$\rho\left(\omega,p,\tau\right) = \bar{\omega}^{-(2-\eta)/z}\, f_\omega\Big(\bar{p}^z/\bar{\omega}, \tau/\bar{\omega}^{1/\nu z}\Big), \tag{4.53}$$

$$\rho\left(\omega,p,\tau\right) = \bar{p}^{-(2-\eta)}\, f_p\Big(\bar{\omega}/\bar{p}^z, \tau/\bar{p}^{1/\nu}\Big), \tag{4.54}$$

$$\rho\left(\omega,p,\tau\right) = |\tau|^{-\gamma}\, f_\tau^\pm\Big(\bar{\omega}/|\tau|^{\nu z}, \bar{p}^{1/\nu}/|\tau|\Big), \tag{4.55}$$

where γ is the static susceptibility exponent with $\gamma = \nu(2-\eta)$ from static scaling relations.

Since the scaling functions in Eqs. (4.53) to (4.55) are all derived from the scaling behavior of the spectral function, the scaling functions f_ω,f_p and $f_\tau^\pm$ are not independent. Denoting the natural arguments of the respective scaling functions as

$$x_\omega = \bar{p}^z/\bar{\omega}, \qquad y_\omega = \tau/\bar{\omega}^{1/\nu z}, \tag{4.56}$$

$$x_p = \bar{\omega}/\bar{p}^z, \qquad y_p = \tau/\bar{p}^{1/\nu}, \tag{4.57}$$

$$x_\tau = \bar{\omega}/|\tau|^{\nu z}, \qquad y_\tau = p^{1/\nu}/|\tau|, \tag{4.58}$$

one finds the following relations between the scaling functions

$$f_p(x_p,y_p) = x_p^{-(2-\eta)/z}\, f_\omega\big(1/x_p, y_p/x_p^{1/\nu z}\big)\,, \tag{4.59}$$

$$f_p(x_p,y_p) = |y_p|^{-\gamma}\, f_\tau^\pm\big(x_p/|y_p|^{\nu z}, 1/|y_p|\big)\,, \tag{4.60}$$

$$f_\tau^\pm(x_\tau,y_\tau) = x_\tau^{-(2-\eta)/z} f_\omega\big(y_\tau^{\nu z}/x_\tau, \pm 1/x_\tau^{1/\nu z}\big)\,, \tag{4.61}$$

where the super-script in $f_\tau^\pm$ is used to distinguish $\mathrm{sgn}(\tau) = \mathrm{sgn}(y_p) = \pm 1$ above/below T_c. Similarly, the Fourier transform of Eq. (4.46) yields in the time domain

$$\rho\left(t,p,\tau\right) = s^{(2-\eta-z)}\rho\left(s^{-z}t, sp, s^{1/\nu}\tau\right), \tag{4.62}$$

from which one can derive the time-domain scaling functions analogous to Eqs. (4.53) to (4.55).

In the following, we aim to extract the scaling functions f_ω, f_p, $f_\tau^\pm$ and their asymptotic behavior from numerical data. Since the critical spectral functions show qualitatively very different characteristics depending on the type of dynamic equations, we split our analysis in two parts, starting with the scaling behavior of dissipative dynamics.

Models A and C

Indeed, the scaling behavior predicted in Eqs. (4.53) to (4.55) is clearly visible in our classical-statistical simulations, as can be seen from Figs. 4.14 to 4.19, where we present results for the scaled spectral functions in the vicinity of the critical point. We note that in order to perform the axis re-scaling in Figs. 4.14 to 4.19, one also needs the value of the dynamic critical exponent z, and if not stated otherwise, we employ the values in last row of Table 4.7, labeled *combined*, with exception of $d = 3$ Model C, where we used the analytic value of $z \approx 2.17$.

By comparing our results for the scaling functions in Figures 4.16 and 4.17, we find that in general, the scaling regions are larger in $d = 2$ than in $d = 3$, and

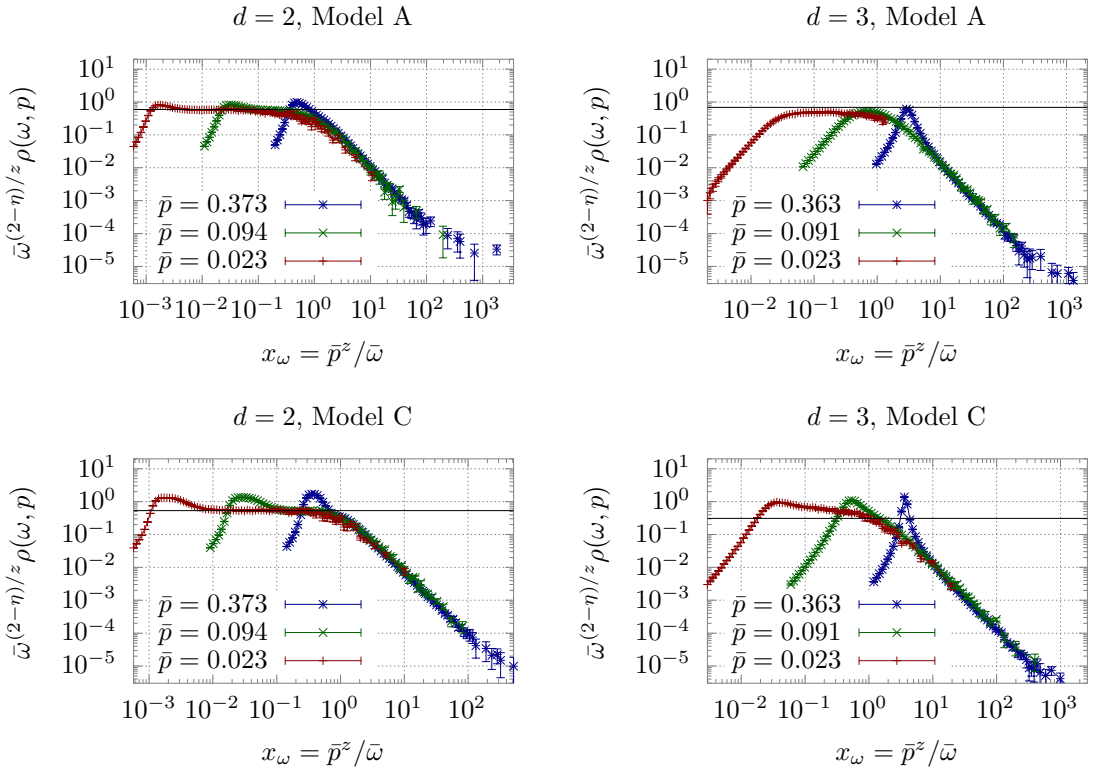

Figure 4.14: Scaling function $f_\omega(x_\omega, 0)$ of the critical spectral function at non-zero spatial momentum for the different critical scenarios with dissipative dynamics. Solid black lines represent the amplitude f_ω obtained from the fit of the universal scaling function in Fig. 4.16 at large x_p. Due to availability of data, we use $\tau = 0.0009(2)$ ($d = 2$) resp. $\tau = -0.00008(5)$ (d=3) as a proxy for the critical temperature. Note that, despite $\tau \approx 0$, finite size effects are not relevant here due to finite spatial momentum.

similarly larger for Model A than for Model C. Specifically, for $d = 3$, it seems that in some cases the standard volumes ($N = 256$) are still not large enough to show critical effects of reasonable strength. Hence, in order to achieve some sufficient overlap for extracting the universal scaling function at finite spatial momentum p, we have generated a single additional data set at $T \approx T_c$ with $N = 512$ in $d = 3$, which allows us to investigate very small spatial momenta, with $p < 0.05$ in lattice units. By inspecting e.g. the upper right panel in Fig. 4.16, it is then clear that for very small p, the overlap region does indeed extend to the right of the maximum, where the slope in the logarithmic plot is determined by the critical power law.

One important advantage of working with finite spatial momenta $p > 0$ is that finite volume effects are essentially irrelevant, as the relevant infrared cut-off is set by the momentum p rather than the system size. Conversely, at $p = 0$, finite volume effects inevitably appear close to criticality, i.e. for very small τ, as can be seen e.g. in Figs. 4.17 and 4.19.

By closer inspection of the results in Figures 4.16 and 4.17, e.g. when comparing models A (upper row) to models C (lower row), one further notices that the spectral functions $\rho(\omega, p, \tau)$ start to deviate from the scaling function when reaching the remnants of the quasi-particle peak, which appear as additional "shoulders" at the high-frequency end. Clearly, this effect is more pronounced in Model C, where high-frequency fluctuations do not receive the additional damping due to the coupling

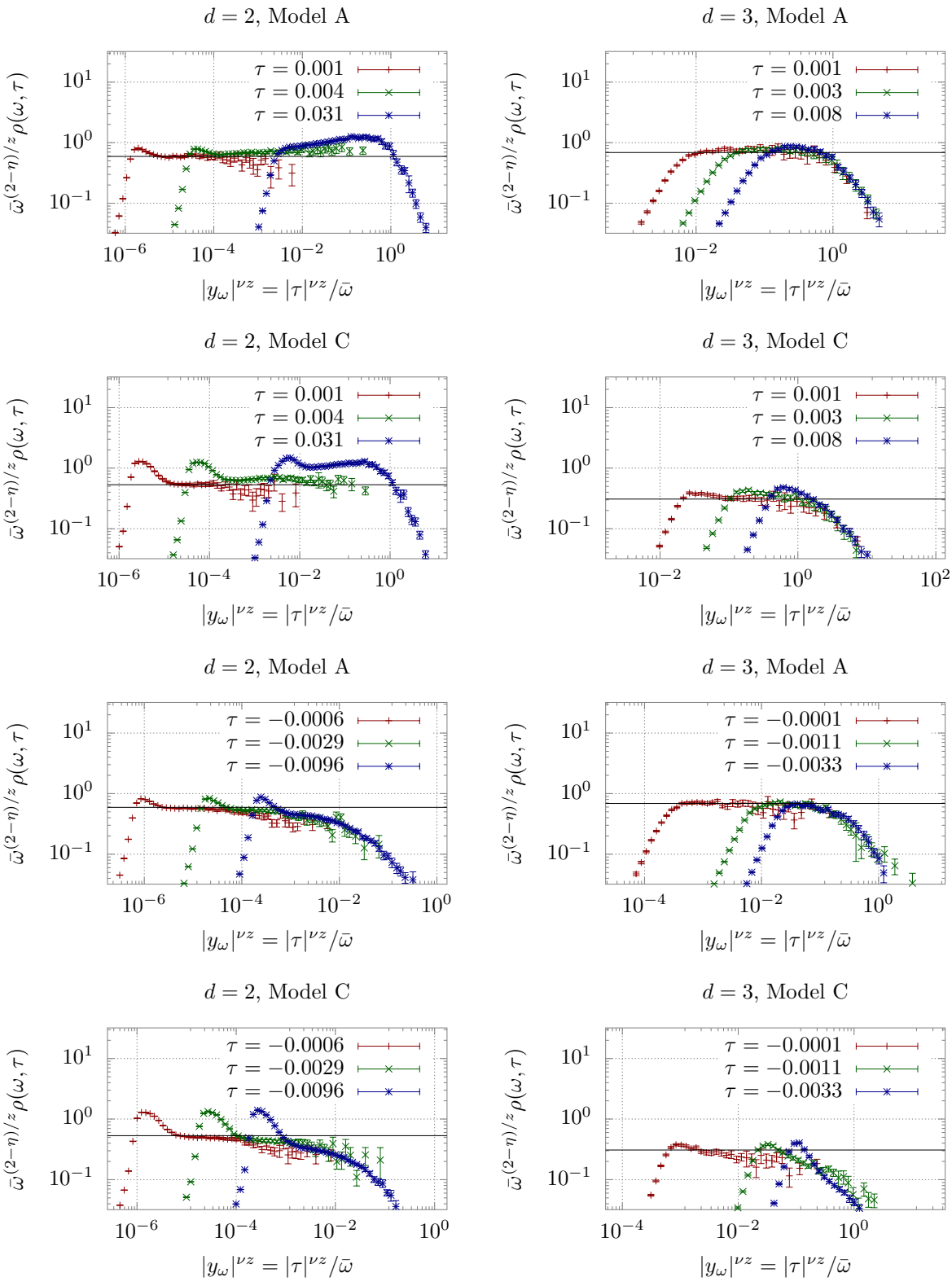

Figure 4.15: Scaling function $f_\omega(0, y_\omega)$ of the spectral function at vanishing spatial momentum for the different critical scenarios with dissipative dynamics. Solid black lines represent the amplitude f_ω resulting from the fit of $f_p(x_p, 0)$ at large x_p in Fig. 4.16, which also describes the behavior of $f_\omega(0, y_\omega)$ when the second argument is small, indicating that the limits $p \to 0$ and $\tau \to \pm 0$ commute. Note that based on the available lattice sizes, finite-size effects start to play a role at very small τ.

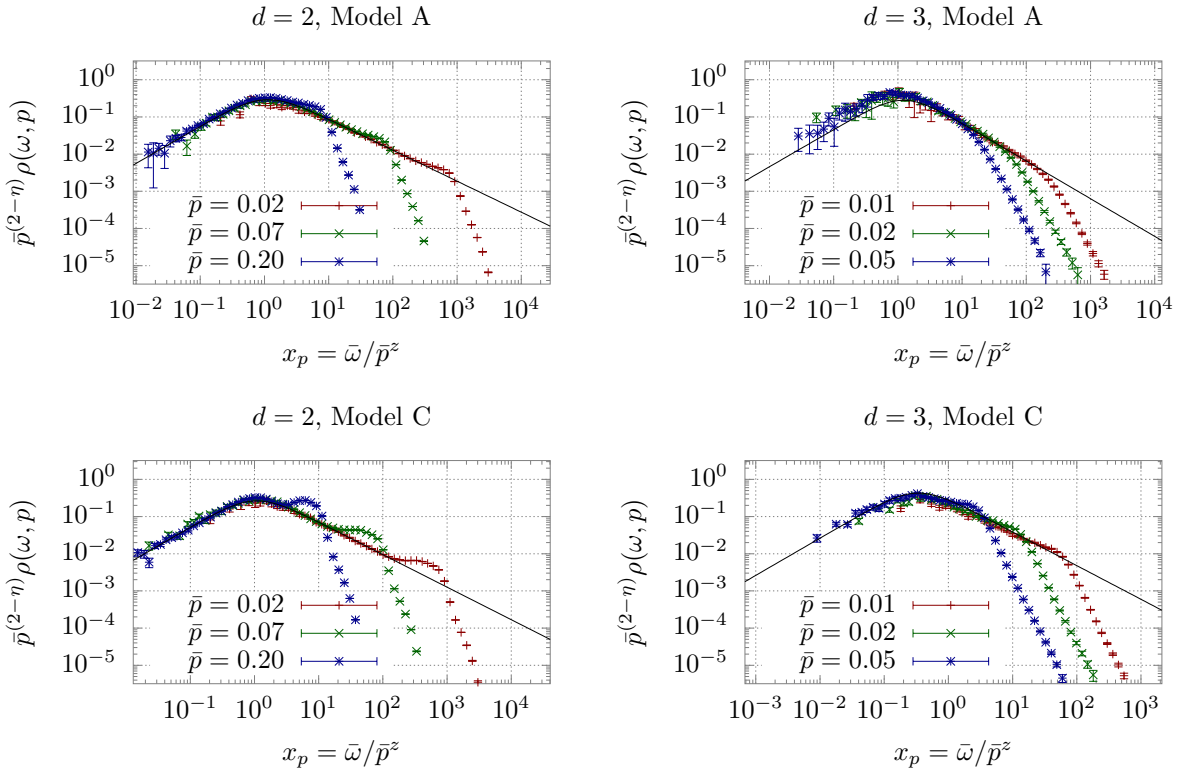

Figure 4.16: Scaling function $f_p(x_p, 0)$ of the spectral function for the different critical scenarios with dissipative dynamics. Due to availability of data, we use $\tau = 0.0009(2)$ ($d = 2$) resp. $\tau = -0.00008(5)$ ($d = 3$) as a proxy for the critical temperature. Solid lines represent the fit to the ansatz in Eq. (4.70), we fit f_ω and a_p as free parameters, and the exponent of the power law for large x_p is given by $(2-\eta)/z_{\text{comb}}$. Note that finite size effects are not relevant here due to finite spatial momentum. To achieve the comparatively very low p in $d = 3$, a single set of data at $N = 512$ very close to T_c was generated.

to the heat bath. By looking at the results for $\tau < 0$ in Fig. 4.17 we also note that the universal scaling of the spectral functions, when approaching criticality from the ordered phase, does not appear to emerge from the remnants of the quasi-particle peak, even in close vicinity of the critical point. Instead, as previously alluded to in the context of the discussion of Fig. 4.5, it rather seems that the universal critical behavior of the spectral function emerges from the soft collective low-frequency excitation in the ordered phase.

We can exploit this scaling behavior to extract the dynamic critical exponent z by minimizing the deviations from perfect scaling, which we quantify in terms of the L^2-norms of pairwise distances of rescaled functions over some frequency interval $[\omega_l, \omega_h]$. Specifically, for the p-rescaled critical spectral functions as depicted in Figure 4.16, based on Eq. (4.54), this amounts to minimizing the quantity

$$\Delta^2(z) = \sum_{p_i} \sum_{p_i<p_j} \int_{\omega_l}^{\omega_h} \mathrm{d}\omega \frac{\left|p_i^{2-\eta}\rho(p_i^z\omega, p_i, 0) - p_j^{2-\eta}\rho(p_j^z\omega, p_j, 0)\right|^2}{\left(p_i^{2-\eta}\Delta\rho(p_i^z\omega, p_i, 0)\right)^2 + \left(p_j^{2-\eta}\Delta\rho(p_j^z\omega, p_j, 0)\right)^2}\,, \tag{4.63}$$

where $\Delta\rho$ denotes the statistical error of the measured spectral functions, which is used to weight the deviations. Similarly, an analogous functional is minimized to optimize the scaling of the τ-rescaled spectral functions at vanishing momentum in

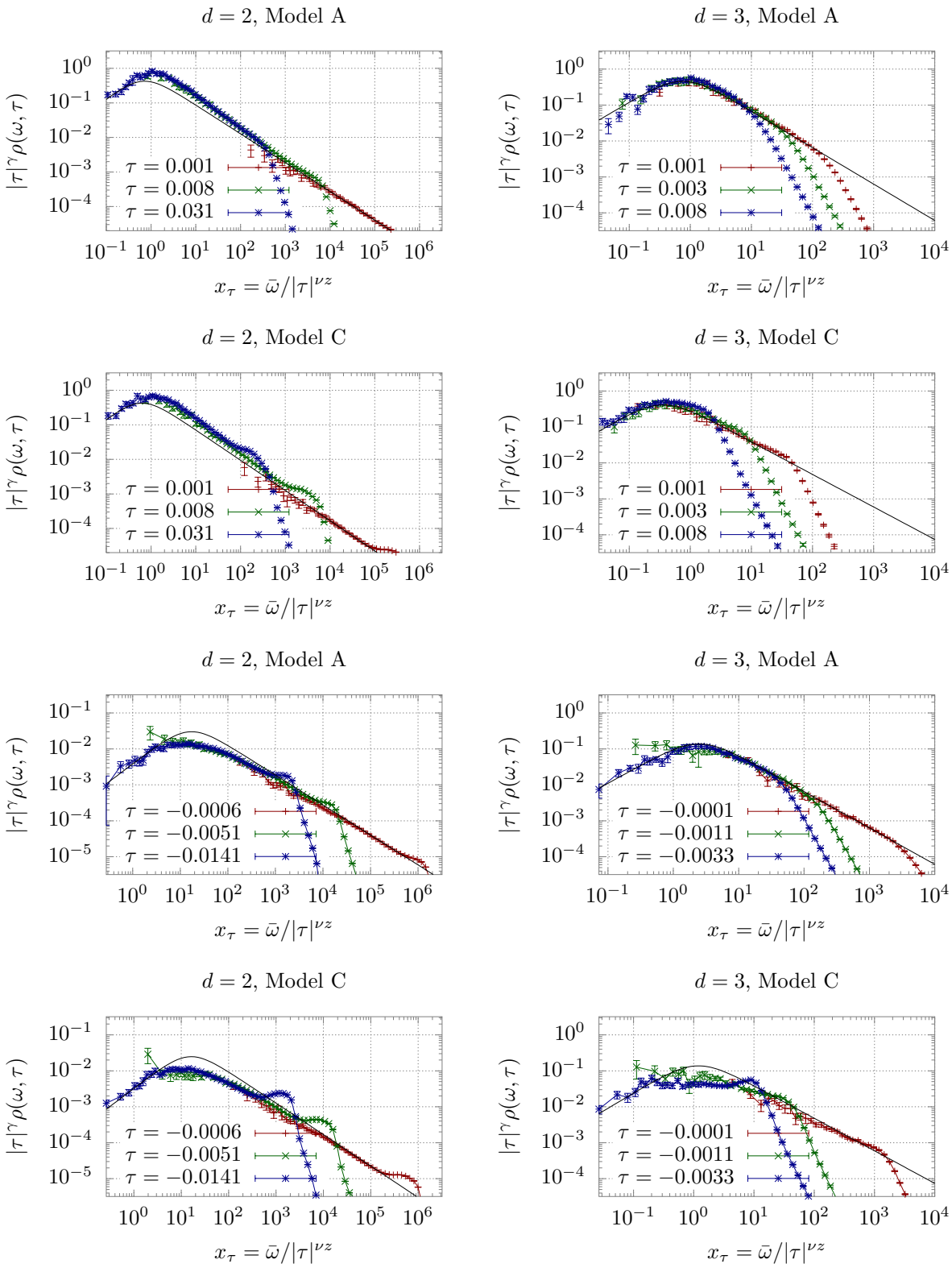

Figure 4.17: Scaling functions $f_\tau^\pm(\bar{\omega}/|\bar{\tau}|^{\nu z}, 0)$ of critical spectral functions at vanishing momenta above (top four) and below (bottom four) T_c for the different critical scenarios with dissipative dynamics. Solid lines represent the fit to the ansatz in Eq. (4.71), where we obtain $a_\tau^\pm$ by fitting Eq. (4.71) to the data at small x, keeping f_ω as obtained from the ansatz in Eq. (4.70) to the data in Fig. 4.16, and $z = z_{\text{comb.}}$. Note that based on the available lattice sizes, finite-size effects start to play a role at small τ.

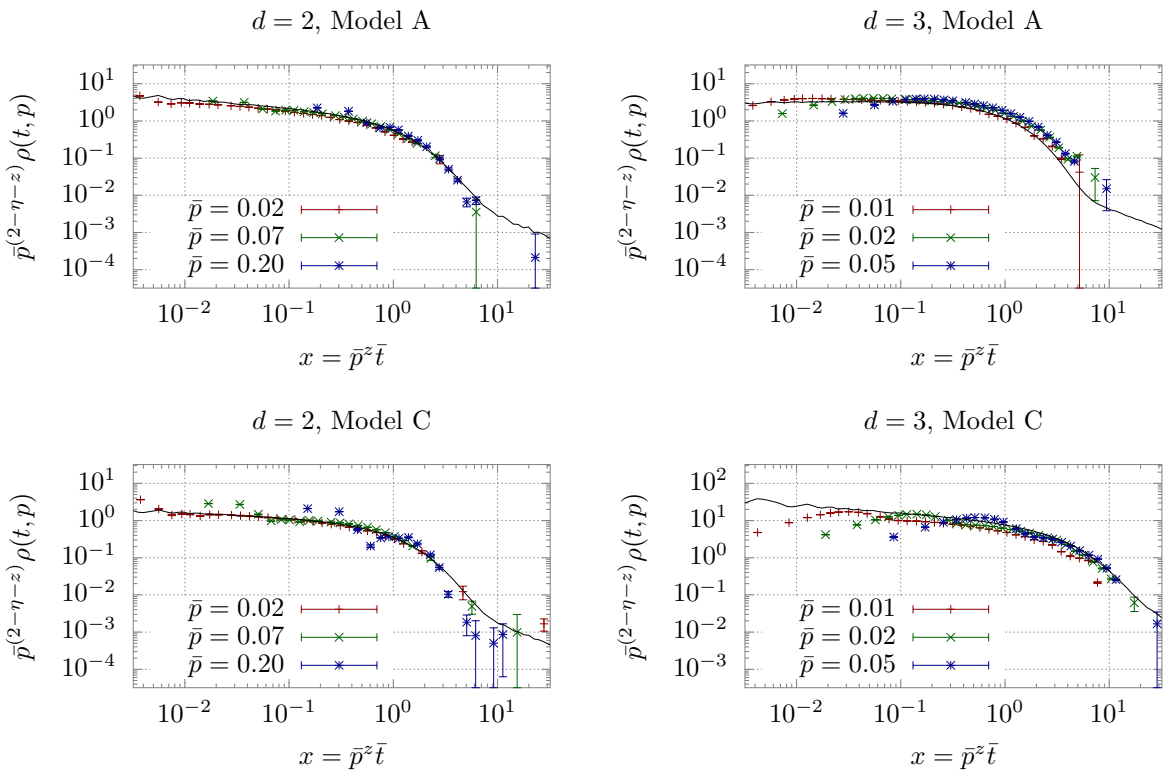

Figure 4.18: Scaling functions $\tilde{f}_p\,(\bar{p}^z \bar{t}, 0)$ of the critical spectral functions in the time domain for the different critical scenarios with dissipative dynamics; cf. Eq. (4.72). Solid lines represent the numerical Fourier transform of the fit to the data in frequency space.

Figure 4.17.

Even though this procedure is in principle very robust, we were not able to completely eliminate the dependence on the upper limit ω_h of the frequency interval. Since this dependence is particularly strong for the τ-rescaled spectral functions, we have disregarded them in the final estimate. By the principle of least sensitivity, i.e. by looking for a plateau in the results for different ω_h, we can then estimate reasonable values for ω_h in case of the p-rescaled spectral functions, which yield a set of plausible values for the dynamic critical exponents that are shown in Table 4.7 in the row labeled *scaling*. However, since the systematic uncertainties associated with this procedure are still somewhat uncontrolled, we have also explored two alternative methods to calculate the dynamic critical exponent z, one of which is based on the limiting behavior of the scaling functions detailed below.

Based on the results of [40], we expect the scaling function $f_\omega(x_\omega, y_\omega)$ to be regular in the origin for Models A and C ($\alpha = 0$), with a constant value $f_\omega \equiv f_\omega(0,0)$, such that the critical zero-momentum spectral function obeys the infrared power law

$$\rho(\omega, 0, 0) = f_\omega\, \bar{\omega}^{-(2-\eta)/z}. \tag{4.64}$$

This expectation is verified in Figs. 4.14 and 4.15, where we present simulation results for $f_\omega(x_\omega, 0) = \omega^{(2-\eta)/z}\rho(\omega, p, 0)$ as a function of x_ω at $\tau \propto y_\omega = 0$ (Fig. 4.14) and respectively $f_\omega(0, y_\omega) = \omega^{(2-\eta)/z}\rho(\omega, 0, \tau)$ as a function of y_ω at $p \propto x_\omega = 0$ (Fig. 4.15). Generally, one observes an excellent scaling collapse of the data for different momenta(reduced temperatures), with deviations only at very small values of $x_\omega(y_\omega)$ where the residual contributions from the quasi-particle peak at finite

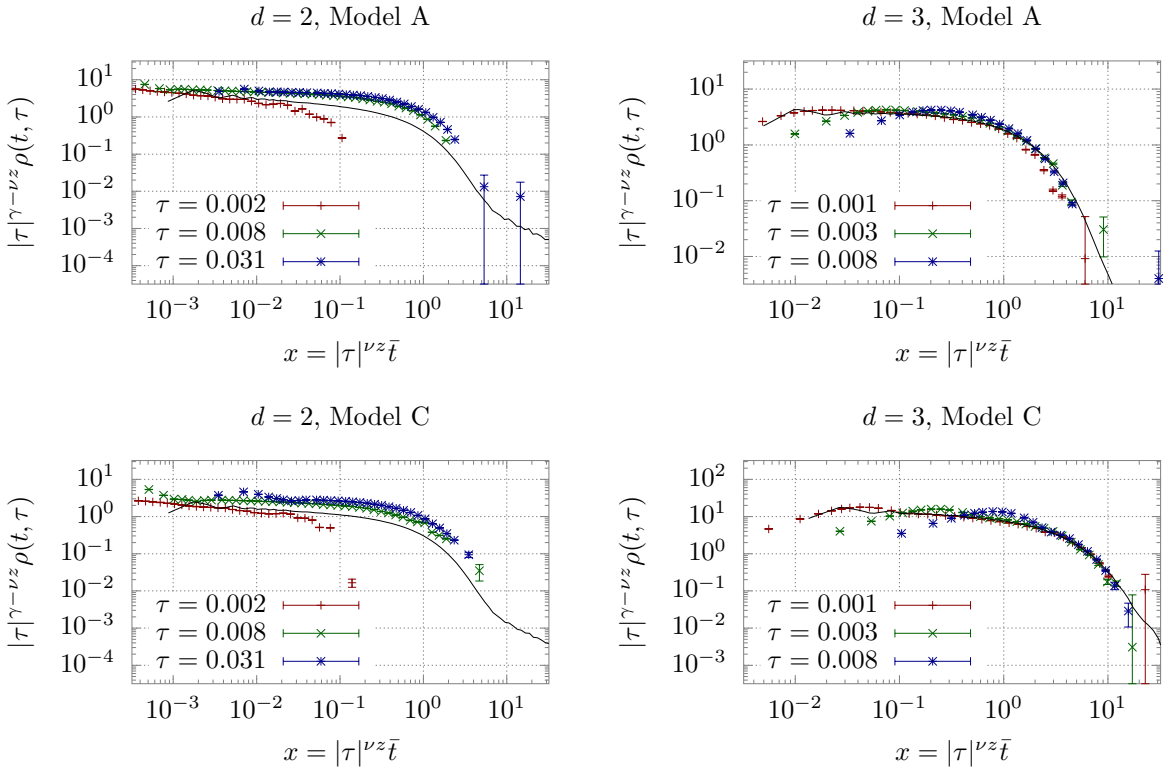

Figure 4.19: Scaling functions $\tilde{f}_\tau^\pm(\bar{t}/|\tau|^{-\nu z}, 0)$ of the spectral functions at vanishing spatial momentum in the time domain for the four different critical scenarios; cf. Eq. (4.73). Solid lines represent the numerical Fourier transform of the fit to the data in frequency space. Finite size effects again shift the data at small τ away from the scaling function.

momentum(reduced temperature) effectively acts as a cut-off. Specifically, for small arguments x_ω or y_ω the two data sets in Figs. 4.14 and 4.15 appear to converge towards the same value f_ω indicated by a solid black line, demonstrating that f_ω is indeed finite and that the limits $p \to 0$ and $\tau \to 0$ commute at small but finite frequency $\bar{\omega} \neq 0$.

Due to the above relations between the scaling functions f_ω, f_p and $f_\tau^\pm$, we can further exploit the regularity of f_ω near the origin $(x_\omega, y_\omega) = (0, 0)$ to deduce the behavior of the scaling functions f_p and $f_\tau^\pm$ for large values of the arguments $x_p = 1/x_\omega$ and $x_\tau = 1/|y_\omega|^{\nu z}$ as

$$\begin{aligned} \bar{p}^{2-\eta}\rho(\omega, p, 0) &= f_p(x_p, 0) \overset{x_p\to\infty}{\to} f_\omega\, x_p^{-(2-\eta)/z}\,, \\ |\tau|^\gamma \rho(\omega, 0, \tau) &= f_\tau^\pm(x_\tau, 0) \overset{x_\tau\to\infty}{\to} f_\omega\, x_\tau^{-(2-\eta)/z}\,. \end{aligned} \tag{4.65}$$

This fixes the high-frequency ($\omega \gg 1/\xi_t(\tau, p)$) behavior of the critical scaling function $f_p(x_p, 0)$ at very low momenta, and that of the zero-momentum scaling function $f_\tau^\pm(x_\tau, 0)$ very close to criticality at the same time. The characteristic time $\xi_t(\tau, p)$ for this asymptotic behavior, from the definition of our scaling variables, behaves as $\xi_t(0, p) \sim 1/p^z$ and $\xi_t(\tau, 0) \sim 1/|\tau|^{\nu z}$ at small p and τ, respectively.

Conversely, the low-frequency ($\omega \ll 1/\xi_t(\tau, p)$) behavior of the spectral function is determined by the behavior of $f_\omega(x_\omega, 0)$ and $f_\omega(0, y_\omega)$ at asymptotically large values of x_ω and y_ω, which conversely can be determined from the behavior of $f_p(x_p, 0)$ and $f_\tau^\pm(x_\tau, 0)$ at small values of the arguments $x_p = 1/x_\omega$ and $x_\tau = 1/|y_\omega|^{\nu z}$. Numerically,

we find from Figs. 4.16 and 4.17 that the leading behavior at small x_p and x_τ is well described by

$$\begin{aligned} f_p(x_p,0) &= a_p\, x_p \;+\; \cdots\,, \\ f_\tau^\pm(x_\tau,0) &= a_\tau^\pm\, x_\tau \;+\; \cdots\,, \end{aligned} \tag{4.66}$$

which corresponds to

$$\begin{aligned} f_\omega(x_\omega,0) &\to a_p\, x_\omega^{-(2-\eta)/z-1}\,, \quad x_\omega \to \infty\,, \\ f_\omega(0,y_\omega) &\to a_\tau^\pm\, |y_\omega|^{-\gamma-\nu z}\,, \quad y_\omega \to \pm\infty\,. \end{aligned} \tag{4.67}$$

Specifically, for the critical spectral function ($\tau = 0$) at finite spatial momentum, Eq. (4.67) implies an infrared behavior, valid asymptotically for $\bar\omega \ll \bar p^z$, of

$$\rho(\omega,p,0) = a_p\, \bar p^{-(2-\eta)}\, \bar\omega/\bar p^z \;+\; \cdots\,. \tag{4.68}$$

Comparing Eq. (4.68) with Eq. (4.64), we see that the limits $p \to 0$ and $\omega \to 0$ do not commute, as the critical spectral function is non-analytic in the origin. In particular, we have $\lim_{\omega\to 0}\rho(\omega,0,0) = \infty$, while $\lim_{p\to 0}\rho(0,p,0) = 0$. Physically, this has the intuitive interpretation that any finite momentum p introduces an effective IR cutoff for the correlation length $\xi \sim 1/p$, which in turn is associated with a finite correlation time $\xi_t(0,p) \sim \xi^z \sim 1/p^z$, that defines the characteristic frequency $\bar\omega \sim \bar p^z$ where the power law changes from (4.64) to (4.68).

Similarly, for the zero-momentum spectral function off criticality we conclude that the infrared behavior for $\bar\omega \ll |\tau|^{\nu z}$ is modified as

$$\rho(\omega,0,\tau) = a_\tau^\pm\, |\tau|^{-\gamma}\, \bar\omega/|\tau|^{\nu z} \;+\; \cdots\,, \tag{4.69}$$

so that for all $\tau \neq 0$ we also have $\lim_{\omega\to 0}\rho(\omega,0,\tau) = 0$, with the characteristic frequency where the power law changes from (4.64) to (4.69) given by $\omega \sim |\tau|^{\nu z}$. Once again, this simply reflects the finiteness of the correlation time at non-vanishing τ, where we now have $\xi_t(\tau,0) \sim \xi^z \sim 1/|\tau|^{\nu z}$.

So far we have analyzed the limiting behavior of the scaling functions for very large and very small arguments. Now, in order to interpolate between these two limits, we observe that the inverse of the scaling functions $f_p(x,0)$ and $f_\tau^\pm(x,0)$ is globally very well described by a sum of the reciprocal power laws (4.65) and (4.66) for large and small x. We therefore use the following parametrizations of the scaling functions to fit our data,

$$f_p(x_p,0) = \frac{1}{(a_p\, x_p)^{-1} + f_\omega^{-1}\, x_p^{(2-\eta)/z}} \quad \text{for} \;\; x_p = \bar\omega/\bar p^z\,, \tag{4.70}$$

$$f_\tau^\pm(x_\tau,0) = \frac{1}{(a_\tau^\pm\, x_\tau)^{-1} + f_\omega^{-1}\, x_\tau^{(2-\eta)/z}} \quad \text{for} \;\; x_\tau = \bar\omega/|\tau|^{\nu z}\,. \tag{4.71}$$

Our results are compactly summarized in Figures 4.16 and 4.17, where we show these parametrizations for the scaling functions $f_p(\bar\omega/\bar p^z,0)$ and $f_\tau^\pm(\bar\omega/|\tau|^{\nu z},0)$ fitted to our data for $\bar p^{(2-\eta)}\rho(\omega,p,0)$ and $|\tau|^\gamma\rho(\omega,0,\tau)$ respectively. The regions where the points overlap are used to determine the universal scaling functions. The numerical results for the parameters a_p, $a_\tau^\pm$, f_ω obtained from the fits with fixed z are listed in Table 4.4. Corresponding plots for the scaling laws in the time domain are shown in

Table 4.4: Extracted fit parameters from fitting Eqs. (4.70) and (4.71) to the scaling functions. The first line corresponds to the results of the fits of Eq. (4.76) with z as a fit parameter, with an estimate of the systematic error. The other lines represent the values obtained by fitting the data in Figs. 4.16 and 4.17 with a fixed value for the dynamic critical exponent, corresponding to the last row of Table 4.7 labeled *combined*, see below. For the latter ones we only give the statistical fit error.

	2D		3D	
	Model A	Model C	Model A	Model C
f_ω	0.73(9)	$0.50^{+0.23}_{-0.14}$	0.56(35)	$1.14^{+0.25}_{-0.56}$
$f_\omega(z_{\text{comb.}})$	0.592(4)	0.536(2)	0.69(1)	0.544(7)
a_p	0.56(1)	0.51(1)	0.46(37)	1.13(10)
a_t^+	1.30(9)	1.43(6)	1.20(10)	1.13(16)
a_t^-	0.0038(2)	0.0032(1)	0.111(8)	0.14(1)

Figs. 4.18 and 4.19, where we plot the Fourier transformed scaling functions $\tilde{f}_p(x,0)$ and $\tilde{f}_\tau^+(x,0)$ from the analogous definitions

$$\rho(t,p,\tau) = \bar{p}^{-(2-\eta-z)}\, \tilde{f}_p(\bar{p}^z \bar{t}, \tau/\bar{p}^{1/\nu})\,, \tag{4.72}$$

$$\rho(t,p,\tau) = |\tau|^{-(2-\eta-z)}\, \tilde{f}_\tau^\pm(|\tau|^{\nu z}\bar{t}, \bar{p}^{1/\nu}/|\tau|)\,. \tag{4.73}$$

By looking at Figures 4.16 and 4.17, one finds that scaled data sets for the spectral functions at different momenta/reduced temperatures overlap with each other to rather good accuracy, and that, apart from $f_\tau^\pm(x_\tau,0)$ in $d=2$ spatial dimensions, the ansätze in Eqs. (4.70) and (4.71) match the overlapping data points exceptionally well. Moreover, the characteristic frequencies $\bar{\omega}_c \sim \bar{p}^z$ and $\bar{\omega}_c \sim \tau^{\nu z}$ mentioned above can be read off directly from the coinciding maxima in the respective scaling variables x_p and x_τ. The above fits (4.70) and (4.71) in turn imply that the frequency scaling function $f_\omega(x_\omega, y_\omega)$, either at criticality ($y_\omega = \tau/\bar{\omega}^{1/\nu z} = 0$) or at zero momentum ($x_\omega = \bar{p}^z/\bar{\omega} = 0$), is equally well described by

$$f_\omega(x_\omega, 0) = \frac{f_\omega}{1 + (f_\omega/a_p)\, x_\omega^{(2-\eta)/z+1}}\,, \tag{4.74}$$

$$f_\omega(0, y_\omega) = \frac{f_\omega}{1 + (f_\omega/a_\tau^\pm)\, |y_\omega|^{\nu z+\gamma}}\,, \tag{4.75}$$

with $a_\tau^\pm$ for $\mathrm{sgn}(y_\omega) = \pm 1$ above and below T_c, which provides a complete description of the scaling function $f_\omega(x_\omega, y_\omega)$ along the two coordinate axes.

We introduce here additionally a second method of extracting the dynamic critical exponent z from our data, exploiting the large x_p and x_τ behavior of the scaling functions $f_p(x_p,0)$ and $f_\tau^\pm(x_\tau,0)$. Based on the scaling form of the spectral function in Eq. (4.53), we extract the infrared power law (4.64) from either the critical spectral function at $\tau = 0$ and some sufficiently small momentum p, or that at zero momentum sufficiently close to criticality. For example, Eq. (4.70) entails that the frequency dependence of the critical spectral function ($\tau = 0$), at a given fixed value of p, is of the form

$$\rho(\omega) = \frac{1}{(a\omega)^{-1} + b\omega^\sigma}\,. \tag{4.76}$$

Likewise, cf. Eq. (4.71), the same form should also describe the frequency dependence of the zero-momentum spectral function at fixed small $\tau \neq 0$, with $\sigma = (2-\eta)/z$ in

each case. We note that the power-law amplitude $b = {f_t^+}^\sigma / f_\omega$ is fixed by the constant f_ω governing the regular behavior of $f_\omega(x_\omega, y_\omega)$ near the origin at $x_\omega = y_\omega = 0$, whereas the parameter a is related to the amplitudes governing the leading small x_p resp. x_τ behavior of $f_p(x_p, 0)$ resp. $f_\tau(x_\tau, 0)$ via the relations

$$a_p = a \, (\bar{p}_{\text{fit}})^{z+2-\eta} \,, \tag{4.77}$$

$$a_\tau^\pm = a \, |\tau_{\text{fit}}|^{\nu z+\gamma} \,, \tag{4.78}$$

where $\bar{p}_{\text{fit}}$, τ_{fit} designate the spatial momentum resp. reduced temperature where the fit was performed.

By fitting this ansatz with the amplitudes a, b and the exponent σ as free parameters to the critical spectral functions ($\tau = 0$) at fixed momentum we obtain reasonably stable results for the dynamic critical exponent z, which are listed in the second row of Table 4.7 with the label *IR power law*. In practice, we simultaneously fit the spectral functions for the smallest two ($d = 3$) or three ($d = 2$) spatial momentum indices to improve statistics. Unfortunately, in $d = 3$ even for our largest possible lattices we can not reach small enough spatial momenta p to obtain a reasonably well constrained signal for z, especially in Model C.

In order to estimate the uncertainty in z, we vary the upper limit of the frequency interval where we fit Eq. (4.76) to the data in a sensible range. We eliminate one third of the results with the largest χ^2/d.o.f. Of the remaining results, we take the highest and lowest values for z as bounds on the confidence interval, and calculate the average of z weighted with the statistical uncertainty. If the weighted average of z is not near the center of the confidence interval, we separately note the uncertainties in both directions.

If one naively repeats this process for the zero-momentum spectral functions at small τ, one arrives at implausible values of z, which drift towards the result at finite spatial momentum upon approaching the critical point at $\tau = 0$. This is due to the fact that, as can be seen in Fig. 4.17, the universal scaling function $f_\tau^\pm$ deviates from the asymptotic power law for intermediate x, but converges to it for large x. We take the convergence of $f_\tau^\pm$ for large x to the same power law that describes $f_p(x, 0)$ for $x \gtrsim 1$ as an indicator that this power law describes the true asymptotic behavior of the universal scaling functions. Nevertheless, since f_p converges much earlier, we believe that the results for z from fits to the spectral function at $\tau = 0$ and small momentum p are much more reliable.

Models B and D

Results from Breit-Wigner fits of the critical spectral function in Models B and D are suggestive of scaling behavior as well. We therefore apply the dynamic scaling hypothesis to the data for diffusive dynamics, in order to extract underlying universal scaling functions.

In order to identify scaling behavior in our classical-statistical simulations, we present results for the spectral function at the critical point in a rescaled manner in Figs. 4.20 and 4.21. Regions of overlapping data reveal an underlying scaling function $f_\omega(x_\omega, 0)$ resp. $f_p(x_p, 0)$. One observes an excellent scaling collapse of the data obtained with finite coupling to the heat bath $\gamma = 0.1$ (Model B), in both 2+1D and 3+1D. For illustration purposes, we use the analytic value for the dynamic critical exponent $z_B = 4 - \eta$ if not stated otherwise. Conversely, for vanishing heat

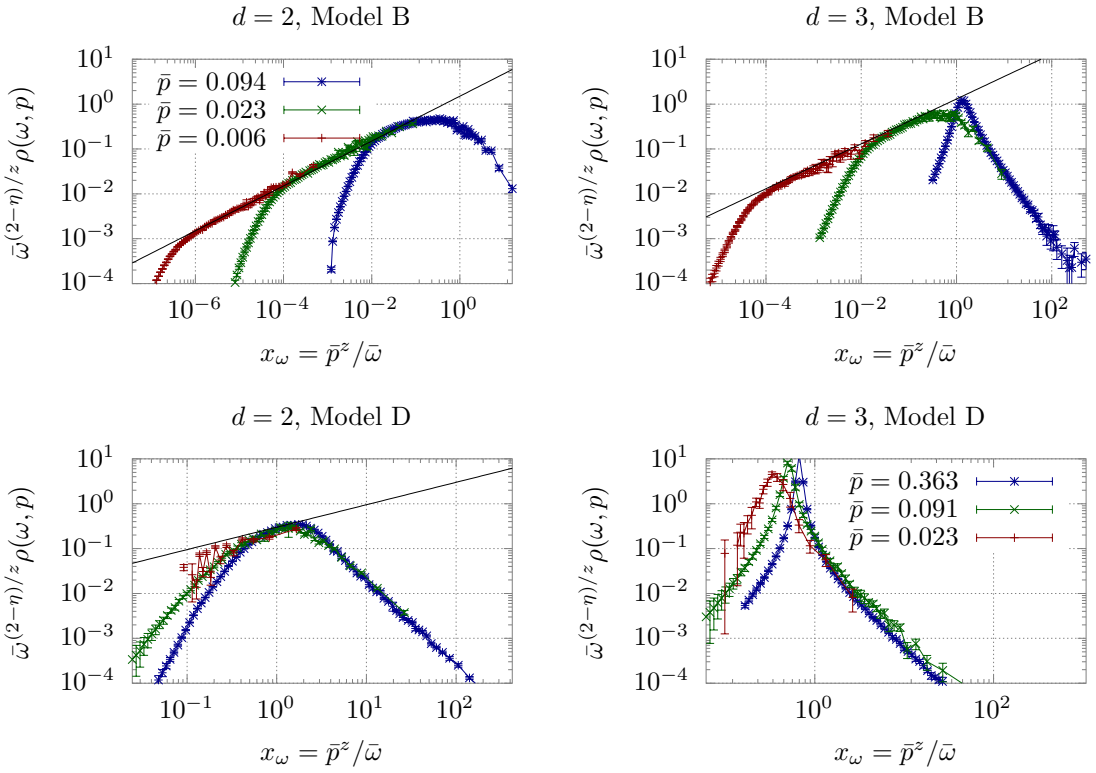

Figure 4.20: Scaling function $f_\omega(x_\omega, 0)$ of the critical spectral function. Due to availability of data, we use $\tau = 0.0009(2)$ ($d = 2$) resp. $\tau = 0.00008(5)$ (d=3) as a proxy for the critical temperature. The data was obtained on lattices of volumes 1024^2 respectively 256^3. The power law emerging for $\gamma = 0.1$ towards $x_\omega \to 0$ indicates the limiting behavior of the scaling function, which vanishes towards zero in a regular fashion as $\lim_{x_\mu \to 0} f_\omega(x_\omega, 0) \sim x^{0.5}$, which is shown as a black line. Even though there is hardly any overlap visible for $\gamma = 0$, one can suspect that the scaling function would start to follow $f_\omega \sim x_\omega^{0.5}$ as well for small enough spatial momentum p.

bath coupling $\gamma = 0$ (Model D), the range of spatial momenta where we observe critical scaling is much narrower, and we can only just recognize the onset of critical scaling behavior at minuscule spatial momentum in 2+1D. For 3+1D, critical scaling behavior is not observed at the momentum scales accessible in feasible lattice volumes. Guided by our results for the autocorrelation times $\xi_t(p)$ (see Section 4.3.3), we use the dynamic critical exponent of Model C $z_C = 2 + \alpha/\nu$, and find that it yields a reasonably good scaling collapse of the data.

Since for a conserved order parameter, the dynamics at vanishing spatial momenta are trivial and the spectral function vanishes identically $\rho(\omega, p = 0, \tau) \equiv 0$, we can only consider data at finite spatial momentum, precluding any dependence on the finite volume.

Upon close inspection of results given in Fig. 4.21, one notices that in contrast to Models A and C (compare Fig. 4.16), the deviations from the scaling function are not as distinctly marked. Rather, we find that the region of overlap in Model B is given by the range of frequencies $\omega < \Gamma$ smaller than the decay width. Only the high-frequency tails of the Breit-Wigner structures, where $\rho(\omega) \sim \omega^{-3}$ (see Eq. (4.36)) do not overlap after rescaling. Although by the given data it is hard to tell, at least the lower left panel of Fig. 4.21 suggests that this does not change in the limit of

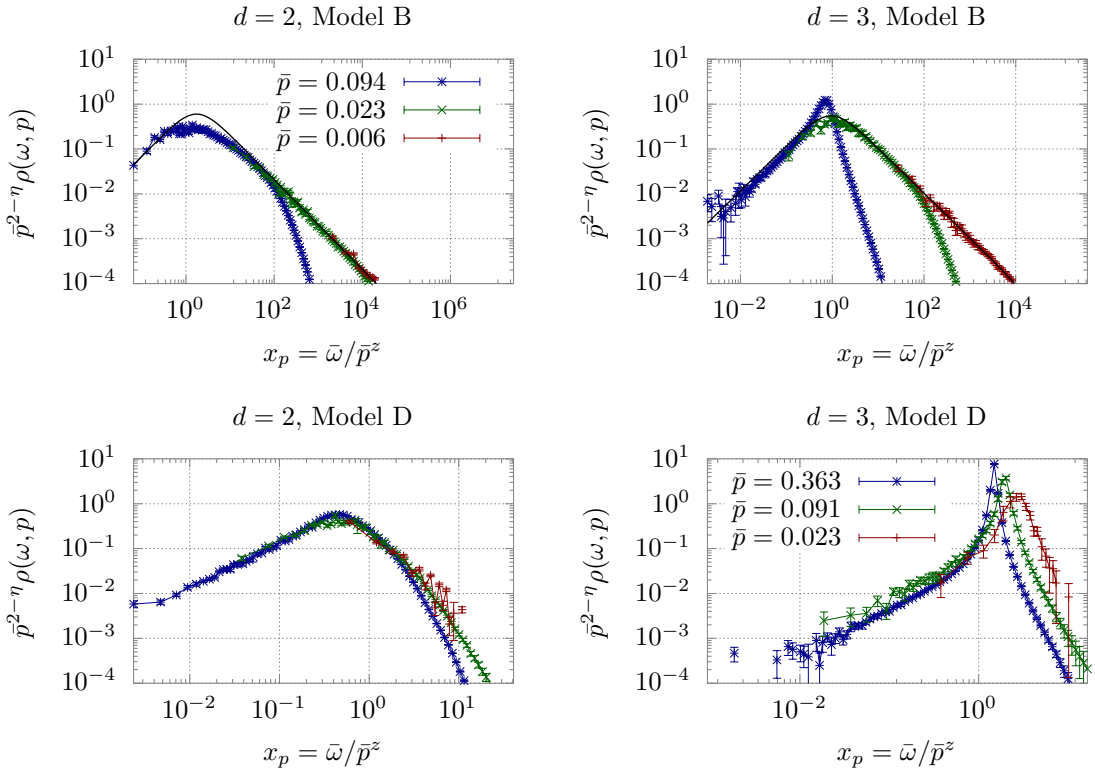

Figure 4.21: Scaling function $f_p(x_p, 0)$ of the critical spectral function. The data points are the same as in Fig. 4.20. Solid lines represent a fit to the Breit-Wigner function (4.41), with Γ and w_p^2 as free parameters. Except for some small region around the peak, the scaling function of Model B ($\gamma = 0.1$) of the spectral function is perfectly described by a Breit-Wigner shape with large decay width $\Gamma \gg \omega_p$. Comparing with the limits of the Breit-Wigner function, we can read off the limiting behavior of the scaling function $f_p(x_p, 0)$ for both small ($f_p(x_p, 0) \sim x_p$) and large ($f_p(x_p, 0) \sim 1/x_p$) values of the argument. At $\gamma = 0$ (Model D), there is hardly any universal scaling behavior visible for $d = 3$, whereas for $d = 2$ one can vaguely discern a region of overlapping data points right of the peak. To observe scaling behavior in 3+1D at $\gamma = 0$, one would need to simulate on much larger lattices.

$\gamma \to 0$ (Model D), even though the dynamic critical exponent changes dramatically.

Exploiting the scaling behavior to extract the dynamic critical exponent z, we repeat the process outlined for Models A and C and minimize the L^2-norms of pairwise distances of rescaled functions given by the quantity $\Delta^2(z)$ in Eq. (4.63). We find similar problems as before, insofar as the results tend to depend on the upper limit ω_h of the considered frequency interval. Again applying the principle of least sensitivity, we estimate reasonable values for ω_h, which lead to the results for the dynamic critical exponent z given in Table 4.7 in the row labeled *scaling*. Especially in the limit of vanishing Langevin damping $\gamma \to 0$ (Model D), where the regions of overlap are very narrow, this procedure essentially amounts to a visual estimate.

We now turn to the asymptotic behavior of the scaling functions. For dissipative dynamics (Models A and C), we found the scaling function of frequencies $f_\omega(0, 0) > 0$ to be regular at the origin. This must change when the order parameter is conserved, since in the limit of vanishing spatial momentum $p \to 0$ the spectral function must always go to zero, and thus its scaling function $f_\omega(0, 0) \stackrel{!}{=} 0$ must vanish as well.

It seems natural to expect the limiting behavior of the scaling function to be of algebraic form, i.e.

$$\lim_{x\to 0} f_\omega(x_\omega, 0) \sim x^\sigma, \tag{4.79}$$

with some positive exponent $\sigma > 0$. This of course via Eq. (4.59) relates directly to the large-x_p behavior of the scaling function $f_p(x, 0)$, for which then holds

$$\lim_{x_p\to\infty} f_p(x_p, 0) \sim x_p^{-(2-\eta)/z-\sigma}, \tag{4.80}$$

fixing the asymptotic high-frequency ($\omega \gg 1/\xi_t(p)$) behavior of the critical scaling function $f_p(x_p, 0)$. Furthermore, this implies for the ultraviolet behavior of the critical spectral function

$$\rho(\bar{\omega}, \bar{p}, 0) \sim \bar{\omega}^{-(2-\eta)/z}(\bar{p}^z/\omega)^\sigma = \bar{\omega}^{-(2-\eta)/z-\sigma}\bar{p}^{\sigma z}. \tag{4.81}$$

Studying Fig. 4.20 we find that the small-x behavior of the scaling function is given by a power law

$$f_\omega(x_\omega, 0) \sim x_\omega^\sigma,\ \sigma = 0.50(3) \tag{4.82}$$

in case of Model B, which is compatible with our considerations above. Unfortunately, the scaling region in Model D is too small to reliably extract the exponent σ in that case.

In Fig. 4.21, we show the rescaled critical spectral functions revealing the scaling function $f_p(x_p, 0)$. Also shown as solid lines are fits of the scaling function to a Breit-Wigner shape, which describes the data for Model B surprisingly well over a wide range of values of x_p. Indeed, only in a small region around the peak in 2+1D are there significant deviations, while the limiting behavior seems to match exactly. For Model B, the large-x_p limit of the scaling function $f_p(x_p, 0)$ seems to correspond to the limit of large decay width Γ of (4.41), where the Breit-Wigner function is proportional to the inverse frequency ω^{-1}, particularly

$$\lim_{\Gamma\to\infty} p^{2-\eta}\rho_B(\omega, p) = \frac{p^{4-\eta}}{\Gamma\omega} \quad \Rightarrow \quad \lim_{x_p\to\infty} f_p(x_p, 0) = \frac{1}{\Gamma x_p}, \tag{4.83}$$

where we use that in this case the dynamic critical exponent is given by $z = 4 - \eta$. By virtue of Eq. (4.59), we thus find for the small-x_ω limit of $f_\omega(x_\omega)$

$$\lim_{x_\omega\to 0} f_\omega(x_\omega, 0) \propto x_\omega^{\left(1-\frac{2-\eta}{z}\right)}. \tag{4.84}$$

Comparing Eq. (4.84) to Eq. (4.82), we find both observations compatible within the estimated error range, since

$$0.5 \approx \sigma = 1 - \frac{2-\eta}{4-\eta} = \begin{cases} \frac{8}{15} \approx .53 & d = 2, \\ 0.5046 & d = 3. \end{cases} \tag{4.85}$$

Re-inserting this result to obtain the ultraviolet behavior of the singular contribution to the critical spectral function (4.81), we find that it is equal to the over-damped limit of the mean-field spectral function given in Eq. (4.40), namely

$$\rho(\bar{\omega}, \bar{p}, \tau = 0) \sim \bar{p}^2/\bar{\omega}. \tag{4.86}$$

Note however that the true ultraviolet behavior is of course not given by critical contributions, and the large-frequency limit of the critical spectral function is given by the high-frequency limit of the Breit-Wigner structure as $\rho(\omega, p, \tau = 0) \sim p^2/\omega^3$.

Unfortunately, our data does not allow to extend this analysis to the limit of vanishing heat-bath coupling $\gamma \to 0$ (Model D). While it looks as if Eq. (4.82) might still hold, we can not confidently claim that it describes the small-x_ω limit of the scaling function $f_\omega(x_\omega, 0)$ here.

Similar to our findings for Models A and C before, we deduce from the numeric results given in Fig. 4.21 that the leading low-frequency ($\omega \ll 1/\xi_t(p)$) behavior of the critical spectral function in Model B is well described by

$$\lim_{x_p \to 0} f_p(x_p, 0) = a_p x_p + \ldots, \tag{4.87}$$

corresponding to

$$\lim_{x_\omega \to \infty} f_\omega(x_\omega, 0) \to a_p x_\omega^{-(2-\eta)/z-1} \tag{4.88}$$

for the critical scaling function $f_\omega(x, 0)$. One can thus infer the asymptotic infrared behavior of the critical spectral function for frequencies $\omega \ll 1/\xi_t(p)$,

$$\lim_{p,\omega \to 0} \rho(\omega, p, 0) = a_p p^{-(2-\eta)-z} \omega. \tag{4.89}$$

We interpret this behavior as an effective IR cutoff introduced by any finite p on the correlation length $\xi \sim 1/p$, which is associated with a finite correlation time $\xi_t \sim \xi^z \sim p^{-z}$. One observes that Eq. (4.89) for $z = 4 - \eta$ perfectly corresponds to the low-frequency limit of the mean-field form given in Eq. (4.35).

4.3.3 Critical behavior of the auto-correlation time ξ_t

We continue by showing explicitly the existence of a singularity in the characteristic time scale of the systems. By use of Eq. (4.62) and setting $s = \bar{t}^{1/z}$, the spectral functions in the time domain satisfy the following scaling relation

$$\rho\,(t, p, \tau) = \bar{t}^{(2-\eta)/z-1}\, f_t\Big(\bar{p}^z \bar{t}, \tau\, \bar{t}^{\,1/\nu z}\Big). \tag{4.90}$$

where the presence of the scaling variables $\tau\, \bar{t}^{\,1/\nu z}$ and $\bar{p}^z\, \bar{t}$ explicitly show that there are temperature-dependent characteristic time scales $\xi_t(p, \tau = 0) \sim p^{-z}$ and $\xi_t(p = 0, \tau) \sim |\tau|^{-\nu z}$ associated with the auto-correlation time of the dominant slow mode. The argument can be made explicitly by defining the auto-correlation time by a ratio of integrals and then inserting the scaling (4.90), such that at the critical point one has

$$\xi_t(p, \tau = 0) = \frac{\int_0^\infty t\rho(t, \mathbf{p}, \tau = 0)\mathrm{d}t}{\int_0^\infty \rho(t, \mathbf{p}, \tau = 0)\mathrm{d}t} = \frac{\int_0^\infty t f_p(tp^z)\mathrm{d}t}{\int_0^\infty f_p(tp^z)\mathrm{d}t} = \frac{p^{-2z}\int_0^\infty u f_p(u)\mathrm{d}u}{p^{-z}\int_0^\infty f_p(u)\mathrm{d}u} \equiv f_t p^{-z}. \tag{4.91}$$

Analogously, one finds

$$\xi_t(p = 0, \tau) = f_t^{\pm} |\tau|^{-\nu z}, \quad U_{\xi,t} \equiv f_t^+ / f_t^-, \tag{4.92}$$

where we define as $U_{\xi,t}$ the ratio of power-law amplitudes f_t^+ above and f_t^- below the critical temperature, which is universal as well.

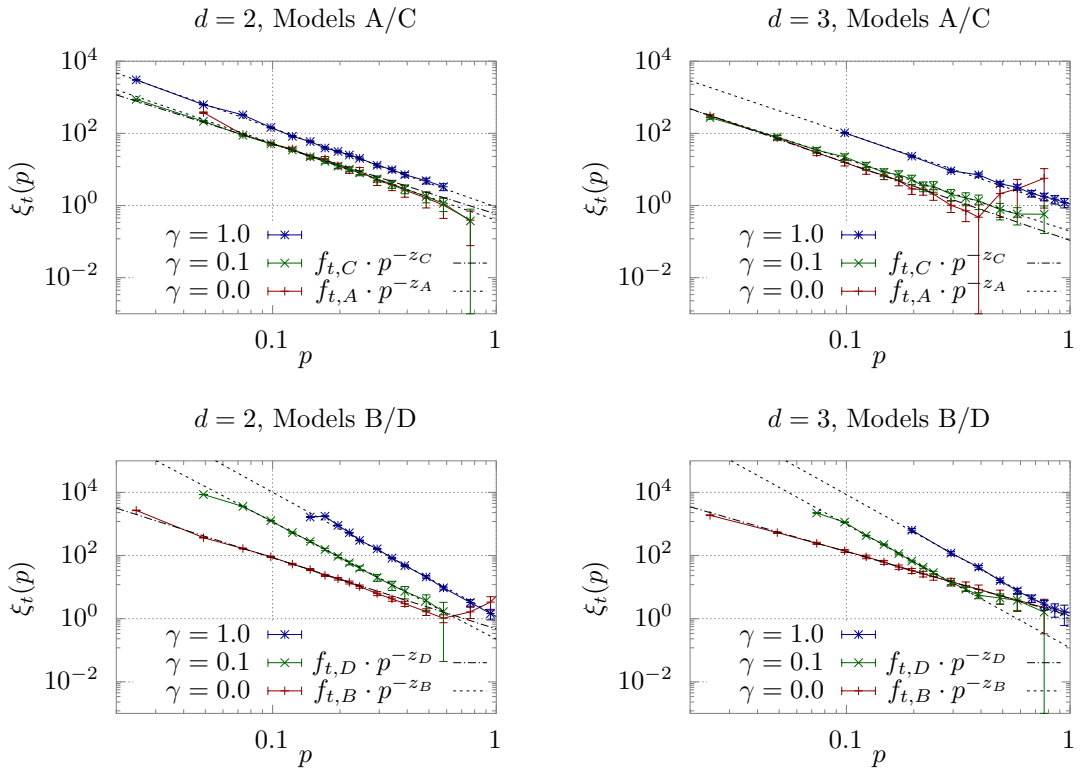

Figure 4.22: Correlation time ξ_t at $\tau = 0$ as a function of spatial momentum p at different values of the Langevin coupling γ. Dashed lines indicate power law fits to the data, the resulting amplitudes and exponents are shown in Table 4.5. Fit intervals were chosen to minimize χ^2/d.o.f. In Models A and C, the literature values for the dynamic critical exponents differ by less than ten percent, which is reflected in the results being very similar. We find that the heat-bath coupling γ has only a weak effect on the amplitude. For Models B and D, the exponents differ much more. The correlation times at vanishing heat-bath coupling γ appear to act as a lower bound on those at finite γ, and we find a strong dependence of the amplitude $f_t(\gamma)$ for $\gamma > 0$.

We start by exploring the divergence of $\xi_t(p, \tau = 0)$ at the critical temperature for finite spatial momentum. Since at least for diffusive dynamics (Models B/D), the spectral function largely still follows the Breit-Wigner shape, we expect the correlation time to be proportional to the ratio Γ/ω^2 in the region of low momentum p (see appendix C for a sketch of the derivation). Based on our findings illustrated in Fig. 4.13 we thus expect to find that the correlation times strongly depend on the Langevin coupling γ. For low spatial momentum, where the decay width Γ is bounded from below by γ, we expect $\xi_t \sim \omega_p^{-2} \sim p^{-4+\eta}$ with an amplitude dependent on γ, which at some point should merge into another power law with a different exponent, as soon as the momentum dependence of the decay width becomes relevant. For vanishing heat-bath coupling $\gamma \to 0$, the autocorrelation times $\xi_t(p)$ are expected to all follow this second power law.

The critical spectral functions for the models A and C do not follow a Breit-Wigner shape, precluding attempts to infer expectations about the behavior of ξ_t in the way as described above. However, since their critical exponents are very close to each other, it may represent a challenge to determine them accurately from the data.

Results for the correlation times obtained from the measured spectral functions

Models:		A	B	C	D
2D	z	2.130(28)	3.716(17)	1.95(8)	2.25(3)
	f_t	0.391(20)	0.223(9)	0.58(10)	0.47(4)
3D	z	1.99(7)	3.91(6)	2.148(28)	2.031(23)
	f_t	0.195(25)	0.119(13)	0.108(10)	1.24(7)

Table 4.5: Amplitudes and exponents obtained from fits to the data in Fig. 4.22, with the data for Models A and B obtained for $\gamma = 0.1$. Errors given here are statistical uncertainties only and generally underestimate the true uncertainties slightly. For Models A and C, the values are close to the expected ones, although lacking in precision. While the exponent of the data at large γ coincides well with the expected dynamic critical exponent in Model B of $z = 4 - \eta$, the data at lower γ seems to converge to a different power law with much smaller exponent, closer to that of Model C, where $z_C = 2 + \alpha/\nu$. Amplitudes are generally smaller in 3+1D.

are illustrated in Fig. 4.22, where we find our conjecture outlined above confirmed. Generally, the data closely follows the expected power-law behavior. It is hard to discriminate between Models A and C, since the exponents of the power laws describing the divergence of the correlation times are very close, and we find a weak dependence of the amplitude of the power law on the Langevin parameter γ.

For diffusive dynamics, i.e. Models B and D, the correlation times $\xi_t(p)$ show the expected behavior in both 2+1 and 3+1 dimensions. For large heat-bath coupling $\gamma = 1$, the results are clearly described by a power law $\xi_t(p) \sim p^{-z_B}$ with the dynamic critical exponent of Model B $z_B = 4 - \eta$. The amplitude of this power law depends on the magnitude of the heat-bath coupling γ. For intermediate values of order $\gamma = 0.1$, the correlation times still follow the power law $\xi_t(p) \sim p^{-z_B}$ at low spatial momentum, but merge into a power law with much smaller exponent at higher momentum p. At vanishing Langevin coupling $\gamma = 0$, there is only the second power law left. Generally, amplitudes are smaller in 3+1D, with the most pronounced difference for $\gamma = 0$, i.e. Models C and D.

We extract the dynamic critical exponent from numerical data via a χ^2-fit to a power law of the form $f_t p^{-z}$. Results for the exponents and amplitudes are given in Table 4.5. While the exponents for finite heat-bath coupling $\gamma > 0$ confirm the prediction by Model B, namely $z_B = 4-\eta$, the exponents at vanishing $\gamma = 0$ are much smaller, and generally more compatible with the Model-C exponent $z_C = 2 + \alpha/\nu$, albeit slightly higher.

We continue with the analysis of the correlation time $\xi_t(p = 0)$ at vanishing spatial momentum, but finite distance $|\tau| > 0$ to the critical point. For Models B and D, the zero-momentum mode of the spectral function $\rho(t, p = 0, \tau) \equiv 0$ vanishes identically. Thus, the following analysis is naturally limited to Models A and C.

We found in Fig. 4.19 that the spectral function near criticality at times larger than the characteristic correlation time $(t/\xi_t(\tau) > 1)$ is well described by a product of a power law and an exponential,

$$\tilde{f}^+_\tau(\tau^{\nu z}\bar{t}, 0) = (\tau\,\bar{t}^{\,1/\nu z})^{\nu(2-\eta-z)}\, f_t\left(0, \tau\,\bar{t}^{\,1/\nu z}\right) \propto \bar{t}^{\,(2-\eta)/z-1} \exp\left(-t/\xi_t(\tau)\right). \quad (4.93)$$

This is used to extract the correlation time ξ_t by fitting the spectral function data with an ansatz of the above form, yielding additional data points to those obtained by the integration method.

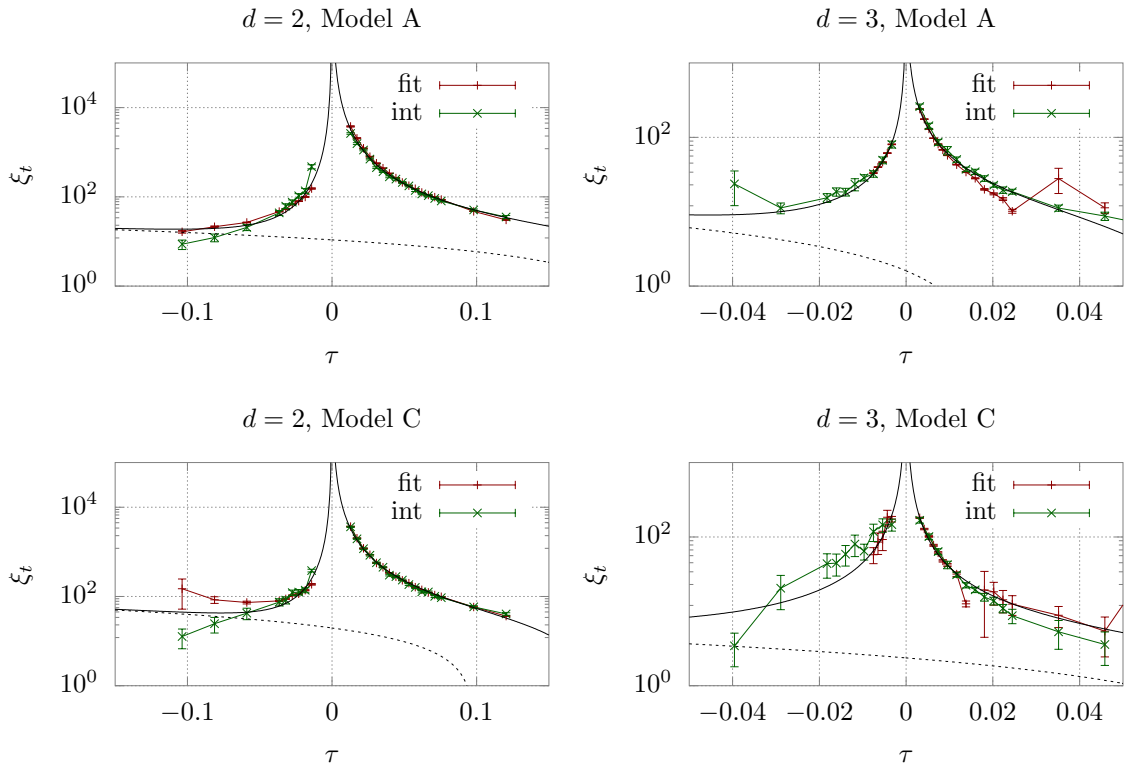

Figure 4.23: Behavior of the correlation time $\xi_t(\tau)$ extracted from fits and integration of the spectral function, as a function of reduced temperature τ. Note that in order to minimize finite volume effects, we only include results for $|\tau|L^{1/\nu} > 2.5$ for $d = 2$, and $|\tau|L^{1/\nu} > 5$ for $d = 3$ obtained on 256^2 and 128^3 lattices. Solid black lines show a fit according to Eq. (4.96); the regular contribution is shown separately as a black dashed line.

Before we present our results, some further remarks are in order. Since we focus on the behavior of modes with vanishing spatial momentum $p = 0$, their auto-correlation time $\xi_t(\tau)$ diverges at the critical point as $\xi_t(\tau) \sim 1/|\tau|^{\nu z}$ in an infinite system. However, in our simulations the divergence of the auto-correlation time is limited by the finite system size L, which in the immediate vicinity of the critical point $\tau \approx 0$ becomes the relevant infrared cut-off. Based on the dynamical finite-size scaling hypothesis, one expects that in this regime the auto-correlation time behaves as

$$\xi_t(\tau, L) = L^z g_\xi(\tau L^{1/\nu}), \tag{4.94}$$

where $g_\xi(x)$ is the finite-size scaling function of the auto-correlation time analogous to the ratio $R = \xi/L$ used for static finite-size scaling. While for all finite values of the finite-size scaling variable $x = \tau L^{1/\nu}$ the divergence of the auto-correlation time is effectively regulated by the finite volume, in order to recover the infinite-volume scaling in Eq. (4.92), one needs asymptotically large values of $\pm x$, where this finite-size scaling function satisfies

$$g_\xi(x \to \pm\infty) \to f_t^\pm |x|^{-\nu z}. \tag{4.95}$$

We present our results for the auto-correlation time in Figs. 4.23 and 4.24, where we study the dependence of $\xi_t(\tau, L)L^{-z}$ as a function of the finite-size scaling variable $\tau L^{1/\nu}$ in Fig. 4.24 and subsequently estimate the magnitude of singular and regular

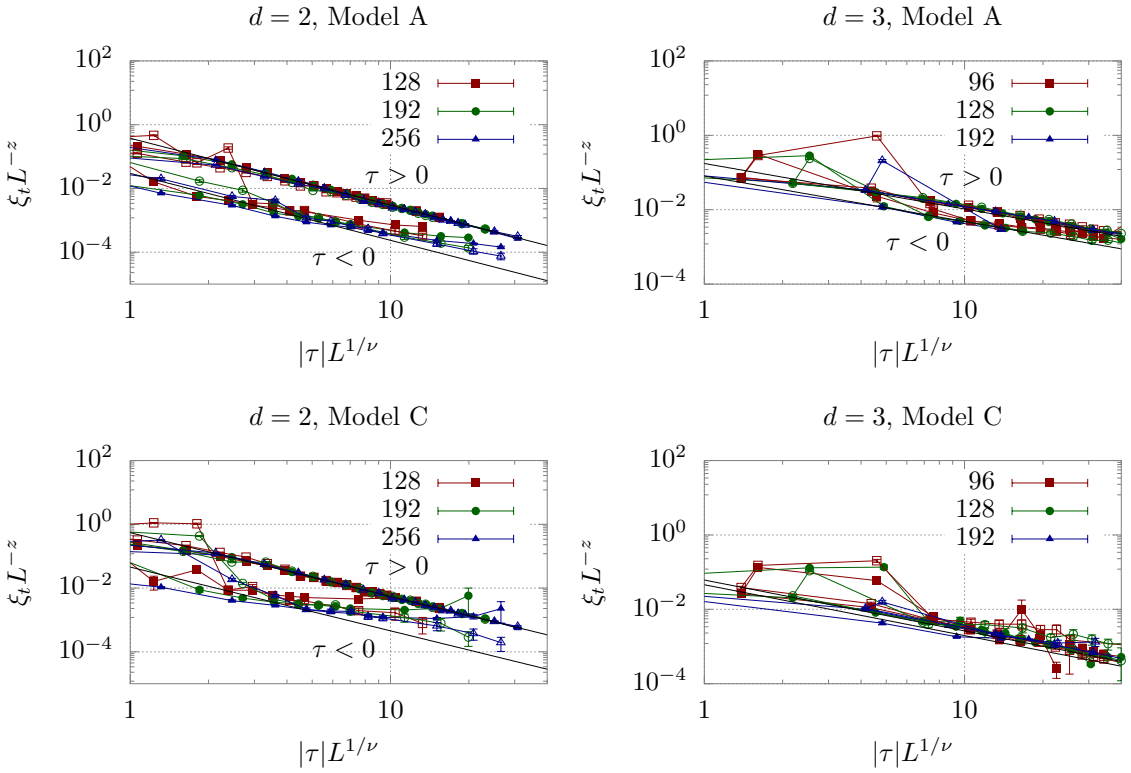

Figure 4.24: Behavior of the auto-correlation time as a function of the finite-size scaling variable $|\tau|L^{1/\nu}$. Different symbols correspond to extractions of the correlation time using fits (filled symbols) and integration (open symbols) of the spectral function; upper curves in each panel correspond to $\xi_t(\tau > 0)$, while lower curves correspond to $\xi_t(\tau < 0)$. Solid lines in each panel correspond to a power law fit according to Eq. (4.95), from which we extract the dynamic critical exponent z along with the non-universal amplitudes $f_t^{\pm}$.

contributions to the correlation length $\xi_t(\tau)$ in Fig. 4.24. Generally, the results of the two different extraction methods (fit and integration) agree very well with each other, although for $\tau < 0$ the integrated ξ_t are somewhat closer to the power law, and the slope of this power law fit produces slightly smaller results for z in Model A. Strikingly, one also observes from Fig. 4.24 that the data exhibits a clear finite-size scaling across different lattice sizes, which we can exploit to extract the dynamic critical exponent as explained in the following.

In order to obtain the dynamic critical exponent z, we first apply finite-size scaling with a plausible estimate for z, to find a region where the data for different lattice sizes shows sufficient overlap. Based on the results depicted in Fig. 4.24 it becomes obvious that this hardly works at $\tau < 0$, but gives a clear power law at large values of $\tau L^{1/\nu}$, for $\tau > 0$. We then fit the power law in Eq. (4.95) for $\tau > 0$ to the un-scaled data in the selected region, to get both the amplitude f_t^+ and the exponent νz. Subsequently, we estimate the amplitude ratio $U_{\xi,t}$ as far as possible by fitting a power law with the exponent obtained earlier to a few data points with $\tau < 0$. Errors are obtained in a similar way as for the power law fit of the IR divergence of the spectral function. By varying the temperature interval where we fit the power law to the correlations times $\xi_t(\tau)$ and keeping two-thirds of the results with the lowest χ^2/d.o.f. as well as eliminating outliers with $\chi^2 > 2\chi^2_{\text{min}}$, we compute the averages weighted by statistical uncertainties and estimate the confidence interval by taking

Table 4.6: Non-universal amplitude f_t^+ and universal amplitude ratio $U_{\xi,t}$ of the correlation time ξ_t, obtained by fits of the data to Eq. (4.92), shown in Fig. 4.24. Since the extraction of the amplitudes is strongly correlated with the extraction of the exponent, the uncertainties are rather large.

	2D		3D	
	Model A	Model C	Model A	Model C
f_t^+	$0.43^{+0.10}_{-0.04}$	$0.54^{+0.07}_{-0.11}$	$0.08^{+0.11}_{-0.04}$	0.028(6)
$U_{\xi,t}$	$8.2^{+4.2}_{-0.9}$	9.0(2.7)	$2.7^{+0.6}_{-0.3}$	$1.2^{+0.5}_{-0.2}$

the highest and lowest values for ξ_t, f_t^+ and U_{ξ_t}. We remark that these parameters are strongly correlated, so a large uncertainty in the dynamic critical exponent z leads to large uncertainties in both f_t^+ and U_{ξ_t}.

The results of this procedure for the non-universal amplitude f_t^+ and the ratio $U_{\xi,t}$ are given in Table 4.6. Those for the dynamic critical exponent z are shown in the row denoted by "ξ_t power law" of Table 4.7. Especially the two large amplitude ratios $U_{\xi,t}$ in $d = 2$ seem quite remarkable when compared to the analytically known amplitude ratio of the spatial correlation length $U_\xi = 2$ [86]. Although the $d = 2$ data for ξ_t below the critical temperature ($\tau < 0$) does not necessarily justify a power law fit all that well, by looking at Fig. 4.24 one is led to conclude that we might rather underestimate this ratio.

While in Fig. 4.24 the data at least in 2+1D perfectly fits a power law above the critical temperature $\tau > 0$, we find that a precise extraction of z remains difficult with the available data. In order to improve the accuracy, one could generate data closer to $\tau \gtrsim 0$ in large volumes to minimize finite-size effects. Below the transition temperature in both 2+1D and 3+1D, we find that the data for the correlation time ξ_t deviates strongly from the expected power law behavior. One reason for this is the (much) smaller value of the non-universal amplitudes f_t^-, which in combination with relatively large regular contributions leads to a suppression of the critical signal. We try to capture the regular contributions by fitting a regular function up to linear order in addition to the power law

$$\xi_t(\tau) = f_t^{\pm}|\tau|^{-\nu z} + f_{r,0} + f_{r,1} \cdot \tau \tag{4.96}$$

The comparison between the resulting fit and the data is shown in Fig. 4.23. The fit now also describes the data away from $\tau = 0$ much better, which is dominated by the regular part, shown in Fig. 4.23 as a dashed line, especially on the low temperature side. However, by introducing these additional degrees of freedom in the fit, we lose precision in the estimate of the dynamic critical exponent z, both in terms of statistical and systematic uncertainties.

Besides providing an alternative means to extract z, one additional advantage of the auto-correlation time method is that it allows for a direct comparison of the critical dynamics of different models. In particular, to estimate the *difference* between the dynamic critical exponents z of Models A and C, one can look at the ratio of the correlation times at the same (reduced) temperature, which satisfy

$$\frac{\xi_{t,A}(\tau)}{\xi_{t,C}(\tau)} \overset{\tau \gtrsim 0}{=} \frac{f_{t,A}^+}{f_{t,C}^+} \cdot \tau^{-\nu(z_A - z_C)} \tag{4.97}$$

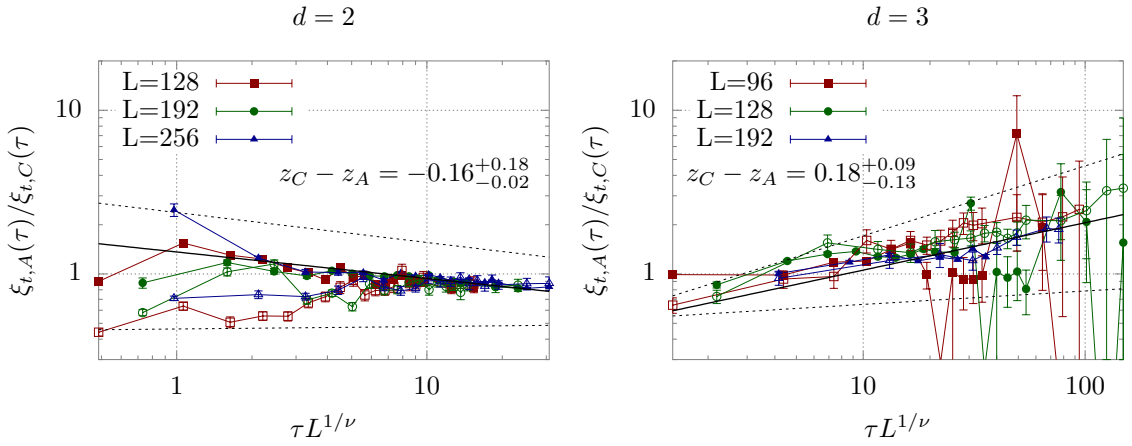

Figure 4.25: Dependence of the ratio of auto-correlation times in Models A and C, on the finite size scaling variable $\tau L^{1/\nu}$. Solid lines in the left and right panels show a power law fit of the large $\tau L^{1/\nu}$ behavior, from which we extract the difference $\nu(z_C - z_A)$ of the dynamic critical exponents (cf. Eq. (4.97)). Dashed lines indicate the confidence interval of the extraction of $\nu(z_C - z_A)$, which is also presented in the figure.

in the infinite volume limit. Such a direct comparison between Models A and C is presented in Figure 4.25, where we show the ratio of the correlation lengths in Eq. (4.97) for the symmetric phase ($\tau > 0$) as a function of the finite-size scaling variable $\tau L^{1/\nu}$. Even though this ratio reveals some tension between the two different extraction methods (exponential fit and integration), the general trends are clearly visible, where in $d = 2$ dimensions, $z_C > z_A$, and the power law at large $\tau L^{1/\nu}$ slopes downwards; while in $d = 3$ dimensions, the difference changes sign $z_C < z_A$ and the slope of the power law is positive. By performing a power law fit to the ratio, we can obtain a direct estimate of $z_C - z_A$, which is also indicated in Figure 4.25, with the quoted errors obtained in the same way as for the power law fit of the correlation times.

So far we have only considered the critical behavior of the spectral function in absence of explicit symmetry breaking ($J = 0$). When introducing a non-zero explicit symmetry breaking ($J \neq 0$), the magnetic scaling hypothesis states that the singular part of the free energy density can be written as

$$f_{\text{sing}}(\tau, \bar{J}) = s^{-d} f_s(s^{1/\nu}\tau, s^{\beta\delta/\nu}\bar{J}) \tag{4.98}$$

allowing one to express the singular behavior of the free energy in terms of scaling functions $\hat{f}_\pm$, f_J (note that $\nu d = 2 - \alpha$)

$$f_{\text{sing}}\left(\tau, \bar{J}\right) = |\tau|^{2-\alpha} \hat{f}_\pm\left(\bar{J}/|\tau|^{\beta\delta}\right), \tag{4.99}$$

$$f_{\text{sing}}\left(\tau, \bar{J}\right) = |\bar{J}|^{(2-\alpha)/\beta\delta} \hat{f}_J\left(\tau/|\bar{J}|^{1/\beta\delta}\right), \tag{4.100}$$

which depend on a single variable $\tau/|\bar{J}|^{1/\beta\delta}$ that combines the τ and $\bar{J}$ dependence. Similarly, one expects an analogous magnetic scaling behavior for unequal-time correlation functions, such that e.g. the auto-correlation time ξ_t is expected to obey the scaling form

$$\xi_t(\tau, \bar{J}) = s^z \xi_t(s^{1/\nu}\tau, s^{\beta\delta/\nu}\bar{J}), \tag{4.101}$$

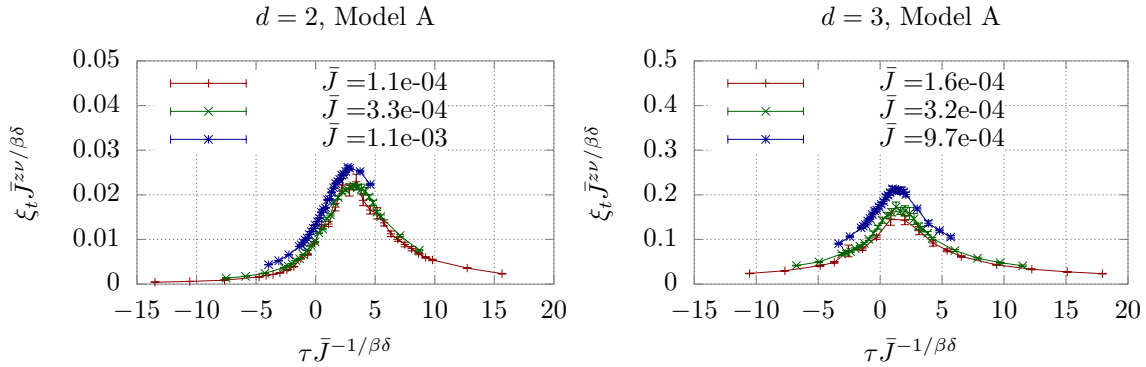

Figure 4.26: Magnetic scaling of the correlation time $\xi_t(\tau, J)$. Overlapping data points correspond to the universal magnetic scaling function of the auto-correlation times $\hat{\xi}_{t,J}(\tau/|\bar{J}|^{1/\beta\delta})$ (cf. Eq. (4.101)). Scaling breaks down when $\bar{J}$ becomes too large, as indicated by the blue data points.

Table 4.7: Extracted values for the dynamic critical exponent z for dissipative dynamics (Models A and C).

	2D		3D	
dissipative z	Model A	Model C	Model A	Model C
scaling	2.03(9)	2.00(8)	1.83(17)	2.13(16)
IR power law	2.24(8)	$1.98^{+0.12}_{-0.21}$	$1.88^{+0.10}_{-0.27}$	$2.47^{+0.10}_{-0.25}$
ξ_t power law	$2.03^{+0.05}_{-0.08}$	$2.00^{+0.07}_{-0.04}$	$2.17^{+0.31}_{-0.18}$	$2.48^{+0.10}_{-0.07}$
combined	2.10(4)	2.00(5)	1.92(11)	2.41(7)
diffusive z	Model B	Model D	Model B	Model D
scaling	3.70(15)	2.2(1)	3.9(2)	2.25(9)
ξ_t power law	3.68(15)	2.09(6)	4.01(8)	2.29(14)
combined	3.69(11)	2.12(5)	3.99(7)	2.26(8)

which by analogy allows to define the magnetic scaling function

$$\xi_t(\tau, \bar{J}) = |\bar{J}|^{-z\nu/\beta\delta} \hat{\xi}_{t,J}(\tau/|\bar{J}|^{1/\beta\delta}). \tag{4.102}$$

We investigate this behavior in Fig. 4.26, where the auto-correlation time $\xi_t(\tau, \bar{J})$ obtained by integration for different values of $\bar{J}$ is rescaled to recover the underlying magnetic scaling function $\hat{\xi}_{t,J}$ as a function of $\tau/|\bar{J}|^{1/\beta\delta}$. Data points for the two smaller values of $\bar{J}$ largely overlap confirming the magnetic scaling of the auto-correlation time. Even though the magnetic scaling starts to break down for the larger $\bar{J}$, as one departs from the critical region, it is clear that in a certain (model dependent) range of $\bar{J}$ and τ, one can extrapolate $\xi_t(J, \tau)$ from the overlap region in Fig. 4.26.

We provide a summary of our results for the dynamic critical exponent z for the different Models in Table 4.7, where we give the results from the different extraction methods, alongside an error-weighted combined average. The table is split to be able to better compare the closely related models with the same equations of motion. For Model A in 2+1D, the overlap method and the power law fit to the correlation times ξ_t give a surprisingly small result for z with a relatively large error. The power law

fit to the infrared divergence of the spectral function yields a result closer to the one of [14], albeit even a bit larger. Combining the results leads to a z that is closer to, but still smaller than the result of [14]. Incidentally, our combined result for Model A in 2+1D is fully consistent with the experimentally measured value of $z = 2.09(6)$ from Ref. [92]. For Model C in 2+1D, we find a value that closely matches the analytic result $z = 2$, with all methods agreeing within their respective statistical errors. In 3+1D, the non-critical effects on the spectral function are strong, leading to very large uncertainties in the power law fits. Since the critical window is smaller than in 2+1D, the uncertainty of the overlap method increases as well. Nevertheless, the combined results in 3+1D for both Model A and Model C are compatible with earlier studies, and with the value predicted from the scaling relation $z = 2 + \alpha/\nu$ for Model C.

In case of Model B, we find that in both 2+1D and 3+1D our results are compatible with the scaling relation $z = 4 - \eta$. Especially at large heat-bath coupling γ, the power law fit to the correlation time ξ_t at finite spatial momentum yields relatively precise results. In the limit of vanishing heat-bath coupling (Model D), we find that the dynamic critical exponent changes drastically. We find results for z of the order of 2, just marginally larger than what one would expect for Model C.

We note that, in order to obtain more precise results e.g. for Models A and C in 3+1D, it would be highly beneficial to consider an improved action and/or larger volumes at temperatures closer to the critical point. For Model A, it may also be beneficial to redo the study for significantly larger heat-bath couplings γ. In 2+1D with larger volumes, one could probe smaller spatial momenta at $\tau = 0$ and increase the precision of the IR power law method. When considering 3+1D, our results in Fig. 4.17 compared to those in Fig. 4.16 clearly indicate that, with our present setup, we were not able to probe low-enough momentum regimes away from the critical temperature. In both cases we are limited by small critical amplitudes of the correlation time ξ_t, especially below the critical temperature at $\tau < 0$.

While our results for Model B leave little to be desired, the critical behavior of Model D needs to be probed at much lower spatial momentum, i.e. simulated on much larger lattices.

4.4 Conclusions

We used the classical field approximation close to a second order phase transition to perform a first-principles calculation of the order-parameter spectral functions of the relativistic Z_2 model. We employed two different sets of dynamic equations, such that we were able to study the model with and without conservation of either energy or the order parameter. By including finite spatial momenta in our analysis, we were able to provide a comprehensive overview of the behavior of the spectral function in all distinct parts of the phase diagram at finite temperature.

We found that generally, the spectral functions of the model with conserved order parameter are well described by a Breit-Wigner shape with a mean-field-like dispersion relation and momentum-dependent decay rate bounded from below by the heat-bath coupling. For dissipative dynamics, when the Z_2 symmetry is spontaneously broken below the critical temperature, we find an additional excitation at low frequencies with a different spectral shape and dispersion indicative of a soft collective mode. At all temperatures, we observed a Breit-Wigner quasi-particle

excitation with relativistic dispersion relation and only weakly momentum-dependent decay rate. The effective masses for both dynamical models generally match. While the effective mass at sufficiently large spatial momenta behaves continuously across the transition, we found clear indications for singular behavior and an IR divergence at the critical point. For the diffusive dynamics, this change is solely mitigated by the vanishing effective mass and therefore mononomial dispersion relation. In case of dissipative dynamics, the second low-frequency mode is the one that transforms into the dominant IR contribution. Since our results have been obtained from first-principles numerical studies in the classical-statistical limit, it may be insightful to compare these results quantitatively to others obtained e.g. by the use of functional methods on the Keldysh contour.

We explicitly verified the dynamic scaling hypothesis by analyzing spectral functions at criticality, and performed a detailed analysis of the scaling properties as a function of frequency, momentum, and (in case of dissipative dynamics) reduced temperature. From those, we extracted the correlation time ξ_t, analyzed its divergence close to the critical point, and demonstrated its finite-size and magnetic scaling properties.

Modifying the classical equations of motion to couple to a heat bath and/or conserve the order parameter, we were able to simultaneously study the behavior in multiple dynamic universality classes. We found the impact of the heat-bath coupling on the shape of spectral functions for Models A and C rather minor, with a hardly measurable change in the dynamic critical exponent. For diffusive dynamics, the changes were much more drastic, since the structure of low-frequency excitations changes as the heat-bath coupling vanishes, leading to a stark change in the dynamic critical exponent.

We successfully extracted the universal scaling functions, which describe the infrared properties of the spectral functions, and carefully assessed the implications for the behavior of spectral functions at small frequencies and momenta. Furthermore, we developed a complete parametrization of the scaling functions in the special cases where either spatial momentum or reduced temperature vanish. By virtue of magnetic scaling, we are further able to predict the dynamic critical properties of the systems in a certain radius around the critical point, which provides the baseline for studying possible signatures of criticality for non-equilibrium systems approaching the critical point in the phase diagram.

5 Energy-momentum tensor on the lattice

Since it became clear that the Quark-Gluon plasma (QGP) generated in heavy-ion collisions at RHIC or the LHC exhibits strong fluid-like collective behavior [100, 101, 102], relativistic hydrodynamic methods attracted tremendous interest outside their traditional applications in cosmology and astrophysics. Even though the theoretical foundations have existed for several decades [61, 62], there are many interesting developments in the direction of efficient numerical simulation methods, which may be able to describe the collective dynamics of quite diverse systems, ranging from fireballs of QGP to merging neutron stars.

When describing dynamic processes close to the QCD critical endpoint, the low-energy degrees of freedom match those of Model H in [13], the dynamic universality class describing the critical dynamics of binary fluids or gas-liquid transitions [15]. Therefore, we aim to lay the groundwork for a possible classical realization of a relativistic version of Model H, e.g. as a lattice field coupled to a fluid. There is of course a possible pitfall for such a hybrid lattice fluid model. The conservation of the energy-momentum tensor is one of the constituitive equations for any hydrodynamic description. It stems from a continuous translation symmetry in spacetime, which is reduced to a discrete symmetry on a lattice. It therefore seems natural for us to investigate the energy-momentum tensor $T^{\mu\nu}$ in our lattice models more closely, and understand how the reduction of translational symmetry affects its conservation. Furthermore, we aim to develop an understanding of how far a lattice theory can accurately reproduce hydrodynamic degrees of freedom and collective phenomena, as e.g. reflected in transport coefficients.

Additionally, a major difference between the dynamical Models A/B and their counterparts with vanishing heat-bath coupling, Models C/D, lies in the exact conservation of energy in the latter ones. We hope to be able to deepen our understanding of the difference in their low-energy degrees of freedom and critical behavior by studying the dynamic properties of the energy density.

We start by defining the energy-momentum tensor $T^{\mu\nu}$, which is non-trivial in the case of diffusive dynamics. Subsequently, we roughly estimate the effects of a finite lattice spacing on the conservation law $\partial_\mu T^{\mu\nu}$, and check the corresponding numerical results. Additionally, in light of recent studies calculating the shear viscosity using classical simulations of a scalar theory on the lattice [103, 104], we raise some concerns about the reliability of those studies regarding the breakdown scales of momentum conservation. Although we find that the method to obtain the shear viscosity via Kubo formulae is at least questionable, we reproduce the aforementioned studies and extend the analysis to our models defined in Section 2.2. We then proceed with a

detailed analysis of the autocorrelation and spectral functions of the energy density, studying its dynamic degrees of freedom at different points in the phase diagram. We finish with an analysis of its dynamic scaling behavior close to the second order phase transition.

5.1 Definition

We start by deriving the energy-momentum tensor of the continuum theories. Since the Lagrangian density of Model C with non-conserved order parameter (2.101) is a function only of ϕ and $\partial_\mu\phi$ and only implicitly depends on the spatial coordinate, we can explicitly calculate the tensor from the Lagrangian and its partial derivative w.r.t. to the field derivatives as

$$T_C^{\mu\nu} \equiv \frac{\partial \mathcal{L}}{\partial\left(\partial_\mu \phi\right)} \partial^\nu \phi - g^{\mu\nu}\mathcal{L}, \tag{5.1}$$

with the independent components

$$T_C^{00} = \frac{\partial \mathcal{L}}{\partial \dot{\phi}} \dot{\phi} - \mathcal{L} = \frac{1}{2}\left(\dot{\phi}^2 + (\nabla\phi)^2\right) + V(\phi) \equiv \epsilon, \tag{5.2}$$

$$T_C^{0i} = \frac{\partial \mathcal{L}}{\partial \dot{\phi}} \partial^i \phi = -\dot{\phi}\nabla_i\phi = T_C^{i0} \equiv \Pi^i, \tag{5.3}$$

$$T_C^{ii} = \frac{\partial \mathcal{L}}{\partial(\partial_i \phi)} \partial^i \phi + \mathcal{L} = (\nabla_i\phi)^2 + \frac{\dot{\phi}^2}{2} - \frac{1}{2}(\nabla\phi)^2 - V(\phi) \equiv P^i, \tag{5.4}$$

$$T_C^{ik} = \frac{\partial \mathcal{L}}{\partial(\partial_i \phi)} \partial^k \phi = (\nabla_i\phi)(\nabla_k\phi), \tag{5.5}$$

which we identify as the energy (ϵ), momentum (Π), pressure (P) and shear-stress density respectively. To compute the energy-momentum tensor from the lattice data, we discretize the expressions above in such a manner that three criteria are met:

1. T^{00} directly relates to the Hamiltonian density in Eq. (2.121),
2. the trace $T^\mu{}_\mu$ vanishes exactly for the scale-free case of $m^2 = 0$ in 3+1D, and
3. all elements are topologically on-site and symmetric.

These lead to the definitions

$$T_x^{00} = \frac{1}{2}\dot{\phi}_x^2 + \frac{1}{4}\sum_i \left[\left(\phi_{x+e_i} - \phi_x\right)^2 + \left(\phi_x - \phi_{x-e_i}\right)^2\right] + V(\phi_x), \tag{5.6}$$

$$T_x^{0i} = -\frac{1}{2}\dot{\phi}_x\left(\phi_{x+e_i} - \phi_{x-e_i}\right), \tag{5.7}$$

$$\begin{aligned} T_x^{ii} = &\frac{1}{2}\left[\left(\phi_{x+e_i} - \phi_x\right)^2 + \left(\phi_x - \phi_{x-e_i}\right)^2\right] \\ &+ \frac{\dot{\phi}_x^2}{2} - \frac{1}{4}\sum_i \left[\left(\phi_{x+e_i} - \phi_x\right)^2 + \left(\phi_x - \phi_{x-e_i}\right)^2\right] - V(\phi_x), \end{aligned} \tag{5.8}$$

$$T_x^{ik} = \frac{1}{4}(\phi_{x+e_i} - \phi_{x-e_i})(\phi_{x+e_k} - \phi_{x-e_k}). \tag{5.9}$$

In case of diffusive dynamics in Model D, the Lagrangian density (2.115) depends on the auxiliary field K as well. Therefore, it also shows up in the energy-momentum tensor, which reads

$$T_D^{\mu\nu} = \frac{\partial \mathcal{L}}{\partial\left(\partial_\mu \phi\right)} \partial^\nu \phi + \frac{\partial \mathcal{L}}{\partial(\partial_\mu K)} \partial^\nu K - g^{\mu\nu} \mathcal{L} \tag{5.10}$$

$$= \left(u^\mu K + \nabla_\lambda \phi \Delta^{\lambda\mu}\right) \partial^\nu \phi + \mu \left(\nabla_\lambda K\right) \Delta^{\lambda\mu} \partial^\nu K - g^{\mu\nu} \mathcal{L} \tag{5.11}$$

with the transverse projector $\Delta^{\mu\nu} \equiv g^{\mu\nu} - u^\mu u^\nu$, the transverse derivative $\nabla_\mu \equiv \Delta_{\mu\nu}\partial^\nu$, and its longitudinal counterpart $D_\tau \equiv u^\mu \partial_\mu$, defined in relation to the local rest-frame four-velocity u^μ. We use a constant heat-bath rest frame of $u^\mu = \delta_0^\mu$, and thus find for the energy density in this frame

$$T_D^{00} = K\dot{\phi} - \mathcal{L} = -\frac{\mu}{2} \left(\nabla_\mu K\right) \nabla^\mu K - \frac{1}{2} \left(\nabla_\mu \phi\right) \nabla^\mu \phi + V(\phi) \tag{5.12}$$

$$= \frac{\mu}{2} (\nabla K)^2 + \frac{1}{2} (\nabla \phi)^2 + V(\phi), \tag{5.13}$$

in agreement with the Hamiltonian density in Eq. (2.96). The nabla symbol either index-less or with Latin index ∇_i denotes the usual spatial derivative. The momentum density components frame become non-symmetric, and we find

$$T_D^{0i} = -K \nabla_i \phi, \tag{5.14}$$

$$T_D^{i0} = -\dot{\phi} \nabla_i \phi - \mu \dot{K} \nabla_i K = \mu (\nabla_i \phi)(\nabla^2 K) - \mu (\nabla_i K) \left(\Delta \phi - V'(\phi)\right), \tag{5.15}$$

where we inserted the equations of motion to eliminate the time-derivative of K. Energy flux T^{i0} and momentum density T^{0i} are not identical. While generally, the canonical energy-momentum tensor is not necessarily symmetric, it also cannot be symmetrized via a Belinfante-Rosenfeld construction [105, 106] in this case. To understand this, it is useful to consider the generalized angular momentum

$$M^\mu{}_{\nu\lambda} = \left(x_\nu T^\mu{}_\lambda - x_\lambda T^\mu{}_\nu\right) + S^\mu{}_{\nu\lambda}, \tag{5.16}$$

where $S^\mu{}_{\nu\lambda}$ contains the contribution of intrinsic spin. If angular momentum is locally conserved, then

$$\partial_\mu M^\mu{}_{\nu\lambda} = 0 \tag{5.17}$$

$$\Rightarrow \quad \partial_\mu S^\mu{}_{\nu\lambda} = T_{\lambda\nu} - T_{\nu\lambda}, \tag{5.18}$$

and the anti-symmetric part of the energy momentum tensor relates to the sources of spin in the system. However, in our case of Model D, there is no field carrying spin. Instead, by introducing explicitly a dependence on the local rest-frame velocity u^μ, some components of generalized angular momentum are no longer conserved.

The purely spatial components receive some corrections as well, namely

$$T_D^{ik} = (\nabla_i \phi)(\partial_k \phi) + \mu (\nabla_i K)(\nabla_k K) - g^{ik} \mathcal{L}. \tag{5.19}$$

While the purely spatial components are at least symmetric for our choice of rest-frame $u^\mu = \delta_0^\mu$, we will nevertheless limit our study of the energy-momentum tensor in this model to the energy density for practical reasons. We discretize this component as

$$T_x^{00} = \frac{1}{2} \dot{\phi}_x K_x + \frac{1}{4} \sum_i \left[\left(\phi_{x+e_i} - \phi_x\right)^2 + \left(\phi_x - \phi_{x-e_i}\right)^2\right] + V(\phi_x), \tag{5.20}$$

where we compute $-\mu K_x = (\nabla^{-2} \dot{\phi})_x$ as the inverse discrete Fourier transform of $|k|^{-2} \dot{\phi}_k$, forcing the zero-momentum mode $\dot{\phi}_{k=0} = 0$ to vanish.

5.1.1 Conservation laws on the lattice

In the continuum, the energy-momentum tensor is the conserved Noether current generated by the symmetry w.r.t. spacetime translations; i.e.

$$\partial_\mu T^{\mu\nu} = 0. \tag{5.21}$$

On the lattice, the continuous symmetry reduces to a discrete one. While we discretize space, we treat the time direction as quasi-continuous in our calculations, justified by the small ratio of $a_t/a = 1/160$. In the following, we calculate the lattice equivalent of $\partial_\mu T^{\mu\nu}$ to gauge the extend to which hydrodynamic treatments are justified, and to find out how exactly (5.21) is violated by the discretization of space. Due to availability of data, we focus on Model-C dynamics.

Looking at the $\nu = 0$ component of the conservation law (5.21), corresponding to translation symmetry in the time direction and therefore conservation of energy, we find

$$\partial_\mu T_C^{\mu 0} = \partial_t T_C^{00} - \nabla(\pi\nabla\phi) \stackrel{!}{=} 0, \tag{5.22}$$

$$\partial_0 T_C^{00} = \partial_t H = \pi\nabla^2\phi + (\nabla\phi)(\nabla\pi) = \nabla(\pi\nabla\phi) = -\partial_i T_C^{i0}. \tag{5.23}$$

When replacing the derivatives with their discrete counterparts, this is still fulfilled up to order $O(a^3)$,

$$\partial_\mu T^{\mu 0} = (\pi'\phi'' + \pi\phi^{(3)})a^3 + O(a^4). \tag{5.24}$$

We therefore expect the lattice data to fulfill the relation $\partial_\mu T^\mu = 0$ over a wide range of parameters. For the spatial components of the conservation law (5.21), we find in the continuum

$$\partial_\mu T^{\mu i} = -\partial_t(\pi\nabla_i\phi) + \nabla\cdot(\nabla\phi)(\nabla_i\phi) + \nabla_i\mathcal{L} \tag{5.25}$$

$$\begin{aligned} &= -\pi\nabla_i\pi - \left(\nabla_k^2\phi - V'(\phi)\right)\nabla_i\phi + \nabla_k(\nabla_k\phi\nabla_i\phi) \\ &\quad + \pi\nabla_i\pi - V'(\phi)\nabla_i\phi - \frac{1}{2}\nabla_i(\nabla_k\phi)^2 \end{aligned} \tag{5.26}$$

$$= -(\nabla_k^2\phi)\nabla_i\phi + (\nabla_k^2\phi)\nabla_i\phi + \nabla_k\phi\nabla_k\nabla_i\phi - \nabla_k\phi\nabla_i\nabla_k\phi = 0, \tag{5.27}$$

where we sum over the repeated spatial index k. On the lattice however, we find that the leading discrepancies are of the form

$$0 \neq -\pi\nabla_i\pi + \frac{1}{2}\nabla_i\pi^2 = a^2\left((\pi_x')^2 + \pi_x''\pi_x\right) + O(a^3), \tag{5.28}$$

$$0 \neq \nabla_i V(\phi) - V'(\phi)\nabla_i\phi = \frac{a^2}{2}\left(m_x^2(\phi_x')^2 + \frac{\lambda}{2}(\phi_x\phi_x')^2\right) + O(a^3). \tag{5.29}$$

While the former indicates a breakdown of $\partial_\mu T^{\mu i}$ at large aT, the latter becomes more relevant if there are large fluctuations of the field ϕ. Additionally, since these effects are of order a^2, we expect to see stronger deviations from conservation of momentum $\partial_\mu T^{\mu i}$ than from conservation of energy $\partial_\mu T^{\mu 0}$.

In order to numerically check the validity of Eq. (5.21) on the lattice, we introduce a short-hand notation for the autocorrelation functions of the energy-momentum tensor

$$F_{T^{\mu\nu}}(t,\mathbf{x}) \equiv \left\langle T^{\mu\nu}(t,\mathbf{x})T^{\mu\nu}(0,0)\right\rangle, \tag{5.30}$$

wherefrom $F_{T^{\mu\nu}}(\omega, \mathbf{p})$ is obtained using a discrete Fourier transform. Evaluating Eq. (5.21) in Fourier space leads to a linear relationship between the individual components

$$0 = \partial_t T^{0\mu}(t, \mathbf{x}) + \sum_k \partial_k T^{k\mu}(t, \mathbf{x}) \quad \Leftrightarrow \quad 0 = \omega T^{0\nu}(\omega, \mathbf{p}) + \sum_k p_k T^{k\nu}(\omega, \mathbf{p}). \tag{5.31}$$

For modes where the spatial momentum $\mathbf{p} = p\mathbf{e}_1$ points along the first direction, this implies a linear relation between the (connected) autocorrelation functions as well. By virtue of Parseval's theorem, it is easily demonstrated[1] that for the Fourier transform of the autocorrelation one has

$$F_{T^{\mu\nu}}(\omega, \mathbf{p}) = |T^{\mu\nu}(\omega, \mathbf{p})|^2 \tag{5.32}$$

$$\Rightarrow \quad \omega^2 F_{T^{0\nu}}(\omega, \mathbf{p}) = |\omega T^{0\nu}(\omega, \mathbf{p})|^2 = |pT^{1\nu}(\omega, \mathbf{p})|^2 = p^2 F_{T^{1\nu}}(\omega, \mathbf{p}). \tag{5.33}$$

This mode of comparison allows us to identify a range of frequencies ω and momenta $\mathbf{p}$ where the conservation law Eq. (5.33) holds.

Numerical results for the energy-momentum tensor autocorrelation functions in Fourier space are illustrated in Figs. 5.1 and 5.2. The autocorrelation functions are rescaled in a manner that allows to read off the region where Eq. (5.33) holds true by checking where the presented data overlaps. We find that for low spatial momentum p, the temporal component of Eq. (5.21), i.e. the continuity equation of the energy density, holds over a wide range of frequencies ω, independent of temperature. With increasing spatial momentum p, the range of overlap shrinks to a region near the peak, as can be seen in Fig. 5.1. While broadly matching our conjecture, there seems to be a systematic deviation in the ordered phase, where the strong quasi-particle–like UV peak at high spatial momentum p in the energy density autocorrelation does not appear in the longitudinal momentum, in both 2+1D and 3+1D.

In contrast, there is strong evidence that the spatial component of Eq. (5.21), i.e. the continuity equation of the momentum density, is violated on the lattice. While there is some correlation of the mid-frequency peaks at medium to high spatial momentum p, there is no overlap of the appropriately scaled transverse momentum and shear-stress density autocorrelation functions in Fig. 5.2. In Section 5.2, Figs. 5.4 and 5.5, we explore the parameter space further and find better in a massless theory agreement at low coupling λT.

Figure 5.3 shows the longitudinal-momentum autocorrelation function in the time domain at finite spatial momentum p. If the total momentum was conserved, the autocorrelation functions $F_{T^{0i}}(t, p = 0)$ would become a constant. We find a strong temperature dependence of the conservation of momentum, i.e. at high temperatures the zero-momentum mode drops off significantly earlier than at low temperatures. This effect is so strong that in 2+1D at $\tau \approx 1.7$, the first finite-momentum modes overlap with the zero-momentum mode, meaning that in those cases the IR cutoff is given not by the spatial momentum p but the decorrelation time scale of total momentum. At low temperature, there is nearly an order of magnitude separating the decorrelation time scale of the first finite-momentum mode and that of the zero-momentum mode, therefore the relevant scale here is indeed the spatial momentum p. We observe a similar, albeit much weaker effect in 3+1D, where the temperature window we are operating in is much narrower in terms of absolute values ($T \in [9, 10]$

[1] $F_T(t) = \int \mathrm{d}\tau T^*(\tau + t)T(\tau) = \frac{1}{2\pi} \int \mathrm{d}\omega T^*(\omega) e^{\mathrm{i}\omega t} T(\omega) = \mathcal{F}^{-1}[|T(\omega)|^2](t)$

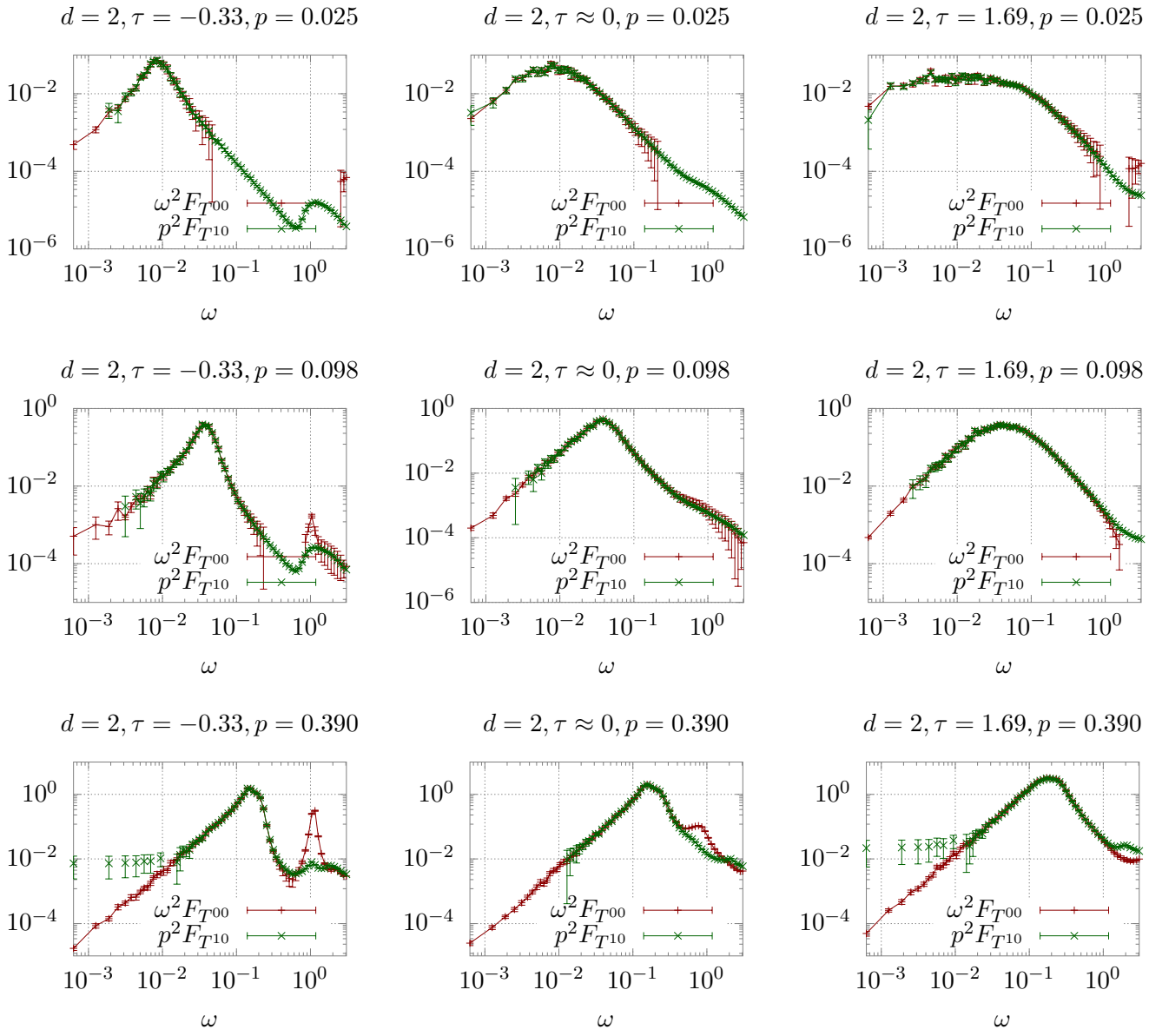

Figure 5.1: Illustration of the conservation law (5.33) in 2+1D, specifically the component encoding energy conservation. Red data show the autocorrelation function of the energy density, green data the autocorrelation function of the longitudinal momentum density. Temperature increases from left to right, starting in the ordered phase, over the critical point in the center panels, to high temperatures deep in the symmetric phase to the right. Spatial momentum increases from top to bottom. We see that, as expected, conservation of energy (Eq. (5.33)) is fulfilled over a wide range of parameters, with some discrepancies emerging at large wavenumber p and large frequencies ω. Not shown here are the results obtained in 3+1D, which agree qualitatively.

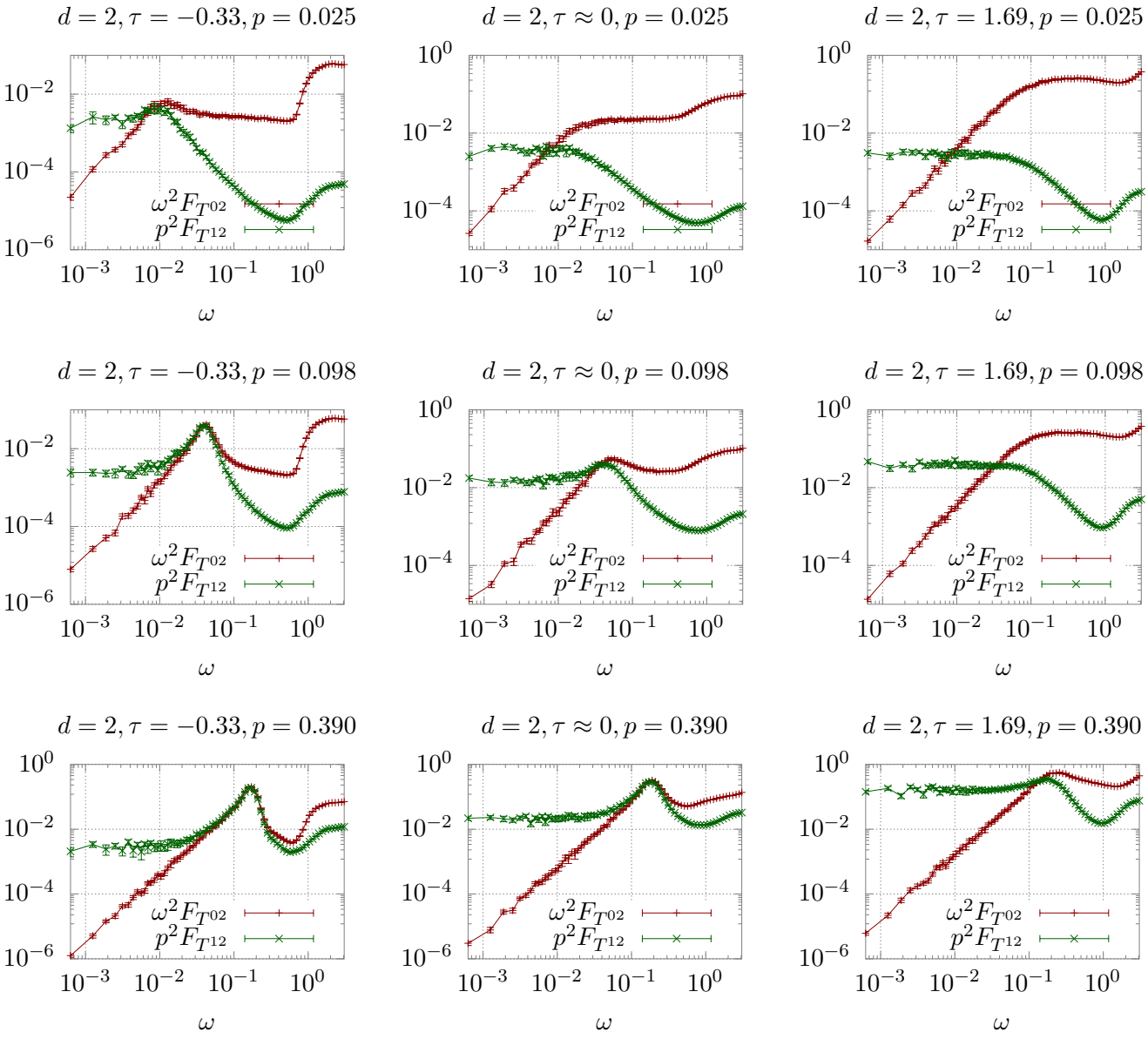

Figure 5.2: Illustration of the conservation law (5.33) in 2+1D, specifically the component encoding conservation of transverse momentum. Red data show the autocorrelation function of the transverse momentum, green data the autocorrelation function of the shear-stress density. In general, there is hardly any overlap, indicating that the reduced translational symmetry on the lattice has a strong effect on momentum conservation. Only for rather larger spatial momentum p at intermediate frequencies do we see similar features around the peak.

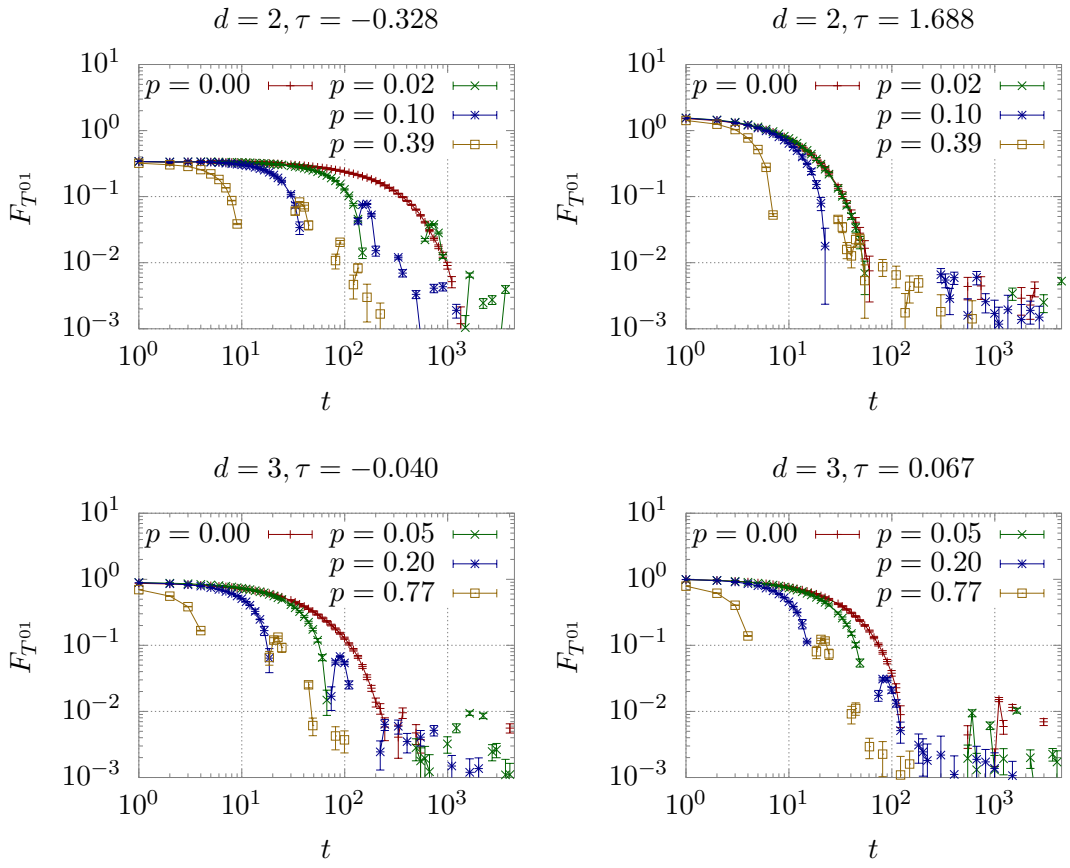

Figure 5.3: Longitudinal momentum autocorrelation functions in Model C at low (left panels) and high temperature (right panels), in 2+1D (top panels) and 3+1D (bottom panels). If momentum were conserved, the data points for vanishing wavenumber $p = 0$ would be constant in time. As the temperature increases, the decorrelation time scale of the total momentum density ($p = 0$) decreases, and imposes a non-physical IR cut-off on the modes with non-zero wavenumber. Then, the first finite-wavenumber modes overlap with the $p = 0$ mode, as is visible in the top right panel. Although not illustrated here, we find very similar results for the transverse momentum density.

vs. $T \in [3, 12]$ in 2+1D). While close to each other, there remains always a significant difference between $p = 0$ and the first mode at $p > 0$.

Conclusion

We have calculated the energy-momentum tensor of the continuum models both with and without the order parameter as a dynamically conserved quantity. The former yields a rather complicated expression, leading us to limit ourselves to studying the energy density, which can be obtained from the lattice variables with justifiable effort. For the model without order parameter conservation, we have demonstrated that some considerations are necessary when choosing the discretization of the individual components. By a brief analytical inspection, we have shown that the continuity equation of the energy density holds on the lattice with deviations of order a^3, while momentum conservation receives corrections of order a^2. A numerical study on autocorrelation functions of components of the energy-momentum tensor has yielded compatible results. While energy continuity can numerically be confirmed over a

wide range of temperatures at low to medium spatial momentum, the continuity of momentum density is only given in a narrow region of intermediate time scales and spatial momenta. The total momentum also is not conserved, with a breakdown scale strongly depending on the temperature.

We conclude that it seems reasonable to treat the energy density as a slow conserved field at most scales, however keeping in mind that hydrodynamic reasoning involving in some way conservation of momentum may not apply.

5.2 Transport coefficients

In a recent study [104] by Matsuda et al., the authors extract the shear viscosity of a massless scalar field using the classical field approximation. They consider the Lagrangian (2.101) with vanishing bare mass $m^2 = 0$, respectively the corresponding discretized Hamiltonian

$$H = \frac{1}{2}\sum_x \left[\pi_x^2 + (\partial_i\phi)_x^2 + \frac{\lambda}{12}\phi_x^4\right], \tag{5.34}$$

where $\partial_i\phi_x \equiv \phi_{x+e_i} - \phi_x$ denotes the *forward* derivative, yielding the same equations of motion as in Eqs. (2.122) and (2.123) with $m^2 = 0$ and $\gamma = 0$ (Model C). They define the off-diagonal spatial elements of the energy-momentum tensor as

$$T_{ik} = (\partial_i^c\phi_x)(\partial_k^c\phi_x), \tag{5.35}$$

where $\partial_i^c \equiv (\phi_{x+e_i} - \phi_{x-e_i})/2$ denotes the *central* derivative, claiming that this definition, since it is located on the same point as the field ϕ_x and symmetric in space directions, gives a better definition than using the forward difference.

To obtain the shear viscosity, one may employ the Green-Kubo formula from linear response theory, which yields the shear viscosity η as the low-frequency limit of the shear-stress autocorrelation function, i.e.

$$\eta \equiv \frac{V}{T}\int_0^\infty \mathrm{d}t \left\langle T^{ij}(t, \mathbf{p}=0)T^{ij}(0, \mathbf{p}=0)\right\rangle = \frac{V}{2T}\lim_{\omega\to 0} F_{T^{ij}}(\omega, \mathbf{p}=0), \tag{5.36}$$

reusing the definition of the autocorrelation function resp. its Fourier transform from Eq. (5.30).

Observing the "scaling property", i.e. that the equations of motion are invariant under transformations of the form

$$\phi \to \phi' = \phi/\sqrt{\alpha}, \quad \pi \to \pi' = \pi/\sqrt{\alpha}, \quad \lambda \to \lambda' = \lambda\alpha, \tag{5.37}$$

with some arbitrary positive parameter α, one can relate results at different T, λ by comparing

$$T(\lambda) = \langle\pi_x^2\rangle_\lambda = \alpha\langle\pi_x^2\rangle_{\alpha\lambda} = \alpha T(\alpha\lambda), \tag{5.38}$$

$$F_{T^{ij}}(\omega, \lambda, T) = \alpha^2 F_{T^{ij}}\left(t, \alpha\lambda, T/\alpha\right), \tag{5.39}$$

$$\eta(\lambda, T) = \alpha\eta(\alpha\lambda, T/\alpha). \tag{5.40}$$

These imply scaling functions for the shear-mode autocorrelation and thus the shear viscosity as

$$\lambda^2 F_{T^{ij}}(\omega, \lambda, T) = f_{F_T,\lambda}(\omega, \lambda T), \tag{5.41}$$

$$\lambda^2 T\eta(\lambda, T) = f_{\eta,\lambda}(\lambda T). \tag{5.42}$$

As it stands, we see two problems with this approach to calculating the shear viscosity. One is related to an inconsistency with the technical definition of the shear stress in Eq. (5.35), which we explain in more detail in the next section. The other, arguably more grave, concerns the fact that the physical momentum density is not perfectly conserved on the lattice, i.e. the Navier-Stokes equation is not satisfied on all scales.

In the original study, the authors show results obtained on 3+1D lattices with sizes $L \in \{16, 32, 64\}$ and couplings $\lambda T \in [0.5, 30]$. In the following sections, we show results obtained on 64^3 lattice volumes, with couplings $\lambda T \in [1, 50]$.

5.2.1 Trace

One property of the massless theory in 3+1D is scale invariance. As the coupling $[\lambda] = 1$ is dimensionless and $m^2 = 0$, there are no dimensional parameters in the Lagrangian. Therefore, the expectation value of the trace of the energy-momentum tensor should vanish, which can be shown by employing the equipartition theorem

$$\langle x_m \frac{\delta H}{\delta x_n} \rangle = \delta_{mn} T \tag{5.43}$$

to compute expectation values of variations of the Hamiltonian w.r.t. the fields as

$$\langle \pi \frac{\delta H}{\delta \pi} \rangle = \langle \pi^2 \rangle = T, \quad \langle \phi \frac{\delta H}{\delta \phi} \rangle = \langle \phi \left(-\nabla^2 \phi + V'(\phi) \right) \rangle = T \tag{5.44}$$

$$\Rightarrow \quad \langle \phi V'(\phi) \rangle = T - \langle (\nabla \phi)^2 \rangle = \langle \pi^2 - (\nabla \phi)^2 \rangle \equiv \langle \partial_\nu \phi \partial^\nu \phi \rangle , \tag{5.45}$$

and inserting into the trace

$$\langle T^\mu_\mu \rangle = \langle \frac{1-d}{2} \partial_\nu \phi \partial^\nu \phi + (d+1) V(\phi) \rangle \tag{5.46}$$

$$= (d+1) \langle V(\phi) \rangle - \frac{d-1}{2} \langle \phi V'(\phi) \rangle , \tag{5.47}$$

that indeed vanishes for $d = 3$ if $V(\phi) \propto \phi^4$.

If one now defines the spatial components of the energy-momentum tensor in analogy to Eq. (5.35) as

$$T_{ik} = (\partial^c_i \phi_x)(\partial^c_k \phi_x) + \delta_{ik} \mathcal{L}, \tag{5.48}$$

one finds that the expectation value differs from zero by a term proportional to $(\partial^c_i \phi_x)^2 - (\partial_i \phi_x)^2$, i.e. the difference between the central and forward derivative. While the definition via the central derivative surely is more practical, the resulting inconsistency is somewhat alarming. To further investigate this one could study a theory with a modified Hamiltonian, where the derivative term entails the central derivative as well, leading to slightly modified equations of motion. For the moment however, we stay with the current definition and just keep in mind that there may be some subtleties when comparing diagonal to off-diagonal elements of the energy-momentum tensor.

5.2.2 Navier-Stokes

In the hydrodynamic framework, one solves equations of motion of the form

$$\partial_\mu j^\mu = 0,\ \partial_\mu T^{\mu\nu} = 0 \tag{5.49}$$

where j^μ denotes some matter current and $T^{\mu\nu}$ the relativistic stress-energy tensor, plus some additional equation of state for the coarse-grained quantity. Considering the spatial components of the continuity equation of the energy-momentum tensor, one finds that they are related to the classical *Navier-Stokes equation* of conserved momentum

$$\partial_\mu T^{\mu i} = 0 \ \rightarrow\ \partial_t(\rho v_i) + \partial_j \Pi_{ji} = 0, \tag{5.50}$$

with the Newtonian stress tensor $\Pi_{ij} = p\delta_{ij} + \rho v_i v_j - \Sigma_{ij}$, whose dissipative part is parametrized as

$$\Sigma_{ij} \equiv \eta\left(\partial_i v_j + \partial_j v_i - \frac{2}{3}\delta_{ij}\partial_k v_k\right) + \zeta\delta_{ij}\partial_k v_k, \tag{5.51}$$

containing the shear (η) and bulk (ζ) viscosities. It seems therefore that conservation of momentum ($\partial_\mu T^{\mu i} = 0$) is a necessary condition to extract a meaningful value for the shear viscosity. As we found however, this is generally not the case for the lattice theory with finite bare mass $m^2 = -1$, compare e.g. Fig. 5.2. Naturally, we repeat our investigation for the massless case. We argued that to check $\partial_\mu T^{\mu\nu} = 0$, it is sufficient to compare the autocorrelation functions as

$$\omega^2 F_{T^{0\nu}}(\omega, \mathbf{p}) = p^2 F_{T^{i\nu}}(\omega, \mathbf{p}), \tag{5.52}$$

where for $\nu = 0$ one has the energy conservation law $\partial_\mu T^{\mu 0}$, and momentum conservation otherwise.

In Figs. 5.4 and 5.5 we show the autocorrelation functions related to energy conservation $\partial_\mu T^{\mu 0}$ (top panels) as well as transverse momentum conservation $\partial_\mu T^{\mu 2}$ (bottom panels). One can read of regions where the respective conservation law is satisfied as the interval where the data points overlap. Figure 5.4 illustrates the dependence on spatial momentum p with fixed coupling λT, and Fig. 5.5 vice versa.

Energy conservation is fulfilled within the error bars over all couplings $\lambda T \in [1, 25]$ considered here for low wavenumber $p \lesssim 0.1$. As p increases, we find that the data overlaps only around some intermediate frequency, where the main peak in the autocorrelation functions is located.

In case of conservation of the transverse momentum, we find that its behavior is essentially the inverse. Even for small $\lambda T = 1$, momentum conservation is only fulfilled in some intermediate frequency region around the main peak (compare lower panels in Fig. 5.4). For larger couplings $\lambda T > 1$, the situation gets worse, as can be seen in the lower panels of Fig. 5.5. If the coupling becomes very large at $\lambda T = 25$, there is no overlap over any part of the observed frequency interval. This is somewhat problematic, as one is supposed to extract the shear viscosity η from the low-frequency limit, where we find no overlap. Therefore, in the range where one wants to extract the shear viscosity, physical momentum is not conserved, i.e. the Navier-Stokes equation does not hold. Ideally, one should be able to extract the same η from the infrared limit of $(\omega/p)^2 F_{T^{02}}(\omega, p)$ as well. Figure 5.5 shows that this is essentially never the case.

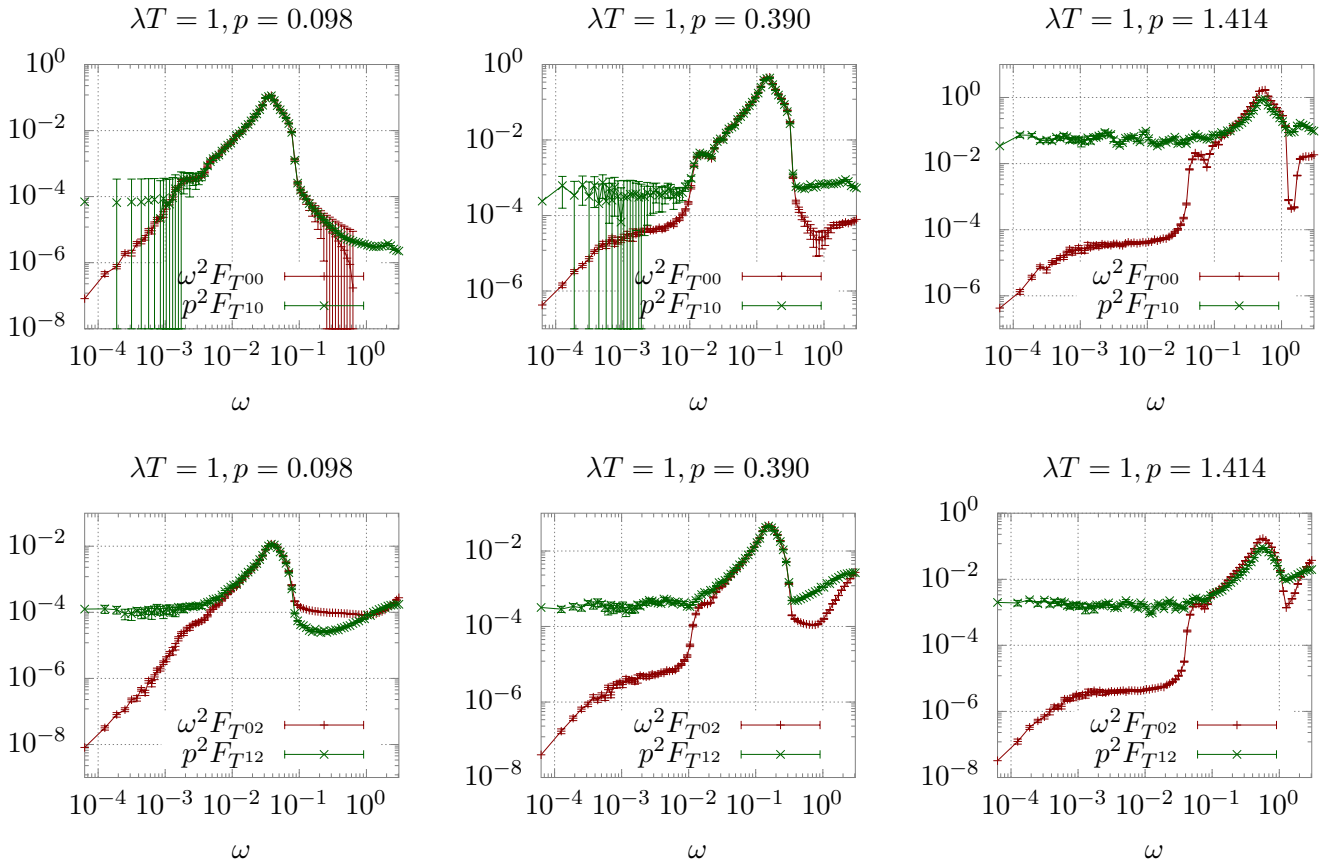

Figure 5.4: Illustration of the conservation law (5.33). Top panels show the energy density vs. longitudinal momentum, bottom panels transverse momentum vs. the corresponding shear stress modes. From left to right, spatial momentum increases while the coupling $\lambda T = 1$ is held constant. The frequency window where the energy flux balances the time derivative of the energy density shrinks with increasing spatial momentum. In contrast, the second component of Eq. (5.33) independently of the spatial momentum has a narrow range of validity shifting with the peak; it is hardly affected as the wavenumber increases.

Nevertheless, the former arguments only hold for finite wavenumber p, and for example Fig. 5.4 might suggest that at least in the limit $p \to 0$, the low-frequency plateau wherefrom η is extracted becomes a region of overlap and momentum conservation holds. However, we also found that total momentum is not conserved either, with the decorrelation time scale depending strongly on λT. Comparing now the autocorrelation functions of total transverse momentum and shear stress in Fig. 5.6, we find that the decorrelation time scales match almost exactly over all observed $\lambda T \in [1, 25]$. It is therefore standing to reason that the relevant effect dominating the IR part of the shear stress autocorrelation (and thus the extracted η) is the breakdown of momentum conservation, not hydrodynamic dissipation.

To estimate the quantitative effect this has on the computed shear viscosities, we revisit the numerical procedure Matsuda et al. use in [104]. After showing that the shear-stress autocorrelation function is dominated by an exponential decay, they find that the most reliable way to obtain the integral over time and thus the shear viscosity is to first fit the correlation function to an exponential ansatz, and then

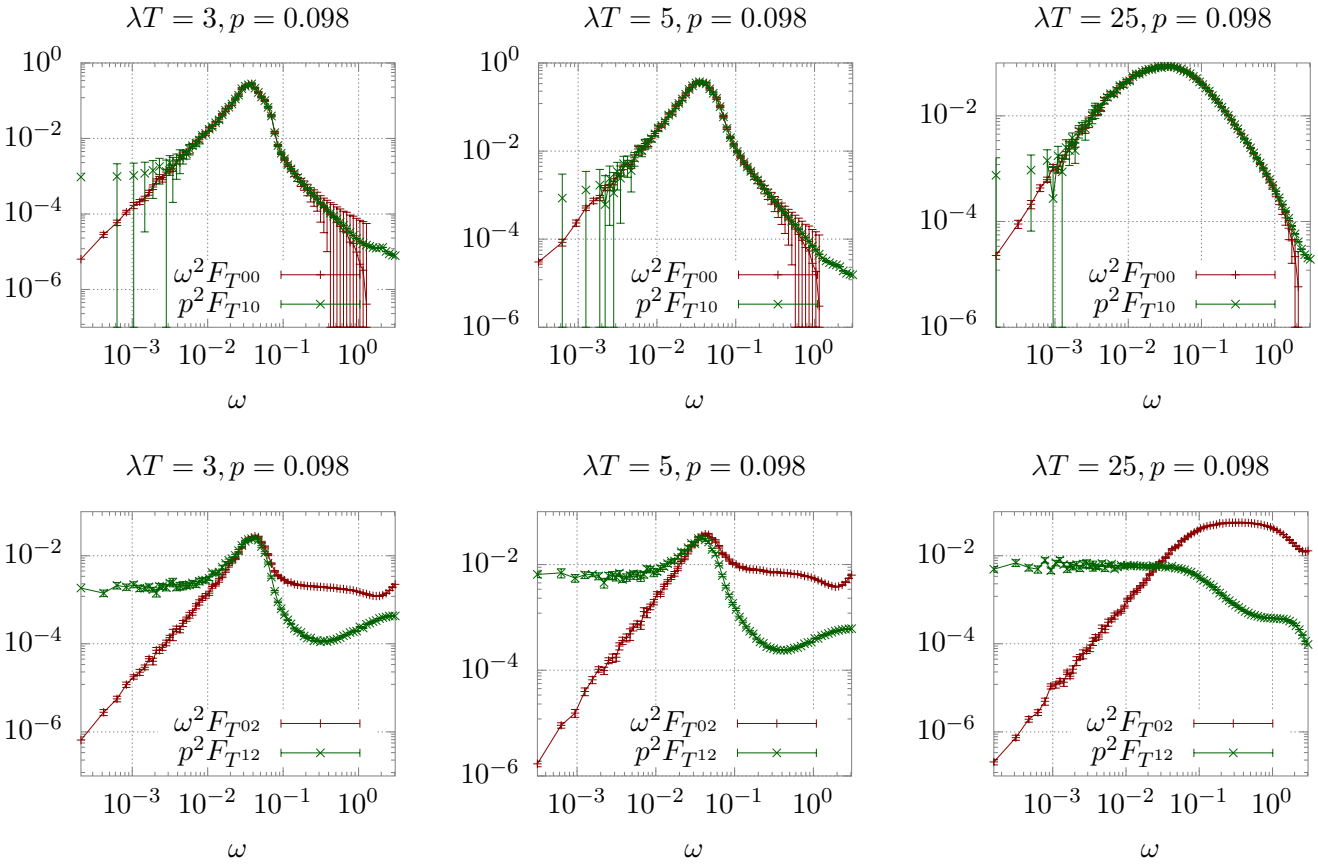

Figure 5.5: Illustration of the conservation law (5.33). Top panels show the energy density vs. longitudinal momentum, bottom panels transverse momentum vs. the corresponding shear stress modes. From left to right, λT increases while spatial momentum is held constant. While the first component of Eq. (5.33) (i.e. conservation of energy) holds very well regardless of λT, the second component is hardly satisfied at any finite spatial momentum for $\lambda T > 1$.

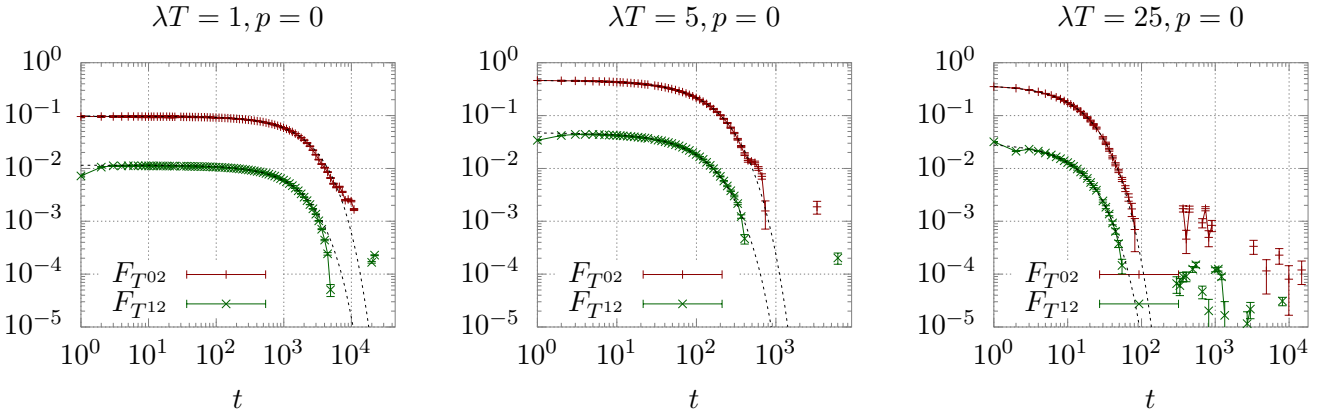

Figure 5.6: Comparison of the autocorrelation functions of total transverse momentum and shear stress in the time domain. Dashed lines indicate fits to an exponential decay. In this illustration, it seems as if the relevant IR cutoff is supplied not by hydrodynamic dissipation, but by the decorrelation of momentum.

Table 5.1: Comparison between the decay constant Γ' of the transverse momentum density autocorrelation and the decay constant Γ of the shear stress autocorrelation. Conservation of physical momentum implies $\Gamma' \to 0$. We find that the decay scales are very close for $\lambda T \gtrsim 10$, casting doubts whether a meaningful result for the shear viscosity can be obtained from Γ.

λT	1	3	5	10	25	50
Γ'/Γ	0.766(5)	0.83(3)	0.83(3)	1.00(8)	0.91(4)	1.04(7)

take the analytic result for the integral, i.e.

$$F_{T^{ij}}(t, \mathbf{p} = 0) \approx A \exp(-\Gamma t) \tag{5.53}$$

$$\Rightarrow \quad \eta = \frac{V}{T} \int_0^\infty F_{T^{ij}}(t, \mathbf{p} = 0) \approx \frac{V}{T} \frac{A}{\Gamma}. \tag{5.54}$$

We find that the transverse-momentum autocorrelation also nearly perfectly follows an exponential decay

$$F_{T^{02}}(t, \mathbf{p} = 0) = A' \exp(-\Gamma' t). \tag{5.55}$$

As long as the decay of the shear correlator is much faster than that of the momentum autocorrelation ($\Gamma'/\Gamma \ll 1$), it seems reasonable to assume that the main effect on the shear correlator is dissipative in nature.

Tabulated in Table 5.1 are the ratios of measured decay constants Γ'/Γ as well as their statistical errors as obtained from our data set. We find however that for medium to large values of $\lambda T \gtrsim 10$, the ratio of decay constants is very close to $\Gamma'/\Gamma \approx 1$. Therefore it is at least uncertain if meaningful results for the shear viscosity can be obtained in this range of parameters.

5.2.3 Shear viscosities

Nevertheless, we reproduce here the results by Matsuda et al., and extend their study to our models. To this end, we record the shear-mode autocorrelation functions at a set of different combinations of coupling λ and temperature T to span roughly the same region of λT as in [104], and confirm that they are dominated by a long-time nearly-exponential decay, with a few initial fluctuations. While in the precursor study [104], autocorrelation functions were fit with an exponential ansatz in the time domain, we extract the infrared limit by fitting a constant to the data points at the lowest frequencies ω. To generate the data, we employ the same process as for the spectral functions of the order parameter outlined in Section 4.2.

By comparing our results at different couplings λT we can check our evaluation mechanism and extract the scaling functions as in Eq. (5.42). Resulting rescaled shear viscosities are given in Fig. 5.7. Since no numerical values were tabulated in [104], we give as the right panel a reprint of their Fig. 7 as a basis of comparison to our results in the left panel. The results appear to match ours inside of numerical uncertainties, leading to the conclusion that we were able to exactly replicate their framework.

We also extend this study to the Model-C dynamics with spontaneous symmetry breaking ($m^2 = -1$) and investigate the effect of a finite heat-bath coupling $\gamma = 0.1$ (Model A). Results for 2+1D and 3+1D are shown in Fig. 5.8. In 2+1D, we find that the product of temperature and shear viscosity $T\eta$ increases weakly with temperature

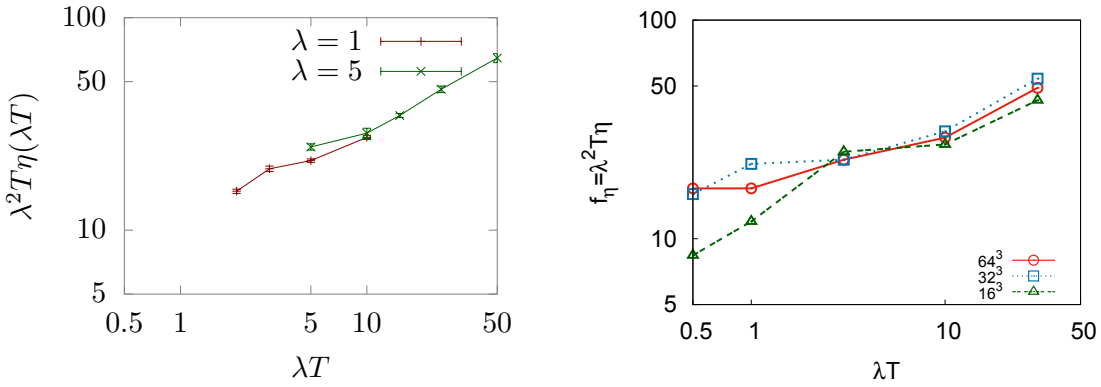

Figure 5.7: Extracted shear viscosities $\eta(T, \lambda)$ in the massless theory in 3+1D, re-scaled to reveal the underlying scaling function $f_\eta(\lambda T)$. The left panel shows our results, the right is a reprint of Figure 7 from [104], depicting the results by Matsuda et al. in the same fashion for lattice volumes 16^3, 32^3 and 64^3. We only show results for $V = 64^3$. While their results were obtained by keeping the temperature $T = 1$ constant and varying λ, we chose two values for $\lambda \in \{1, 5\}$ and varied T. Although we do not have exact numerical values to compare, the results look sufficiently similar.

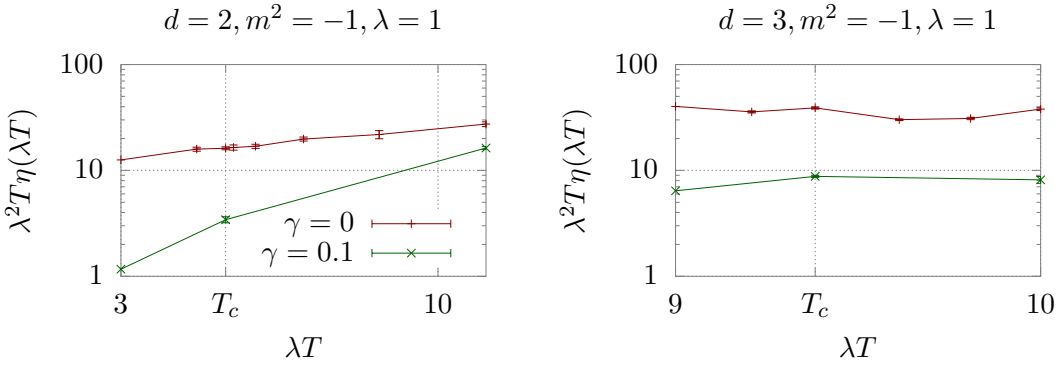

Figure 5.8: Rescaled shear viscosities, extracted at finite bare mass $m^2 = -1$, with the critical temperature marked on the λT-axis. We find that generally, the viscosities at finite heat-bath coupling $\gamma = 0.1$ are much smaller than at $\gamma = 0$. While in 3+1D, we observe some enhancement around the critical point at $T = T_c$ in accordance with a study by Homor and Jakovac [103], we do not find any signs of critical enhancement in 2+1D.

for vanishing Langevin coupling $\gamma = 0$. For $\gamma = 0.1$, the shear viscosities are much smaller, but also increasing with temperature. It seems as if they are offset by some finite amount compared to the results at $\gamma = 0$. We see no enhancement around the critical temperature T_c.

In 3+1D, we find the product $T\eta$ to be roughly constant over the observed temperature range. Again, the results for finite heat-bath coupling $\gamma = 0.1$ are much smaller and also roughly constant over the temperature T. Here we find a slight enhancement at the critical temperature $T = T_c$, which is however too weak to even begin to analyze critical scaling.

In summary, we are able to reproduce and extend the studies in [104]. There remains however significant doubt about their robustness in terms of the interpretation of the results as transport coefficients. If one were to look deeper into this issue, we recommend studying the theory while decreasing the spatial lattice spacing a, simultaneously monitoring conservation of spatial momentum and shear viscosity. The argument here is that with decreasing lattice spacing a, spatial momentum should be conserved on longer time scales, excluding the decorrelation of momentum by discretization effects as a potential error source. Ideally, the measured shear viscosities should then become independent of a for small enough (but finite) lattice spacing.

5.3 Equilibrium dynamics of the energy density

So far in this chapter, we found that the energy density seems to be the component of the energy-momentum tensor least affected by discretization effects. This section is therefore concerned with its equilibrium dynamics as seen in its autocorrelation and spectral functions. We investigate its behavior in our relativistic models with and without order parameter conservation and/or coupling to a heat bath (Models A through D) in both 2+1 and 3+1 dimensions. Starting with an overview over the general behavior of the spectral function of the energy density at different points in the phase diagram, we move on to extract its dispersion relation in the symmetric phase. We subsequently turn to investigate the critical scaling behavior of the energy density autocorrelation in the time domain and extract its underlying universal scaling function, before closing this chapter with some final remarks.

5.3.1 Overview

In analogy to the spectral functions of the order parameter (c.f. Eqs. (2.140) and (2.143)), we obtain the spectral functions of the energy density in the classical limit via the fluctuation-dissipation-relation

$$\rho_{T^{00}}(\omega, \mathbf{p}) = \frac{\omega}{T} F_{T^{00}}(\omega, \mathbf{p}) \tag{5.56}$$

from the energy-density autocorrelation.

Figures 5.9 and 5.10 show the spectral functions of the energy densities for the different models at different points in the phase diagram in 2+1D, Fig. 5.11 shows planes of fixed spatial momentum p. We observe that, generally, the spectral function of the energy density seems to be comprised of two excitations. In all models, the low-momentum region is dominated by a structure whose dispersion strongly depends on the heat-bath coupling γ. While for $\gamma = 0$, the right panels of Figs. 5.9 and 5.10 indicate that the central frequencies scale with some power of spatial momentum, the left panels at the same place suggest a lower boundary of order $\gamma = 0.1$ on the central frequencies, acting as a kind of finite mass. In Models A and C with dissipative dynamics, there is a second excitation which, judging from its shape and position, appears to be related to the quasi-particle excitation of the order parameter with a dispersion relation $\omega_p^2 = m^2 + p^2$. However, its amplitude also increases strongly with spatial momentum, such that it is best visible at low temperatures $\tau < 0$, high frequencies, and large spatial momentum $p \gtrsim 1$. Its dispersion is hardly affected by the heat-bath coupling γ, i.e. only the width changes as one would expect. For the diffusion dynamics of Models B and D, there also is a double-peak structure at low temperatures, however it is hardly visible in Fig. 5.10. We therefore show cuts of the spectral function of the energy density at fixed spatial momentum in Fig. 5.11, where in the ordered phase (lower right panel) one can observe two peaks close together, with a distinct valley in between. The relative position of those local maxima hardly changes with momentum, indicating that they both follow a similar dispersion relation closely related to (4.43). We assume that, similarly to the case of Models A and C, one of these peaks may be related to the excitation of the order parameter.

At the critical point, we observe stronger contributions in the IR in all models, which may be related to the dynamic critical behavior of the mode related to the

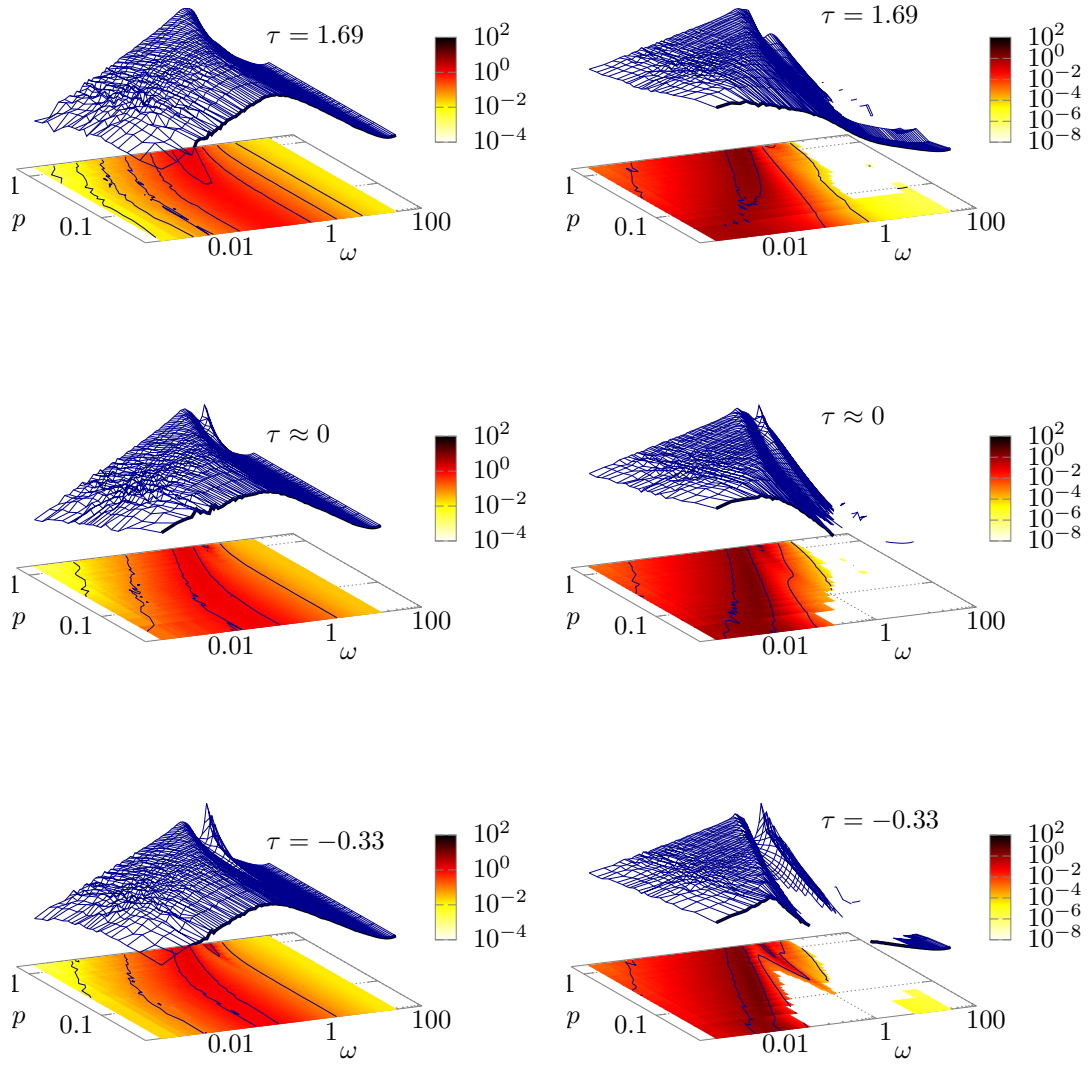

Figure 5.9: Overview of the behavior of the spectral function of the energy density $\rho_{T^{00}}(\omega, p)$ for dissipative dynamics in 2+1D, with Model A ($\gamma = 0.1$) in left panels, Model C ($\gamma = 0$) in right panels, in the symmetric phase (top panels), near the critical point T_c (central panels), and in the ordered phase (bottom panels). Generally, one finds two distinct excitations. Dominating the low-momentum region is a broad structure with central frequencies bounded from below by $\omega_p^2 > \gamma$ and otherwise nearly quadratic dispersion. At high spatial momentum, a sharp quasi-particle peak appears at large frequencies, which is suppressed as the temperature increases. Its position and shape suggest that it is related to the quasi-particle excitation of the order-parameter mode.

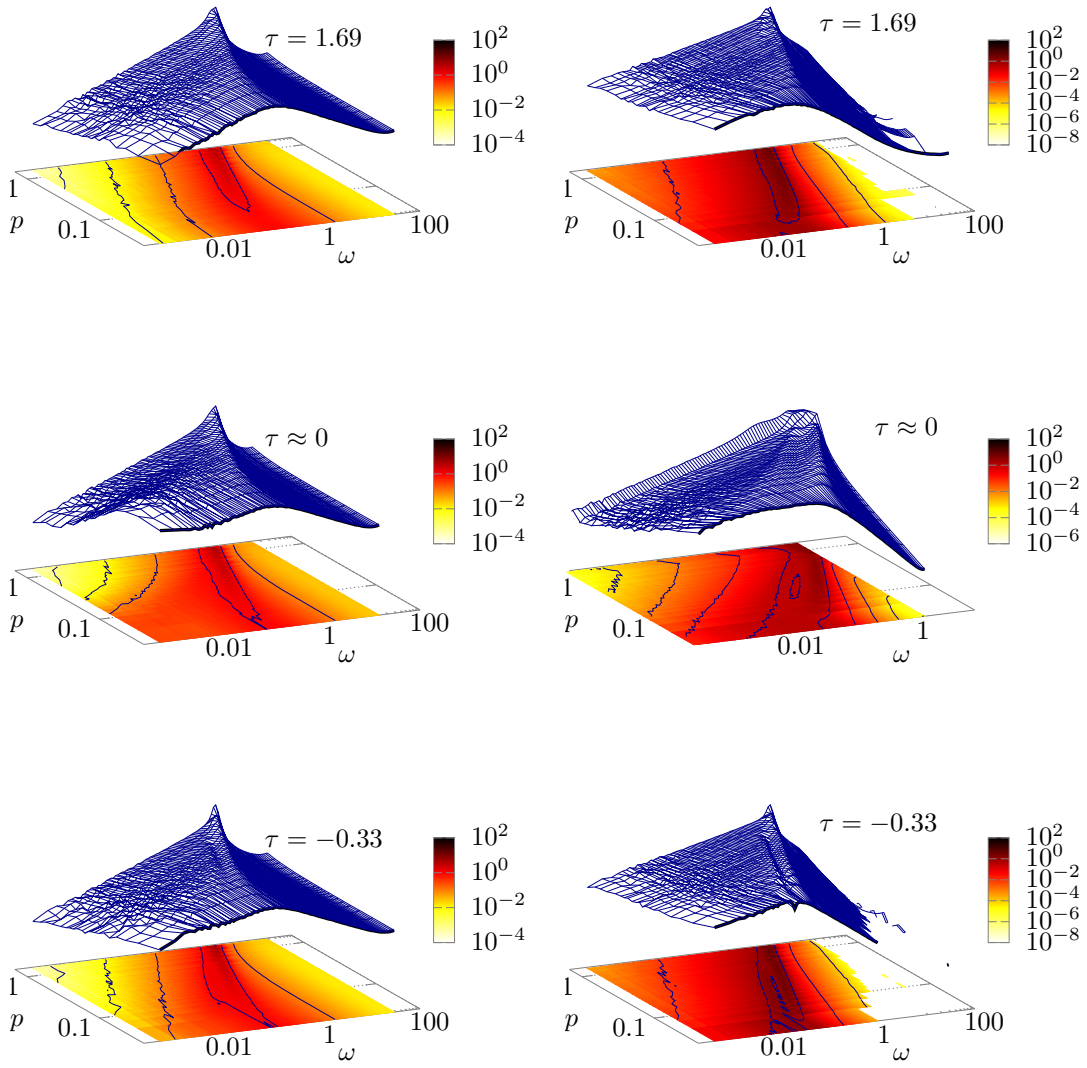

Figure 5.10: Overview of the behavior of the spectral function of the energy density $\rho_{T^{00}}(\omega, p)$ for diffusive dynamics in 2+1D, with Model B ($\gamma = 0.1$) in left panels, Model D ($\gamma = 0$) in right panels, in the symmetric phase (top panels), near the critical point T_c (central panels), and in the ordered phase (bottom panels). Similarly to the case of dissipative dynamics in Fig. 5.9, dominating the low-momentum region is a broad structure, with central frequencies bounded from below by the heat-bath coupling $\omega_p^2 > \gamma$ and otherwise nearly quadratic dispersion. Close to the critical point in Model B (center left panel), one notices an emerging infrared contribution independent of the main excitation. At low temperatures and vanishing heat-bath coupling $\gamma = 0$, the peak seems to split at low to intermediate spatial momentum, revealing a second excitation with a similar dispersion relation, however with central frequencies slightly offset by a factor close to 2 and not bounded from below by the Langevin coupling.

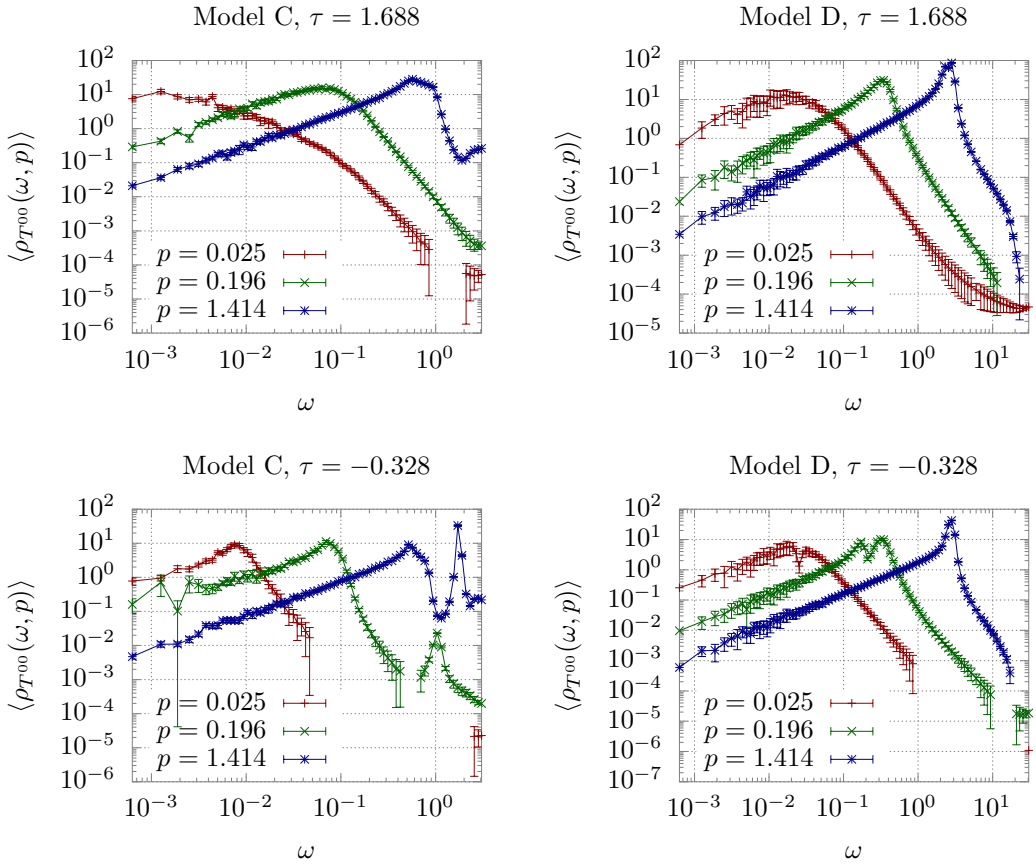

Figure 5.11: Cuts of the spectral functions of the energy density $\rho_{T^{00}}(\omega, p)$ at fixed spatial momentum p, for dissipative dynamics (Model C, left panels) as well as diffusive dynamics (Model D, right panels) with vanishing heat-bath coupling $\gamma = 0$ in 2+1D. At low temperatures (bottom panels) in Model C, one can clearly see the quasi-particle peak building up at large momentum. In Model D, one can make out the double-peak at low to intermediate momentum. At high temperatures, there is only the one dominant structure visible in both models. Results for 3+1D agree qualitatively and are thus omitted.

order parameter. This is best visible in Model B (center left panel of Fig. 5.10): At low wavenumbers and frequencies a separate structure emerges, which is clearly distinct from the main energy-diffusion mode, which has its central frequency at low spatial momentum bounded from below by the Langevin coupling γ. A more detailed analysis of possible scaling behavior follows in the next section.

At high temperatures in the symmetric phase, the excitation related to the order parameter is suppressed, and the spectral function of the energy density is dominated by a single structure, whose dispersion and other properties are similar as for low temperatures, with the heat-bath coupling γ again acting as a mass-like parameter. Since in this case there is only one dominant structure visible, we attempt to extract its quantitative behavior via fits to a Breit-Wigner ansatz, the results of which are illustrated in Fig. 5.12. While one obtains reasonable results with $\chi^2/\text{d.o.f.} \approx 1$ for vanishing heat-bath coupling $\gamma = 0$ and intermediate spatial momentum p, the fit starts to break down for finite $\gamma = 0.1$ and very low wavenumbers, where the structures become relatively broad.

Nevertheless, we find that the squares of the central frequencies roughly scale with

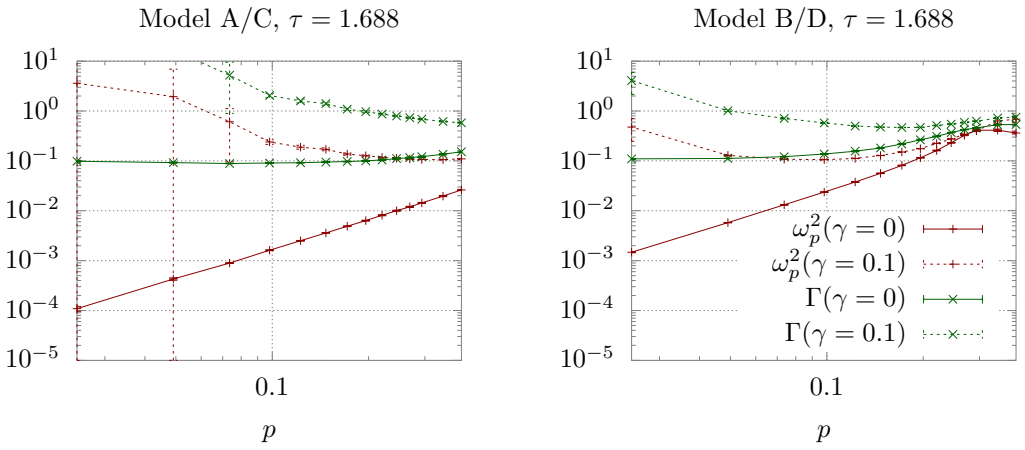

Figure 5.12: Results of a Breit-Wigner fit to the spectral functions of the energy density $\rho_{T^{00}}(\omega)$ in 2+1D in the symmetric phase for different values of the heat-bath coupling γ. Numerical values are given in lattice units. The left panel shows results from dissipative dynamics, the right panel shows diffusive dynamics, where the order parameter is conserved. The dispersion is reminiscent of a diffusive mode (compare Eq. (4.43)), with the decay width coincidentally approaching a constant value of $\Gamma(p) \approx 0.1$ at low spatial momentum for $\gamma = 0$. Clearly, the Langevin coupling γ acts as a lower bound on the square mass-like term ω_p^2, while additionally increasing the decay widths substantially. If the spatial momentum p becomes too small, the decay widths at $\gamma = 0.1$ grow very large and the fit breaks down. Again, results in 3+1D agree qualitatively.

the square of spatial momentum p^2, but are bounded from below by the heat-bath coupling γ. The decay widths in all cases are relatively large. Coincidentally, for vanishing Langevin coupling $\gamma = 0$ they approach a fixed value of $\Gamma(p) \approx 0.1$ in the limit of small spatial momentum $p \to 0$. For finite heat-bath coupling $\gamma = 0.1$, the decay widths are generally larger, and increase even further towards small momenta along with their uncertainty.

The effect of the Langevin coupling γ on the central frequencies is easily understood in the time domain. At $\gamma = 0$, the total energy is conserved, implying that any fluctuations of the energy density must be purely diffusive. This is given to high precision even on the lattice, as shown before in Section 5.1 and illustrated additionally in Fig. 5.13, where we show the autocorrelation functions of the energy density in the time domain in the symmetric phase. In the right panel, where the Langevin coupling $\gamma = 0$ is turned off, we see that the mode with zero spatial momentum $p = 0$ is up to output precision given by a constant. Not shown here is the connected autocorrelation function, where we subtracted the constant contribution. There, one then finds that the remaining fluctuations on top of the constant are separated by ten orders of magnitude from modes at finite momentum. Additionally, it is clear that the characteristic time scale of the autocorrelation function depends strongly on spatial momentum p. For non-zero γ however, the dissipation and fluctuations introduced into Eqs. (2.83) and (2.85) allow fluctuations of the total energy on a time scale given by $1/\gamma$, limiting the range of the autocorrelation functions in the top panel of Fig. 5.13.

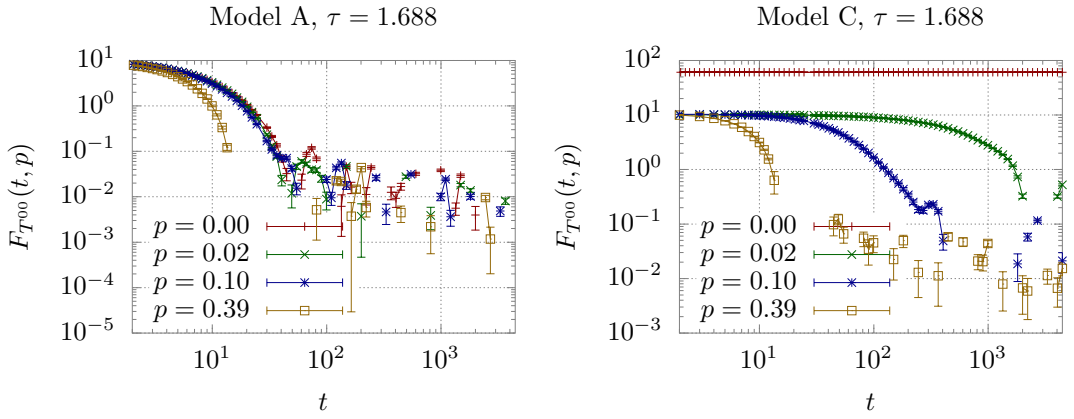

Figure 5.13: Energy density autocorrelation in the time domain for dissipative dynamics in the symmetric phase at high temperature. The data at vanishing momentum $p = 0$ in Model C is scaled by a factor of 10^{-4} to better fit the frame. At finite heat-bath coupling $\gamma = 0.1$ (left panel), all modes below a certain spatial momentum coincide, since the IR cut-off is given by $1/\gamma$. If the Langevin coupling $\gamma = 0$ vanishes (right panel), the total energy is conserved, and the cut-off scale at late times is given by the spatial momentum p. Not shown here is the connected part of the autocorrelation function at vanishing spatial momentum, where one finds that the remaining fluctuations are smaller by ten orders of magnitude. We find qualitatively very similar results for diffusion dynamics (Models B/D) and in 3+1D, which are thus omitted.

5.3.2 Critical behavior

Focusing on the critical behavior of the energy-density autocorrelation, we find that there are strong late-time contributions emerging (compare Fig. 5.14). In contrast to the energy-diffusion modes at high temperature, these are not suppressed at times $t > 1/\gamma$ larger than the inverse Langevin coupling. As such, they may be the result of scale invariance in the system.

Reformulating the dynamic scaling hypothesis for the energy-density autocorrelation, one finds

$$F_{T^{00}}(t, \mathbf{p}, \tau) = s^{\alpha/\nu} F_{T^{00}}\left(s^{-z} t, s\mathbf{p}, s^{1/\nu}\tau\right), \tag{5.57}$$

$$\Rightarrow \quad F_{T^{00}}(t, \mathbf{p}, \tau) = p^{-\alpha/\nu} f_{p,T^{00}}\left(t/p^z\right), \tag{5.58}$$

where in the second line we have explicitly chosen $s = 1/p$, and introduced a universal scaling function $f_{p,T^{00}}$. Its canonical scaling dimension only is non-zero in $d = 3$, where $\alpha = .11$. If the late-time contributions originate from dynamic critical phenomena, one should observe them to scale with some time scale $\xi_t \sim p^{-z}$.

Illustrations in Figs. 5.15 and 5.16 confirm this hypothesis. By rescaling the energy-density autocorrelation functions to reveal the underlying universal scaling function $f_{p,T^{00}}(t/p^z)$, we find an excellent scaling collapse for the modes with lowest spatial momentum p when rescaling the time axis with the same critical exponents as the order parameter in Section 4.3. At higher spatial momentum $\bar{p} \gtrsim 0.1$, we find strong non-critical contributions for Models A and C.

For the Models B and D with conserved order parameter, the scaling collapse extends to even higher spatial momentum. We find however that in Model B the modes with the smallest momentum indices do not collapse on the scaling function,

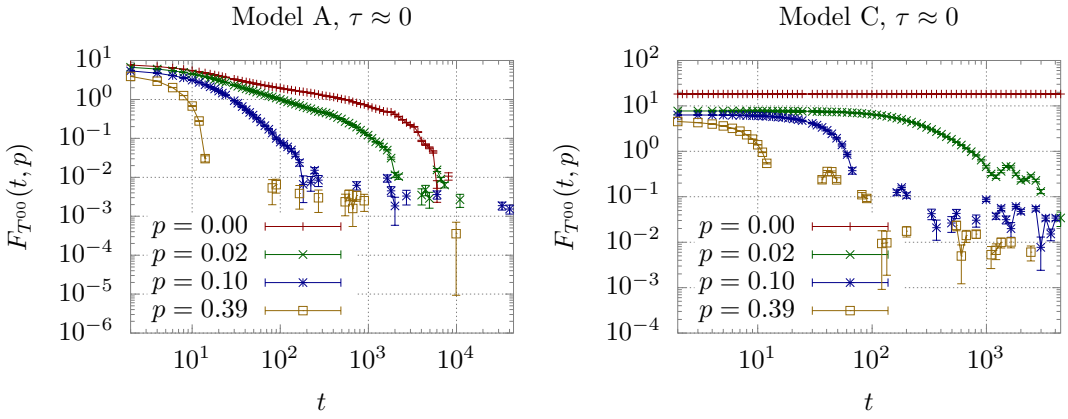

Figure 5.14: Energy density autocorrelation in the time domain for dissipative dynamics at the critical point. The data at vanishing momentum $p = 0$ in Model C is scaled by a factor of 10^{-4} to better fit the frame. We observe that in addition to a non-critical component limited by $1/\gamma$, there is a "long-range" correlation related to the critical behavior of the order parameter. Again, we observe qualitatively similar results for 3+1D and/or diffusive dynamics (Models B and C), the difference in the latter scenario being a much larger scaling exponent in case of $\gamma = 0.1$ ($4 - \eta = z_B > z_a \approx 2.17$), i.e. more severely diverging late-time contributions.

which is especially striking in 3+1D (upper right panel of Fig. 5.16). This is due to the limited total simulation time: The characteristic time scales of modes with low spatial momentum diverge as p^{-z}, and the dynamic critical exponent of Model B $z_B = 4 - \eta$ is large. Thus, one needs to evolve the system for very large absolute times to fully resolve the dynamic behavior at lowest momentum. The deviation for wavenumbers $\bar{p} < .05$ in the upper right panel of Fig. 5.16 are caused by the limited simulation runtime, i.e. we simply did not generate data on these time scales. However, at intermediate momentum scales, the scaling collapse is excellent, therefore we see no reason to invest the necessary computation time to extend the analysis further.

Since for Models A and B with $\gamma = 0.1$ also the autocorrelation function of the total energy density $T^{00}(t, p = 0)$ is non-trivial, we can conduct a finite-size scaling analysis. At criticality, the autocorrelation time of the infinite system diverges with the spatial correlation length as $\xi_t \sim \xi^z$. In our simulations however, the divergence of the correlation length and therefore the autocorrelation time is limited by the finite system size L, which becomes the relevant cut-off scale in the infrared at the critical point. Extending the dynamic scaling hypothesis onto the system size, one expects for the autocorrelation functions

$$F_{T^{00}}(t, L, \tau) = s^{\alpha/\nu} F_{T^{00}}\left(s^{-z}t, L/s, s^{1/\nu}\tau\right) \tag{5.59}$$

$$s = L \Rightarrow \quad F_{T^{00}}(t, L, \tau = 0) = L^{\alpha/\nu} f_{L,T^{00}}(t/L^z, 1, 0), \tag{5.60}$$

$$\tag{5.61}$$

introducing the volume dependence of the time scale $\xi_t \sim L^z$.

Illustrated in Fig. 5.17 is the data rescaled according to Eq. (5.61). Overlap in the data revealing the scaling function $f_{L,T^{00}}$ confirms the extended scaling hypothesis. Although we find stronger non-critical contributions at small volumes for Model

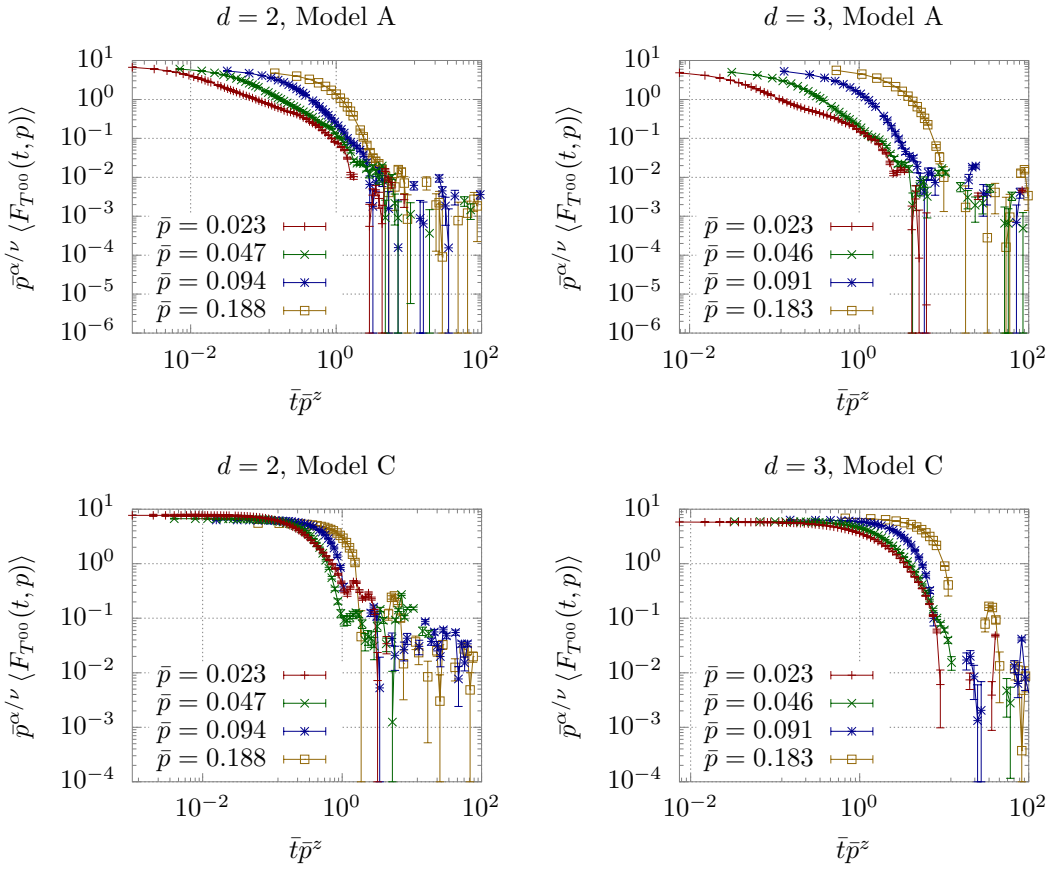

Figure 5.15: Rescaled energy density autocorrelation in the time domain for diffusive dynamics (Models A/C). Overlapping data reveal the scaling function $f_{p,T^{00}}(\bar{t}/\bar{p}^z)$. Modes with lowest spatial momentum start to overlap at $x = \bar{t}\bar{p}^z \approx 1$ for Model A. For higher spatial momentum, the critical contribution is suppressed compared to the non-critical part. In Model C, scaling behavior is barely visible even for the modes of lowest spatial momentum.

A, the dynamic scaling exponents of the order parameter yield excellent overlap at larger volumes. For Model B, we find a deviation for the largest volume, where the autocorrelation function seems to break down too early, which is again explained by the limited total simulation time, obscuring correlations at even later time scales.

5.3.3 Conclusions

Studying the spectral functions of the energy density, we find that there are at least two excitations in all but the symmetric phases. At low spatial momentum, the spectral functions of the energy density are dominated by a structure whose spectral shape and dispersion is reminiscent of a diffusion mode, but with a lower limit on central frequencies given by the heat-bath coupling γ. The second excitation generally seems closely related to the dominant order parameter excitation. For models without conserved order parameter, this is a quasi-particle excitation, which is enhanced at high spatial momentum and low temperatures. In case of the diffusive dynamics of Model D, the second excitation seems to follow the same dispersion relation as the dominant energy diffusion mode, with central frequencies only differing

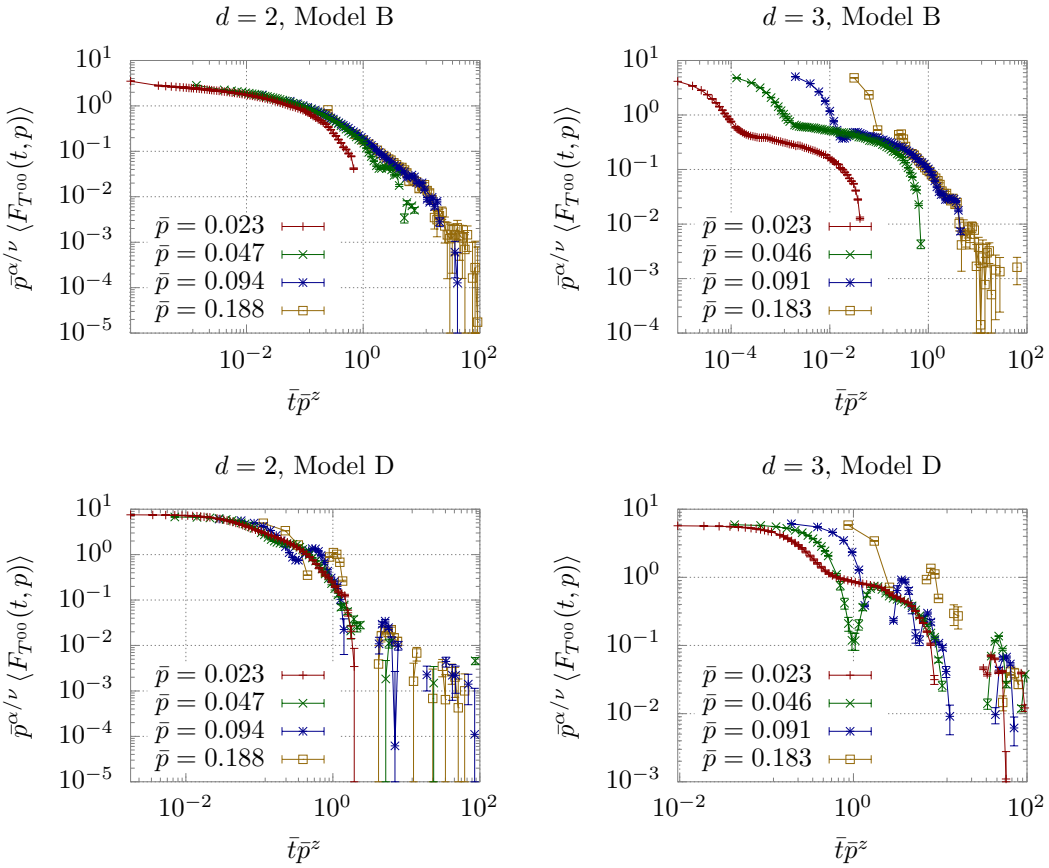

Figure 5.16: Rescaled energy density autocorrelation in the time domain for diffusive dynamics (Models B/D). Overlapping data reveal the scaling function $f_{p,T^{00}}(\bar{t}/\bar{p}^z)$. We observe an excellent scaling collapse in Model B ($\gamma = 0.1$), with some outliers at the lowest spatial momentum. These outliers are caused by the limited total simulation runtime, i.e. we did simply not let the simulation run long enough to record the full extend of the late-time correlations. In Model D, the lowest-momentum modes collapse as expected, while modes at higher momentum receive strong non-critical contributions and therefore start to deviate from the universal scaling function.

by a constant factor. Autocorrelation functions in the time domain are generally suppressed after time scales proportional to the inverse Langevin coupling $1/\gamma$.

Tuning the external parameters to their critical values, we however find late-time contributions that persist much longer, especially at low spatial momentum. By rescaling the autocorrelation functions of the energy density at the critical point in an extension of the dynamic scaling hypothesis, we show that the late-time behavior is controlled by underlying universal scaling functions. In all models, the dynamic critical exponent z seems identical to that controlling the critical behavior of the order parameter.

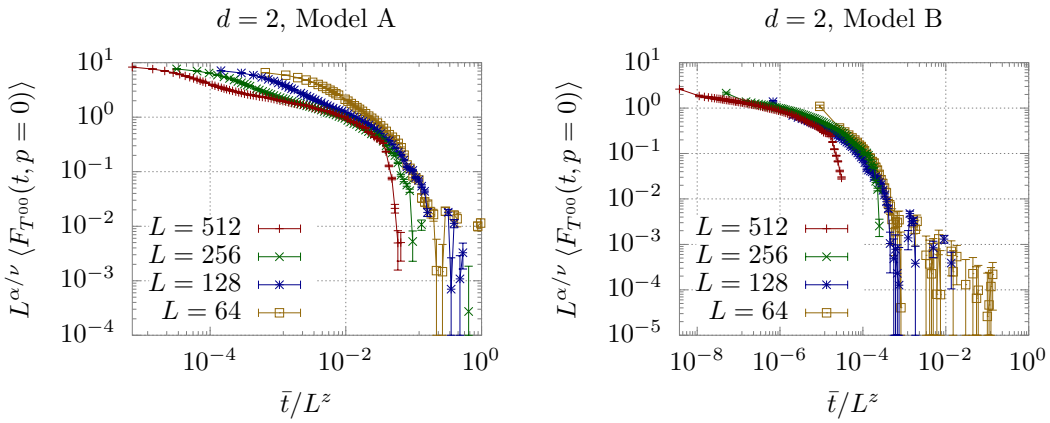

Figure 5.17: Rescaled total energy density autocorrelation in the time domain for finite Langevin coupling $\gamma = 0.1$ in 2+1D. Overlapping data reveal the finite-size scaling function. In Model A, data for the largest volumes collapse, while smaller volumes are largely dominated by non-critical contributions. For Model B, we observe an excellent scaling collapse even for rather small volumes. Deviations for the data at largest volumes are due to the limited total simulation time (compare caption of Fig. 5.16).

6 | Non-equilibrium phenomena

The case for studying non-equilibrium phenomena using the classical lattice model is strong. In context of the search of the QCD critical endpoint in heavy-ion collisions, a deep understanding of the out-of-equilibrium dynamics of the system will be necessary to make well-grounded predictions for signatures in final states. As the system comes close to the critical point, it will at some point inevitably fall out of equilibrium as the relaxation times diverge, and evolve in an out-of-equilibrium state before either re-equilibrating further away from criticality, or freezing out. In-depth knowledge about the evolution of observables like the correlation length during thermalization is therefore valuable, especially since it was shown by Berdnikov and Rajagopal [45] that the sensitivity of the final state on the passing distance to the critical point is rather low. Recent studies [47, 48] furthermore demonstrate the value of universal scaling functions describing the off-equilibrium evolution of higher-order cumulants, which are highly sensitive to the correlation length and thus interesting as signatures of a second-order phase transition. Using the classical lattice model developed in earlier chapters naturally offers itself, as the changes needed to enable non-equilibrium studies are negligible, and boil down to dynamically changing two external parameters.

While there are a multitude of possible ways to drive the system out of equilibrium, the simplest but still interesting approach is to impose a sudden quench on an equilibrated system. After the quench, the system may exhibit different sorts of non-equilibrium behavior depending on the specific dynamic equations governing the evolution. In case of Model-A dynamics, it will slowly relax to equilibrium. Janssen et al. [107] and Huse [108] found independently that the short-time dynamics of a classical system after a quench to the critical point show universal scaling behavior. These universal non-equilibrium dynamics introduce a new dynamic critical exponent θ', related to the scaling dimension of the order parameter at the initial time sheet, and manifesting itself in an algebraic increase of the order parameter during the early phase of thermalization. After some time, the initial conditions become irrelevant and the order parameter starts an algebraic aging decay, with an exponent containing the equilibrium dynamic critical exponent z. The whole process is controlled by an underlying universal non-equilibrium scaling function. Knowing this function, one can exactly predict the evolution of the order parameter, the only input being its initial value.

While there is also recent progress in studying the dynamic critical exponents of Model A with a functional renormalization-group scheme [109], these processes are very amenable to high-precision Monte-Carlo studies. Since one does not need to prepare a system in thermal equilibrium at the critical point, one can efficiently extract critical exponents from the short-time critical dynamics on large-volume lattices with plenty different models [51, 53, 54, 110]. To maximise the signal on

critical exponents, it is beneficial to control the initial conditions very precisely, and prepare the initial state at either zero or very high temperature. Thereby, one can isolate the initial-slip increase from the late-time aging decay, which most of the aforementioned studies do. Here, we aim to connect the two scaling regimes by extracting the underlying universal scaling function, starting from a range of initial values of the order parameter, mediated by thermal initial conditions at different points in the phase diagram.

This chapter is organized as follows: We start by defining the extension of our classical model which enables us to drive the system out of equilibrium, and shortly recap the universal short-time scaling theory. We show that the evolution of the correlation length itself is also governed by a (in case of Model A non-trivial) universal scaling function. Subsequently, we investigate our numerical results and extract the initial-slip exponent θ' as well as the dynamic critical exponent z. Using those results, we rescale the data to obtain the universal non-equilibrium scaling function and its dependence on the initial conditions for both the order parameter and the correlation length, which allows us to fully uncover the "phase diagram" of critical quenches. The last section then gives a summary of our results, and highlights possible further applications of this framework.

6.1 Setup and Theory

We extend the lattice theory defined by Eqs. (2.121) to (2.123) by making both the temperature of the heat bath T as well as the symmetry-breaking term J functions of the simulation time t, such that the equations of motion for the order parameter field ϕ_x on the lattice read

$$\partial_t \phi_x = \frac{\partial H_A}{\partial \pi_x}, \quad \partial_t \pi_x = -\frac{\partial H_A}{\partial \phi_x} - \gamma\, \pi_x + \sqrt{2\gamma T(t)}\, \eta_x(t), \tag{6.1}$$

where the partial lattice derivatives are given by

$$\frac{\partial H_A}{\partial \pi_x} = \pi_x, \quad \frac{\partial H_A}{\partial \phi_x} = -\sum_{y\sim x} (\phi_y - \phi_x) + \left(m^2 + \frac{\lambda}{6}\phi_x^2\right)\phi_x + J(t), \tag{6.2}$$

and the lattice spacing was set to $a = 1$ for simplicity. This setup enables us to drive the system out of equilibrium and observe its non-equilibrium dynamic critical behavior.

For this study, we choose for the time-dependence of external field and temperature the following parametrization

$$J(t) \equiv J_0 \Theta(t_q - t), \tag{6.3}$$

$$T(t) \equiv T_c + (T_0 - T_c)\Theta(t_q - t), \tag{6.4}$$

with the Heaviside step function $\Theta(t)$. Resulting quench trajectories in the phase diagram are illustrated in Fig. 6.1. The system thermalizes for times $t < t_q$ at some point $J = J_0$, $T = T_0$ in the phase diagram. At $t = t_q$, the parameters are instantly changed to their critical values $J = 0$, $T = T_c$, quenching the system onto the critical point. To ease notation, we set $t_q \equiv 0$.

The evolution of the system after the quench can be separated into three time scales. For very short times $t < t_0$, the fastest modes equilibrate to the heat bath.

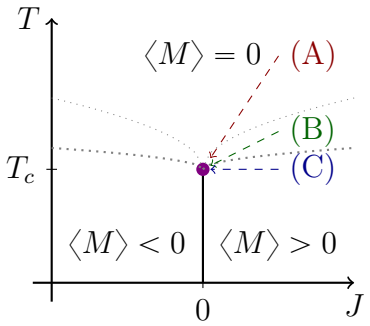

Figure 6.1: Qualitative phase diagram with quench trajectories. The labeled quench trajectories are color-coded to match the data shown in Fig. 6.2. Quench (A) corresponds to very small initial magnetization $m_0 = \langle M \rangle (T_0, J_0)$, which leads to a long initial-slip regime. Trajectories (B) and (C) start at higher m_0, leading to an earlier onset of the aging decay.

Processes on this scale are strictly dependent on microscopic properties of the system and thus do not exhibit universal behavior. In the asymptotic long-time regime for $t \to \infty$, when all modes but the slowest order-parameter mode are in equilibrium and any initial conditions are irrelevant, the system dynamics are characterized by the equilibrium dynamic critical exponent z. It was first shown by Janssen, Schaub and Schmittmann [107] that in between those scales exists a temporal window where initial conditions are still relevant, but the dynamics are already governed by universal functions and an additional critical exponent.

Specifically, the evolution of the k-th moment of the order parameter

$$M^{(k)} = \left(\frac{1}{V} \sum_x \phi_x \right)^k \tag{6.5}$$

after a quench to $J = 0, \tau$ is given by the scaling form

$$M^{(k)}(t, \tau, m_0) = s^{-k\beta/\nu} M^{(k)} \left(s^{-z} t, s^{1/\nu} \tau, s^{x_0} m_0 \right), \tag{6.6}$$

where m_0 denotes the order parameter $M(t = t_q)$ on the initial time sheet, and s is an arbitrary scale parameter. At the critical point, the reduced temperature $\tau \equiv T/T_c - 1$ vanishes. By letting $s = t^{1/z}$, one then has for the evolution of the k-th moment of the order parameter

$$M^{(k)}(t, \tau = 0, m_0) = t^{\frac{-k\beta}{\nu z}} M^{(k)}(1, 0, t^{x_0/z} m_0). \tag{6.7}$$

with the universal *non-equilibrium scaling functions* $M^{(k)}(1, 0, x)$. Since in the limit of late times, the magnetization and its higher moments should become independent of the value m_0 of the magnetization on the initial time sheet, the large-x behavior of the scaling function must be given by

$$\lim_{x \to \infty} M^{(k)}(1, 0, x) \sim \text{const}, \tag{6.8}$$

leading to an algebraic decay of the moments of the order parameter as $M^{(k)}(t) \sim t^{-k\beta/\nu z}$. Inversely, its small-$x$ limit is given by

$$\lim_{x \to 0} M^{(k)}(1, 0, x) \sim x^k, \tag{6.9}$$

as the system responds linearly to the initial condition. This leads to the order parameter increasing algebraically at early times as

$$M^{(k)}(t, \tau = 0, m_0) = t^{k\left(\frac{-\beta}{\nu z} + \frac{x_0}{z}\right)} m_0 \sim t^{k\theta'}, \tag{6.10}$$

with the *initial-slip exponent* $\theta' \equiv x_0/z - \beta/\nu z$ compactifying the notation. When focusing on the early-time behavior, it is useful to rewrite Eq. (6.7) as

$$\begin{aligned} M^{(k)}(t, \tau = 0, m_0) &= t^{\frac{-k\beta}{\nu z}} M^{(k)}(1, 0, t^{x_0/z}\, m_0) && (6.11)\\ &= m_0^k t^{k\left(\frac{-\beta}{\nu z} + \frac{x_0}{z}\right)} \left(\frac{M^{(k)}(1, 0, t^{x_0/z}\, m_0)}{(t^{x_0/z}\, m_0)^k} \right) && (6.12)\\ &\equiv m_0^k t^{k\theta'} f_{M,k}(m_0 t^{\theta' + \beta/\nu z}), && (6.13) \end{aligned}$$

where we defined the universal non-equilibrium scaling function $f_{M,k}(x) \sim M^{(k)}(1, 0, x)/x^k$. Its limits can be easily deduced from Eqs. (6.8) and (6.9) as

$$\lim_{x \to 0} f_{M,k}(x) \sim \text{const}, \tag{6.14}$$

$$\lim_{x \to \infty} f_{M,k}(x) \sim x^{-k}. \tag{6.15}$$

While previous studies exist that determine the initial-slip exponent θ' in Ising-like models (see e.g. [111] for a review), they typically control the initial conditions very precisely, and start from a sharp distribution for the initial magnetization m_0. Since this is hardly a valid assumption for natural systems, for example in the context of heavy-ion collisions, we investigate how a more realistic (i.e. thermal) distribution of the initial magnetization effects the emergence of universal behavior. Additionally, we aim to quantify the connection between short-time universal behavior controlled by the initial-slip exponent θ' and long-time decay controlled by the dynamic critical exponent z, which is mediated by the universal non-equilibrium scaling function $f_k(x)$ defined above. This will enable us to identify the "phase-diagram" of critical quenches by relating the dominant short-time behavior to the starting point of the critical quench in the phase diagram of the theory.

Additionally, we consider the evolution of the correlation length $\xi(t)$. In analogy to Eq. (6.6), we write down a scale-invariant ansatz for the evolution of the correlation length as some universal function governing the time evolution depending on the final reduced temperature τ and the initial condition m_0 as

$$\xi(t, \tau, m_0) = s\xi(s^{-z}t, s^{1/\nu}\tau, s^{x_0} m_0). \tag{6.16}$$

By letting $s \equiv t^{1/z}$, we remove the dependence on the first parameter and define the scaling function $g(x, y)$ of the correlation length, such that its evolution is given by

$$\xi(t, \tau, m_0) = t^{1/z} g(t^{x_0/z} m_0, t^{1/\nu z}\tau). \tag{6.17}$$

At finite distance to the critical point $|\tau| > 0$, the correlation length saturates at its equilibrium value in the limit of large waiting time $t \to \infty$. Therefore, the dependence on the time t must cancel in this limit, and we have

$$\lim_{t \to \infty} \xi(t, m_0, \tau) = \lim_{t \to \infty} t^{1/z} g(t^{x0/z} m_0, t^{1/\nu z}\tau) \to f^{\pm} |\tau|^{-\nu}. \tag{6.18}$$

This holds true independently of the initial condition m_0, thus fixing the limits of the scaling function for diverging second argument, namely

$$\lim_{y\to\pm\infty} g(0,y) = \lim_{y\to\pm\infty}\lim_{x\to\infty} g(x,y) = f^{\pm}|y|^{-\nu}. \tag{6.19}$$

If the system is quenched to the critical point, i.e. $\tau = 0$, we instead have

$$\xi(t,\tau\to 0,m_0) = t^{1/z} g(t^{x_0/z}m_0, 0). \tag{6.20}$$

At large times t, the correlation length must again become insensitive to the initial condition, yielding

$$\lim_{x\to\pm\infty} g(x,0) = \text{const.} \equiv g_\infty \tag{6.21}$$

Concerning the small-x limit, we remark that for symmetry reasons, one expects $g(x,0) = g(-x,0)$ to be even in its first argument and regular at $x = 0$. We thus write

$$g(0,0) \equiv g_0 > 0. \tag{6.22}$$

If the initial magnetization vanishes, e.g. when starting the quench in the symmetry-restored phase with $m_0 = 0$, the correlation length will grow algebraically with the same exponent as for large m_0, but possibly with a different amplitude. For intermediate values of x, the scaling function $g(x,0)$ might not be constant, as the two limits g_∞ and g_0 are not necessarily identical. Nevertheless we certainly should find that rescaling data as

$$t^{-1/z}\xi(t,\tau=0,m_0) = g(t^{x0/z}m_0, 0) \tag{6.23}$$

reveals the scaling function of the correlation length, asymptotically approaching a constant for both small and large values of the argument $x = t^{x_0/z}m_0$.

6.2 Non-equilibrium scaling

We start our numerical studies by observing the evolution of the order parameter. Data presented here is typically obtained by averaging over ~ 100 ensembles with sizes 512^2 respectively 512^3 if not stated otherwise. Since the systems thermalize at some distance to the critical point, equilibration from a hot start does not take too long, but we use $t_{\text{eq}} = 1000$ in 2+1D and $t_{\text{eq}} = 250$ in 3+1D in lattice units to be on the safe side. Any observables are averaged over the independent ensembles.

In Fig. 6.2 we show time histories of the expectation value $\langle M(t)\rangle$ after a quench to the critical point with different initial conditions. We see that generally, the lower the initial magnetization, the longer becomes the initial-slip phase where the order parameter first grows, before it hits the late-time decay. The amplitude of the late-time decay is independent of the initial conditions, confirming Eqs. (6.8) and (6.15). This matches the qualitative predictions from the limiting behavior of the universal non-equilibrium scaling function $f_{M,1}(x)$. The initial algebraic growth of the order parameter is controlled by the initial-slip exponent θ'. We find it is weaker in 3+1D than in 2+1D, which would imply that the corresponding initial-slip exponent θ' is smaller. Combined with the fact that the decay exponent $\beta/\nu z$ is much larger in 3+1D, this means that to observe long enough initial slip to obtain a sufficient signal, one has to start at very small values of the initial magnetization

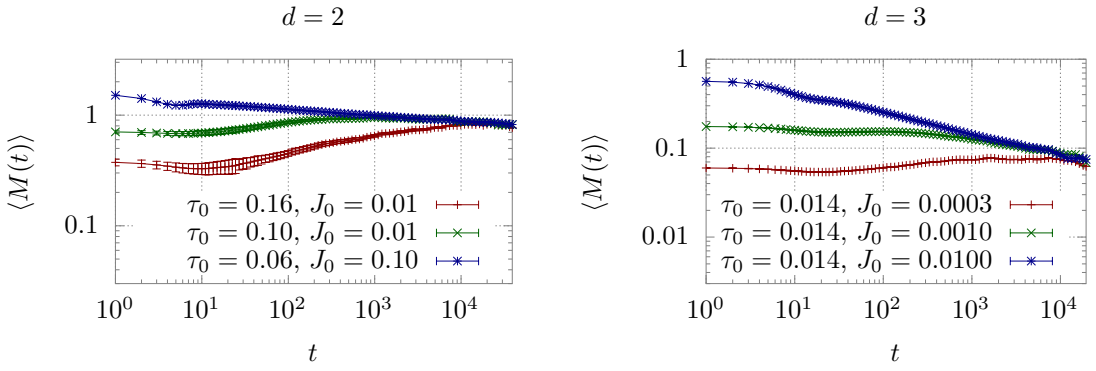

Figure 6.2: Order parameter over time after an instant quench to the critical point from different thermal initial states τ_0, J_0. The lower the initial magnetization m_0, the longer the initial slip takes before the curves collapse onto the late-time decay, which in contrast is independent of m_0. The initial-slip exponent θ' is ostensibly smaller in 3+1D, since the initial growth of the order parameter is much less steep.

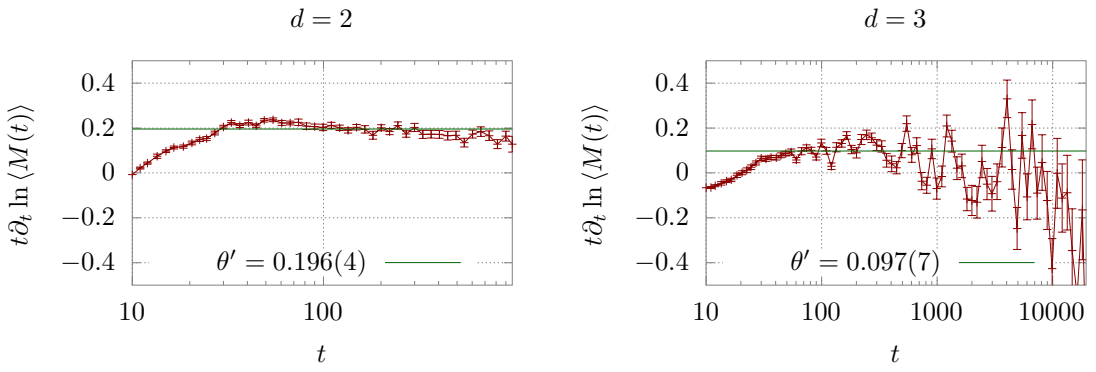

Figure 6.3: Logarithmic derivative w.r.t. $\ln t$ of the order parameter, to extract the initial-slip exponent θ' as outlined in Eq. (6.24) Data in 2+1D was averaged over 9000 ensembles of size 256^2 to minimize noise. In 3+1D, we only have about 120 ensembles of volume 512^3, leading to much larger fluctuations in the effective exponent and thus larger uncertainty. We determine the plateau used to fit the initial-slip exponent θ' by minimizing χ^2/d.o.f. for the fit to a constant over different intervals.

m_0, which can only be realized on relatively large lattices. In 2+1D however, the larger θ' and smaller $\beta/\nu z$ mean that one can obtain a sufficient signal already with larger m_0 and thus smaller lattice volumes.

We proceed by extracting the exponent θ' from the time history of $\langle M(t) \rangle$ of ensembles with sufficiently small initial magnetization m_0 maximize the signal while keeping computation times ecologically sensible. Equation (6.10) implies that we can obtain the exponent by taking the logarithmic time-derivative

$$\theta'_{\text{eff}}(t) = t\partial_t \ln M(t), \tag{6.24}$$

where we look for a plateau in the data, which we then fit with a constant to estimate the true θ'. We illustrate the numerical procedure in Fig. 6.3. We find $\theta' = .196(4)$ for 2+1D and $\theta' = .097(7)$ for 3+1D, which is in range of the results $\theta' = .191(3)$ in 2+1D and $\theta' = .104(3)$ in 3+1D obtained in the Ising model on large lattices by Grassberger [51].

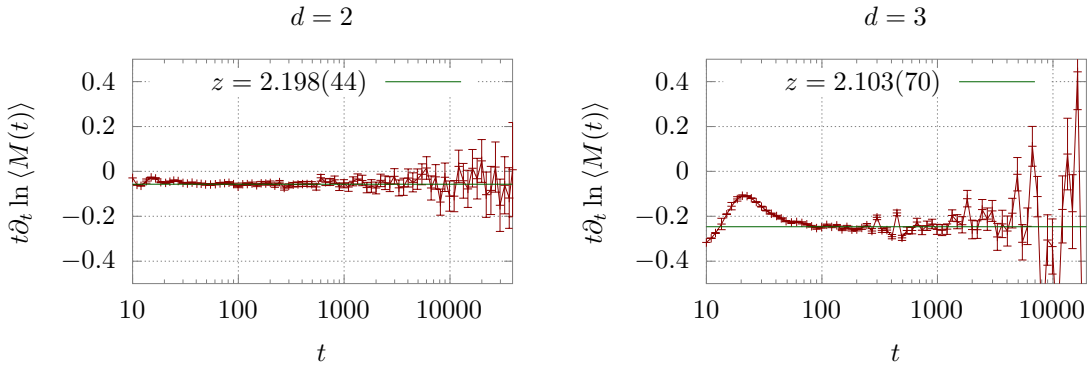

Figure 6.4: Illustration of Eq. (6.25) to extract the dynamic critical exponent z in a fashion analogous to Fig. 6.3. Note that now the effective exponent corresponds to $-\frac{\beta}{\nu z}$. For this data set, 1000 ensembles were averaged for the 2+1D data and about 120 for 3+1D. In both cases, we used lattices of size $L = 512$, to maximize the time before decorrelation due to finite-size effects limiting the correlation time ξ_t.

With the same technique, illustrated in Fig. 6.4, we extract the dynamic critical exponent z from the decay of the order parameter at late times, again taking the logarithmic derivative to obtain

$$z^{-1} = -\frac{\nu}{\beta}(t\partial_t \ln M(t)). \tag{6.25}$$

In contrast to before, we now take a data set with comparatively large magnetization m_0 on the initial time sheet, so that the data immediately collapses onto the large-x branch of the scaling function $f_{M,1}(x) \sim x^{-1}$. We find significantly stronger noise, leading to a larger error on the extracted exponents $z = 2.20(4)$ in 2+1D and 2.10(7) 3+1D, compared to $z = 2.172(6)$ and $z = 2.032(4)$ by Grassberger [51]. Our results are also compatible with those obtained by the analysis of the scaling behavior of the spectral functions in Section 4.3.

Now that we extracted and confirmed the relevant dynamic critical exponents, we proceed with rescaling the time histories of $\langle M(t)\rangle$ shown in Fig. 6.2 to reveal the underlying scaling function. In Fig. 6.5, we show that the curves given in Fig. 6.2 are well described by a universal non-equilibrium scaling function, with the only exception of microscopic relaxation times at $t < \gamma^{-1} = 10$ of the order of the inverse heat-bath coupling. Taking for the initial magnetization $m_0 \equiv M(t = 0)$ and rescaling the data to reveal $f_{M,1}(x)$ from Eq. (6.13), we find that the data points fall nicely onto a single curve. The qualitative shape of the universal function shown in Fig. 6.5 indicates that the limiting small-x behavior of $f_{M,1}(x) \sim$ constant is indeed observed.

We parametrize the universal function describing the crossover between initial-slip and aging using the heuristic ansatz

$$f_{M,1}(x) = \frac{a}{(b + x^c)^{1/c}}, \tag{6.26}$$

with free parameters a, b, c. This function describes the curve connecting the initial-slip with the aging decay surprisingly well. While a corresponds to the amplitude of the aging decay, c controls the radius of the curve, and the combination $a/b^{1/c}$ yields the small-x limit.

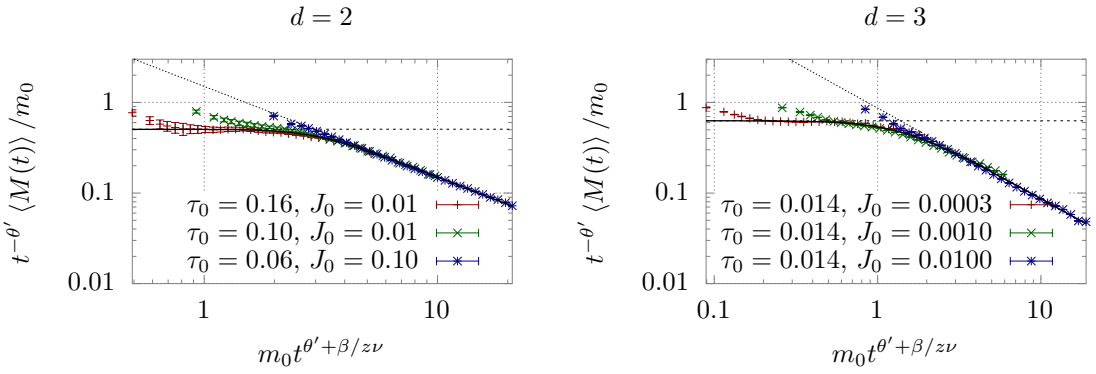

Figure 6.5: Order parameter over time, rescaled to reveal the universal non-equilibrium scaling function. With exception of the microscopic equilibration time scale $\sim 1/\gamma$, the data is well described by a single function $f_{M,1}(x)$. Both the small-x limit $f_{M,1}(x) \to \text{const}$ (dashed line) as well as the large-x limit $f_{M,1}(x) \to 1/x$ (dotted line) can be observed. Solid lines show a simple heuristic parametrization using three parameters defined in Eq. (6.26).

Having established a parametrization of the universal non-equilibrium scaling function $f_{M,1}(x)$ *for all* x, we can predict the time history of the magnetization $\langle M(t) \rangle$ after a quench to the critical point for *any* starting point in the phase diagram. The only ingredient missing so far is the initial magnetization $m_0(\tau, J)$, for which we can also extract a universal function controlling its critical contribution. In a region around the critical point, we can use scale invariance again to derive for the equilibrium magnetization

$$\langle M \rangle (\tau, J) = s^{-\beta/\nu} \langle M \rangle (s^{1/\nu}\tau, s^{\beta\delta/\nu} J) \tag{6.27}$$

$$= |\tau|^{-\beta} m_{\pm}(|\tau|^{\beta\delta}/J), \tag{6.28}$$

where we set $s = -|\tau|^{\nu}$ and inverted the dependence on the symmetry breaking without changing the physical content. Thus, we have $m(x)$ as the universal scaling function of the magnetization in equilibrium. Figure 6.6 shows exemplary results for $m(x)$ in 2D. By interpolating the data, one can infer the initial condition $\langle M \rangle (T_0, J_0) \equiv m_0$ for thermal initial conditions at T_0, J_0. We therefore have all necessary prerequisites to predict the evolution of $M(t)$ for any quench trajectory starting in a neighborhood of the critical point.

Finally, we investigate the time evolution of the correlation length $\xi(t)$, which we extract from line-(plane-)correlation functions $G(n)$ at separation n as

$$\xi_{\text{eff.}}(n) = \frac{-1}{\ln\left(\bar{G}(n+1)/\bar{G}(n)\right)}, \tag{6.29}$$

where we subsequently identify a plateau in $\xi_{\text{eff.}}$ to fit ξ, analogously to the procedure outlined in Section 4.1, Eqs. (4.10) to (4.12). Since in the finite lattice volume, the correlation length is bounded from above by the system size $\xi \leqslant L$, it will saturate at some time $t_f \sim L^z$, after which other observables will be compromised by finite-size effects as well. Therefore it is a useful sanity check to see if our numerical setup can show the anticipated non-equilibrium behavior of the order parameter, by examining whether the correlation length $\xi(t)$ saturates within the time-scale of our observations. Figure 6.7 shows the algebraic growth of the correlation length after a quench to

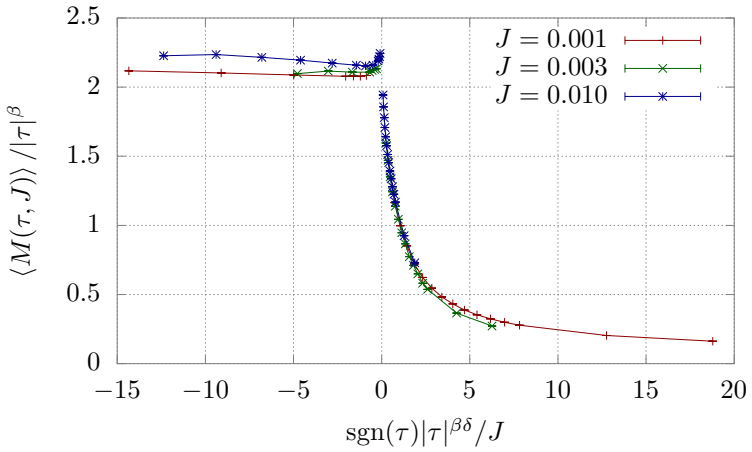

Figure 6.6: Universal scaling function $m(\tau^{\beta\delta})$ of the equilibrium magnetization. One can infer the expectation value of the order parameter in a region around the critical point. Using the result as input for the universal non-equilibrium scaling function $f_{M,1}(x)$ allows us to predict the evolution of $M(t)$ after a critical quench starting at any T_0, J_0 in a region around the critical point.

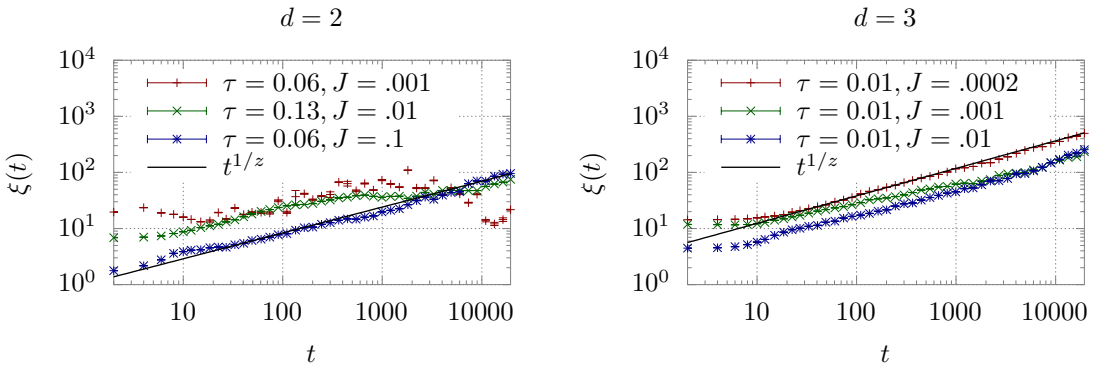

Figure 6.7: Correlation length $\xi(t)$ over time after an instant quench from τ, J to the critical point in Model A at $\gamma = 0.1$. Dashed lines exemplary show the predicted algebraic growth $\sim t^{1/z}$. After some microscopic relaxation time of the order of the inverse heat-bath coupling strength γ^{-1}, the correlation length starts to grow algebraically as expected. There is indication of the correlation length saturating at $\xi \sim L$ in 2+1D at large $t \sim 10^4$, as the data was generated on lattice volumes of 256^2. For 3+1D, saturation is not reached in the observed time frame.

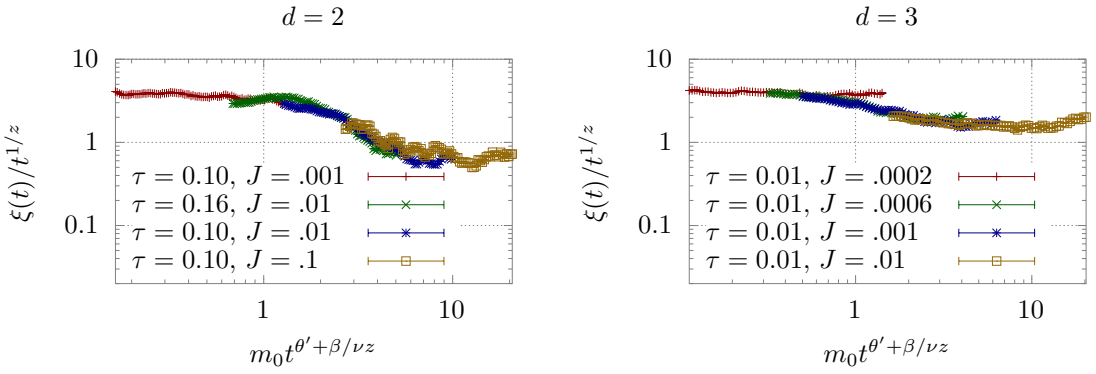

Figure 6.8: Rescaled time histories of $\xi(t)$ to reveal the universal non-equilibrium scaling function $g(x, 0)$. Since the correlation length is extracted indirectly, one observes rather large fluctuations. Especially if $\xi(t)$ becomes large, the method described in Eq. (6.29) becomes less reliable. Nevertheless we find clear evidence that $g(x, 0)$ is not constant for intermediate values of $x \sim 1$, and that the limits differ as well, with $g_{t,0} > g_{t,\infty}$.

the critical point. The first few time steps show that during the initial microscopic relaxation time, which is of the order of the inverse heat-bath coupling $\gamma^{-1} = 10$, the correlation length hardly changes. Afterwards, it begins to grow algebraically as $t^{-1/z}$ with the dynamic critical exponent z, until it runs into its finite-volume limit at $\xi(t) \sim L$. We find however that for the ensembles we investigate, the saturation time $t_f \gg 10^4$ at $L = 512$ is sufficiently large to fully take advantage of all the data gathered in the following.

One thing that stands out is that the time histories of $\xi(t)$ seem to distinctly fall into two "channels" depending on the initial conditions, and at some point switch from a power-law with a larger amplitude to one with lower amplitude. It turns out that the time scale of this crossing-over is identical to the time scale on which the order parameter behavior changes from initial-slip growth to aging decay. This is compatible with the assumption that the evolution of $\xi(t)$ is governed by an underlying scaling function $g(t^{x_0/z} m_0, 0)$ with the same argument as the scaling function of the order parameter $f_M(t^{x_0/z} m_0)$. We thus present in Fig. 6.8 the time histories of $\xi(t)$ rescaled in such a way to reveal the underlying scaling function $g(x, 0)$. As expected, we find that both its small-x and large-x limit are given by constants, and we find in both 2+1D and 3+1D that $g_0 > g_\infty$. For intermediate values of $x \sim 1$, the universal scaling function $g(x, 0)$ decreases monotonically. The two "channels" observed in the un-rescaled version in Fig. 6.7 correspond to the two different constant limits.

The function $g(x, 0)$ in combination with the knowledge of $m_0 = \langle M \rangle (\tau_0, J_0)$ allows to exactly predict the evolution of $\xi(t)$ for times $t \gtrsim \gamma^{-1}$ after a quench to the critical point. If the initial magnetization $m_0 > 0$ is small but nonzero, the correlation length will grow as $\xi(t) = g_0 t^{1/z}$ up to some cross-over timescale $t_c \approx m_0^{-z/x_0}$, where growth will slow down temporarily, until it resumes growing with $g_\infty t^{1/z}$. For larger m_0, the first two stages happen faster and the system crosses over to $\xi(t) \sim g_\infty t^{1/z}$ earlier. If there is no initial magnetization, the evolution of the correlation length is given by a single power law $\xi(t) \sim g_0 t^{1/z}$.

6.3 Conclusions

We have investigated the non-equilibrium critical behavior after a quench to the critical point of a relativistic scalar theory with a Z_2 order-parameter symmetry in 2+1D and 3+1D. During the relaxation process, we observed the expected universal scaling behavior of the order parameter, interpolating between an initial increase governed by the initial-slip exponent θ' depending on the initial condition, and algebraic decay at late times governed by the equilibrium dynamic critical exponent z. We obtained the exponents by investigating the logarithmic derivative w.r.t. logarithmic time. The accuracy of this process proved sufficient to rescale the data to reveal the underlying universal non-equilibrium scaling function governing the evolution of the order parameter. Using a heuristic parametrization of this function, we are now able to predict the critical contribution of the time evolution of the order parameter after quenching to the critical point from some arbitrary thermal initial state in a region around the critical point.

We ensured that finite-size effects do not affect our results by observing the evolution of the correlation length and its saturation time scale. Using the exponents obtained from the evolution of the order parameter, we were able to rescale the data for the correlation length to reveal its underlying universal non-equilibrium scaling function as well. We found non-trivial behavior around the same region as for the scaling function of the order parameter.

With these tools, we are now well equipped to explore more realistic non-equilibrium processes. The most trivial extension would be to quench the system to a point close to, but not directly at the critical endpoint, and investigate how much of the time evolution is still given by the non-equilibrium universal function. We conjecture that, as long as the equilibrium correlation length is much larger than the actual one, quench-like behavior will be dominant.

This study can be extended to more possible non-equilibrium processes, where the heat-bath temperature and external field are changed continuously over time and closely pass the critical point. Such a study on this model is currently in preparation, planning to test the applicability of the Kibble-Zurek framework [112] and investigating the non-equilibrium evolution of higher-order cumulants, which are especially interesting in the context of the search for the QCD critical point [113].

7 | Summary & Outlook

We have demonstrated the power of the classical-statistical approach to study real-time properties of a relativistic Z_2 field theory in 2+1D and 3+1D. We have developed continuum models with two distinct sets of dynamic equations sharing the same stationary equilibrium, however with very different dynamic properties. Deriving lattice representations of these models and their dynamics enabled us to non-perturbatively calculate static as well as dynamic observables from first principles.

Computing the spectral function of the order parameter enabled us to identify the relevant dynamic degrees of freedom for the different dynamics in all regions of the phase diagram. We have observed that for the diffusive dynamics with conserved order parameter, the spectral function generally stays similar to its mean-field form, while in Models A and C an additional soft collective excitation appears in the ordered phase at low frequencies, which vanishes in the symmetric phase. Close to the critical point, we found singular behavior in the characteristic relaxation time scales, supportive of the dynamic universality hypothesis. When determining the dynamic critical exponents, we found the expected behavior for Models A, B, and C, while confirming that our relativistic definition of Model D shows critical dynamics which are fundamentally different from its non-relativistic counterpart. Furthermore, we were able to extract two-variable universal dynamic scaling functions, which describe the critical contributions to the spectral functions exactly.

Studying the energy-momentum tensor of our models, we found that while energy conservation could be fulfilled to numerical accuracy, the reduction of the continuous spatial translation symmetry to a discrete one leads to deviations from momentum conservation. We highlighted several resulting problems of earlier studies aiming to extract transport coefficients from lattice calculations, and reproduced those studies with our models. We concluded that studies at smaller spatial lattice spacings are required to clarify how the computed quantities are related to physical transport coefficients. Additionally, we have analyzed autocorrelation- and spectral functions of the energy density in a manner similar to our analysis of the order parameter equilibrium dynamics. We were able to observe critical scaling behavior of the energy density as well, which matched our observations of the critical dynamics of the order parameter.

After trivially extending our model to account for dynamic changes in external symmetry-breaking field and heat-bath temperature, we have investigated universal non-equilibrium behavior of Model A after an instant quench to the critical point. In particular, we have observed the anticipated universal scaling behavior of both order parameter and correlation length, and we were able to compute the relevant dynamic critical exponents with sufficient accuracy. This enabled us to extract the respective universal non-equilibrium scaling functions and their limits, allowing us to

predict the evolution of correlation length and magnetization after instant quenches to the critical point starting in a large region around the critical point.

Now that we have demonstrated the power of universal scaling functions in both equilibrium and non-equilibrium settings, a natural next target lies in the analysis of more complex non-equilibrium phenomena involving finite quenching rates to be analyzed in the context of the Kibble-Zurek framework [112]. One might study more realistic trajectories, e.g. adiabatic processes, and investigate if there is any measurable difference in observed final states. Conceivably, one may also modify the framework to study the classical dynamics of expanding systems. This could serve as a rigorous test of the back-of-the-envelope calculation in [45]. The ultimate goal is to develop a reconstruction protocol for the location of the critical endpoint, based only on knowledge about some thermal initial conditions and the observed final state.

At some point, one would however have to introduce a more complex QCD-like model, which shares not only the static 3D Ising universality class, but whose dynamics are also described by Model H in [13]. Here, we made an important step by introducing a relativistic lattice version of Model B. The extension to Model H involves the coupling of the Model-B order parameter to a conserved transverse vector field via an advection term. We are as of today unsure of how to implement this; some first ideas involve for example a coupled system of a lattice order parameter and a relativistic fluid, whose equations of motion could be solved with a relativistic lattice Boltzmann method (see [114] for a review).

On a similar note, it may be beneficial to extend our study on the energy-momentum tensor of classical lattice theories to components other than the energy density, studying in detail the regions where the systems main excitations can effectively be described by hydrodynamic equations. Not only crucial to gauging the validity of computing transport coefficients on the lattice, this might also help with our understanding of the dynamics of Model H.

While we have shown that we can learn a lot from classical-statistical models, it is interesting and important to quantify the corrections to this limit due to quantum fluctuations. Exciting new approaches to that end include the development of functional renormalization group methods on the Keldysh contour [115]. These encounter their own new challenges, since additionally to choosing a suitable truncation scheme, one has to make sure that the regulator functions preserve causality. First-principles classical-statistical simulations can function as a very effective benchmark for scalar theories, since the classical theory is recovered by simply eliminating the quantum interaction vertex and all associated diagrams. Preliminary results for spectral functions of the relativistic scalar theory with Model-A dynamics are very promising in this regard.

Another approach currently under development is the Gaussian state approximation [116, 117]. Assuming that the full quantum state is given by an ensemble of Gaussian states, one can derive classical equations of motion for a system with $N + N^2$ degrees of freedom, evolving both expectation values as well as two-point correlation functions in time. Challenges of applying this method to a field theory include the computational effort growing quadratically with the volume, as well as consistently constructing a heat bath. A review comparing the Gaussian state approximation to both the classical-statistical method as well as FRG on the Keldysh contour is currently in preparation.

Bibliography

[1] Y. Aoki, G. Endrődi, Z. Fodor, S. D. Katz, and K. K. Szabó. The order of the quantum chromodynamics transition predicted by the standard model of particle physics. *Nature*, 443(7112):675–678, October 2006. Number: 7112 Publisher: Nature Publishing Group.

[2] Szabolcs Borsányi, Zoltán Fodor, Christian Hoelbling, Sándor D. Katz, Stefan Krieg, Claudia Ratti, and Kálmán K. Szabó. Is there still any Tcmystery in lattice QCD? Results with physical masses in the continuum limit III. *Journal of High Energy Physics*, 2010(9):73, September 2010.

[3] HotQCD Collaboration, A. Bazavov, Tanmoy Bhattacharya, C. DeTar, H.-T. Ding, Steven Gottlieb, Rajan Gupta, P. Hegde, U. M. Heller, F. Karsch, E. Laermann, L. Levkova, Swagato Mukherjee, P. Petreczky, C. Schmidt, C. Schroeder, R. A. Soltz, W. Soeldner, R. Sugar, M. Wagner, and P. Vranas. Equation of state in ($2+1$)-flavor QCD. *Physical Review D*, 90(9):094503, November 2014. Publisher: American Physical Society.

[4] M. Stephanov, K. Rajagopal, and E. Shuryak. Signatures of the Tricritical Point in QCD. *Physical Review Letters*, 81(22):4816–4819, November 1998. arXiv: hep-ph/9806219.

[5] M. Stephanov, K. Rajagopal, and E. Shuryak. Event-by-Event Fluctuations in Heavy Ion Collisions and the QCD Critical Point. *Physical Review D*, 60(11):114028, November 1999. arXiv: hep-ph/9903292.

[6] R. Rapp, T. Schaefer, E. V. Shuryak, and M. Velkovsky. Diquark Bose Condensates in High Density Matter and Instantons. *Physical Review Letters*, 81(1):53–56, July 1998. arXiv: hep-ph/9711396.

[7] J. Berges and K. Rajagopal. Color Superconductivity and Chiral Symmetry Restoration at Nonzero Baryon Density and Temperature. *Nuclear Physics B*, 538(1-2):215–232, January 1999. arXiv: hep-ph/9804233.

[8] Grazyna Odyniec. RHIC Beam Energy Scan Program: Phase I and II. In *Proceedings of 8th International Workshop on Critical Point and Onset of Deconfinement — PoS(CPOD 2013)*, volume 185, page 043. SISSA Medialab, September 2013.

[9] Adam Bzdak, ShinIchi Esumi, Volker Koch, Jinfeng Liao, Mikhail Stephanov, and Nu Xu. Mapping the Phases of Quantum Chromodynamics with Beam Energy Scan. *Physics Reports*, 853:1–87, April 2020. arXiv: 1906.00936.

[10] Philippe de Forcrand. Simulating QCD at finite density. *arXiv:1005.0539 [cond-mat, physics:hep-lat]*, June 2010. arXiv: 1005.0539.

[11] M. Bluhm, M. Nahrgang, A. Kalweit, M. Arslandok, P. Braun-Munzinger, S. Floerchinger, E. S. Fraga, M. Gazdzicki, C. Hartnack, C. Herold, R. Holzmann, Iu Karpenko, M. Kitazawa, V. Koch, S. Leupold, A. Mazeliauskas, B. Mohanty, A. Ohlson, D. Oliinychenko, J. M. Pawlowski, C. Plumberg, G. W. Ridgway, T. Schäfer, I. Selyuzhenkov, J. Stachel, M. Stephanov, D. Teaney, N. Touroux, V. Vovchenko, and N. Wink. Dynamics of critical fluctuations: Theory – phenomenology – heavy-ion collisions. *arXiv:2001.08831 [hep-ph, physics:nucl-ex, physics:nucl-th]*, January 2020. arXiv: 2001.08831.

[12] K. Rajagopal and F. Wilczek. Static and Dynamic Critical Phenomena at a Second Order QCD Phase Transition. *Nuclear Physics B*, 399(2-3):395–425, July 1993. arXiv: hep-ph/9210253.

[13] P. C. Hohenberg and B. I. Halperin. Theory of dynamic critical phenomena. *Reviews of Modern Physics*, 49(3):435–479, July 1977.

[14] M. P. Nightingale and H. W. J. Blöte. The Dynamic Exponent of the Two-Dimensional Ising Model and Monte Carlo Computation of the Sub-Dominant Eigenvalue of the Stochastic Matrix. *Physical Review Letters*, 76(24):4548–4551, June 1996. arXiv: cond-mat/9601059.

[15] D. T. Son and M. A. Stephanov. Dynamic universality class of the QCD critical point. *Physical Review D*, 70(5):056001, September 2004. arXiv: hep-ph/0401052.

[16] Guy D. Moore and Omid Saremi. Bulk viscosity and spectral functions in QCD. *Journal of High Energy Physics*, 2008(09):015–015, September 2008.

[17] Mark Jarrell and J. E. Gubernatis. Bayesian inference and the analytic continuation of imaginary-time quantum Monte Carlo data. *Physics Reports*, 269(3):133–195, May 1996.

[18] M. Asakawa, Y. Nakahara, and T. Hatsuda. Maximum entropy analysis of the spectral functions in lattice QCD. *Progress in Particle and Nuclear Physics*, 46(2):459–508, January 2001.

[19] Yannis Burnier and Alexander Rothkopf. Bayesian Approach to Spectral Function Reconstruction for Euclidean Quantum Field Theories. *Physical Review Letters*, 111(18):182003, October 2013.

[20] Bastian B. Brandt, Anthony Francis, Harvey B. Meyer, and Daniel Robaina. Pion quasiparticle in the low-temperature phase of QCD. *Physical Review D*, 92(9):094510, November 2015.

[21] David Dudal, Orlando Oliveira, and Paulo J. Silva. K\"all\'en-Lehmann spectroscopy for (un)physical degrees of freedom. *Physical Review D*, 89(1):014010, January 2014.

[22] L. Schlessinger. Use of Analyticity in the Calculation of Nonrelativistic Scattering Amplitudes. *Physical Review*, 167(5):1411–1423, March 1968.

[23] R. A. Tripolt, I. Haritan, J. Wambach, and N. Moiseyev. Threshold energies and poles for hadron physical problems by a model-independent universal algorithm. *Physics Letters B*, 774:411–416, November 2017.

[24] Lukas Kades, Jan M. Pawlowski, Alexander Rothkopf, Manuel Scherzer, Julian M. Urban, Sebastian J. Wetzel, Nicolas Wink, and Felix Ziegler. Spectral Reconstruction with Deep Neural Networks. *arXiv:1905.04305 [hep-lat, physics:hep-ph, physics:physics]*, May 2019. arXiv: 1905.04305.

[25] Ralf-Arno Tripolt, Philipp Gubler, Maksim Ulybyshev, and Lorenz von Smekal. Numerical analytic continuation of Euclidean data. *Computer Physics Communications*, 237:129–142, April 2019.

[26] Dirk Roeder, Joerg Ruppert, and Dirk H. Rischke. Selfconsistent calculations of spectral densities in the O(N) model: improving the Hartree-Fock approximation by including nonzero decay widths. *Nuclear Physics A*, 775(1-2):127–151, August 2006. arXiv: hep-ph/0503042.

[27] Linda Shen, Jürgen Berges, Jan Pawlowski, and Alexander Rothkopf. Thermalization and dynamical spectral properties in the quark-meson model. *arXiv:2003.03270 [hep-ph]*, March 2020. arXiv: 2003.03270.

[28] Jens A. Mueller, Christian S. Fischer, and Dominik Nickel. Quark spectral properties above Tc from Dyson-Schwinger equations. *The European Physical Journal C*, 70(4):1037–1049, December 2010. arXiv: 1009.3762.

[29] Christian S. Fischer, Jan M. Pawlowski, Alexander Rothkopf, and Christian A. Welzbacher. Bayesian analysis of quark spectral properties from the Dyson-Schwinger equation. *Physical Review D*, 98(1):014009, July 2018. arXiv: 1705.03207.

[30] Jan Horak, Jan M. Pawlowski, and Nicolas Wink. Spectral functions in the ϕ^4-theory from the spectral DSE. *arXiv:2006.09778 [hep-ph, physics:hep-th]*, June 2020. arXiv: 2006.09778.

[31] Stefan Floerchinger. Analytic continuation of functional renormalization group equations. *Journal of High Energy Physics*, 2012(5):21, May 2012.

[32] Kazuhiko Kamikado, Nils Strodthoff, Lorenz von Smekal, and Jochen Wambach. Real-Time Correlation Functions in the O(N) Model from the Functional Renormalization Group. *The European Physical Journal C*, 74(3):2806, March 2014. arXiv: 1302.6199.

[33] Ralf-Arno Tripolt, Nils Strodthoff, Lorenz von Smekal, and Jochen Wambach. Spectral Functions for the Quark-Meson Model Phase Diagram from the Functional Renormalization Group. *Physical Review D*, 89(3):034010, February 2014. arXiv: 1311.0630.

[34] Ralf-Arno Tripolt, Lorenz von Smekal, and Jochen Wambach. Flow equations for spectral functions at finite external momenta. *Physical Review D*, 90(7):074031, October 2014.

[35] D. Mesterházy, J. H. Stockemer, and Y. Tanizaki. From quantum to classical dynamics: The relativistic $O(N)$ model in the framework of the real-time functional renormalization group. *Physical Review D*, 92(7):076001, October 2015.

[36] Jan M. Pawlowski and Nils Strodthoff. Real time correlation functions and the functional renormalization group. *Physical Review D*, 92(9):094009, November 2015.

[37] Nils Strodthoff. Self-consistent spectral functions in the $O(N)$ model from the functional renormalization group. *Physical Review D*, 95(7):076002, April 2017.

[38] Jan M. Pawlowski, Nils Strodthoff, and Nicolas Wink. Finite temperature spectral functions in the O(N)-model. *Physical Review D*, 98(7):074008, October 2018. arXiv: 1711.07444.

[39] Gert Aarts. Spectral function at high temperature in the classical approximation. *Physics Letters B*, 518(3-4):315–322, October 2001. arXiv: hep-ph/0108125.

[40] J. Berges, S. Schlichting, and D. Sexty. Dynamic critical phenomena from spectral functions on the lattice. *Nuclear Physics B*, 832(1-2):228–240, June 2010. arXiv: 0912.3135.

[41] Sören Schlichting, Dominik Smith, and Lorenz von Smekal. Spectral functions and critical dynamics of the $O(4)$ model from classical-statistical lattice simulations. *arXiv:1908.00912 [cond-mat, physics:hep-lat, physics:hep-ph, physics:nucl-th]*, July 2019. arXiv: 1908.00912.

[42] Ryogo Kubo. Statistical-Mechanical Theory of Irreversible Processes. I. General Theory and Simple Applications to Magnetic and Conduction Problems. *Journal of the Physical Society of Japan*, 12(6):570–586, June 1957.

[43] Paul C. Martin and Julian Schwinger. Theory of Many-Particle Systems. I. *Physical Review*, 115(6):1342–1373, September 1959.

[44] Giorgio Parisi and Jonathan Machta. Statistical Field Theory. *American Journal of Physics*, 57(3):286–287, March 1989.

[45] Boris Berdnikov and Krishna Rajagopal. Slowing Out of Equilibrium Near the QCD Critical Point. *Physical Review D*, 61(10):105017, April 2000. arXiv: hep-ph/9912274.

[46] M. A. Stephanov. Non-Gaussian fluctuations near the QCD critical point. *Physical Review Letters*, 102(3):032301, January 2009. arXiv: 0809.3450.

[47] Swagato Mukherjee, Raju Venugopalan, and Yi Yin. Real time evolution of non-Gaussian cumulants in the QCD critical regime. *Physical Review C*, 92(3):034912, September 2015. arXiv: 1506.00645.

[48] Swagato Mukherjee, Raju Venugopalan, and Yi Yin. Universal off-equilibrium scaling of critical cumulants in the QCD phase diagram. *Physical Review Letters*, 117(22):222301, November 2016. arXiv: 1605.09341.

[49] R. Matz, D. L. Hunter, and Naeem Jan. The dynamic critical exponent of the three-dimensional Ising model. *Journal of Statistical Physics*, 74(3):903–908, February 1994.

[50] F. Wang, N. Hatano, and M. Suzuki. Study on dynamical critical exponents of the Ising model using the damage spreading method. *Journal of Physics A: Mathematical and General*, 28(16):4543–4552, August 1995.

[51] Peter Grassberger. Damage spreading and critical exponents for "model A" Ising dynamics. *Physica A: Statistical Mechanics and its Applications*, 214(4):547–559, April 1995.

[52] Z. Li, L. Schülke, and B. Zheng. Finite Size Scaling and Critical Exponents in Critical Relaxation. *Physical Review E*, 53(3):2940–2948, March 1996. arXiv: cond-mat/9508148.

[53] A. Jaster, Jacques Mainville, L. Schülke, and Biaowen Zheng. Short-time critical dynamics of the 3-dimensional Ising model. *Journal of Physics A-mathematical and General - J PHYS-A-MATH GEN*, 32:1395–1406, February 1999.

[54] B Zheng. Monte Carlo simulations and numerical solutions of short-time critical dynamics. *Physica A: Statistical Mechanics and its Applications*, 283(1):80–85, August 2000.

[55] B. Zheng. Monte Carlo Simulations of Critical Dynamics with Conserved Order Parameter. *Physics Letters A*, 277(4-5):257–261, December 2000. arXiv: cond-mat/0103133.

[56] Dominik Schweitzer, Sören Schlichting, and Lorenz von Smekal. Spectral functions and dynamic critical behavior of relativistic Z_2 theories. *Nuclear Physics B*, 960:115165, November 2020. arXiv: 2007.03374.

[57] Takeo Matsubara. A New Approach to Quantum-Statistical Mechanics. *Progress of Theoretical Physics*, 14(4):351–378, October 1955.

[58] Julian Schwinger. The Special Canonical Group. *Proceedings of the National Academy of Sciences*, 46(10):1401–1415, October 1960. Publisher: National Academy of Sciences Section: Physics.

[59] L. V. Keldysh. Diagram technique for nonequilibrium processes. *Zh. Eksp. Teor. Fiz.*, 47:1515–1527, 1964.

[60] Alex Kamenev. Field Theory of Non-Equilibrium Systems by Alex Kamenev, September 2011.

[61] W. Israel and J. M. Stewart. Transient relativistic thermodynamics and kinetic theory. *Annals of Physics*, 118(2):341–372, April 1979.

[62] W. Israel. Thermodynamics of relativistic systems. *Physica A: Statistical Mechanics and its Applications*, 106(1):204–214, March 1981.

[63] K. Boguslavski and A. Piñeiro Orioli. Unraveling the nature of universal dynamics in $O(N)$ theories. *Phys.Rev.D*, 101(9), November 2019. Number: arXiv:1911.04506.

[64] Asier Piñeiro Orioli and Jürgen Berges. Breaking the Fluctuation-Dissipation Relation by Universal Transport Processes. *Physical Review Letters*, 122(15):150401, April 2019. Publisher: American Physical Society.

[65] ISO/IEC JTC 1/SC 22. ISO/IEC 14882:2020: Programming languages — C++.

[66] Péter Vingelmanm and Frank H.P. Fitzek. CUDA Toolkit, July 2013.

[67] GCC, the GNU Compiler Collection - GNU Project.

[68] CMake.

[69] L. Dagum and R. Menon. OpenMP: an industry standard API for shared-memory programming. *IEEE Computational Science and Engineering*, 5(1):46–55, March 1998.

[70] GPU Cluster 2019.

[71] Cori.

[72] Guido van Rossum, Fred L. Drake, and Guido Van Rossum. *The Python language reference*. Number Guido van Rossum; Fred L. Drake [ed.] ; Pt. 2 in Python documentation manual. Python Software Foundation, Hampton, NH, release 3.0.1 [repr.] edition, 2010. OCLC: 837611997.

[73] Charles R. Harris, K. Jarrod Millman, Stéfan J. van der Walt, Ralf Gommers, Pauli Virtanen, David Cournapeau, Eric Wieser, Julian Taylor, Sebastian Berg, Nathaniel J. Smith, Robert Kern, Matti Picus, Stephan Hoyer, Marten H. van Kerkwijk, Matthew Brett, Allan Haldane, Jaime Fernández del Río, Mark Wiebe, Pearu Peterson, Pierre Gérard-Marchant, Kevin Sheppard, Tyler Reddy, Warren Weckesser, Hameer Abbasi, Christoph Gohlke, and Travis E. Oliphant. Array programming with NumPy. *Nature*, 585(7825):357–362, September 2020.

[74] Alfred V. Aho, Brian W. Kernighan, and Peter J. Weinberger. *The AWK programming language*. Addison-Wesley Pub. Co, Reading, Mass, 1988.

[75] Bash (5.1.4) [Unix shell program].

[76] Philipp K. Janert. *Gnuplot in action*. Manning Publications Co, Shelter Island, NY, second edition edition, 2016. OCLC: ocn913335042.

[77] G. E. P. Box and Mervin E. Muller. A Note on the Generation of Random Normal Deviates. *The Annals of Mathematical Statistics*, 29(2):610–611, 1958. Publisher: Institute of Mathematical Statistics.

[78] Robert C. Tausworthe. Random numbers generated by linear recurrence modulo two. *Mathematics of Computation*, 19(90):201–209, 1965.

[79] Hubert Nguyen and NVIDIA Corporation, editors. *GPU gems 3*. Addison-Wesley, Upper Saddle River, NJ, 2008. OCLC: ocn141855070.

[80] Radford M. Neal. MCMC using Hamiltonian dynamics. *arXiv:1206.1901 [physics, stat]*, June 2012. arXiv: 1206.1901.

[81] Michel Le Bellac. *Thermal Field Theory*. Cambridge Monographs on Mathematical Physics. Cambridge University Press, 1996.

[82] Lars Onsager. Crystal Statistics. I. A Two-Dimensional Model with an Order-Disorder Transition. *Physical Review*, 65(3-4):117–149, February 1944.

[83] Filip Kos, David Poland, David Simmons-Duffin, and Alessandro Vichi. Precision Islands in the Ising and $O(N)$ Models. *Journal of High Energy Physics*, 2016(8):36, August 2016. arXiv: 1603.04436.

[84] Zohar Komargodski and David Simmons-Duffin. The Random-Bond Ising Model in 2.01 and 3 Dimensions. *Journal of Physics A: Mathematical and Theoretical*, 50(15):154001, April 2017. arXiv: 1603.04444.

[85] J. Engels, L. Fromme, and M. Seniuch. Correlation lengths and scaling functions in the three-dimensional O(4) model. *Nuclear Physics B*, 675(3):533–554, December 2003. arXiv: hep-lat/0307032.

[86] Andrea Pelissetto and Ettore Vicari. Critical Phenomena and Renormalization-Group Theory. *Physics Reports*, 368(6):549–727, October 2002. arXiv: cond-mat/0012164.

[87] J. Engels, L. Fromme, and M. Seniuch. Numerical equation of state and other scaling functions from an improved three-dimensional Ising model. *Nuclear Physics B*, 655(3):277–299, April 2003. arXiv: cond-mat/0209492.

[88] B. Dammann and J. D. Reger. Dynamical Critical Exponent of the Two-Dimensional Ising Model. *Europhysics Letters (EPL)*, 21(2):157–162, January 1993.

[89] Martin-D. Lacasse, Jorge Vinals, and Martin Grant. New Dynamic Monte Carlo Renormalization Group Method. *Physical Review B*, 47(10):5646–5652, March 1993. arXiv: cond-mat/9206004.

[90] M. Silvério Soares, J. Kamphorst Leal da Silva, and F. C. SáBarreto. Numerical method to evaluate the dynamical critical exponent. *Physical Review B*, 55(2):1021–1024, January 1997.

[91] M. P. Nightingale and H. W. J. Blöte. Universal Ising dynamics in two dimensions. *Physica A: Statistical Mechanics and its Applications*, 251(1):211–223, March 1998.

[92] M. J. Dunlavy and D. Venus. Critical slowing down in the two-dimensional Ising model measured using ferromagnetic ultrathin films. *Physical Review B*, 71(14):144406, April 2005.

[93] Wei Zhong, Gerard T. Barkema, Debabrata Panja, and Robin C. Ball. Critical dynamical exponent of the two-dimensional scalar ${\ensuremath{\phi}}^{4}$ model with local moves. *Physical Review E*, 98(6):062128, December 2018.

[94] Martin Hasenbusch. The dynamic critical exponent z of the three-dimensional Ising universality class: Monte Carlo simulations of the improved Blume-Capel model. *Physical Review E*, 101(2):022126, February 2020. arXiv: 1908.01702.

[95] D. Niermann, C. P. Grams, P. Becker, L. Bohatý, H. Schenck, and J. Hemberger. Critical slowing down near the multiferroic phase transition in MnWO$_4$. *Physical Review Letters*, 114(3):037204, January 2015. arXiv: 1408.1557.

[96] B. I. Halperin, P. C. Hohenberg, and Shang-keng Ma. Renormalization-group methods for critical dynamics: I. Recursion relations and effects of energy conservation. *Physical Review B*, 10(1):139–153, July 1974. Publisher: American Physical Society.

[97] R. Folk and G. Moser. Critical dynamics: a field-theoretical approach. *Journal of Physics A: Mathematical and General*, 39(24):R207–R313, May 2006. Publisher: IOP Publishing.

[98] M. C. Yalabik and J. D. Gunton. Monte Carlo renormalization-group studies of kinetic Ising models. *Physical Review B*, 25(1):534–537, January 1982. Publisher: American Physical Society.

[99] Aurelia R. Honerkamp-Smith, Benjamin B. Machta, and Sarah L. Keller. Experimental observations of dynamic critical phenomena in a lipid membrane. *arXiv:1104.2613 [cond-mat, physics:physics, q-bio]*, May 2012. arXiv: 1104.2613.

[100] Li Yan. Hydrodynamic modeling of heavy-ion collisions. *Nuclear Physics A*, 967:89–96, November 2017. arXiv: 1704.06643.

[101] Wojciech Florkowski, Michal P Heller, and Michał Spaliński. New theories of relativistic hydrodynamics in the LHC era. *Reports on Progress in Physics*, 81(4):046001, April 2018.

[102] Paul Romatschke and Ulrike Romatschke. *Relativistic Fluid Dynamics In and Out of Equilibrium: And Applications to Relativistic Nuclear Collisions*. Cambridge Monographs on Mathematical Physics. Cambridge University Press, Cambridge, 2019.

[103] M. M. Homor and A. Jakovac. Shear viscosity of the Φ^4 theory from classical simulation. *Physical Review D*, 92(10):105011, November 2015. arXiv: 1505.00930.

[104] Hidefumi Matsuda, Teiji Kunihiro, Akira Ohnishi, and Toru T. Takahashi. Shear viscosity of classical fields in scalar theory. *arXiv:1904.02419 [cond-mat, physics:hep-ph, physics:nucl-th]*, April 2020. arXiv: 1904.02419.

[105] F. J. Belinfante. On the spin angular momentum of mesons. *Physica*, 6(7):887–898, July 1939.

[106] F. J. Belinfante. On the current and the density of the electric charge, the energy, the linear momentum and the angular momentum of arbitrary fields. *Physica*, 7(5):449–474, May 1940.

[107] H. K. Janssen, B. Schaub, and B. Schmittmann. New universal short-time scaling behaviour of critical relaxation processes. *Zeitschrift für Physik B Condensed Matter*, 73(4):539–549, December 1989.

[108] David A. Huse. Remanent magnetization decay at the spin-glass critical point: A new dynamic critical exponent for nonequilibrium autocorrelations. *Physical Review B*, 40(1):304–308, 1989.

[109] Alessio Chiocchetta, Andrea Gambassi, Sebastian Diehl, and Jamir Marino. Universal short-time dynamics: boundary functional renormalization group for a temperature quench. *Physical Review B*, 94(17):174301, November 2016. arXiv: 1606.06272.

[110] K. P. do Nascimento, L. C. de Souza, André L. M. Vilela, H. Eugene Stanley, and A. J. F. de Souza. Short-time Monte Carlo simulation of the majority-vote model on cubic lattices. *arXiv:2008.11861 [cond-mat]*, August 2020. arXiv: 2008.11861 version: 2.

[111] E. V. Albano, M. A. Bab, G. Baglietto, R. A. Borzi, T. S. Grigera, E. S. Loscar, D. E. Rodriguez, M. L. Rubio Puzzo, and G. P. Saracco. Study of phase transitions from short-time non-equilibrium behaviour. *Reports on Progress in Physics*, 74(2):026501, January 2011. Publisher: IOP Publishing.

[112] W. H. Zurek. Cosmological experiments in condensed matter systems. *Physics Reports*, 276(4):177–221, November 1996.

[113] Swagato Mukherjee, Raju Venugopalan, and Yi Yin. Universality regained: Kibble-Zurek dynamics, off-equilibrium scaling and the search for the QCD critical point. *Nuclear Physics A*, 967:820–823, November 2017. arXiv: 1704.05427.

[114] A. Gabbana, D. Simeoni, S. Succi, and R. Tripiccione. Relativistic Lattice Boltzmann Methods: Theory and Applications. *arXiv:1909.04502 [gr-qc, physics:hep-lat, physics:hep-ph, physics:hep-th, physics:physics]*, May 2020. arXiv: 1909.04502.

[115] Sven Huelsmann, Soeren Schlichting, and Philipp Scior. Spectral functions from the real-time functional renormalization group. *arXiv:2009.04194 [hep-ph, physics:hep-th, physics:nucl-th]*, September 2020. arXiv: 2009.04194.

[116] Pavel Buividovich, Masanori Hanada, and Andreas Schäfer. Real-time dynamics of matrix quantum mechanics beyond the classical approximation. *EPJ Web of Conferences*, 175:08006, 2018. arXiv: 1711.05556.

[117] P. V. Buividovich, M. Hanada, and A. Schäfer. Quantum chaos, thermalization and entanglement generation in real-time simulations of the BFSS matrix model. *Physical Review D*, 99(4):046011, February 2019. arXiv: 1810.03378.

[118] Erkan Tüzel, Guoai Pan, and Daniel M. Kroll. Dynamics of thermally driven capillary waves for two-dimensional droplets. *The Journal of Chemical Physics*, 132(17):174701, May 2010. Publisher: American Institute of Physics.

Appendices

A | Vertex structure

Fourier Transformation

We define the Fourier transformation as

$$\tilde{\phi}(\mathbf{k}) = \int \mathrm{d}^d x \phi(\mathbf{x}) e^{-\mathrm{i}\mathbf{k}\mathbf{x}} \tag{A.1}$$

$$\phi(\mathbf{x}) = \int \frac{\mathrm{d}^d k}{(2\pi)^d} \tilde{\phi}(\mathbf{k}) e^{\mathrm{i}\mathbf{k}\mathbf{x}} \tag{A.2}$$

for the field and analogous for the conjugate momentum π. The variational/partial derivatives become

$$\frac{\delta\tilde{\phi}(\mathbf{k})}{\delta\phi(\mathbf{x})} = e^{-\mathrm{i}\mathbf{k}\mathbf{x}}, \tag{A.3}$$

$$\frac{\delta\phi(\mathbf{x})}{\delta\tilde{\phi}(\mathbf{k})} = e^{\mathrm{i}\mathbf{k}\mathbf{x}}, \tag{A.4}$$

which necessitates the absorbption of the factor $(2\pi)^d$ into $\delta/\delta\tilde{\phi}(\mathbf{k})$ to not introduce inconsistencies.

Four-point vertex for diffusive dynamics

We proposed in Eq. (2.100) a possible alternative Hamiltonian for diffusive dynamics, where the field only appears in form of even powers of its gradient $\nabla\phi$. While it is easy to write down for the free theory, the interaction term is not immediately obvious.

The expected equation of motion for Model B contains a non-local interaction term of the form $4\nabla^2\phi^2(x)$, which should arise via a variation of the Hamiltonian w.r.t. the field as

$$\frac{\delta}{\delta\phi(x)}\mathcal{H}_I' = 4\nabla^2\phi(x)^3 = \int \mathrm{d}^d k \mathrm{d}^d k_1 \mathrm{d}^d k_2 \mathbf{k}^2 \phi(\mathbf{k}_1)\phi(\mathbf{k}_2)\phi(-\mathbf{k}-\mathbf{k}_1-\mathbf{k}_2)e^{\mathrm{i}\mathbf{k}\mathbf{x}} \tag{A.5}$$

To find $\mathcal{H}_I'$, we start with a generic ansatz, assuming spatial translation symmetry and thus conservation of momentum,

$$\mathcal{H}_I' = \int \mathrm{d}^d k \mathrm{d}^d k_1 \mathrm{d}^d k_2 f\left(\mathbf{k}, \mathbf{k}_1, \mathbf{k}_2\right) \tilde{\phi}(\mathbf{k})\tilde{\phi}(\mathbf{k}_1)\tilde{\phi}(\mathbf{k}_2)\tilde{\phi}(-\mathbf{k}-\mathbf{k}_1-\mathbf{k}_2), \tag{A.6}$$

where $f(\mathbf{k}, \mathbf{k}_1, \mathbf{k}_2)$ is a scalar function of the momenta. Variation w.r.t. $\tilde{\phi}(\mathbf{k}')$ gives

$$\frac{\delta}{\delta\tilde{\phi}(\mathbf{k}')}\mathcal{H}'_I = \frac{\delta}{\delta\tilde{\phi}(\mathbf{k}')}\int \mathrm{d}^d k \mathrm{d}^d k_1 \mathrm{d}^d k_2 f\left(\mathbf{k}, \mathbf{k}_1, \mathbf{k}_2\right) \tilde{\phi}(\mathbf{k})\tilde{\phi}(\mathbf{k}_1)\tilde{\phi}(\mathbf{k}_2)\tilde{\phi}(-\mathbf{k}-\mathbf{k}_1-\mathbf{k}_2)$$

(A.7)

$$\begin{aligned}
= & \int \mathrm{d}^d k_1 \mathrm{d}^d k_2 f(\mathbf{k}', \mathbf{k}_1, \mathbf{k}_2)\tilde{\phi}(\mathbf{k}_1)\tilde{\phi}(\mathbf{k}_2)\tilde{\phi}(-\mathbf{k}'-\mathbf{k}_1-\mathbf{k}_2) \\
& + \int \mathrm{d}^d k \mathrm{d}^d k_2 f(\mathbf{k}, \mathbf{k}', \mathbf{k}_2)\tilde{\phi}(\mathbf{k})\tilde{\phi}(\mathbf{k}_2)\tilde{\phi}(-\mathbf{k}-\mathbf{k}'-\mathbf{k}_2) \\
& + \int \mathrm{d}^d k \mathrm{d}^d k_1 f(\mathbf{k}, \mathbf{k}_1, \mathbf{k}')\tilde{\phi}(\mathbf{k})\tilde{\phi}(\mathbf{k}_1)\tilde{\phi}(-\mathbf{k}-\mathbf{k}_1-\mathbf{k}') \\
& + \int \mathrm{d}^d k_1 \mathrm{d}^d k_2 f(-\mathbf{k}'-\mathbf{k}_1-\mathbf{k}_2, \mathbf{k}_1, \mathbf{k}_2)\tilde{\phi}(-\mathbf{k}'-\mathbf{k}_1-\mathbf{k}_2)\tilde{\phi}(\mathbf{k}_1)\tilde{\phi}(\mathbf{k}_2)
\end{aligned}$$

(A.8)

$$\begin{aligned}
= & \int \mathrm{d}^d k_1 \mathrm{d}^d k_2 \tilde{\phi}(\mathbf{k}_1)\tilde{\phi}(\mathbf{k}_2)\tilde{\phi}(-\mathbf{k}'-\mathbf{k}_1-\mathbf{k}_2) \\
& \qquad \cdot \left[f(\mathbf{k}', \mathbf{k}_1, \mathbf{k}_2) + f(\mathbf{k}_1, \mathbf{k}', \mathbf{k}_2) + f(\mathbf{k}_2, \mathbf{k}_1, \mathbf{k}') + f(-\mathbf{k}'-\mathbf{k}_1-\mathbf{k}_2, \mathbf{k}_1, \mathbf{k}_2)\right]
\end{aligned}$$

(A.9)

$$\stackrel{!}{=} \int \mathrm{d}^d k_1 \mathrm{d}^d k_2 \mathbf{k}'^2 \tilde{\phi}(\mathbf{k}_1)\tilde{\phi}(\mathbf{k}_2)\tilde{\phi}(-\mathbf{k}'-\mathbf{k}_1-\mathbf{k}_2), \tag{A.10}$$

where we renamed $\mathbf{k} \to \mathbf{k}_{1,2}$ in the second step. This leads to the defining equation for f

$$\mathbf{k}'^2 \stackrel{!}{=} \left[f(\mathbf{k}', \mathbf{k}_1, \mathbf{k}_2) + f(-\mathbf{k}'-\mathbf{k}_1-\mathbf{k}_2, \mathbf{k}_1, \mathbf{k}_2) + f(\mathbf{k}_1, \mathbf{k}', \mathbf{k}_2) + f(\mathbf{k}_2, \mathbf{k}_1, \mathbf{k}')\right], \tag{A.11}$$

and thus

$$f\left(\mathbf{k}, \mathbf{k}_1, \mathbf{k}_2\right) = \frac{\mathbf{k}^4}{2\left(\mathbf{k}^2 + \mathbf{k}\mathbf{k}_1 + \mathbf{k}\mathbf{k}_2 + \mathbf{k}_1^2 + \mathbf{k}_1\mathbf{k}_2 + \mathbf{k}_2^2\right)} \tag{A.12}$$

$$= \frac{\mathbf{k}^4}{\mathbf{k}^2 + \mathbf{k}_1^2 + \mathbf{k}_2^2 + \left(\mathbf{k} + \mathbf{k}_1 + \mathbf{k}_2\right)^2}, \tag{A.13}$$

whereby we find for the interaction term up to maybe a sign and some factors of 2π

$$\mathcal{H}'_I = \int \mathrm{d}^d k \mathrm{d}^{2d} k_{1,2} \frac{\mathbf{k}^4 \tilde{\phi}(\mathbf{k})\tilde{\phi}(\mathbf{k}_1)\tilde{\phi}(\mathbf{k}_2)\tilde{\phi}(-\mathbf{k}-\mathbf{k}_1-\mathbf{k}_2)}{\mathbf{k}^2 + \mathbf{k}_1^2 + \mathbf{k}_2^2 + (\mathbf{k} + \mathbf{k}_1 + \mathbf{k}_2)^2}, \tag{A.14}$$

which will turn into a non-local and probably very complicated expression in coordinate space.

B | Hydrodynamic Green's functions

We compute in the following the propagator of the field evolving under Israel-Stewart hydrodynamics [61, 62]. Starting point is the conservation law and the definition of the current

$$\partial_\mu j^\mu = 0 \ , \quad j^\mu = \phi u^\mu + \nu_\mu, \tag{B.1}$$

such that $\phi = j^\mu u_\mu$ and $\nu^\mu = \Delta^\mu{}_\nu j^\nu$ with $\Delta^{\mu\nu} = g^{\mu\nu} - u^\mu u^\nu$, where u^μ denotes the local rest-frame velocity, and we employ the metric convention $g^{\mu\nu} = \mathrm{diag}(+,-,-,-)$. Without loss of generality the evolution equation then takes the form

$$u^\mu \partial_\mu \phi + \theta\phi = -\nabla_\mu \nu^\mu \ , \tag{B.2}$$

where $\theta = \partial_\mu u^\mu$ is the expansion rate and $\nabla^\mu = \Delta^{\mu\nu}\partial_\nu$ denotes the transverse derivative. In Israel-Stewart hydrodynamics, the dissipative field obeys the equation of motion

$$u^\mu \partial_\mu \nu^\mu = -\frac{1}{\tau_R}(\nu^\mu - \nu^\mu_{\mathrm{NS}}) \ , \tag{B.3}$$

relaxing to the Navier-Stokes limit $\nu^\mu_{\mathrm{NS}} = D\nabla^\mu\phi$ with relaxation time τ_R. Thus, in the limit of *vanishing* relaxation times τ_R for a static fluid $u^\mu = \mathrm{const}$, the evolution equation takes the form of a simple diffusion equation

$$u^\mu \partial_\mu \phi = D\Delta\phi \ , \tag{B.4}$$

where $\Delta = -\nabla_\mu\nabla^\mu$ is the transverse Laplacian.

Spectral function for Israel-Stewart Hydrodynamics

In the following, we operate under the assumption of $u^\mu = (1,0,0,0) = \mathrm{const}$ to facilitate notation. We define the Laplace transform of the field $\phi(t,\mathbf{x})$ as

$$\phi(z,\mathbf{k}) = \int_0^\infty dt e^{\mathrm{i}zt} \int d^3\mathbf{x} e^{-i\mathbf{k}\mathbf{x}} \phi(t,\mathbf{x}) \ , \tag{B.5}$$

and remark that under this transformation, the time derivative transforms as $\dot{\phi}(t,\mathbf{x}) \to -\mathrm{i}z\phi(z,\mathbf{k}) - \phi(t=0,\mathbf{k})$. Abbreviating the longitudinal components of the dissipative currents as $\nu_\parallel = \nabla_\mu\nu^\mu$, we find that the constituitive equations (B.1) and (B.3) transform as

$$-\mathrm{i}z\phi(z,\mathbf{k}) + \nu_\parallel(z,\mathbf{k}) = \phi(t=0,\mathbf{k}) \ , \tag{B.6}$$

$$-\mathrm{i}z\tau_R\nu_\parallel(z,\mathbf{k}) = \tau_R\nu_\parallel(t=0,\mathbf{k}) - (\nu_\parallel(z,\mathbf{k}) - D\mathbf{k}^2\phi(z,\mathbf{k})) \ . \tag{B.7}$$

Solving for the Laplace transform of the field, we obtain

$$\phi(z,\mathbf{k}) = \frac{-\tau_R \nu_\parallel(t=0,\mathbf{k})}{(-\mathrm{i}z + D\mathbf{k}^2)(1-\mathrm{i}z\tau_R)} + \frac{(1-\mathrm{i}z\tau_R)\phi(t=0,\mathbf{k})}{(-\mathrm{i}z(1-\mathrm{i}z\tau_R) + D\mathbf{k}^2)}. \tag{B.8}$$

If we further assume that the initial conditions are uncorrelated ($\langle \nu_\parallel(0,\mathbf{k})\phi(0,\mathbf{k})\rangle = 0$), we find the field propagator

$$G(z,\mathbf{k}) \equiv \int \mathrm{d}t e^{\mathrm{i}zt} \int \mathrm{d}^d\mathbf{x} e^{-\mathrm{i}\mathbf{k}\mathbf{x}} \Theta(t) \langle \phi(t,\mathbf{x})\phi(0,\mathbf{0})\rangle \tag{B.9}$$

$$= \frac{(1-\mathrm{i}z\tau_R)T\chi(\mathbf{k})}{D\mathbf{k}^2 - \tau_R z^2 - \mathrm{i}z} \tag{B.10}$$

with the static susceptibility $\chi(\mathbf{k}) \equiv T^{-1}\langle \phi(t=0,\mathbf{k})\phi(t=0,-k)\rangle$. The two-point function has poles at

$$z = \frac{-\mathrm{i}}{2\tau_R} \pm \frac{\mathrm{i}}{2\tau_R}\sqrt{1 - 4D\mathbf{k}^2\tau_R}\ . \tag{B.11}$$

In the limit of small spatial momentum $\mathbf{k} \to 0$, we recover Navier-Stokes dynamics plus an additional non-hydrodynamic mode

$$z_{\mathrm{hydro}} = -\mathrm{i}D\mathbf{k}^2\ , \qquad z_{\mathrm{non-hydro}} = -\frac{\mathrm{i}}{\tau_R}\ . \tag{B.12}$$

Comparing our model

We repeat here the equation of motion for diffusive dynamics, disregarding the noise such that we have

$$u^\mu \partial_\mu \nu^\mu = -\gamma\left(\nu^\mu - \frac{\mu}{\gamma}\nabla^\mu(V'(\phi) - \nabla^2\phi)\right). \tag{B.13}$$

Comparing to the Israel-Stewart equation of motion (B.3) and comparing coefficients leads us to identify

$$\tau_R \equiv \gamma^{-1}, \tag{B.14}$$

$$D \equiv \frac{\mu}{\gamma}(m_{\mathrm{eff}}^2 + k^2). \tag{B.15}$$

The poles of the propagator are therefore located at

$$z = \frac{-\mathrm{i}\gamma}{2} \pm \frac{\mathrm{i}\gamma}{2}\sqrt{1 - 4\frac{\mu}{\gamma^2}(m_{\mathrm{eff}}^2 + \mathbf{k}^2)\mathbf{k}^2}\ . \tag{B.16}$$

While for finite Langevin coupling γ the limit of low momentum still contains the Navier-Stokes–like mode, the limit $\gamma \to 0$ fundamentally changes the infrared structure of the dynamics. We are then in the limit of *infinite* relaxation times, with only real poles at

$$z = \mp\sqrt{\mu(m_{\mathrm{eff}}^2 + \mathbf{k}^2)}|\mathbf{k}|. \tag{B.17}$$

We can therefore realistically expect also the critical behaviour to change significantly, as opposed to the case of the non-relativistic Model D described e.g. in [96, 97].

C | Breit-Wigner function

The order-parameter spectral functions obtained from mean-field calculations in the models considered are of Breit-Wigner shape, i.e.

$$\rho(\omega) \propto \frac{\omega}{(\omega^2 - m_p^2)^2 + \gamma^2\omega^2}, \tag{C.1}$$

where the central frequencies are given by $m_p^2 = \bar{p}^\alpha(m^2 + p^2)$. To transform it into the time domain, one first performs a slight reparametrization of the form

$$M_p^2 = m_p^2 - \frac{\gamma^2}{2}, \tag{C.2}$$

$$\Gamma^2 = \frac{\gamma^2}{2}\frac{4m_p^2 - \gamma^2}{2m_p^2 - \gamma^2}, \tag{C.3}$$

such that the spectral functions become

$$\rho(\omega) \propto \frac{\omega}{(\omega^2 - M_p^2)^2 + \Gamma^2 M_p^2}. \tag{C.4}$$

The Fourier transform of the latter form can be expressed as

$$\tilde{\rho}(t) \propto e^{-A|t|}\left(e^{\mathrm{i}Bt} - e^{-\mathrm{i}Bt}\right) \tag{C.5}$$

with parameters

$$A \equiv \mathrm{i}m\sqrt{\frac{1}{2} + \sqrt{1 + \frac{\Gamma^2}{M_p^2}}}, \tag{C.6}$$

$$B \equiv -\frac{m}{\sqrt{1 - \sqrt{1 + \frac{\Gamma^2}{M_p^2}}}}. \tag{C.7}$$

Breit-Wigner autocorrelation time

Starting with the mean-field shape of the spectral function (4.33), we find

$$\int_0^\infty t\rho(t)\mathrm{d}t \overset{\rho(t)\,\mathrm{odd}}{=} \frac{1}{2}\int_{-\infty}^\infty t\rho(t)\mathrm{d}t = \mathrm{i}\,\frac{\mathrm{d}}{\mathrm{d}\omega}\rho(\omega)\bigg|_{\omega=0} \propto \frac{\Gamma}{\omega_p^4}, \tag{C.8}$$

$$\int_0^\infty \rho(t)\mathrm{d}t = \int_{-\infty}^\infty \Theta(t)\rho(t)\mathrm{d}t = \int \mathrm{d}\omega' \mathcal{F}\left[\Theta(t)\right](\omega')\rho(\omega - \omega')\bigg|_{\omega=0} \tag{C.9}$$

$$\int \mathrm{d}\omega' \left(\frac{-\mathrm{i}}{\omega'} + \pi\delta(\omega')\right)\rho(\omega') \tag{C.10}$$

but since $\rho(\omega = 0) = 0$, the δ-term does not contribute. For the remaining integral, we employ the residue theorem. We note that the function

$$\rho_{\mathrm{BW}}(\omega, \mathbf{p})/\omega = \frac{p^a \Gamma}{\left(\omega^2 - \omega_p^2\right)^2 + \Gamma^2 \omega^2} \tag{C.11}$$

has four first-order poles in ω, namely

$$\omega_R^2 = -\frac{\Gamma^2 - 2\omega_p^2}{2} \pm \sqrt{\left(\frac{\Gamma^2 - 2\omega_p^2}{2}\right)^2 - \omega_p^4} \tag{C.12}$$

$$= -\frac{1}{2}\left(A \pm B\right), \tag{C.13}$$

where we abbreviate $A \equiv \Gamma^2 - 2\omega_p^2$, $B \equiv \Gamma\sqrt{\Gamma^2 - 4\omega_p^2}$. One can thus express

$$\frac{\rho_{\mathrm{BW}}(\omega)}{p^a \Gamma \omega} = \left[\left(\omega^2 + \frac{1}{2}(A+B)\right)\left(\omega^2 + \frac{1}{2}\left(A-B\right)\right)\right]^{-1} \tag{C.14}$$

$$= \left[\left(\omega + \frac{\mathrm{i}}{\sqrt{2}}(A+B)^{1/2}\right)\left(\omega - \frac{\mathrm{i}}{\sqrt{2}}\left(A+B\right)^{1/2}\right)\right. \\ \left.\left(\omega + \frac{\mathrm{i}}{\sqrt{2}}\left(A-B\right)^{1/2}\right)\left(\omega - \frac{\mathrm{i}}{\sqrt{2}}\left(A-B\right)^{1/2}\right)\right]^{-1} \tag{C.15}$$

$$\equiv \left[\left(\omega - \omega_1\right)\left(\omega - \omega_2\right)\left(\omega - \omega_3\right)\left(\omega - \omega_4\right)\right]^{-1}, \tag{C.16}$$

where of course $\omega_1 = -\omega_2$ and $\omega_3 = -\omega_4$. One now has to distinguish two cases for the real parameters Γ, ω_p: By Taylor expansion of B one quickly finds

$$\text{case 1}: \ \Gamma > 2\omega_p > 0: \quad \Rightarrow \quad A > B > 0, \qquad \Rightarrow \qquad \Im(\omega_2) > 0,\ \Im(\omega_4) > 0, \tag{C.17}$$

$$\text{case 2}: \ 2\omega_p > \Gamma > 0: \quad \Rightarrow \quad \Re(B) = 0,\ \Im(B) > 0 \qquad \Rightarrow \qquad \Im(\omega_2) > 0,\ \Im(\omega_3) > 0. \tag{C.18}$$

By Taylor expansion of B one quickly finds that $A > B > 0$ if $\Gamma^2 > 2\omega_p^2$, which is a reasonable assumption for low momentum p (compare Fig. 4.13). We choose to complete the integration contour by a semi-circle over the positive half plane, where always two of the poles lie. For the residues one finds

$$\mathrm{Res}_{\omega_2} = \left[\left(\omega_2 - \omega_1\right)\left(\omega_2 - \omega_3\right)\left(\omega_2 - \omega_4\right)\right]^{-1} \tag{C.19}$$

$$= \left[\frac{2i}{\sqrt{2}}\left(A+B\right)^{1/2}\left(\frac{-1}{2}(A+B) + \frac{1}{2}(A-B)\right)\right]^{-1} \tag{C.20}$$

$$= \left[\frac{-2i}{\sqrt{2}}\left(A+B\right)^{1/2} B\right]^{-1}, \tag{C.21}$$

$$\mathrm{Res}_{\omega_3} = \left[\frac{-2i}{\sqrt{2}}\left(A-B\right)^{1/2} B\right]^{-1}, \tag{C.22}$$

$$\mathrm{Res}_{\omega_4} = \left[\frac{2i}{\sqrt{2}}\left(A-B\right)^{1/2} B\right]^{-1}, \tag{C.23}$$

For the critical spectral function at low spatial momentum, mostly $\Gamma \gg \omega_p$, so we consider here only the first case, and find

$$\int \mathrm{d}\omega \frac{\rho_{\mathrm{BW}}(\omega)}{p^a \Gamma \omega} = 2\pi \mathrm{i} \left\{ \mathrm{Res}_{\omega_2} + \mathrm{Res}_{\omega_4} \right\} \tag{C.24}$$

$$= 2\pi \mathrm{i} \left\{ \frac{\sqrt{2}\mathrm{i}}{2B} \frac{\sqrt{A-B} - \sqrt{A+B}}{\sqrt{A^2 - B^2}} \right\} \tag{C.25}$$

$$\approx 2\pi \mathrm{i} \left\{ \frac{\sqrt{2}\mathrm{i}}{2B} \frac{-\sqrt{2B}}{2\omega_p^2} \right\} \approx 2\pi \left\{ \frac{1}{2\Gamma^2} \frac{\Gamma}{\omega_p^2} \right\} = \frac{\pi}{\Gamma \omega_p^2}. \tag{C.26}$$

where we used that $A^2 - B^2 = 4\omega_p^4$ and, for $\Gamma \gg \omega_p$ one has $A \approx B \approx \Gamma^2$. This implies for the autocorrelation time the relation

$$\xi_{t,\mathrm{BW}} = \frac{\int_0^\infty t\rho(t)\mathrm{d}t}{\int_0^\infty \rho(t)\mathrm{d}t} \sim \frac{\Gamma}{\omega_p^2}. \tag{C.27}$$

D | Structure of the spectral function at low temperatures

In the ordered phase, at $\tau < 0$, the spectral functions show not only a quasi-particle structure, but also a second mode at lower frequencies. If one plots the spectral function over the squares of spatial momentum and frequency, it becomes apparent that the two structures are separated by the light cone, i.e. the low-frequency excitation inhabits the space-like region. Tracking the maximum $\rho(\omega_{\max}, p) = \max \rho(\omega, p)|_{\omega^2 < p^2}$ of the spectral function in that region, one finds for the dispersion relation roughly a power-law behavior of the form,

$$\omega_{\max}^2 \propto p^d, \tag{D.1}$$

in d spatial dimensions. For $d = 3$ this agrees with the well-known dispersion relation of thermally driven capillary waves. In $d = 2$ spatial dimensions the situation seems less clear. In Ref. [118] for example, the excitation spectra of two-dimensional fluid droplets have been studied with resulting dispersion relations that depend on the details of the fluid parameters.

In Fig. D.1 we show exemplary low-temperature spectral functions in $d = 2$ and 3 spatial dimensions, as functions of frequency and momentum squared. The time-like and space-like parts are separated by different colors, and the light-cone is shown as a solid line in the colormap projection in the bottom plane. The light-cone marks the separation between the quasi-particle and the soft mode. In $d = 3$ dimensions this soft mode closely follows the power-law dispersion relation of thermally driven capillary waves as seen in the bottom right panel of Fig. D.1 where we plot a solid line with $\omega = p^{3/2}$ for comaprison. Bottom left we show the corresponding quasi-particle mode above and soft mode below the light-cone in $d = 2$ dimensions together with an ideal sound-wave dispersion $\omega = p/\sqrt{3}$ to guide the eye.

Close to the critical temperature, the low-frequency part grows in magnitude and seems to merge with the quasi-particle. In the symmetric phase, at $\tau > 0$, there is only the quasi-particle peak left.

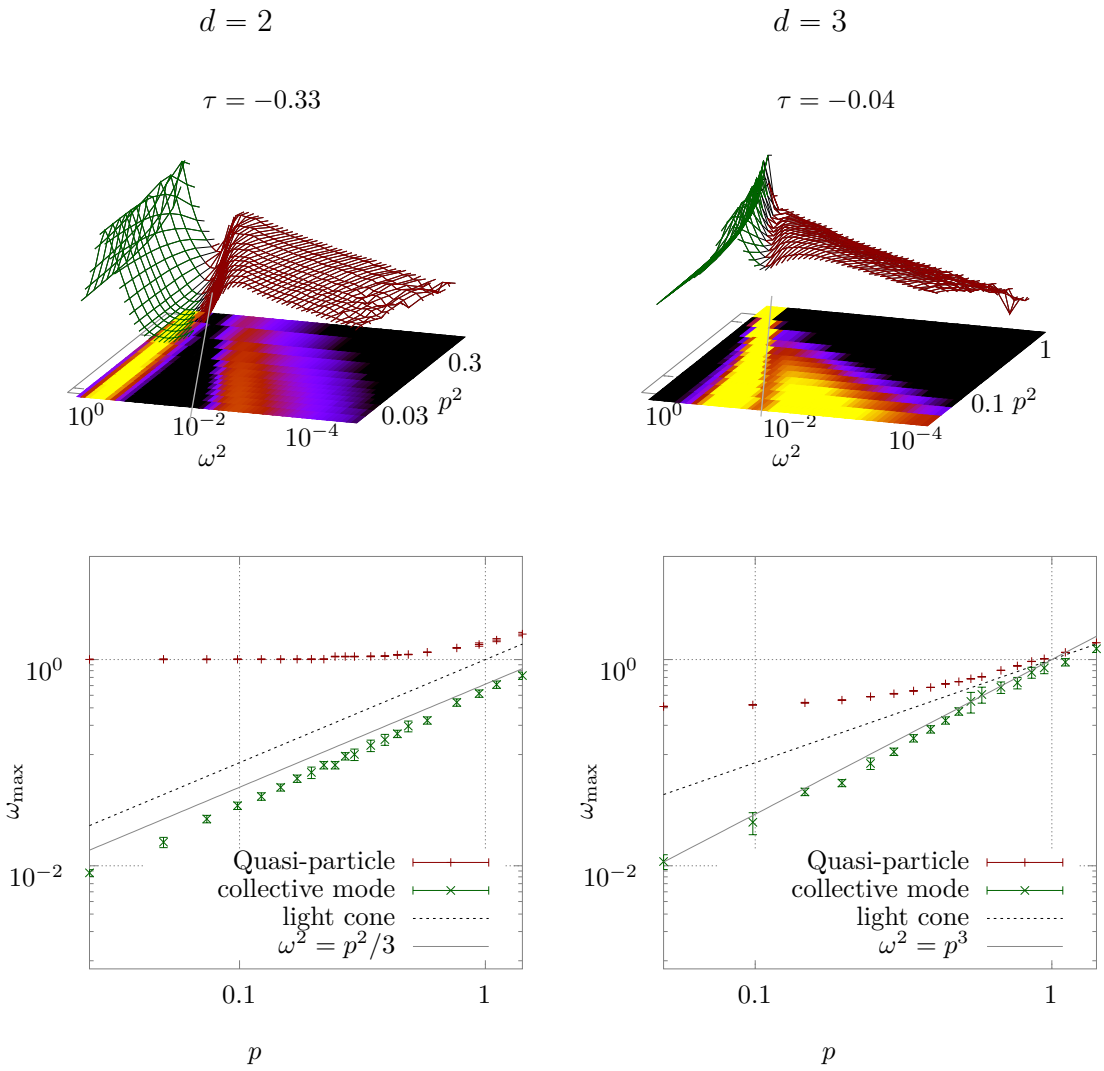

Figure D.1: Spectral functions in the low-temperature phase for Hamiltonian dynamics (Model C, $\gamma = 0$) in $d = 2$ (left) and $d = 3$ (right) spatial dimensions. Time-like parts (where $\omega^2 - p^2 > 0$ are plotted with green lines, space-like parts (where $\omega^2 - p^2 < 0$) with red lines. The colormap-projections at the bottom also show solid lines where $\omega^2 - p^2 = 0$, indicating the light-cone. In the bottom panels we show the corresponding dispersion relations of the quasi-particle peaks (above) and the soft modes (below the light-cone), by tracing the positions of the respective local maxima in the spectral function. For comparison, we also plot solid lines, for an ideal sound-wave dispersion relation $\omega^2 = p^2/3$ in $d = 2$ (left), and for cappillary waves with $\omega^2 = p^3$ in $d = 3$, to guide the eye. At high spatial momenta p, the soft mode dissolves in 3+1D.

Acknowledgments

The author acknowledges support by the Deutsche Forschungsgemeinschaft (DFG, German Research Foundation) through the CRC-TR 211 'Strong-interaction matter under extreme conditions'– project number 315477589 – TRR 211.

Personally, I want to thank my supervisor, Professor Lorenz von Smekal, for the opportunity to study this project, and to profit from his immense knowledge and experience, as well for as his encouragement along the way. My gratitude extends also to Professor Sören Schlichting for helpful discussions, competent advice and highly productive times at Bielefeld University.

I also want to express my gratefulness towards my friends and colleagues at the Institut für Theoretische Physik. Although our time together was sadly very limited by pandemic circumstances in the last year, I very much enjoyed the supportive environment and pleasant atmosphere. Special thanks go to Julian Bernhardt and Milad Ghanbarpour, for their bright insights on polyhedra, collaboration on common art projects, and lots of fun facts about Hilbert spaces.

I want to thank my family and friends for their unconditional support and encouragement.

But undoubtedly the most gratitude I owe to Claire, for her patience enduring all my highs and lows, for taking care of my sanity, and always believing in me.

Selbstständigkeitserklärung

Ich erkläre: Ich habe die vorgelegte Dissertation selbständig und ohne unerlaubte fremde Hilfe und nur mit den Hilfen angefertigt, die ich in der Dissertation angegeben habe. Alle Textstellen, die wörtlich oder sinngemäß aus veröffentlichten Schriften entnommen sind, und alle Angaben, die auf mündlichen Auskünften beruhen, sind als solche kenntlich gemacht. Bei den von mir durchgeführten und in der Dissertation erwähnten Untersuchungen habe ich die Grundsätze guter wissenschaftlicher Praxis, wie sie in der "Satzung der Justus-Liebig-Universität Gießen zur Sicherung guter wissenschaftlicher Praxis" niedergelegt sind, eingehalten.

Ort, Datum

Unterschrift